UNIVERSITY OF CALIFORNIA

Santa Barbara

# Tailorable Biomaterials for Additive Manufacturing

A dissertation submitted in partial satisfaction of the

requirements for the degree Doctor of Philosophy

in Chemistry

by

Ronnie Vincent Garcia

Committee in charge:

Professor Craig J. Hawker, Co-Chair

Professor Javier Read de Alaniz, Co-Chair

Professor Angela Pitenis

Professor Christopher Bates

Professor Matthew Helgeson

March 2024

The dissertation of Ronnie V. Garcia is approved.

Professor Christopher M. Bates

Professor Matthew Helgeson

Professor Angela Pitenis

Professor Javier Read de Alaniz, Committee Co-Chair

Professor Craig J. Hawker, Committee Co-Chair

March 2024

Tailorable Biomaterials for Additive Manufacturing



by

Ronnie Vincent Garcia

This dissertation is dedicated to my niece (Andrea Rose), godfather (Jose Tapias), and grandma (Emiteria). Y'all saw me start my PhD journey but did not stick around long enough to see me finish. Puedes descansar en paz proque por fin soy doctor.

# Acknowledgments

First, I would like to thank my two advisors, Craig and Javier. Their guidance, patience, and mentorship played a crucial role in my development as a scientist, making choosing UCSB over other schools one of the best decisions in my life. Craig gave me the flexibility to grow as a curious chemist/material scientist and challenged me to be a better version of myself. He taught me the importance of return on investment (ROI), cashing out at a global maximum rather than a local minimum, and knowing when to cut your losses, all in the context of research (and potentially in business, too). Craig's emphasis on science communication and good presentation skills have taught me how to effectively present my work, which always leaves audience members impressed. This has made me a connoisseur of good presentation and I now unconsciously cringe at bad presentation or non-green laser pointers. Also, I would like to thank his ability to recruit great talent and foster a collaborative environment.

Javier has been a wonderful advisor and cheerleader throughout my Ph.D., and I know I can always rely on him for a pick-me-upper after rough times. His excitement for science is contagious and I am glad to be able to spitball wild ideas with him. Although he has a lot on his plate, he always made time for me, whether for research help, administrative help, or to reassure me everything would be fine. I know Javier is always excited about the science in his group, but he is more excited about the future and potential of his students. I hope to one day grow up with his never-ending enthusiasm for science and patience.

I would also like to thank my mentors who served as advisors throughout my PhD journey and illuminated the path forward. Dr. Robert Murphy took me under his wing and

taught me everything I know about polypeptide synthesis and biomaterials. Although it was a rough time during the global pandemic, Rob always kept me excited and hopeful about research and made the night shift during lockdown a fun time. He always served as a reliable source of wisdom, knowledge, and empathy, even when he was thousands of miles away. I hope one day to help you open a San Diego branch of your future successful company. Dr. Nairiti Sinha, now Professor Nairiti Sinha, complimented Rob's synthetic training by training me in characterization and self-assembly. She always got excited and got me excited about the potential secondary, tertiary, and quaternary structures my materials were making. I know I can always rely on her to help me understand the complex physics of my systems. I would like to thank another Hawker alumni, Dr. Justin Poelma, for taking a chance with me and letting me intern at Carbon. It was one of my favorite summers during my Ph.D., and you taught me that there is still a lot of opportunity for curiosity-based research in industry.

I also would not be as successful without great colleagues in the Hawker and Read de Alaniz group. I truly believe we are one of the most collaborative academic environments, and I would like to thank everyone for making work fun and exciting. A special thanks to all my collaborators and co-authors, my papers would not have been possible without everyone's contribution. I want to give a shout-out to my cohort that joined the lab at the same time as me: Declan Shannon, Dr. Lindsay Robinson, Patrick "Pat" Getty, Michael "Mike" Czuczola, and Thi Tran. We faced this wild ride together, and our hangouts were much-needed time to celebrate and complain about the ups and downs of PhD.

The faculty and staff of UCSB enabled me to pursue excellence in research. Thank you to my committee Chris Bates, Matthew Helgeson, and Angela Pitenis. It is not common for a

student to say they interact with their committee members often, but I had the pleasure of constantly interacting with my committee for their guidance and wisdom. I would like to give a special thanks to the unsung heroes, the staff and staff scientists of MRL, CNSI, BioPacific, and Chemistry including Rachel Behrens, Juan Manuel Urueña Vargas, Amanda Strom, Jen Smith, Hongjun Zhou, Morgan Bates, Paul Sarte, Jess Henry, Wendy Ibsen, Arica Lubin, Dotty Pak, Julie Standish. I would also like to thank my fellow leadership team of Chemistry Professional Development (ChemPD) because we enabled students to grow professionally together.

Last but certainly not least, I would like to thank my friends and my family. My high school friends, thank you for keeping me rooted every time I returned home and reminding me how far I had gotten. My undergraduate friends, thank you for reminding me how much ambition and drive I had in my UCLA days to get a Ph.D. and evoking that energy. My PhD friends, thank you for sharing the ups and downs of graduate school. Although keeping the work talk to a minimum was difficult, you made my life fun outside of the lab. My family has been the best thing I could have asked for, and their infinite support, especially to my mom (Maria Rosalba), my dad (Gerardo), my sister (Araseli), and my nephew/godson (Brandon). I know these last 5 years have been plagued with tragedies, but together, we healed and became stronger. None of this would have been possible without your support. Gracias a mi familia por ser mi sistema de apoyo. Estos últimos años han sido los más difícil, pero juntos logramos el difícil.

# Vita of Ronnie V. Garcia

## EDUCATION

**University of California, Santa Barbara** 03/2019 – present
Santa Barbara, California

- Doctor of Philosophy, Materials Chemistry
- Thesis: "Tailorable Biomaterials for Additive Manufacturing"
- GPA: 3.98

**University of California, Los Angeles** 2014 – 2019
Los Angeles, California

- B.S., Chemistry-Material Science, Organic Concentration
- GPA: 3.3

## RESEARCH EXPERIENCE

**Hawker and Read de Alaniz Research Groups** 03/2019-current
Department of Chemistry and Materials, UCSB
Graduate Researcher

- Dr. Craig J. Hawker and Dr. Javier Read de Alaniz, principal investigators

Synthesized, characterized, and processed copolypeptide hydrogel for 3D bioprinting
Parsed mechanical properties, microstructure, and failure analysis using various rheology techniques to quantify structure-function relationship and extrudability
Developed enzymatic digestion for controlled degradation of polypeptide material
Collaborated with colleagues on synthesizing and testing biomimetic materials and co-authored papers
Developed synthetic method to post-functionalized 3D printed surfaces to modulate surface properties
Funded through NSF GRFP and Biopacific MIP

**Carbon** 06/2022 – 09/2022
Redwood City, California
Materials Engineer Graduate Intern, Materials Division

- Dr. Justin Poelma, supervisor
- Utilized Design of Experiment (DOE) to explore cost-effective formulation spaces and material processes that will lower production costs
- Optimized rigid urethane formulation that increased heat deflection temperature by 50% and impact strength by 290% compared to current product with 25% cheaper material
- Evaluated fillers and processing in elastomeric composites for impact modifiers

**Garcia-Garibay Research Group** 09/2015 – 12/2019
Dept. of Chemistry, UCLA
Undergraduate Research Assistant

- Dr. Miguel Garcia-Garibay, principal investigator
- Strategized diverging synthesis of functional pentiptycene: D4h organic building blocks
- Synthesizing a molecular dirotor with varying solid-state absorption, fluorescence, and birefringence
- Perform air and water-free synthesis using pyrophoric chemicals

**Meijer Research Group** 06/2018 – 10/2018
Dept. of Chemistry and Chemical Biology, Eindhoven University of Technology
Visiting Researcher

- Dr. Beirt Meijer, principal investigator
- Fabricated photo-thermal actuators that convert UV light into mechanical energy
- Investigated the synchronization of multi-oscillating cantilever and study the mechanism of coupling
- Funded through NSF MRSEC

**Hawker Research Group** 09/2012 – 09/2013
Material Research Lab, UCSB
Visiting Researcher

- Dr. Craig J. Hawker, principal investigator
- Assisted in developing a novel 3D printer with fast production rates (>1m/hr), which greatly exceeded rates of
  traditional layer-based techniques (10-50 mm/hr)
- Tested polymerization kinetics of resins for optimized formulation
- Quantified mechanical properties of different polymer materials using tensile testing and digital image correlation
- Funded through UC LEADS

## PUBLICATIONS *equal contribution

1. **Garcia, R.V.,** Murphy, E., Sinha N., Okayama, Y., Urena J.M., Helgeson M.E., Bates, C.H., Hawker, C.J., Murphy, R.D., Read de Alaniz, J. "Tailoring Writabilility and Performance of Star Block Copolypeptides Hydrogels through Side-Chain Design" *Small*. **2023** 2302794
2. **Garcia, R.V.*,** Murphy, R.D.*, Oh, S.J., Wood T.J., Jo K.D., Read de Alaniz, J., Perkins, Ed., Hawker, C.J. "Tailored Polypepitde Star Copolymer for 3D printing of Bacterial Composites Via Direct Ink Writing" *Adv. Mater*. **2022**, 2207542
3. Shannon, D.P., Moon, J.D., Barney C.W., Sinha N.J., Yang K.C., Jones S.D., **Garcia R.V.,** Helgeson M.E., Segalman, R.A., Valentine M.T., Hawker C.J. "Modular Synthesis of Patterning of High-Stiffness Networks by Postpolymerization Functionalization with Iron─Catechol Complexes" *Macromolecules* **2023**, 56, 2268
4. Murphy, R. D., **Garcia, R.V.,** Heise, A., Hawker, C.J. "Peptides as 3D printable Feedstocks: Design Strategies and Emerging Application" *Prog in Polym. Sci,* **2021,** 124, 101487
5. Yang, K.C., Mirabal, D. R., **Garcia, R.V.**, Nguyen P.H., Mengel S.D., Shell S.M., Hawker, C.J., Segalman R.A. "Crystallization Induced Flower-like Superstructures via Peptoid Helix Assembly" *submitted*.
6. **Garcia, R.V.,** Orias H., Read de Alaniz J., Hawker, C.J. "Star copolypeptide as Degradable Rheological Modifiers for Direck Ink Writing of Gelatin" *in progress*
7. Murphy R.M., **Garcia R.V.**, Fattah S., Fallon M., Heise A., Hawker C.J. "Antimicrobial Polypeptide Hydrogels as Resin for Direct Laser Writing" *in preparation*
8. Kaneko T., Bailey S.J., **Garcia R.V**., Urena J.N. ,Hawker C.J., Read de Alaniz J. "Development of a 3D Printable Resin Cured via Diels-Alder Photoclick Chemistry" *in progress*
9. Howe, M.E., Barbour, N. A., **Garcia, R. V.,** Garcia-Garibay, M. A. "Fluorescence Anisotropy Decay of Molecular Rotors with Acene Rotators in Viscous Solution" *J. Org. Chem.*, **2020**, 85, 6877
10. Dolinski, N. D., Page, Z. A., Callaway, E. B., Eisenreich, F., **Garcia, R. V**., Chavez, R., Bothman, D. P., Hecht, S., Zok, F. W., Hawker, C. J. "Solution Mask Liquid Lithography (SMaLL) for One-Step, Multimaterial 3D Printing" *Adv. Mater*. **2018**, 30, 1800364.

## ORAL AND POSTER PRESENTATIONS

Title: Engineering Star Block copolypeptides for 3D Printing

- Material Research Society (MRS) Spring Conference, San Francisco,CA, April 10-14 2023, oral presentation
- Material Research Outreach Program (MROP), Santa Barbara,CA, January 25-26 2023, poster presentation

Title: Efficient Synthesis of Pentiptycene: Symmetrical Organic Building Blocks for New Material

- UCLA CARE Summer Programs for Undergraduate Research Poster Presentation, UCLA, August 29, 2016. Poster Presentation
- Annual Biomedical Research Conference for Minority Student (ABRCMS), Tampa, FL, November 9-12, 2016. Poster Presentation
- UC LEADS Symposium. UCLA. March 11, 2017. Poster Presentation.
    - Distinguished Poster Presentation, Physical Science
- ACS Southern Undergraduate Research Conference. UCLA. April 29,2017. Poster Presentation
- UCLA Undergraduate Research Poster Session. UCLA. May 23, 2017. Poster Presentation

Title: A New Avenue for 3D Printing: Making Materials with Variable Mechanical and Chemical Properties

- UCSB Undergraduate and Graduate Student Research Colloquium. UC Santa Barbara. August 12, 2017. Poster Presentation
- Annual Biomedical Research Conference for Minority Students (ABRCMS). Phoenix, AZ. November 1-4, 2017. Poster Presentation
    - Distinguished Poster Presentation, Engineering
- UC LEADS Symposium. UC Santa Barbara. March 10, 2018. Poster Presentation

Title: Development of Efficient Syntheses of Pentiptycene Derivatives for Constructing Molecular Gyroscopes

- UCLA Undergraduate Research Poster Session. UCLA. May 23, 2018. Poster Presentation

Title: Coupled Motion of Soft Actuators: Potential in Organic Sensors

- Program for Excellence in Education and Research in the Sciences (PEERS) Poster Session. UCLA. November 8, 2018. Poster Presentation
- Annual Biomedical Research Conference for Minority Students (ABRCMS). Indianapolis, IN. November 14-17, 2018. Poster Presentation

## FELLOWSHIP, SCHOLARSHIPS, AWARDS, AND HONORS

- ACS Career Jumpstart, 2023
- Dow's BEST, 2023
- Heeger Fellowship, 2023
- Chase Mabel Fellowship, 2023
- BioPacific MIP Fellowship, 2021
- NSF Graduate Research Fellowship Program (GRFP), 2019
- Elmer Carvey Scholarship, 2017
- Alpha Chi Sigma Research Scholarship, 2017
- Walt Disney Scholarship, 2017
- UC LEADS and IMSD scholar, 2016
- Hispanic Scholarship Foundation Recipient, 2015
- Wilson Scholarship, 2014

## MEMBERSHIPS AND AFFILIATIONS

- Alpha Chi Sigma Professional Chemistry Fraternity
- American Chemical Society
- Material Research Society

## SKILLS

- Innately organized and highly proficient at effective time management practices and multi-tasking.
- Excellent verbal and written communication, leadership, and lab management skills.
- Small molecule synthesis, Schlenk line technique
- Polymer synthesis: ring-opening polymerization (ROP), free-radical polymerization (FRP), ring-opening metathesis polymerization (ROMP)
- Chromatography: size exclusion chromatography (SEC), high-performance liquid chromatography (HPLC), flash column chromatography
- Rheology: oscillatory, flow, photo, viscometry
- Spectroscopy: nuclear magnetic resonance (NMR), fourier transform infrared spectroscopy (FTIR), UV-Vis, fluorescence
- Mass Spectrometry: matrix-assisted laser desorption ionization time-of-flight (MALDI TOF), electrospray ionization (ESI)
- Assays: TNBSA assay, live-dead staining, enzyme degradation
- Thermo-Mechanical Testing: dynamic mechanical analysis (DMA), differential scanning calorimetry (DSC), thermalgravimetric analysis (TGA)
- Material Testing: tensile testing, compression, Izod impact testing
- ChemDraw, Microsoft Office, Igor, Windows, Uncountable, JMP.
- Python programming languages.
- Spanish (native speaking, reading, and writing skills).

## MENTORING

- Roz Borah, undergraduate student
- Holden Orias, undergraduate student
- Marializ Nieves, undergraduate student
- Takashi Kaneko, graduate student

## NON-LABORATORY EXPERIENCE

**Chemistry Professional Development (ChemPD)** 10/22-present
Alumni Chair

- Organized annual Chemistry Career Day, a student lead event that invites industry recruiter
- Fundraised and applied for grants to fund career day and industry seminars
- Invited industry guest speakers for seminars and professional development workshop

**MRL Outreach** 10/19-present
Volunteer

- Participated in various material science theme demos for K-12 outreach events

**CNSI's School for Scientific Thought** 03/22
Course Instructor

- Created a two-day course on hydrogels to teach high school students its use in everyday life and biomedical research
- Developed hands-on demos and labs where students can get hands-on experience with the scientific method

**AVID Alumni Association** 10/15-10/18
External Vice-President

- Organized on-campus visitation for underrepresented minorities in high school
- Applied for internal and external funds to support our efforts

# Abstract

Tailorable Biomaterials for Additive Manufacturing

by

Ronnie V. Garcia

Additive Manufacturing, also commonly known as 3D Printing, has significant potential for personalized medicine and biomedical devices, owing to its streamlined design-to-production workflow. Unlike traditional manufacturing techniques, 3D printing allows for the creation of highly tailored products that can be precisely designed to meet the specific needs of individual patients. Current printable biomaterials are limited to synthetic and biological polymers and their range in material properties. Although synthetic polymers are tunable, they lack degradability. Unlike synthetic polymers, biopolymers are biodegradable, but their properties are limited to those found in nature. Therefore, there is a need for tunable and biodegradable materials in 3D printing to help expand its capability.

In **Chapter 1**, the 3D printing hydrogel literature is surveyed, and polypeptides based on *N*-carboxyanhydride (NCA) are recognized as a potential feedstock that can diversify the printable material palette. In **Chapter 2** and **Appendix A**, a library of star block copolypeptide composed of a consistent inner hydrophilic block and different β-sheet outer blocks were synthesized. By varying the β-sheet forming domains, shear-processable hydrogels with diverse microstructure and mechanical properties were prepared and structure-function relationships were determined. The versatile synthesis of these star block copolypeptides provides a robust platform to tune material properties based solely on molecular design.

Utilizing these systems in 3D printing, specifically Direct Ink Writing (DIW), eliminates the necessity for additives and provides a synthetic handle to tailor its functionality.

In **Chapter 3** and **Appendix B**, photocrosslinkable groups were facilely integrated into the star block copolypeptide scaffold to allow subsequent chemical crosslinking with visible light after DIW. *Escherichia Coli* was integrated into these hydrogel inks and biological composites with complex geometries were achieved in these bioinert printing conditions. Furthermore, the tunable properties of different copolypeptide networks enable control over proliferation and colony formation for embedded microbes as demonstrated based on green fluorescent protein (GFP) expression. Opening the possibility of controlling integrated biological behavior through the molecular design of the star copolypeptide matrix.

To demonstrate the ease of use of these star copolypeptides, **Chapter 4** and **Appendix C** delve into their utilization as rheological modifiers within the widely used Gelatin Methacrylamide (GelMA) bioinks. The temperature stability of the star copolypeptide networks allows these GelMA hybrids to be extruded at physiological temperatures, facilitating their utilization for integrating mammalian cells for bioprinting. In contrast to conventional rheological modifiers, the star copolypeptide participates in photochemical crosslinking with GelMA while preserving its natural biodegradability. This approach, employing star copolypeptides as rheological modifiers for DIW, showcases the prospective integration of bioactive materials and fluids, paving the way for modular bioinks. This thesis aims to unveil the unexplored capabilities of star copolypeptides as a tailorable material, propelling the frontier of bioprinting.

# Table of Contents

# List of Figures

Ponte las pilas

-Anonymous

# Chapter 1. Introducing Peptides as a Tailorable 3D Printable Feedstock

Portions of this work were published in:

Robert D. Murphy, Ronnie V. Garcia, Andreas Heise, and Craig J. Hawker Peptides as 3D printable feedstocks: Design strategies and emerging applications, *Prog in Polym. Sci.* **2022**, 101487. Reproduced with permission from Elsevier.

## 1.1 Motivation for 3D printing

Recent technological advances in wearable sensor, machine learning, and data science have led to a revolution in personalized medicine where each patient's unique molecular, anatomical, and genetic characteristics are influential and addressed during treatment. For this individualized model, prosthetic parts,[1] dental implants,[2] surgical models,[3] bone implants,[4] and implantable tissue scaffolds [5] are coupled with modern medical imaging tools to enable rapid acquisition of 3D models of patient's organs and tissues. However, a major hurdle with this approach is matching manufacturing with the speed and customizability of imaging. Successful integration of high throughput imaging, modeling, and fabrication of implants has the potential to push the boundaries of precision medicine. While traditional manufacturing strategies, such as injection molding are rapid, they lack the desired customizability. Three-dimensional (3D) printing, or additive manufacturing (AM), is a material manufacturing method capable of addressing such challenges. Using a range of different deposition methodologies and with the assistance of computer aided design (CAD), recent advances in 3D printing methodologies have simplified the rapid design/generation of structurally complex architectures and geometries, otherwise unattainable using fabrication techniques such as molding or casting.[6] Utilized materials range from thermosetting polymer filaments to bulk monomer resins with implementation dependent on the demands of the 3D printing system. More recently, hydrogelating polymers have emerged as viable, tunable feedstocks in a broad range of 3D printing applications.[7] To illustrate their versatility, synthetic hydrogels have been employed in a range of 3D printing techniques (Fig. 1) including, direct ink writing (DIW), inkjet printing, stereolithography (SLA), and digital light processing (DLP). While each method has its own unique set of working parameters, the fidelity and resolution of deposited 3D structures

is heavily dependent on material selection. This chapter will cover the limitation in traditional synthetic and natural biopolymer inks and the growing need to use new tailorable biomaterials. Second, the different types of 3D printing technologies and recent advances in using protein and sequence define peptides will be discussed. Finally, the synthesis of polypeptide based on *N*-carboxyanhydride (NCA) ring opening polymerization (NCA ROP) will be discussed and how the polymer composition, architecture, and secondary structure can be tuned to expand the 3D printable material palette. Utilization of NCA-derived polypeptide for 3D printing is an underexplored area of research, and this thesis hopes to showcase that it is an emerging feedstock with great potential.

## 1.2 The Need for New Printable Biomaterials

Advances in the 3D printing of hydrogels has found use in biomedical science, specifically in tissue engineering (TE). In traditional TE, cells and growth factors are combined with prefabricated hydrogel 3D scaffolds, forming an implantable 'bioactive' scaffold.[8] Recent work has shown that using a combination of TE and 3D printing, termed '3D bioprinting', scaffolds can be produced on-demand with a higher degree of control over cell distribution and growth factor loading compared to scaffolds prepared via conventional methods. This allows microstructural patterning similar to that found in the extracellular matrix (ECM) of native tissue [9] with this bioprinting promise highlighted by recent advances in personalized medicine,[10] synthetic organ printing,[11] microfluidics,[12] and drug screening.[5] While the majority of feedstock materials in 3D bioprinting are based on commercially available natural polymers, including gelatin,[13] and hyaluronic acid,[14] these building blocks possess a number of inherent limitations. Chemical derivatization is required in order to impart crosslinks, while significant

batch-to-batch variation and poor mechanical properties prevail. Moreover, high material concentration is needed for sufficient gelation, a necessity for homogenous cellular distribution and successful 'curing' of constructs in bioprinting .[9] Given these limitations, efforts to develop synthetic or semi-synthetic materials with more desirable chemical and physical characteristics are a major avenue for future research.

Synthetic hydrogels of interest, particularly peptide based, represent promising candidates as they have a defined (macro)molecular structure and comprise ubiquitous amino acid building blocks. The synthetic availability of different peptide sequences has grown in recent years, allowing a greater diversity of challenges in biomedical science to be addressed. For example, structural stabilization of hydrogels may be mediated through self assembly of their chiral backbone, adopting different secondary structures which in turn are controlled by processing conditions and the chemistry of the amino acid side chain residue(s).[15] The assembly of peptide chains can be fine-tuned by sequence control, molecular weight and backbone chemistry which allows for physical assembly of the peptide through hydrogen bonding, ionic bonding and/or hydrophobic interactions. In addition, the derivatization of specific amino acid residues is well known and offers the possibility of further fine-tuning the physicochemical properties and, thus, the mechanical properties of the hydrogel material,[16] highlighting the versatility of peptide-based systems.

## 1.3 3D Printing of Peptidic Hydrogels

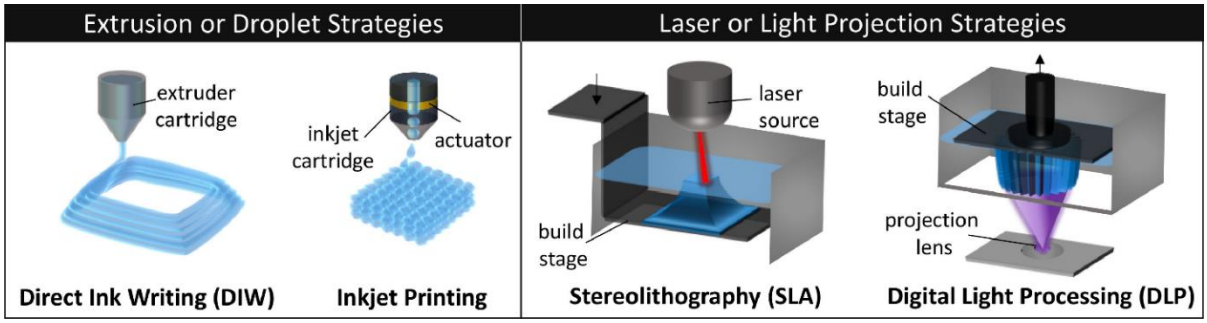


**Figure 1.1.** Graphical illustration of conventional 3D printing technology[17] Reproduced with permission from Elsevier.

### 1.3.1 Direct Ink Writing

Direct ink writing (DIW), also termed extrusion printing, is a widespread manufacturing method for precise fabrication of microfluidic devices and scaffolds for tissue engineering.[14] Pneumatic, piston or screw-based pressure systems are typically used, extruding the hydrogel on to a build stage in a predetermined path programed by a computer model in a 'layer-by-layer' approach. Generally the extrudable 'ink' is in the form of hydrogels or colloidal suspensions, although solvent based extrusion and evaporation techniques have also been reported.[18] Nelson et al. have exploited the low gelation temperature of Pluoronic F127-dimethacrylate hydrogels as 3D extrudable matrices containing embedded yeast cells.[19] At reduced temperatures (4 °C), the low viscosity Pluronic solution allows yeast cells and glucose to be easily dispersed and upon increasing the temperature (23 °C), gelation is observed (Fig. 2A–C). Shear-thinning of the hydrogel during extrusion allows for deposition of high-resolution cube lattice structures which can be subsequently cured with UV light (365 nm) (Fig. 2D). Significantly, the 3D printed yeast-laden hydrogel maintained its catalytic activity, with glucose fermentation to ethanol occurring over multiple cycles.

Recently, Hartgerink has shown that a extrudable ink for DIW can be achieved by mixing oppositely charged peptides that self-assemble into nanofibrous hydrogel at low concentration.[20]

Differences in mammalian cell function can be achieved by varying the overall charge of the peptidic scaffold. There is a growing interest in utilizing supramolecular chemistry's reversible bonds to make new shear processable inks for DIW. The variety of non-covalent chemistry allows the tunability of material properties and function but still maintain the rheological performance for DIW as highlighted in this recent review.[21]

### 1.3.2 Inkjet Printing

Similar to DIW, inkjet printing is an extrusion process where layers are printed sequentially. However instead of continuous line printing, ink-jet printing rapidly deposits small volume droplets from one or more nozzles onto the growth platform. Drop coalescence and liquid-to-solid phase transformation (i.e. solvent evaporation, gelation, or polymerization) controls the mechanical properties of the final printed object. The power of this method is the spatial resolution driven by drop size and the ability of multi-nozzle inkjet printers to both reduce printing times as well as allow for multi-material printing. The combination of acrylated poly(ethylene glycol) (PEG) and acrylated GRGDS or GCRDGPQGIWGQDRCG peptide building blocks has been shown by the Cui group to allow for continuous inkjet printing leading to well defined cylindrical hydrogel objects.[22] Stabilization through photopolymerization proved to be a viable strategy with the codeposition of embedded human mesenchymal stem cells (hMSCs) resulting in 3D printed hydrogels showing osteogenic and chondrogenic differentiation after immersion in cell media. Inkjet printing can also be used to

pattern hydrogel surfaces by depositing volumetric aqueous solutions which can complex or etch the surface resulting in shape deformation, swelling/deswelling and subsequent 3D structure formation.

### 1.3.3 SLA Printing

Unlike DIW, that is limited solely to extrusion, SLA permits simultaneous irradiation in the x-y direction and allows for a significant increase in fabrication speed. After creating one layer, the build stage lowers exposing a new layer of resin and the photopolymerization repeated; this stepwise process proceeds multiple times to achieve the final object. Typically, the resin consists of a mixture of one or more monomers/macromonomers and a dispersed photoinitiator with the resin forming a crosslinked network when stimulated by light. This has been demonstrated by the Nelson group, through the crosslinking of methacrylated bovine serum albumin (BSA) with PEG acrylates, giving rise to 3D printed objects with active functions.[23] In this case, employing a BSA-based crosslinker affords a semi-synthetic hydrogel construct with good mechanical properties, high cell viability over 21 days, and biodegradability in the presence of proteolytic enzymes. In a more recent study, these BSA hydrogels provided access to shape memory functionalities, arising from the protein's heat responsive globular structure.[24] 3D printed BSA wires could undergo plastic deformation through elongation to afford a metastable state and could recover their original shape via heating or immersion in aqueous solution (Fig. 3) Other recent advances in SLA, specifically the use of light sources with bicompatabile wavelengths and intensities, has permitted successful material interfacing with biological systems either through cell cultering,[25] or introduction of antimicrobial,[26] or antifouling properties.[26]

### 1.3.4 DLP Printing

Although similar in the underlying nature to lithographic processes, DLP printing differs from conventional SLA through the ability to employ multi-beam patterning. As a result, the CAD image is projected through a lens with slices of the image penetrating into the resin bed, the pattern of which is achieved using digital micromirror device (DMD) technology where an array of rotating mirrors directs the light path toward or away from the resin. This permit curing of the resin via spatiotemporal illumination at different locations within the layer. To my knowledge, there has been no reported printing of peptidic hydrogel utilizing DLP printer. The translation from high light intensity SLA might be limited due to the lower light intensity of DLP.

## 1.4 NCA ROP Polypeptide, an Underexplored Printable Feedstock

### 1.4.1 Synthesis of Polypeptide

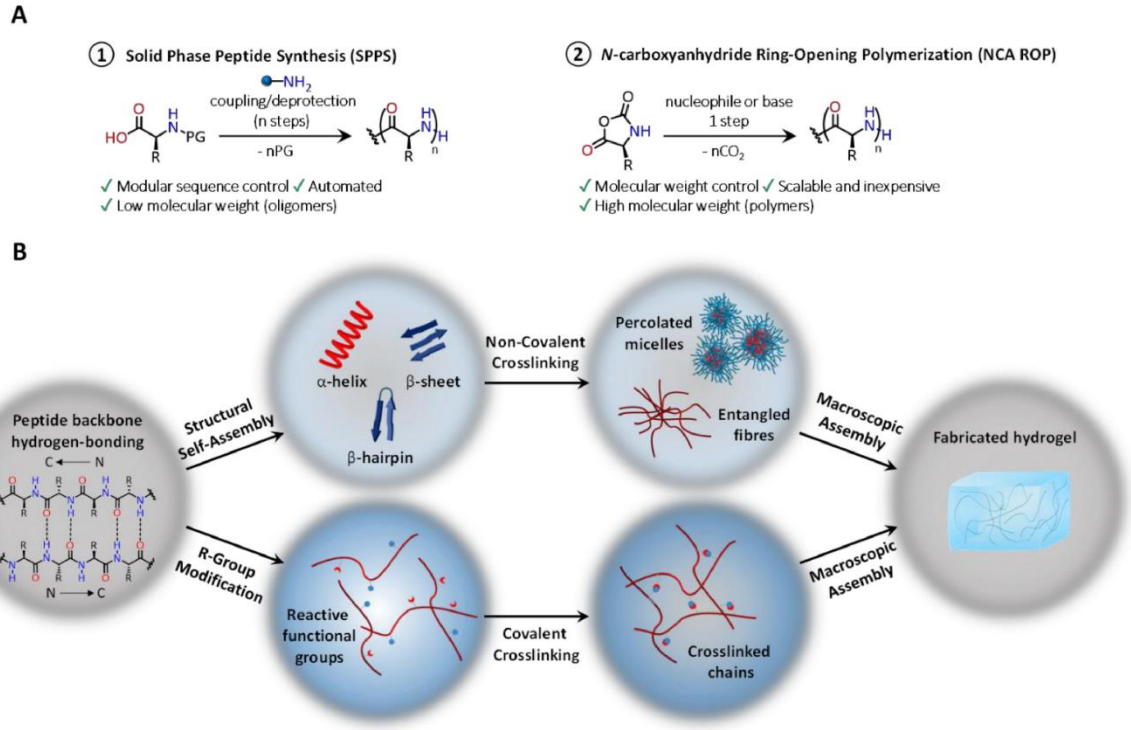


**Figure 1.2.** (A) Chemical strategy to access synthetic peptides via (1) solid-phase peptide synthesis (SPPS) and (2) *N*-carboxyanhdyride (NCA) ring opening polymerization (ROP) (B) Scheme of how 3D printable polypeptide hydrogel can be access through physical and/or chemical crosslinking design strategies.[17] Reproduced with permission from Elsevier.

Previously mentioned short, sequence-defined peptides can be traditionally synthesized via solid or solution phase peptide synthesis (SPPS), while scalable synthesis of high molecular weight peptides is available using amino acid *N*-carboxyanhydride (NCA) ring opening polymerization (NCA ROP). SPPS offers control of amino acid sequences and with straightforward automation can be used to prepare moderate quantities of material.[27] In a complimentary fashion, NCA ROP provides a more scalable platform for peptide synthesis

though with more limited degrees of sequence control**,** but has access to a verity of architecture available due to polymer chemistry.[28] Ultimately, both systems generate peptide (macro)molecules that can be synthetically customized to yield hydrogels via non-covalent or covalent crosslinking strategies (Fig. 5B). Since scalability and ease to synthesize are attractive features for translating materials into printable feedstock, polypeptide based on NCA ROP is an attractive candidate for additive manufacturing.

A strategy in peptide hydrogel design is through modulation of amphiphilic balance of the backbone sequence, with optimized arrangement of hydrophobic-hydrophilic units allowing for spontaneous non-covalent (physical) gelation.[29] This design can be driven by native protein folding mechanisms via side group supramolecular interactions (H-bonding, charge-charge interactions, π-π stacking) leading to distinct secondary structures such as α-helices, β-sheet and hairpin motifs.[30,31] Additionally, sequences and architectures designed for degradation and/or biocompatibility profiles can be engineered into peptide hydrogels which increases the potential of these materials for bioprinting applications. These non-covalent interactions differentiate peptide hydrogels from many of their synthetic counterparts, exhibiting a range of favorable properties including biomimetic stiffness and high porosity. For example, physical crosslinking provides peptide hydrogels with the capability to deform under induced stress and re-stabilize upon stress removal, a key asset for translation to 3D extrusion printing systems. In particular, assemblies based on β-motif directors endow peptide hydrogels with mechanical robustness and can be readily prepared using SPPS methods.[31] In addition, macromolecular peptide amphiphiles prepared via NCA ROP procedures allow for controlled assembly of hydrophobic domains and represent a versatile platform for hydrogel

design .[32] Similar to short SPPS derived peptides, NCA derived materials have drawn a wide range of interest as injectable biomaterials as they are stable, static matrices which undergo stress-mediated flow behavior and have high water retention. Many reports of NCA ROP derived peptide hydrogels utilizing secondary structures have been pioneered by Nowak et al.[33] with physical hydrogel networks being formed through assembled α-helical or β-sheet structures linked to charged hydrophilic sequences. The choice of amino acid, block length and architecture further allows for tuning of the resulting mechanical properties.[34,35]

### 1.4.2 3D Printing of Polypeptide

For these systems, the highly scalable nature of polypeptides synthesized through NCA ROP leads to hydrogels with programmable properties based on sequences or defined chain end functionalization. For example, hybrid polypeptide-DNA hydrogels, crosslinked through DNA hybridization were developed by Duncan et al. for extrusion type 3D printing.[36] This two-component system incorporated a statistical copolymer of glutamic acid and propargyl-glutamate, which was modified with single stranded DNA (ssDNA). The complementary second component was a double stranded DNA (dsDNA) crosslinker with "sticky ends". Using inkjet printing, dual deposition of both bio-inks allowed for rapid formation of hydrogels through DNA hybridization, with extruded millimeter scale constructs having fine resolution structures and high cell viability. More suited for robust 3D structures are designer polypeptide hydrogels that contain a photocrosslinkable group that allows spatial and temporal control of the final printed object. For example, macroscopic hydrogels comprising star shaped blocks of glutamic acid and valine were fabricated and functionalized with photo-polymerizable allyl groups.[37] These physically entangled shear-thinning hydrogel networks could then be mixed

with a photoinitiator and fabricated into a range of objects using DIW extrusion 3D printing and subsequently crosslinked with UV light to form a mechanically robust interpenetrating poly-allyester network. The cured hydrogel constructs are capable of releasing DOX drug cargo during degradation and were found to be non-cytotoxic in a leachate viability assay of 3T3 fibroblast cells. Building on these successes, a photo responsive polypeptide hydrogel system based on thiol-yne chemical crosslinking was recently described.[38] In this systems, statistical copolypeptides of glutamic acid and nitrobenzyl cysteine (NBC) with a β-sheet forming isoleucine block (PECI-2) forms mechanically robust hydrogels that could be blended with 4-arm PEG-propiolate building blocks and 3D printed via DIW extrusion. Hydrogel shear thinning and subsequent UV initiation of catalyst free thiol–yne click coupling between cysteine and propiolate groups could then give a covalently stabilized network (Fig. 12). Moreover, human dermal fibroblast cells showed good viability in both surface and cell-laden culture assays with the hydrogel ink, suggesting its potential as a candidate in 3D bioprinting. Other polypeptide materials with tailored antimicrobial properties have also been devised for DIW printing,[39] further demonstrating their expandability in 3D printing applications.

Recently, Murphy et. al. synthesized linear and star statistical copolypeptide based on the β-sheet forming vinylbenzyl-L-cysteine that can self-assemble into physical hydrogel and subsequently photocrosslinked.[40] Tunable viscoelasticity can be achieved due to the architectural control of NCA ROP which allows the DIW of the mechanically robust linear copolypeptide and the direct laser writing (DLW) of the lower viscosity star copolypeptide. In our group, we utilized star block copolypeptide β-sheet hydrogelator so that we could control its material properties and printability through β-sheet strength.[41] Through the facile

integration of the methacrylate into the glutamate residue of these star block copolypeptide, mechanically robust biological composites with integrated *E. Coli.* can be accessed post-extrusion by crosslinking with visible light.[42]

### 1.5 Summary and Outlook

As 3D printing is maturing as a technology and finding applications that cannot be reached by traditional manufacturing, there is a growing need to expand the material capabilities that can be manufactured from additive manufacturing. An adaptation of 3D printing with great interest is known as "bioprinting", a strategy that permits the spatial and temporal distribution of living cells with the goal of enabling cell proliferation and maturation. While derivatized hydrogels from natural polymers have facilitated many successful studies in bioprinting, the lack of more reproducible, tunable material platform has prevented significant expansion within the field. As an under-explored building block, peptide hydrogels offer a number of advantages for the field of 3D printing. Their highly modular platform, natural building block origins and unique properties endow them with promising potential to address the limitations associated with currently used materials. This thesis will explore utilization of tailorable peptidic material, specifically star polypeptide, for additive manufacturing. In chapter two, structure-function relationship of these star block copolypeptide were explored and showcased that material properties and printability can be tuned through side chain design. In the third chapter, these star block copolypeptide were functionalized with photocrosslinkable group that allow DIW of *E. Coli* composites and subsequent crosslinking with visible light. To make these photocrosslinkable peptidic materials more user-friendly, the fourth chapter consists of using these feedstock materials as rheological modifiers with an eye toward mammalian cell printing.

With a growth in printable material based on tunable peptides, there is potential to contribute to the overall success of bioprinting.

### 1.6 References


[1] Mohammadi, A.; Lavranos, J.; Zhou, H.; Mutlu, R.; Alici, G.; Tan, Y.; Choong, P.; Oetomo, D. A Practical 3D-Printed Soft Robotic Prosthetic Hand with Multi-Articulating Capabilities. *PLoS One* **2020**, *15*.

[2] Park, M.; Islam, S.; Kim, H.-E.; Korostoff, J.; Blatz, M. B.; Hwang, G.; Kim, A.; Park, M.; Islam, S.; Kim, A.; Kim, H.; Blatz, M. B.; Hwang, G.; Korostoff, J. Human Oral Motion-Powered Smart Dental Implant (SDI) for In Situ Ambulatory Photo-Biomodulation Therapy. *Adv. Healthc. Mater.* **2020**, *9*, 2000658.

[3] Qiu, K.; Zhao, Z.; Haghiashtiani, G.; Guo, S. Z.; He, M.; Su, R.; Zhu, Z.; Bhuiyan, D. B.; Murugan, P.; Meng, F.; Park, S. H.; Chu, C. C.; Ogle, B. M.; Saltzman, D. A.; Konety, B. R.; Sweet, R. M.; McAlpine, M. C. 3D Printed Organ Models with Physical Properties of Tissue and Integrated Sensors. *Adv. Mater. Technol.* **2018**, *3*, 1700235.

[4] Song, X.; Tetik, H.; Jirakittsonthon, T.; Parandoush, P.; Yang, G.; Lee, D.; Ryu, S.; Lei, S.; Weiss, M. L.; Lin, D. Biomimetic 3D Printing of Hierarchical and Interconnected Porous Hydroxyapatite Structures with High Mechanical Strength for Bone Cell Culture. *Adv. Eng. Mater.* **2019**, *21*, 1800678.

[5] Yang, W.; Cai, S.; Chen, Y.; Liang, W.; Lai, Y.; Yu, H.; Wang, Y.; Liu, L. Modular and Customized Fabrication of 3D Functional Microgels for Bottom-Up Tissue Engineering and Drug Screening. *Adv. Mater. Technol.* **2020**, *5*, 1900847.

[6] Conner, B. P.; Manogharan, G. P.; Martof, A. N.; Rodomsky, L. M.; Rodomsky, C. M.; Jordan, D. C.; Limperos, J. W. Making Sense of 3-D Printing: Creating a Map of Additive Manufacturing Products and Services. *Addit. Manuf.* **2014**, *1–4*, 64–76.

[7] Jungst, T.; Smolan, W.; Schacht, K.; Scheibel, T.; Groll, J. Strategies and Molecular Design Criteria for 3D Printable Hydrogels. *Chem. Rev.* **2016**, *116*, 1496–1539.

[8] Langer, R.; Vacanti, J. P. Tissue Engineering. *Science (80-. ).* **1993**, *260*, 920–926.

[9] Chimene, D.; Lennox, K. K.; Kaunas, R. R.; Gaharwar, A. K. Advanced Bioinks for 3D Printing: A Materials Science Perspective. *Ann. Biomed. Eng.* **2016**, *44*, 2090–2102.

[10] Vo, A. Q.; Zhang, J.; Nyavanandi, D.; Bandari, S.; Repka, M. A. Hot Melt Extrusion Paired Fused Deposition Modeling 3D Printing to Develop Hydroxypropyl Cellulose Based Floating Tablets of Cinnarizine. *Carbohydr. Polym.* **2020**, *246*, 116519.

[11] Grigoryan, B.; Paulsen, S. J.; Corbett, D. C.; Sazer, D. W.; Fortin, C. L.; Zaita, A. J.; Greenfield, P. T.; Calafat, N. J.; Gounley, J. P.; Ta, A. H.; Johansson, F.; Randles, A.;

Rosenkrantz, J. E.; Louis-Rosenberg, J. D.; Galie, P. A.; Stevens, K. R.; Miller, J. S. Multivascular Networks and Functional Intravascular Topologies within Biocompatible Hydrogels. *Science (80-. ).* **2019**, *364*, 458–464.

[12] Iuliano, A.; van der Wal, E.; Ruijmbeek, C. W. B.; in 't Groen, S. L. M.; Pijnappel, W. W. M. P.; de Greef, J. C.; Saggiomo, V. Coupling 3D Printing and Novel Replica Molding for In House Fabrication of Skeletal Muscle Tissue Engineering Devices. *Adv. Mater. Technol.* **2020**, *5*, 2000344.

[13] Colosi, C.; Shin, S. R.; Manoharan, V.; Massa, S.; Costantini, M.; Barbetta, A.; Dokmeci, R.; Dentini, M.; Khademhosseini, A.; Khademhosseini, A.; Khademhosseini, H. A.-; Colosi, C.; Costantini, M.; Barbetta, A.; Dentini, M.; Shin, S. R.; Dokmeci, M. R.; Massa, S. Microfluidic Bioprinting of Heterogeneous 3D Tissue Constructs Using Low-Viscosity Bioink. *Adv. Mater.* **2016**, *28*, 677–684.

[14] Ouyang, L.; Highley, C. B.; Rodell, C. B.; Sun, W.; Burdick, J. A. 3D Printing of Shear-Thinning Hyaluronic Acid Hydrogels with Secondary Cross-Linking. *ACS Biomater. Sci. Eng.* **2016**, *2*, 1743–1751.

[15] Song, Z.; Fu, H.; Wang, R.; Pacheco, L. A.; Wang, X.; Lin, Y.; Cheng, J. Secondary Structures in Synthetic Polypeptides from N-Carboxyanhydrides: Design, Modulation, Association, and Material Applications. *Chem. Soc. Rev.* **2018**, *47*, 7401–7425.

[16] Rong, L.; Qin, S. Y.; Zhang, C.; Cheng, Y. J.; Feng, J.; Wang, S. B.; Zhang, X. Z. Biomedical Applications of Functional Peptides in Nano-Systems. *Mater. Today Chem.* **2018**, *9*, 91–102.

[17] Murphy, R. D.; Garcia, R. V.; Heise, A.; Hawker, C. J. Peptides as 3D Printable Feedstocks: Design Strategies and Emerging Applications. *Prog. Polym. Sci.* **2022**, *124*.

[18] Larson, C. M.; Choi, J. J.; Gallardo, P. A.; Henderson, S. W.; Niemack, M. D.; Rajagopalan, G.; Shepherd, R. F. Direct Ink Writing of Silicon Carbide for Microwave Optics. *Adv. Eng. Mater.* **2016**, *18*, 39–45.

[19] Saha, A.; Johnston, T. G.; Shafranek, R. T.; Goodman, C. J.; Zalatan, J. G.; Storti, D. W.; Ganter, M. A.; Nelson, A. Additive Manufacturing of Catalytically Active Living Materials. *ACS Appl. Mater. Interfaces* **2018**, *10*, 13373–13380.

[20] Farsheed, A. C.; Thomas, A. J.; Pogostin, B. H.; Hartgerink, J. D.; Farsheed, A. C.; Pogostin, B. H.; Hartgerink, J. D.; Thomas, A. J. 3D Printing of Self-Assembling Nanofibrous Multidomain Peptide Hydrogels. *Adv. Mater.* **2023**, *35*, 2210378.

[21] Tang, M.; Zhong, Z.; Ke, C. Advanced Supramolecular Design for Direct Ink Writing of Soft Materials. *Chem. Soc. Rev.* **2023**, *52*, 1614–1649.

[22] Gao, G.; Yonezawa, T.; Hubbell, K.; Dai, G.; Cui, X. Inkjet-Bioprinted Acrylated Peptides and PEG Hydrogel with Human Mesenchymal Stem Cells Promote Robust Bone and Cartilage Formation with Minimal Printhead Clogging. *Biotechnol. J.* **2015**,

*10*, 1568–1577.

[23] Smith, P. T.; Narupai, B.; Tsui, J. H.; Millik, S. C.; Shafranek, R. T.; Kim, D. H.; Nelson, A. Additive Manufacturing of Bovine Serum Albumin-Based Hydrogels and Bioplastics. *Biomacromolecules* **2020**, *21*, 484–492.

[24] Sanchez-Rexach, E.; Smith, P. T.; Gomez-Lopez, A.; Fernandez, M.; Cortajarena, A. L.; Sardon, H.; Nelson, A. 3D-Printed Bioplastics with Shape-Memory Behavior Based on Native Bovine Serum Albumin. *ACS Appl. Mater. Interfaces* **2021**, *13*, 19193–19199.

[25] Elomaa, L.; Pan, C. C.; Shanjani, Y.; Malkovskiy, A.; Seppälä, J. V.; Yang, Y. Three-Dimensional Fabrication of Cell-Laden Biodegradable Poly(Ethylene Glycol-Co-Depsipeptide) Hydrogels by Visible Light Stereolithography. *J. Mater. Chem. B* **2015**, *3*, 8348–8358.

[26] Garcia, C.; Gallardo, A.; López, D.; Elvira, C.; Azzahti, A.; Lopez-Martinez, E.; Cortajarena, A. L.; González-Henríquez, C. M.; Sarabia-Vallejos, M. A.; Rodríguez-Hernández, J. Smart PH-Responsive Antimicrobial Hydrogel Scaffolds Prepared by Additive Manufacturing. *ACS Appl. Bio Mater.* **2018**, *1*, 1337–1347.

[27] Behrendt, R.; White, P.; Offer, J. Advances in Fmoc Solid-Phase Peptide Synthesis. *J. Pept. Sci.* **2016**, *22*, 4–27.

[28] Song, Z.; Tan, Z.; Cheng, J. Recent Advances and Future Perspectives of Synthetic Polypeptides from N-Carboxyanhydrides. **2019**, *52*, 8521–8539.

[29] Dasgupta, A.; Das, D. Designer Peptide Amphiphiles: Self-Assembly to Applications. *Langmuir* **2019**, *35*, 10704–10724.

[30] Banwell, E. F.; Abelardo, E. S.; Adams, D. J.; Birchall, M. A.; Corrigan, A.; Donald, A. M.; Kirkland, M.; Serpell, L. C.; Butler, M. F.; Woolfson, D. N. Rational Design and Application of Responsive α-Helical Peptide Hydrogels. *Nat. Mater.* **2009**, *8*, 596–600.

[31] Li, J.; Du, X.; Hashim, S.; Shy, A.; Xu, B. Aromatic-Aromatic Interactions Enable α-Helix to β-Sheet Transition of Peptides to Form Supramolecular Hydrogels. *J. Am. Chem. Soc.* **2017**, *139*, 71–74.

[32] Zhou, X.; Li, Z.; Hydrogels Zhou, P. X.; Li, Z.; Zhou, X. Advances and Biomedical Applications of Polypeptide Hydrogels Derived from α-Amino Acid N-Carboxyanhydride (NCA) Polymerizations. *Adv. Healthc. Mater.* **2018**, *7*, 1800020.

[33] Nowak, A. P.; Breedveld, V.; Pakstis, L.; Ozbas, B.; Pine, D. J.; Deming, T. J. Rapidly Recovering Hydrogel Scaffolds from Self-Assembling Diblock Copolypeptide Amphiphiles. *Nature* **2002**, *417*, 424–428.

[34] Lu, C.; Quan, G.; Su, M.; Nimmagadda, A.; Chen, W.; Pan, M.; Teng, P.; Yu, F.; Liu, X.; Jiang, L.; Du, W.; Hu, W.; Yao, F.; Pan, X.; Wu, C.; Liu, D.; Cai, J. Molecular

Architecture and Charging Effects Enhance the In Vitro and In Vivo Performance of Multi-Arm Antimicrobial Agents Based on Star-Shaped Poly(l-Lysine). *Adv. Ther.* **2019**, *2*, 1900147.

[35] Li, Z.; Deming, T. J. Tunable Hydrogel Morphology via Self-Assembly of Amphiphilic Pentablock Copolypeptides. *Soft Matter* **2010**, *6*, 2546–2551.

[36] Li, C.; Faulkner-Jones, A.; Dun, A. R.; Jin, J.; Chen, P.; Xing, Y.; Yang, Z.; Li, Z.; Shu, W.; Liu, D.; Duncan, R. R. Rapid Formation of a Supramolecular Polypeptide–DNA Hydrogel for In Situ Three-Dimensional Multilayer Bioprinting. *Angew. Chemie Int. Ed.* **2015**, *54*, 3957–3961.

[37] Murphy, R.; Walsh, D. P.; Hamilton, C. A.; Cryan, S. A.; In Het Panhuis, M.; Heise, A. Degradable 3D-Printed Hydrogels Based on Star-Shaped Copolypeptides. *Biomacromolecules* **2018**, *19*, 2691–2699.

[38] Murphy, R. D.; Kimmins, S.; Hibbitts, A. J.; Heise, A. 3D-Extrusion Printing of Stable Constructs Composed of Photoresponsive Polypeptide Hydrogels. *Polym. Chem.* **2019**, *10*, 4675–4682.

[39] Murphy, R.; Kordbacheh, S.; Skoulas, D.; Ng, S.; Suthiwanich, K.; Kasko, A. M.; Cryan, S. A.; Fitzgerald-Hughes, D.; Khademhosseini, A.; Sheikhi, A.; Heise, A. Three-Dimensionally Printable Shear-Thinning Triblock Copolypeptide Hydrogels with Antimicrobial Potency. *Biomater. Sci.* **2021**, *9*, 5144–5149.

[40] Murphy, R. D.; Delaney, C.; Kolagatla, S.; Florea, L.; Hawker, C. J.; Heise, A. Design of Statistical Copolypeptides as Multipurpose Hydrogel Resins in 3D Printing. *Adv. Funct. Mater.* **2023**, *33*, 2306710.

[41] Garcia, R. V.; Murphy, E. A.; Sinha, N. J.; Okayama, Y.; Urueña, J. M.; Helgeson, M. E.; Bates, C. M.; Hawker, C. J.; Murphy, R. D.; Read de Alaniz, J. Tailoring Writability and Performance of Star Block Copolypeptides Hydrogels through Side-Chain Design. *Small* **2023**, *19*, 2302794.

[42] Murphy, R. D.; Garcia, R. V.; Oh, S. J.; Wood, T. J.; Jo, K. D.; Read de Alaniz, J.; Perkins, E.; Hawker, C. J. Tailored Polypeptide Star Copolymers for 3D Printing of Bacterial Composites Via Direct Ink Writing. *Adv. Mater.* **2023**, *35*, 2207542.

# Chapter 2. Tailoring Writability and Performance of Star Block Copolypeptides Hydrogels Through Side-Chain Design

Portions of this work were published in:

Ronnie V. Garcia,Elizabeth A. Murphy,Nairiti J. Sinha,Yoichi Okayama, Juan Manuel Urueña, Matthew E. Helgeson, Christopher M. Bates,Craig J. Hawker, Robert D. Murphy,Javier Read de Alaniz, Tailoring Writability and Performance of Star Block Copolypeptides Hydrogels Through Side-Chain Design, *Small.* **2023**, 2302794. Reproduced with permission from John Wiley & Sons Inc.

## 2.1 Abstract

Shear-recoverable hydrogels based on block copolypeptides with rapid self-recovery hold potential in extrudable and injectable 3D-printing applications. In this work, a series of 3-arm star-shaped block copolypeptides composed of an inner hydrophilic poly(l-glutamate) domain and an outer β-sheet forming domain was synthesized with varying side chains and block lengths. By changing the β-sheet forming domains, hydrogels with diverse microstructures and mechanical properties were prepared and structure–function relationships determined using scattering and rheological techniques. Differences in the properties of these materials are amplified during direct-ink writing (DIW) with a strong correlation observed between printability and material chemistry. Significantly, it was observed that non-canonical β-sheet blocks based on phenyl glycine form more stable networks with superior mechanical properties and writability compared to more widely used natural amino acid counterparts. The versatile design available through block copolypeptide materials provides a robust platform to access tunable material properties based solely on molecular design. These systems can be exploited in extrusion-based applications such as 3D-printing without the need for additives.

## 2.2 Introduction

Additive manufacturing or 3D-printing of hydrogels combines complex geometrical control with functional material selection for diverse applications in electronics,[1] structural materials,[2] and biomedicine.[3] Consequently, 3D-printed hydrogels are an emerging area of focus with advantages including tunability, high water content, and potential biocompatibility.[4–6] For light-based 3D-printing such as stereolithography (SLA) and digital-light processing (DLP), hydrogels must be formulated to have low viscosities and undergo rapid photocrosslinking.[7–9]

In contrast, extrusion techniques like direct-ink writing (DIW) rely on formulations with a shear-recoverable yield stress to achieve high-fidelity shapes.[10,11] Traditionally, 3D-printable hydrogels are based on natural biopolymers such as gelatin or alginate as the key biopolymer building block.[12] However, these materials suffer from several limitations including batch-to-batch variation and an inability to systematically tune their molecular structure.[13] Due to these constraints, the printability of natural biopolymers can only be modulated by concentration,[14] additives,[15] or multicomponent blends.[16,17] For example, native alginate cannot be used directly in DIW; calcium ions or clay particles are required to achieve the necessary shear-thinning properties.[13] Although synthetic material systems such as poloxamers are chemically tunable, there are still drawbacks. For example, poloxamer 407 sol-gel temperature is sensitive to a multitude of factors, and poloxamers lack inherent biodegradility that is desirable for biological applications.[18] To further expand this area of research and diversify the palette of 3D-printable hydrogels, there is a need to explore shear-recoverable materials that can be synthetically tuned without sacrificing the inherent benefits of biopolymers, ranging from degradability to sustainable sourcing and biocompatibility.

Block copolypeptides with controllable composition, molecular weight, and topology are attractive alternatives to traditional biopolymers for DIW 3D-printing application. An enabling synthetic technique to access these materials involves the ring-opening polymerization (ROP) of *N*-carboxyanhydrides (NCAs) leading to scalable block copolypeptides with well-defined molecular weight and architectures.[19] A variety of non-covalent bonding interactions, such as hydrogen bonding and π–π stacking, can be further integrated into these materials by engineering the peptide backbone and side chain to create hierarchical structures. The intrinsic

chirality of the peptide backbone also allows for adoption of distinct secondary structures such as α-helices, β-sheet, and hairpin motifs to further influence material properties.[11,20–27] Through rational design, copolypeptide inner blocks that contain electrostatics promote high water absorption, while careful choice of the outer block(s) yields strongly associating β-sheet domains that lead to robust hydrogel networks stabilized by reversible physical crosslinks.[28] These properties have high utility for extrusion and rapid recovery, eliminating the need for rheological additives.[29] Based on a similar principle, Hartgerink and co-workers have also developed nanofibrous hydrogel comprised of multidomain peptides with good viscoelastic properties for DIW.[30] Designer block copolypeptides have therefore found use as injectable carriers, tissue engineering scaffolds, antimicrobial materials, and more recently 3D-printable bioinks.[31–37]

Recently, our group demonstrated the synthetic versatility of block copolypeptides and their applicability to the development of bioinks that can be chemically crosslinked with visible light.[38] This strategy generates well-defined, viable biocomposites with *Escherichia coli,* controlling the behaviour of embedded bacteria by modulating mechanical properties of the host block copolypeptide hydrogel through a functional-group change in associating domains. Further understanding structure–function relationships in these physically crosslinked junctions is critical to extend the generality of this approach and tune performance by varying block chemistry, concentration, and architecture.[39–42] In particular, the effect of side-chain amino acids has not been studied extensively and is hypothesized to dictate associating-domain formation and related hydrogel properties such as rheological regimes, which are crucial for extrusion-based applications.

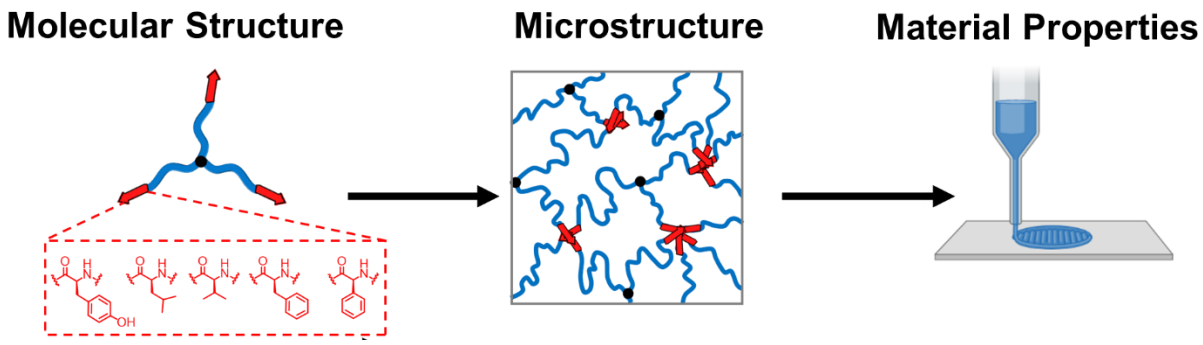


**Figure 2.1.** Modular design of 3-arm block copolypapeides enables tunable microstructure and properties based on amino acid selection.[43] Reproduced with permission from John Wiley & Sons Inc.

## 2.3 Results and discussion

### 2.3.1 Molecular Design and Synthesis.

Hydrophobic and hydrophilic amino acids were selected to investigate a wide variety of supramolecular interactions and structures by modulating β-sheet assemblies which give rise to physically crosslinked junctions. Specifically, *N*-carboxyanhydride (NCA) monomers based on γ-benzyl-l-glutamate (BLG), l-tyrosine (LT), l-leucine (LL), l-phenylalanine (LPA), l-phenylglycine (LPG), and l-valine (LV) were prepared using a procedure adapted from literature based on epichlorohydrin as an HCl scavenger.[44] The trifunctional initiator tris(2-aminoethyl)amine (TREN) was then selected for controlled *N*-carboxyanhydride ring-opening polymerization (NCA ROP) of γ-benzyl-l-glutamate (BLG) NCA. The 3-arm architecture was chosen due to the ability of outer block domains to form 3D extended networks at lower weight percentages, enabling access to superior hydrogels compared to linear analogues.[39,45] High conversions were observed with Fourier-transform infrared spectroscopy (FTIR) spectroscopy for 3-arm poly(benzyl-l-glutamate) (3-PBLG$_{80}$) with a degree of polymerization (DP) equal to

~80 based on $^{1}$H nuclear magnetic resonance ($^{1}$H NMR) spectroscopy.[46] The 3-PBLG$_{80}$ macroinitiator was then used to chain extend *in-situ* with NCA's based on LT, LL, LPA, LPG, or LV, leading to β-sheet forming polymer blocks with a target DP of 45. The library of 3-arm block copolypeptides (CP) included poly(benzyl-l-glutamate-*b*-l-tyrosine) (3-PBLG$_{80}$-b-PLT$_{33}$ [**3-CP-T**]), poly(benzyl-l-glutamate-*b*-l-valine) (3-PBLG$_{80}$-*b*-PLV$_{36}$ [**3-CP-V**]), poly(benzyl-l-glutamate-*b*-l-leucine) (3-PBLG$_{80}$-*b*-PLL$_{39}$ [**3-CP-L**]), poly(benzyl-l-glutamate-*b*-l-phenylalanine) (3-PBLG$_{80}$-*b*-PLPA$_{37}$ [**3-CP-PA**]), and poly(benzyl-l-glutamate-*b*-l-phenylglycine) (3-PBLG$_{80}$-*b*-PLPG$_{30}$ [**3-CP-PG**]), which were fully characterized via $^{1}$H NMR spectroscopy (**Figure 2**). To understand the effect of molecular weight on hydrogel assembly, two additional block copolypeptides (3-PBLG$_{76}$-*b*-PLPG$_{16}$ [**3-CP-PG-1**] and 3-PBLG$_{76}$-*b*-PLPG$_{28}$ [**3-CP-PG-2**]) were also prepared from a common macroinitiator, 3-PBLG$_{76}$. Note that the sample nomenclature places the degree of polymerization for each block as a subscript.

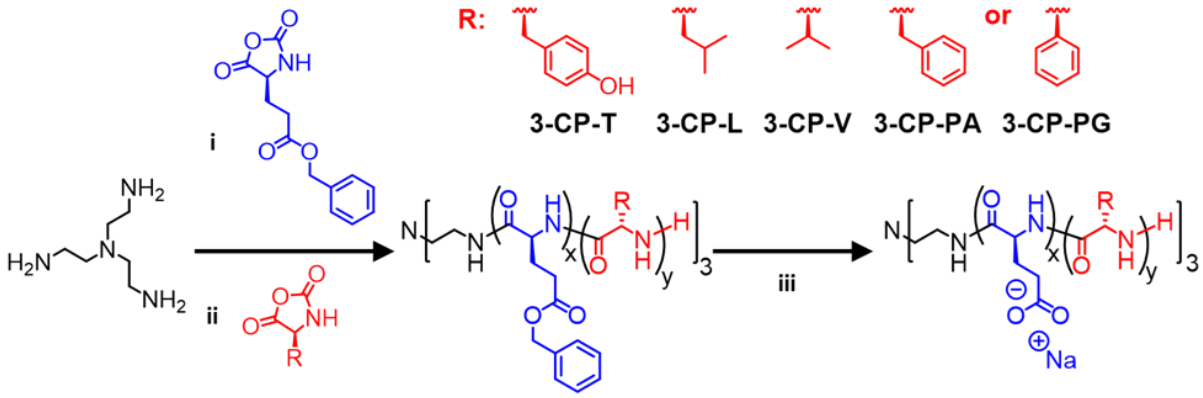


**Figure 2.2.** (i) $CHCl_3$/DMF, 18 h, rt. (ii) DMF (for l-tyrosine NCA) or $CHCl_3$/DMF (for other NCAs), 18 h, rt. (iii) TFA/$CHCl_3$, HBr 33 wt% in AcOH, 18 h, rt; NaOH, dialysis, 3 days. [43] Reproduced with permission from John Wiley & Sons Inc.

The chemical structure and DP of each block copolypeptide were confirmed using $^{1}H$ NMR spectroscopy, with molecular weights and dispersities characterized by diffusion-ordered spectroscopy (DOSY) and size-exclusion chromatography (SEC) (Figures A7–A23). It is noteworthy that high end-group retention during polymerization enabled efficient block extensions as supported by SEC and the observation of a single population by DOSY NMR for all samples. Moreover, excellent control over the ring-opening polymerization initiated by TREN was evidenced by low molar-mass dispersities ($Đ \approx 1.1$), with good agreement between experimental and targeted molecular weights. Some high-molecular-weight assemblies were observed by SEC for both valine and phenyl glycine block copolypeptides, likely due to strong association of their β-sheet secondary structures in the eluent hexafluoroisopropanol (HFIP). The size of observable diblock assemblies for phenyl glycine appeared to be dependent on length (Figures S21 and S23). Interestingly, DOSY NMR displays a single population due to the ability of the solvent, 15% trifluoracetic acid in deuterated chloroform ($CDCl_3$), to disrupt β-sheet formation more efficiently compared to the SEC eluent (HFIP). To afford the desired water soluble 3-arm block copolypeptides, the benzyl protecting group on the glutamate blocks was deprotected using 33 wt% HBr in acetic acid, followed by ionization to the sodium salt using sodium hydroxide (NaOH). Subsequent dialysis of block copolypeptides using a 10 kDa molecular weight cut off (MWCO) membrane was used to remove impurities and the resulting 3-arm star block copolypeptides were lyophilized and stored as dry powders for subsequent studies.

### 2.3.2 Characterization of Physical Hydrogel Self-Assembly in Water

The desired weight fraction (wt%) of 3-arm star block copolypeptides were dispersed in deionized water by mechanically mixing solid and water until a homogenous translucent physical hydrogel is achieved. To confirm the formation of the β-sheet secondary structure at these molecular weights and dispersity of these hydrogels, FTIR in deuterated water ($D_2O$) showed the expected amide I bands from 1630–1690 $cm^{-1}$ (Figure 2.7).[47]

Since the gelation of these materials is driven by network formation of β-motif-rich junctions, SAXS was further employed to gain insight into the impact of side-chain chemistry on microstructure. For subsequent studies, all physical hydrogels were compared at 40wt% to get adequate contrast between water and the network topology on SAXS. The presence of negatively charged glutamate residues in the internal block domains inserts interaction peaks into the scattering signal, which precludes accurate interpretation of the data with respect to the impact of outer block characteristics (Figure 2.8-2.9). Therefore, SAXS measurements were performed using different concentrations of sodium chloride in water to screen electrostatic interactions.[48] Figure 3 shows the SAXS curves for the five amino acid types in 50 mM salt that highlight the key differences between the nanostructures of the different amino acids employed within the outer block.

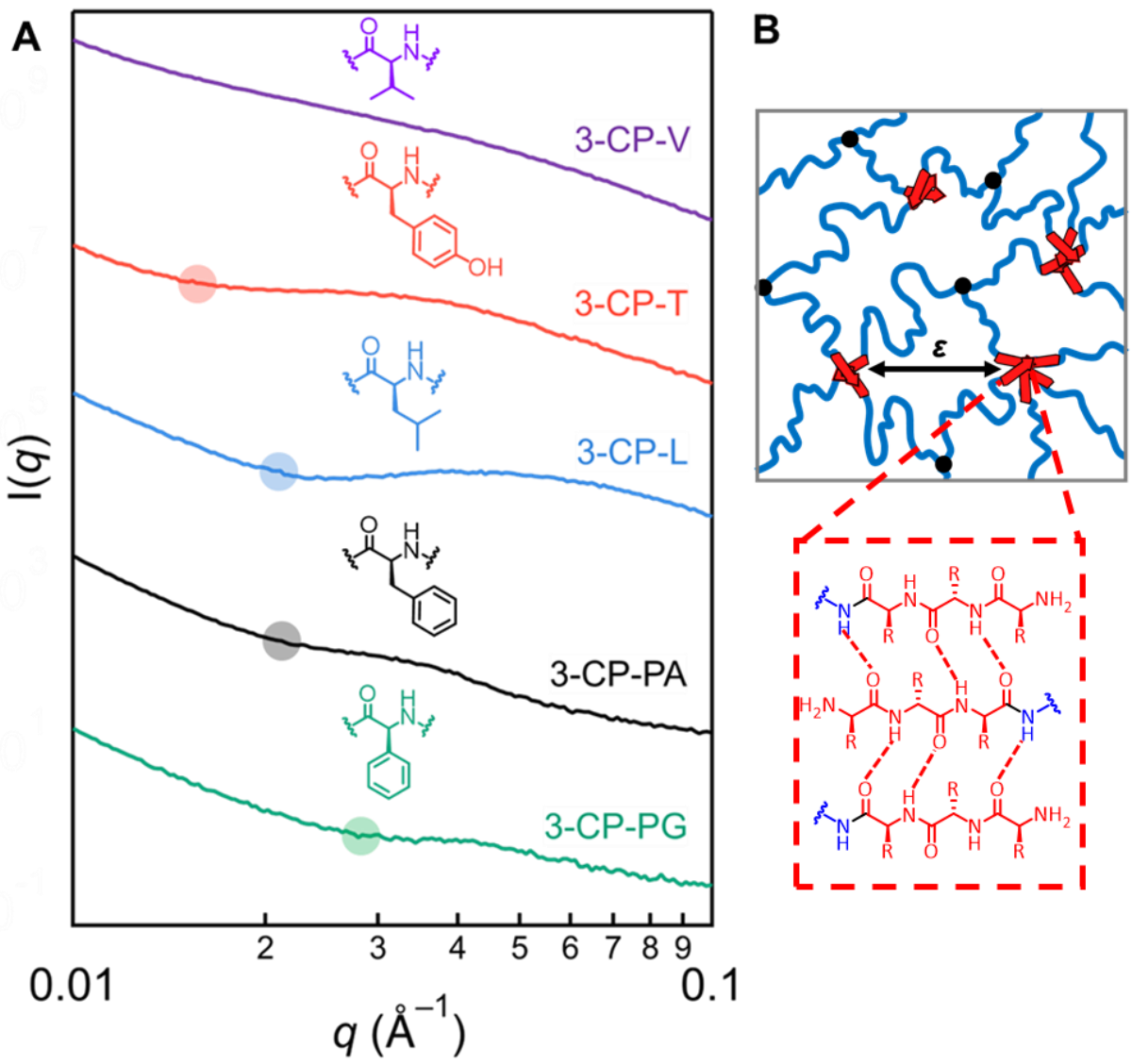


**Figure 2.3.** Small angle X-ray scattering (SAXS) profiles of a 3-arm block copolypeptide library at 40 wt% in 50 mM NaCl solution with the highlighted q values corresponding to each average interdomain spacing (ε). (B) Schematic depicts change in ε as aggregate sizes increase due to increase in β-sheet proclivity.[43] Reproduced with permission from John Wiley & Sons Inc.

In SAXS measurements, the scattering intensity $I(q)$ is a function of the magnitude of the scattering wave vector $q$ with an approximate correspondence with a length scale $d \sim 2\pi/q$.[49] The scattering profiles of 3-arm block copolypeptide physical gels reveal two features

consistent with previous studies. The first is a broad shoulder at high $q$-values indicative of interdomain spacing of the β-sheet forming amino acids that comprise the physical crosslinks within the hydrogel.[49,50] The second region is a low-$q$ increase in scattering intensity that is related to a the fractal-like characteristics of the overall network structure.[51] The $q$-value at the transition, $q^*$, was used to estimate an apparent interdomain spacing, $\varepsilon = 2\pi/q^*$ within the physically-crosslinked networks. A step minimum is used to extrapolate the value of $q^*$ for each hydrogel and is shown on the curves in Figure 3A with colored circles (see Table S1 for values). Specifically for **3-CP-V**, unrestricted β-sheet aggregation causes the formation of a network of aggregates from which an interdomain spacing could not be extracted.[52,53] In the remainder of the series of physical gels with fixed length of the outer block domain, **3-CP-PG** exhibited the smallest ε whereas **3-CP-T** exhibited the largest. This is consistent with the choice of amino acid in the outer-block, whereby we expect that changes in the degree of β-sheet aggregation can be correlated to changes in the average size and number of aggregate domains within the network, and therefore the average value of ε for materials at a fixed polypeptide concentration. Compared to the other samples, it should be noted that **3-CP-L** shows a stronger helical character in the glutamate inner core, along with β-sheet assembly due to the outer leucine block (Figure A24), with the interplay between these two assembly processes complicating structure-function interpretation. To further probe the impact of outer-block arm length on $\varepsilon$, we synthesized two different molecular weight 3-arm stars, **3-CP-PG-1** and **3-CP-PG-2**, with a DP of 16 and 28, respectively for the outer block length. SAXS measurements demonstrated a slight increase in ε with longer β-sheet–forming outer blocks (Figure 2.9 and Table A1), again consistent with the formation of larger aggregates. We therefore infer that the amino-acid selection and DP of the outer-block impacts characteristic

length scales within hydrogel networks based on their proclivity to form β-sheet aggregate domains, where the trend follows **3-CP-V>3-CP-T**> **3-CP-L**> **3-CP-PA**>**3-CP-PG**.

### 2.3.3 Tunable Viscoelasticity Based on Side-Chain Design

An advantage of this tunable material platform is an opportunity to control rheological properties via molecular design. To probe the stability and shear processing behavior of the networks, oscillatory shear measurements were conducted at different frequencies and strain amplitudes using a fixed concentration of 20 wt% copolypeptide. This concentration was chosen to minimize the use of material during optimization studies while staying above the critical concentration of the weakest hydrogelator. The strongest hydrogelator, 3-CP-PG and 3-CP-PA, can form hydrogel as low as 5wt%, while the weakest hydrogelator such as 3-CP-L and 3-CP-T need 20wt% to form stable homogenous hydrogels. At low strain amplitudes in the linear viscoelastic regime, the storage modulus ($G'$) is higher than the loss modulus ($G''$) at all measured frequencies, consistent with a robust physical gel (Figure A28). The same is also true under low imposed stresses, indicating the hydrogels behave like stable viscoelastic solids (Figure 2.10). The yield stress, associated with deviation from the plateau of the linear viscoelastic regime (LVR), can be attributed to chain pull out between β-sheet domains (Figure 3).[54] The yield point was estimated from a critical value of tan $\delta$ as indicated in Figure A30 to extract the apparent yield stress. Furthermore, the pronounced flow point where tan $\delta$ = 1 is related to the loss of mechanical rigidity due to a sufficient number of chains between β-sheet domains no longer being connected to form the overall network (Figure 2.10-2.11).[54,55] These two properties are critical to consider for extrusion based 3D-printing.

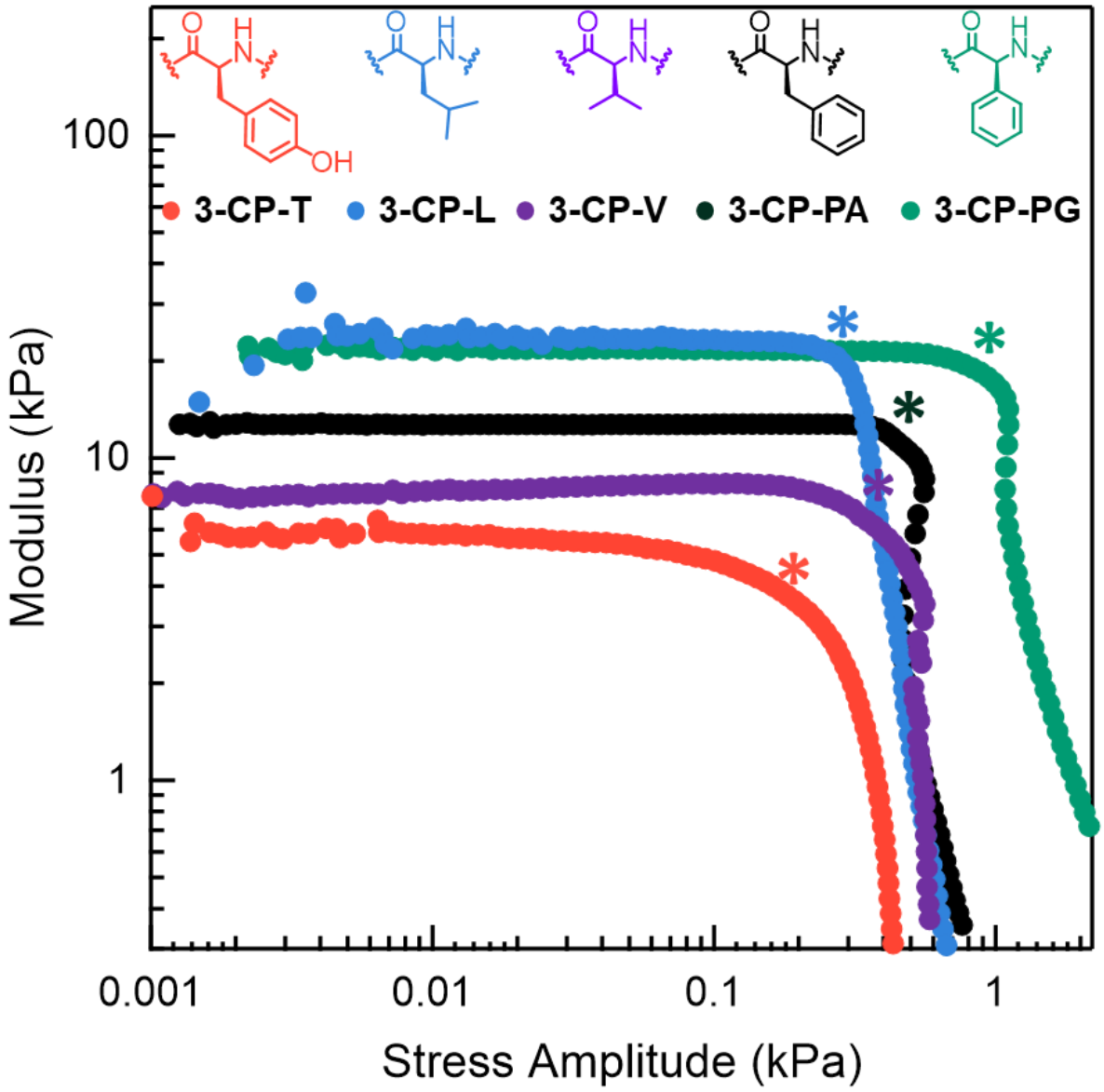


**Figure 2.4.** Storage modulus (*G'*) of 3-arm block copolypeptide hydrogel series at 20 wt% in an oscillatory amplitude stress sweep at a constant 6.2 rad/s with yield points marked with (*).[43] Reproduced with permission from John Wiley & Sons Inc.

This system enables the creation of materials with modulus and yielding behavior influenced specifically by the side-chain amino acid chemistry with analysis under identical concentrations (Figures 2.10-2.12 S29–S31). For example, aryl-containing materials **3-CP-PG**

and **3-CP-PA** exhibited a higher yield stress due to strong π–π interactions within β-sheet domains. By contrast, weaker alkyl hydrophobic interactions formed in **3-CP-L** and **3-CP-V** hydrogels lead to lower yield stresses. The use of **3-CP-T** demonstrated that altering the polarity of the β-sheet domain by incorporating more polar phenolic side chains resulted in the weakest hydrogel network.

Phenyl glycine was selected as the lead material for subsequent studies, since its lack of flexible hydrocarbon spacer in comparison to phenyl alanine allows for improved β-sheet stability. This subtle deviation from **3-CP-PA** proved to be critical as **3-CP-PG** outperformed other materials, exhibiting the highest modulus and yield point. The imposed stresses associated with yielding were consisted with the hydrogel interdomain spacing, where hydrogels having smaller average interdomain spacing ε (i.e., higher density of physical crosslinking centers) exhibit higher elastic modulus and yield stress. Overall, the combined structural and rheological measurements reveal the side chain chemistry to be an important and synthetically tunable parameter that controls β-sheet interactions, physical crosslinking structure, and the corresponding rheological properties of these hydrogels.

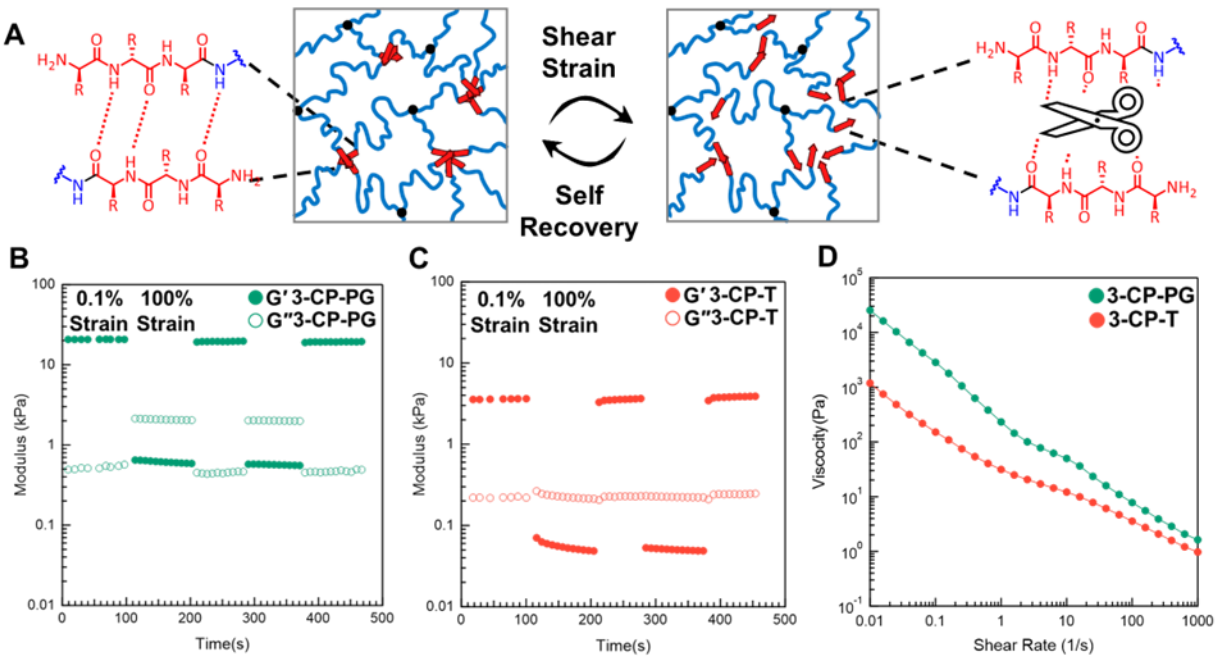


**Figure 2.5.** (A) Illustration of reversible yielding behavior in copolypeptide hydrogels due to the breaking and reforming of peptide backbone H-bonding. Cyclic oscillatory strain experiments on 20 wt% (B) 3-CP-PG and (C) 3-CP-T showing the network response to low (0.1%) and high (100%) strains at intervals of 100 s with a constant angular frequency of 6.2 rad/s. (D) Viscosity sweep with increasing shear rate illustrating shear-thinning behavior.[43] Reproduced with permission from John Wiley & Sons Inc.

### 2.3.4 Direct Ink Writing (DIW) Printing

The yielding and rapid self-recovery behavior of hydrogel networks are crucial rheological features necessary for extrusion applications, especially with 3D-printing techniques such as direct-ink writing (DIW). While linear block copolypeptides may undergo gelation via the formation of complex 2D assemblies, assembly is slow. In contrast, 3-arm star-shaped analogues are observed to assemble faster into 3D hydrogel networks with rapid reassociation of β-sheet domains leading to self-recovery after shear-based extrusion.[45] To simulate such an

extrusion process, shear processing properties and recovery of samples with the highest (**3-CP-PG**) and lowest (**3-CP-T**) yield stresses were evaluated using cyclic oscillatory experiments, in which the strain amplitude was cycled in a step-wise fashion. Specifically, hydrogels were subjected to 0.1% and 100% strain for fixed periods of 100 s, allowing network stability at low strains and shear-yielding behavior at higher strains to be demonstrated. The storage modulus of **3-CP-PG** decreased from 20 kPa to 0.6 kPa, but quickly recovered back to its original value, signifying network recovery (Figure 2.5D). In contrast, **3-CP-T** forms weaker networks (3 kPa) that rapidly decrease to 0.05 kPa and reform over similar strain cycles (Figure 2.5C). Because effective extrusion necessitates fast hydrogel yielding in the printer nozzle and shear-thinning during deposition onto the platform, rotational rheometry was used to better understand the non-Newtonian properties of these materials (Figure 2.5D). Although **3-CP-PG** forms a more viscous fluid at low shear compared to **3-CP-T**, both materials flow similarly after yielding at high shear rates, simulating the printing extrusion process. Given these similarities in flow, the faster recovery and higher quiescent modulus of **3-CP-PG** make it a better candidate for DIW compared to **3-CP-T**.

To further demonstrate the impact of β-sheet structure on printability, **3-CP-PG** and **3-CP-T** were evaluated on a commercial DIW 3D-printer. Block copolypeptide hydrogels (20 wt%) were loaded into a 3 mL syringe (27-gauge nozzle), with filament size and print uniformity studied at various applied pressures during extrusion using Image J (Figure 5A). **3-CP-PG** required higher applied pressures to extrude a stable filament, which directly correlates with the higher yield stress observed by rheometry. Both samples could form stable filaments with a width of 200 μm at their respective lowest extrudable pressures, although **3-CP-PG** produced more consistent filaments with better shape fidelity. The larger variability in filament size for

**3-CP-T** is likely related to slower network recovery and lower yield/flow point.[56] While we have previously shown the ability of analogous hydrogels to print multilayered 3D structures, here the resolution of intricate two layered patterns were studied.[38] In particular, the differences in filament uniformity is exacerbated when printing a two layer complex lattice in the x-y plane that can be semi-quantified using printability ($P_r$) values (Equation A2).[14,56] The fast recovering, higher yield-stress **3-CP-PG** gives a $P_r$ value of 1.03 at 170 kPa, while the slower recovering and weaker **3-CP-T** gives a $P_r$ value of 1.2 at 40 kPa (Figure 5B, Figure A33). In addition, **3-CP-PG** hydrogels clearly show enhanced shape fidelity and better performance in 3D-printing. The modular nature of this 3-arm block copolypeptide platform provides good control over molecular design, architecture, hydrogel microstructure, rheological properties, and 3D-printability through synthetically tunable chemistry and eliminates the need for additives that are typically required to enhance the viscosity and shear-thinning properties of traditional, structurally fixed biopolymer inks.

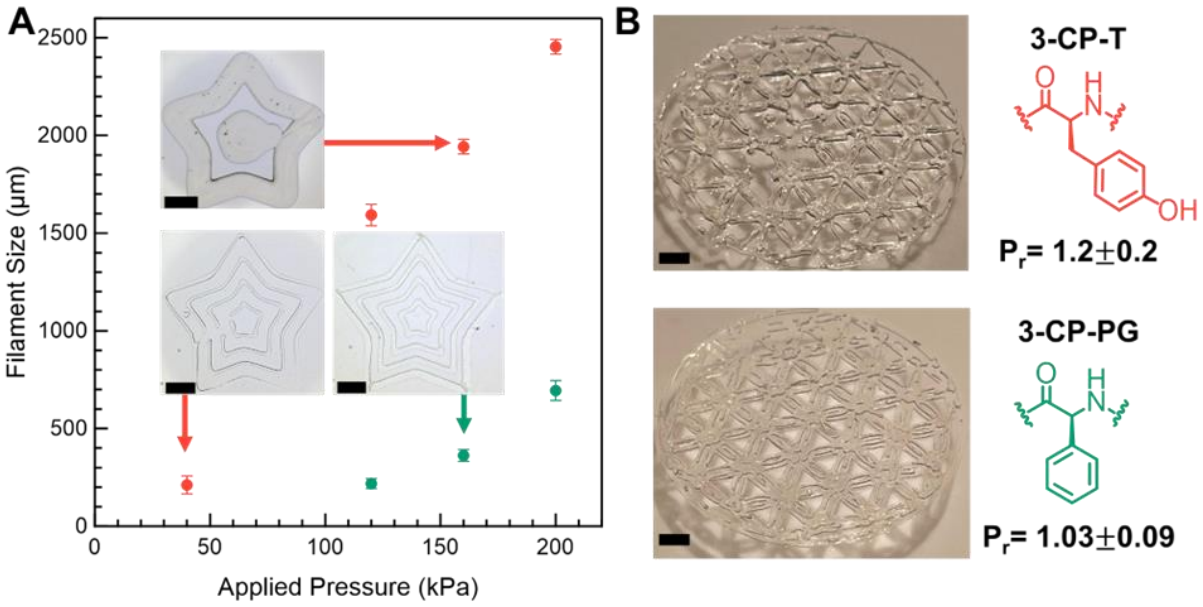


**Figure 2.6.** (A) Filament width as a function of applied pressure and representative prints. (B) 3-CP-T extruded at 40 kPa (top) and 3D-printed lattice of 3-CP-PG extruded at 170 kPa through a 27G needle (bottom) (Scale bars: 2 mm). [43] Reproduced with permission from John Wiley & Sons Inc.

## 2.4 Conclusion

In summary, we describe a robust strategy to create additive-free 3D-printable biomaterials based on β-sheet–driven hydrogelation of 3-arm star block copolypeptides that are readily synthesized using NCA ROP. The effects of changing spacer length and side-chain polarity on network properties were studied using valine, leucine, phenyl glycine, phenyl alanine, and tyrosine. All 3-arm block copolypeptides spontaneously form stable hydrogels with network structure and viscoelasticity determined by outer-block chemistry and degree of polymerization. The strategy provides access to different engineered properties, such as tailored thixotropy, yielding, and recovery. Significantly, these rheological differences were apparent during direct-ink writing, as the yielding and strain recovery trends correlate with filament uniformity and overall shape fidelity. In summary, our findings provide a basis to rationally design the 3D-printability and performance of sustainable, biocompatible polymers using amino-acid building blocks in tunable hydrogels.

## 2.5 Additional Experimental Results

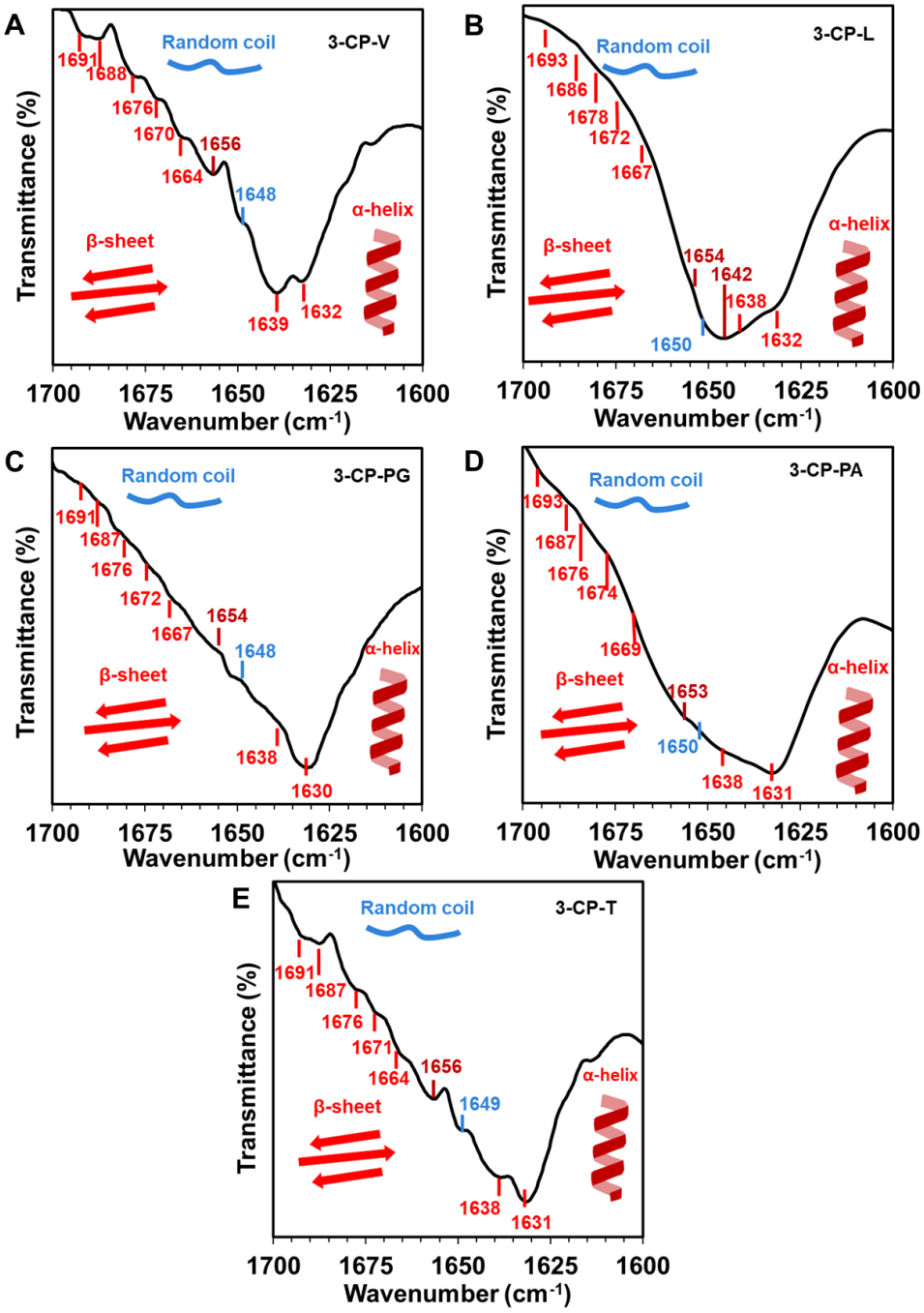


**Figure 2.7.** FTIR spectra showing secondary structures of (A) 3-CP-V, (B) 3-CP-L, (C) 3-CP-PG, (D) 3-CP-PA, and (E) 3-CP-T physical hydrogels in D2O. [43] Reproduced with permission from John Wiley & Sons Inc.

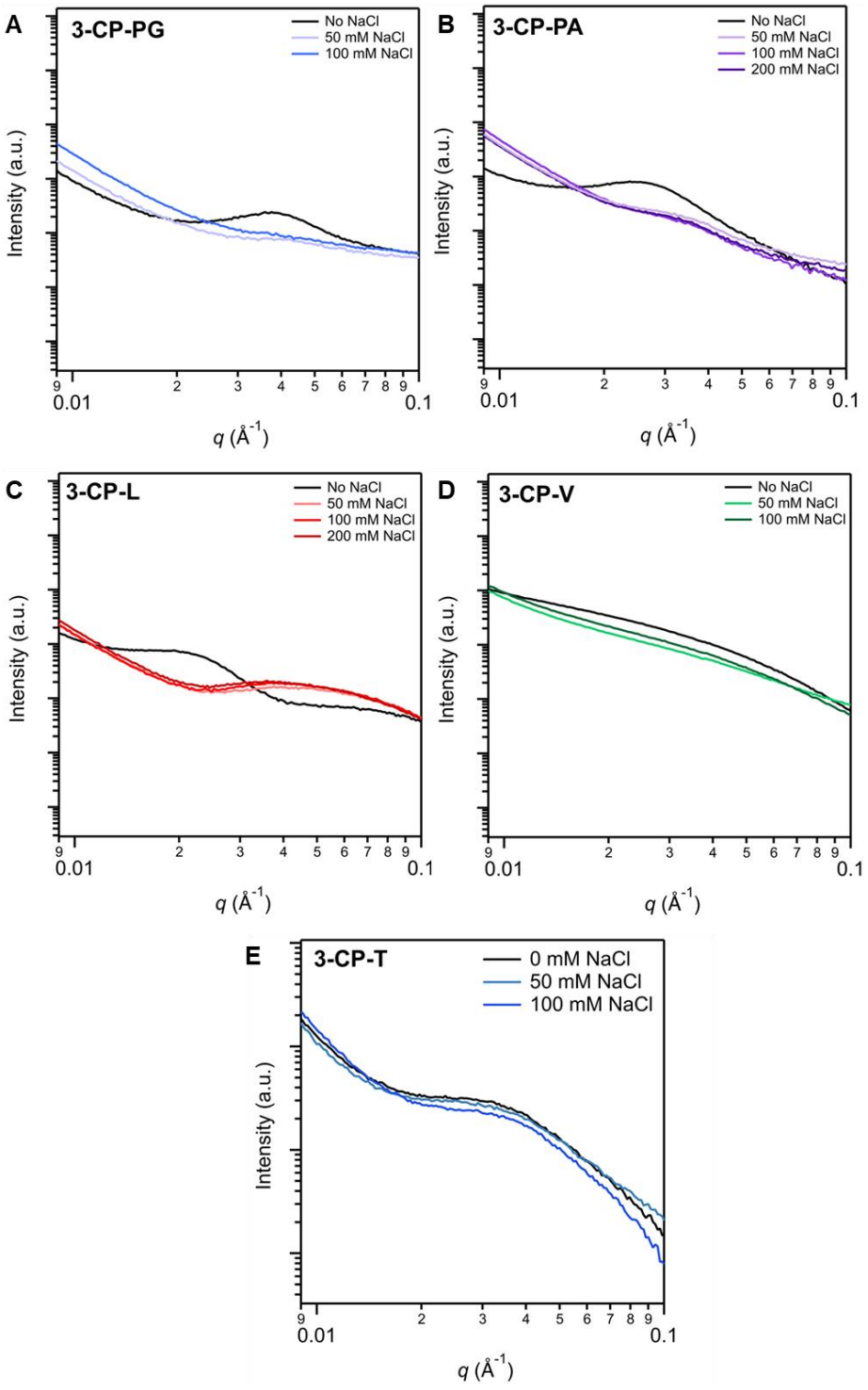


**Figure 2.8.** SAXS of 40 wt% of (A) 3-CP-PG, (B) 3-CP-PA, (C) 3-CP-L, (D) 3-CP-V, and (E) 3-CP-T in various aqueous solution. [43] Reproduced with permission from John Wiley & Sons Inc.

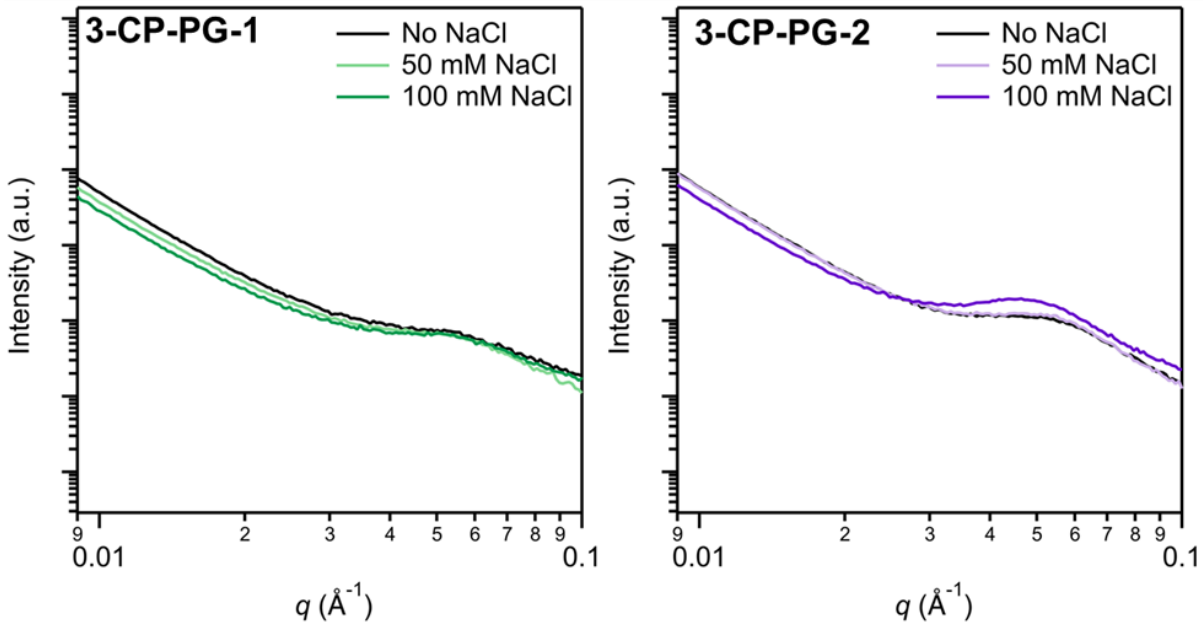


**Figure 2.9.** SAXS of 40 wt% of 3-CP-PG-1 and 3-CP-PG-2 in various aqueous solution. [43] Reproduced with permission from John Wiley & Sons Inc.

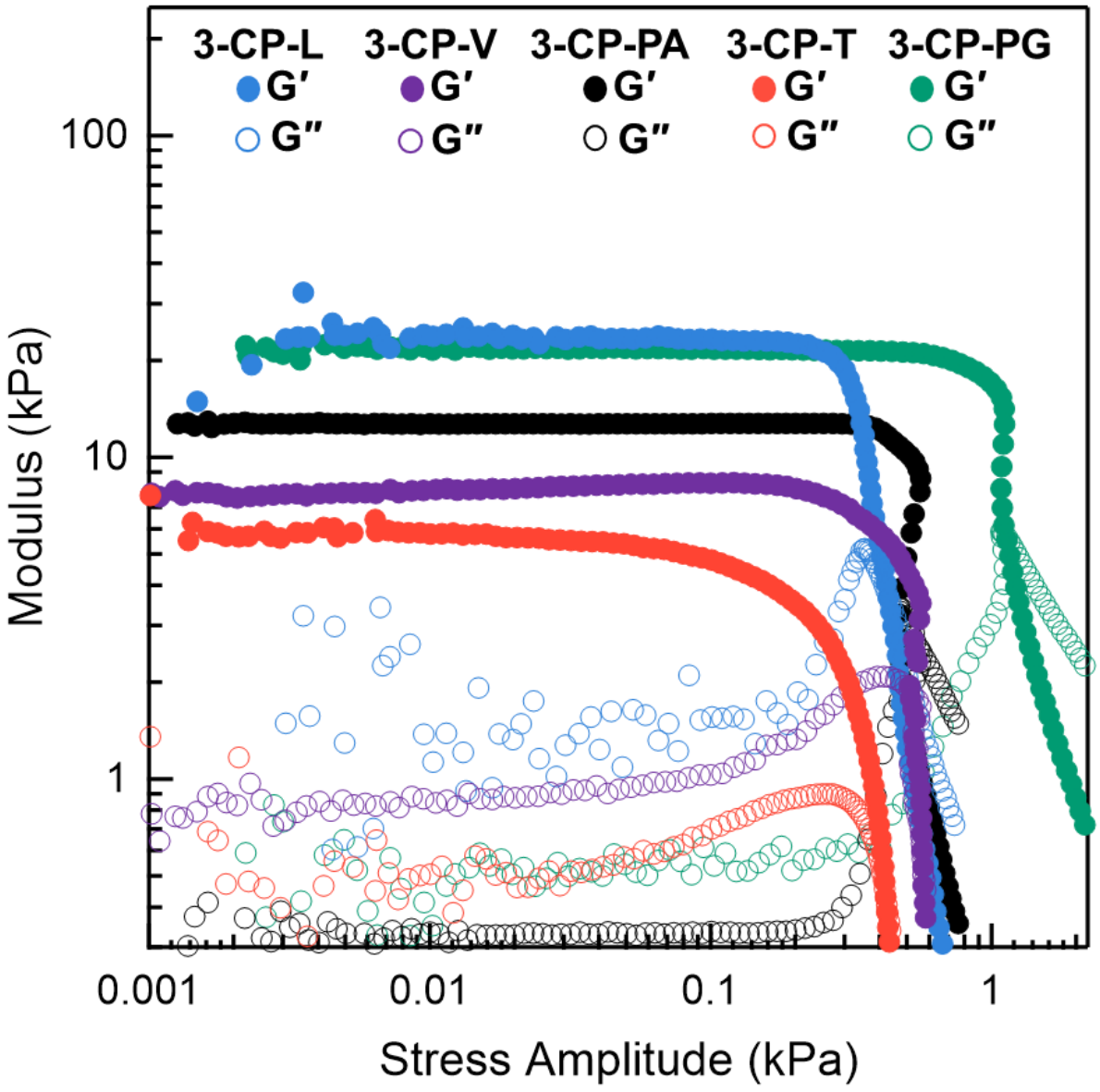


**Figure 2.10.** Stress amplitude sweep of 20 wt% (green) 3-CP-PG, (blue) 3-CP-L, (purple) 3-CP-V, (black) 3-CP-PA, and (pink) 3-CP-T hydrogels at 6.2 rad/s.[43] Reproduced with permission from John Wiley & Sons Inc.

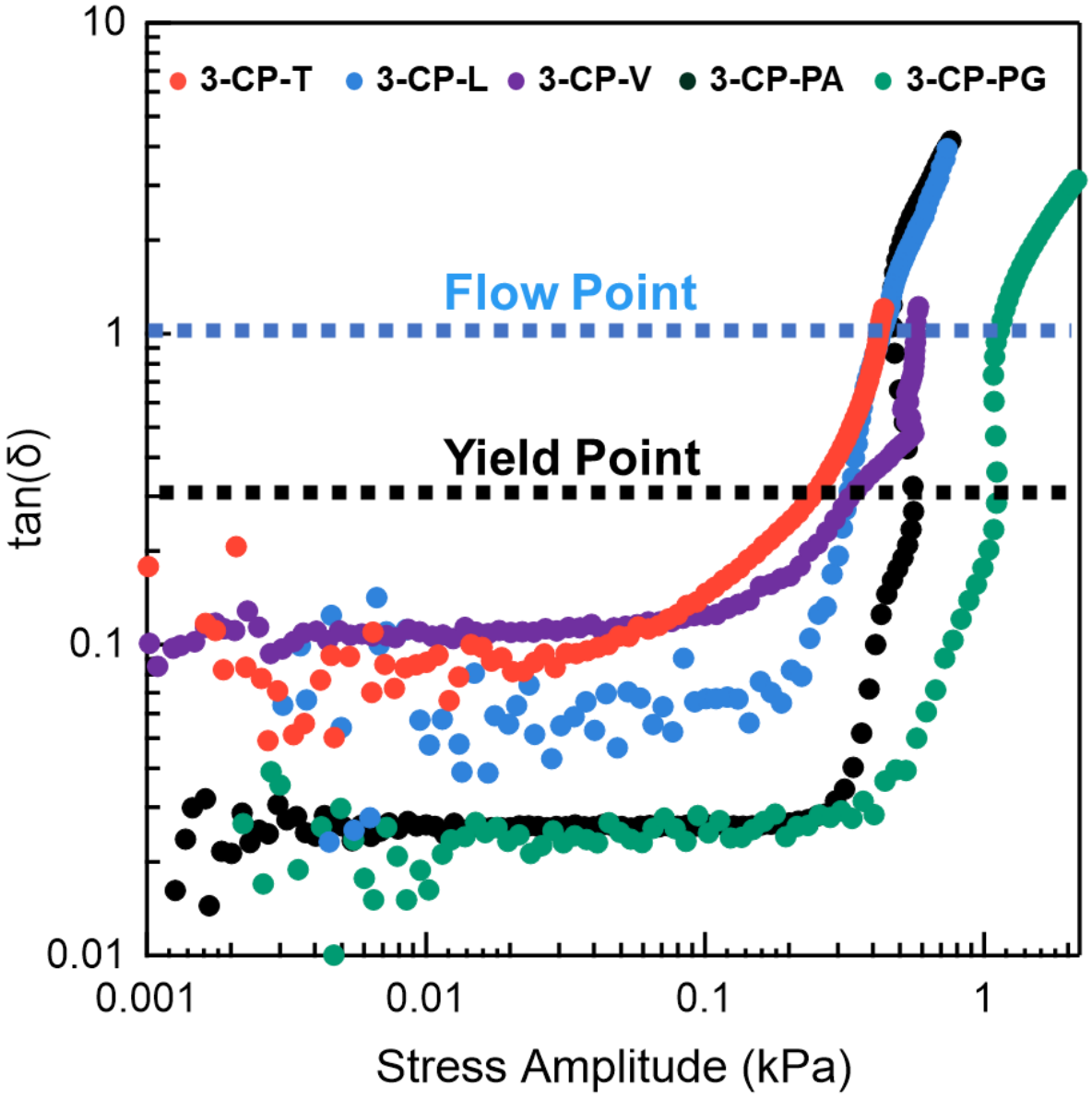


**Figure 2.11.** Tan δ of amplitude sweep of 20wt% hydrogel with flow and yield point marked with a dash arrow.[43] Reproduced with permission from John Wiley & Sons Inc.

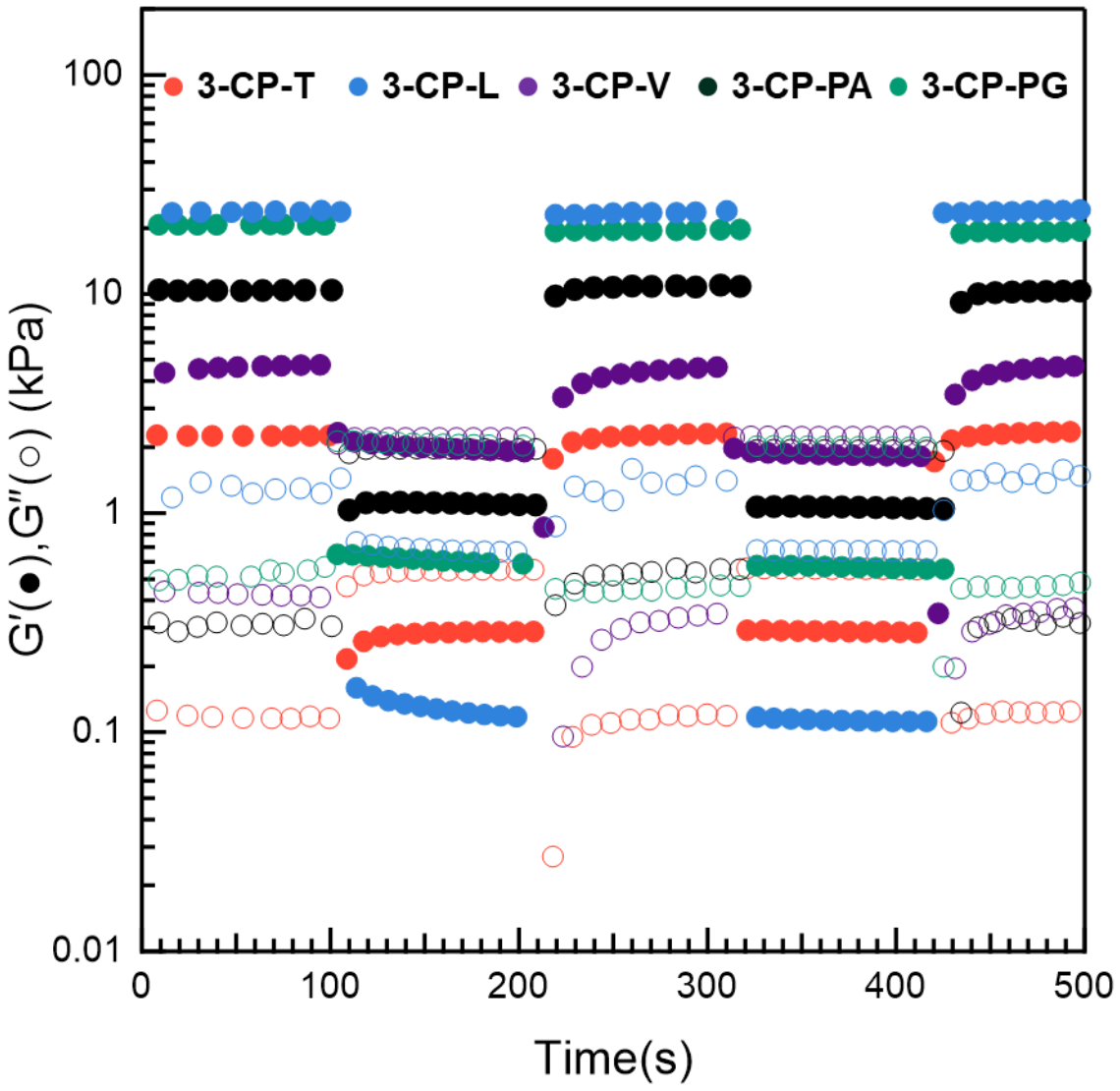


**Figure 2.12.** Cyclic dynamic time sweep of 20wt% (green) 3-CP-PG, (blue) 3-CP-L, (purple) 3-CP-V, (black) 3-CP-PA, and (pink) 3-CP-T hydrogels at 6.2 rad/s with 100 s interval of 0.1% strain and 100% strain.[43] Reproduced with permission from John Wiley & Sons Inc.

## 2.6 References


[1] Tian, K.; Bae, J.; Bakarich, S. E.; Yang, C.; Gately, R. D.; Spinks, G. M.; In Het Panhuis, M.; Suo, Z.; Vlassak, J. J. 3D Printing of Transparent and Conductive Heterogeneous Hydrogel–Elastomer Systems. *Adv. Mater.* **2017**, *29*, 1604827.

[2] Howard, E.; Li, M.; Kozma, M.; Zhao, J.; Bae, J. Self-Strengthening Stimuli-Responsive Nanocomposite Hydrogels. *Nanoscale* **2022**, *14*, 17887–17894.

[3] Hull, S. M.; Brunel, L. G.; Heilshorn, S. C.; Hull, S. M.; Brunel, L. G.; Heilshorn, S. C. 3D Bioprinting of Cell-Laden Hydrogels for Improved Biological Functionality. *Adv. Mater.* **2022**, *34*, 2103691.

[4] Yu, C.; Schimelman, J.; Wang, P.; Miller, K. L.; Ma, X.; You, S.; Guan, J.; Sun, B.; Zhu, W.; Chen, S. Photopolymerizable Biomaterials and Light-Based 3D Printing Strategies for Biomedical Applications. *Chem. Rev.* **2020**, *120*, 10695–10743.

[5] Liu, A. P.; Appel, E. A.; Ashby, P. D.; Baker, B. M.; Franco, E.; Gu, L.; Haynes, K.; Joshi, N. S.; Kloxin, A. M.; Kouwer, P. H. J.; Mittal, J.; Morsut, L.; Noireaux, V.; Parekh, S.; Schulman, R.; Tang, S. K. Y.; Valentine, M. T.; Vega, S. L.; Weber, W.; Stephanopoulos, N.; Chaudhuri, O. The Living Interface between Synthetic Biology and Biomaterial Design. *Nat. Mater.* **2022**, *21*, 390–397.

[6] Correa, S.; Grosskopf, A. K.; Lopez Hernandez, H.; Chan, D.; Yu, A. C.; Stapleton, L. M.; Appel, E. A. Translational Applications of Hydrogels. *Chem. Rev.* **2021**, *121*, 11385–11457.

[7] Dubbin, K.; Dong, Z.; Park, D. M.; Alvarado, J.; Su, J.; Wasson, E.; Robertson, C.; Jackson, J.; Bose, A.; Moya, M. L.; Jiao, Y.; Hynes, W. F. Projection Microstereolithographic Microbial Bioprinting for Engineered Biofilms. *Nano Lett.* **2021**, *21*, 1352–1359.

[8] Sanchez-Rexach, E.; Smith, P. T.; Gomez-Lopez, A.; Fernandez, M.; Cortajarena, A. L.; Sardon, H.; Nelson, A. 3D-Printed Bioplastics with Shape-Memory Behavior Based on Native Bovine Serum Albumin. *ACS Appl. Mater. Interfaces* **2021**, *13*, 19193–19199.

[9] Smith, P. T.; Altin, G.; Millik, S. C.; Narupai, B.; Sietz, C.; Park, J. O.; Nelson, A. Methacrylated Bovine Serum Albumin and Tannic Acid Composite Materials for Three-Dimensional Printing Tough and Mechanically Functional Parts. *ACS Appl. Mater. Interfaces* **2022**, *14*, 19193–19199.

[10] Karis, D. G.; Ono, R. J.; Zhang, M.; Vora, A.; Storti, D.; Ganter, M. A.; Nelson, A. Cross-Linkable Multi-Stimuli Responsive Hydrogel Inks for Direct-Write 3D Printing. *Polym. Chem.* **2017**, *8*, 4199–4206.

[11] Tang, M.; Zhong, Z.; Ke, C. Advanced Supramolecular Design for Direct Ink Writing of Soft Materials. *Chem. Soc. Rev.* **2023**, *52*, 1614–1649.

[12] Lee, U. N.; Day, J. H.; Haack, A. J.; Bretherton, R. C.; Lu, W.; Deforest, C. A.; Theberge, A. B.; Berthier, E. Layer-by-Layer Fabrication of 3D Hydrogel Structures Using Open Microfluidics. *Lab Chip* **2020**, *20*, 525–536.

[13] Shahbazi, M.; Jäger, H. Current Status in the Utilization of Biobased Polymers for 3D Printing Process: A Systematic Review of the Materials, Processes, and Challenges. *ACS Appl. Bio Mater.* **2021**, *4*, 325–369.

[14] Ouyang, L.; Yao, R.; Zhao, Y.; Sun, W. Effect of Bioink Properties on Printability and Cell Viability for 3D Bioplotting of Embryonic Stem Cells. *Biofabrication* **2016**, *8*, 035020.

[15] Gladman, A.; Matsumoto, E. A.; Nuzzo, R. G.; Mahadevan, L.; Lewis, J. A. Biomimetic 4D Printing. *Nat. Mater.* **2016**, *15*, 413–418.

[16] Gao, T.; Gillispie, G. J.; Copus, J. S.; Kumar, A. P. R.; Seol, Y. J.; Atala, A.; Yoo, J. J.; Lee, S. J. Optimization of Gelatin-Alginate Composite Bioink Printability Using Rheological Parameters: A Systematic Approach. *Biofabrication* **2018**, *10*, 4106.

[17] Yu, A. C.; Smith, A. A. A.; Appel, E. A. Structural Considerations for Physical Hydrogels Based on Polymer–Nanoparticle Interactions. *Mol. Syst. Des. Eng.* **2020**, *5*, 401–407.

[18] Cook, M. T.; Haddow, P.; Kirton, S. B.; Mcauley, W. J.; Cook, M. T.; Haddow, P.; Kirton, S. B.; Mcauley, W. J. Polymers Exhibiting Lower Critical Solution Temperatures as a Route to Thermoreversible Gelators for Healthcare. *Adv. Funct. Mater.* **2021**, *31*, 2008123.

[19] Rasines Mazo, A.; Allison-Logan, S.; Karimi, F.; Chan, N. J. A.; Qiu, W.; Duan, W.; O'Brien-Simpson, N. M.; Qiao, G. G. Ring Opening Polymerization of α-Amino Acids: Advances in Synthesis, Architecture and Applications of Polypeptides and Their Hybrids. *Chem. Soc. Rev.* **2020**, *49*, 4737–4834.

[20] He, H.; Sofman, M.; Wang, A. J. S.; Ahrens, C. C.; Wang, W.; Griffith, L. G.; Hammond, P. T. Engineering Helical Modular Polypeptide-Based Hydrogels as Synthetic Extracellular Matrices for Cell Culture. *Biomacromolecules* **2020**, *21*, 566–588.

[21] Hiew, S. H.; Mohanram, H.; Ning, L.; Guo, J.; Sánchez-Ferrer, A.; Shi, X.; Pervushin, K.; Mu, Y.; Mezzenga, R.; Miserez, A. A Short Peptide Hydrogel with High Stiffness Induced by 310-Helices to β-Sheet Transition in Water. *Adv. Sci.* **2019**, *6*, 1901173.

[22] Song, Z.; Fu, H.; Wang, R.; Pacheco, L. A.; Wang, X.; Lin, Y.; Cheng, J. Secondary Structures in Synthetic Polypeptides from N-Carboxyanhydrides: Design, Modulation, Association, and Material Applications. *Chem. Soc. Rev.* **2018**, *47*, 7401–7425.

[23] Huesmann, D.; Birke, A.; Klinker, K.; Türk, S.; Räder, H. J.; Barz, M. Revisiting Secondary Structures in NCA Polymerization: Influences on the Analysis of Protected

Polylysines. *Macromolecules* **2014**, *47*, 928–936.

[24] Krejchi, M. T.; Atkins, E. D. T.; Waddon, A. J.; Fournier, M. J.; Mason, T. L.; Tirrell, D. A. Chemical Sequence Control of SS-Sheet Assembly in Macromolecular Crystals of Periodic Polypeptides. *Science (80-. ).* **1994**, *265*, 1427–1432.

[25] Bera, S.; Mondal, S.; Rencus-Lazar, S.; Gazit, E. Organization of Amino Acids into Layered Supramolecular Secondary Structures. *Acc. Chem. Res.* **2018**, *51*, 2187–2197.

[26] Sinha, N. J.; Wu, D.; Kloxin, C. J.; Saven, J. G.; Jensen, G. V.; Pochan, D. J. Polyelectrolyte Character of Rigid Rod Peptide Bundlemer Chains Constructed via Hierarchical Self-Assembly. *Soft Matter* **2019**, *15*, 9858–9870.

[27] Hilderbrand, A. M.; Ford, E. M.; Guo, C.; Sloppy, J. D.; Kloxin, A. M. Hierarchically Structured Hydrogels Utilizing Multifunctional Assembling Peptides for 3D Cell Culture. *Biomater. Sci.* **2020**, *8*, 1256–1269.

[28] Nowak, A. P.; Breedveld, V.; Pine, D. J.; Deming, T. J. Unusual Salt Stability in Highly Charged Diblock Co-Polypeptide Hydrogels. *J. Am. Chem. Soc.* **2003**, *125*, 15666–15670.

[29] Jangizehi, A.; Ahmadi, M.; Seiffert, S. Emergence, Evidence, and Effect of Junction Clustering in Supramolecular Polymer Materials. *Mater. Adv.* **2021**, *2*, 1425–1453.

[30] Farsheed, A. C.; Thomas, A. J.; Pogostin, B. H.; Hartgerink, J. D.; Farsheed, A. C.; Pogostin, B. H.; Hartgerink, J. D.; Thomas, A. J. 3D Printing of Self-Assembling Nanofibrous Multidomain Peptide Hydrogels. *Adv. Mater.* **2023**, *35*, 2210378.

[31] Murphy, R. D.; Garcia, R. V.; Heise, A.; Hawker, C. J. Peptides as 3D Printable Feedstocks: Design Strategies and Emerging Applications. *Prog. Polym. Sci.* **2022**, *124*.

[32] Murphy, R.; Walsh, D. P.; Hamilton, C. A.; Cryan, S. A.; In Het Panhuis, M.; Heise, A. Degradable 3D-Printed Hydrogels Based on Star-Shaped Copolypeptides. *Biomacromolecules* **2018**, *19*, 2691–2699.

[33] Byrne, M.; Murphy, R.; Kapetanakis, A.; Ramsey, J.; Cryan, S. A.; Heise, A. Star-Shaped Polypeptides: Synthesis and Opportunities for Delivery of Therapeutics. *Macromol. Rapid Commun.* **2015**, *36*, 1862–1876.

[34] Zhang, S.; Alvarez, D. J.; Sofroniew, M. V.; Deming, T. J. Design and Synthesis of Nonionic Copolypeptide Hydrogels with Reversible Thermoresponsive and Tunable Physical Properties. *Biomacromolecules* **2015**, *16*, 1331–1340.

[35] Gonzalez, M. A.; Simon, J. R.; Ghoorchian, A.; Scholl, Z.; Lin, S.; Rubinstein, M.; Marszalek, P.; Chilkoti, A.; López, G. P.; Zhao, X. Strong, Tough, Stretchable, and Self-Adhesive Hydrogels from Intrinsically Unstructured Proteins. *Adv. Mater.* **2017**, *29*, 1604743.

[36] Chan, N. J.; Lentz, S.; Gurr, P. A.; Scheibel, T.; Qiao, G. G. Mimicry of Silk Utilizing

Synthetic Polypeptides. *Prog. Polym. Sci.* **2022**, *130*, 101557.

[37] Weiss, A. C. G.; Shirbin, S. J.; Kelly, H. G.; Besford, Q. A.; Kent, S. J.; Qiao, G. G. Plasma Corona Protects Human Immune Cells from Structurally Nanoengineered Antimicrobial Peptide Polymers. *ACS Appl. Mater. Interfaces* **2021**, *13*, 33821–33829.

[38] Murphy, R. D.; Garcia, R. V.; Oh, S. J.; Wood, T. J.; Jo, K. D.; Read de Alaniz, J.; Perkins, E.; Hawker, C. J. Tailored Polypeptide Star Copolymers for 3D Printing of Bacterial Composites Via Direct Ink Writing. *Adv. Mater.* **2023**, *35*, 2207542.

[39] Tang, C. C.; Zhang, S. H.; Phan, T. H. M.; Tseng, Y. C.; Jan, J. S. Block Length and Topology Affect Self-Assembly and Gelation of Poly(l-Lysine)-Block-Poly(S-Benzyl-l-Cysteine) Block Copolypeptides. *Polymer (Guildf).* **2021**, *228*, 123891.

[40] Sun, Y.; Deming, T. J. Self-Healing Multiblock Copolypeptide Hydrogels via Polyion Complexation. *ACS Macro Lett.* **2019**, *32*, 553–557.

[41] Breedveld, V.; Nowak, A. P.; Sato, J.; Deming, T. J.; Pine, D. J. Rheology of Block Copolypeptide Solutions: Hydrogels with Tunable Properties. *Macromolecules* **2004**, *37*, 3943–3953.

[42] Wu, B.; Hanay, S. B.; Kimmins, S. D.; Cryan, S. A.; Hermida Merino, D.; Heise, A. Ion-Triggered Hydrogels Self-Assembled from Statistical Copolypeptides. *ACS Macro Lett.* **2022**, *11*, 323–328.

[43] Garcia, R. V.; Murphy, E. A.; Sinha, N. J.; Okayama, Y.; Urueña, J. M.; Helgeson, M. E.; Bates, C. M.; Hawker, C. J.; Murphy, R. D.; Read de Alaniz, J. Tailoring Writability and Performance of Star Block Copolypeptides Hydrogels through Side-Chain Design. *Small* **2023**, *19*, 2302794.

[44] Tian, Z. Y.; Zhang, Z.; Wang, S.; Lu, H. A Moisture-Tolerant Route to Unprotected α/β-Amino Acid N-Carboxyanhydrides and Facile Synthesis of Hyperbranched Polypeptides. *Nat. Commun.* **2021**, *12*, 1–11.

[45] Shen, Y.; Zhang, S.; Wan, Y.; Fu, W.; Li, Z. Hydrogels Assembled from Star-Shaped Polypeptides with a Dendrimer as the Core. *Soft Matter* **2015**, *11*, 2945–2951.

[46] Zhao, W.; Gnanou, Y.; Hadjichristidis, N. From Competition to Cooperation: A Highly Efficient Strategy towards Well-Defined (Co)Polypeptides. *Chem Commun* **2015**, *51*, 3663–3666.

[47] Yang, H.; Yang, S.; Kong, J.; Dong, A.; Yu, S. Obtaining Information about Protein Secondary Structures in Aqueous Solution Using Fourier Transform IR Spectroscopy. *Nat. Protoc.* **2015**, *10*, 382–396.

[48] Prabhu, V. M.; Amis, E. J.; Bossev, D. P. Counterion Associative Behavior with Flexible Polyelectrolytes. *J. Chem. Phys* **2004**, *121*, 4424.

[49] Solomon, M. J.; Spicer, P. T. Microstructural Regimes of Colloidal Rod Suspensions,

Gels, and Glasses. *Soft Matter* **2010**, *6*, 1391.

[50] De Molina, P. M.; Lad, S.; Helgeson, M. E. Heterogeneity and Its Influence on the Properties of Difunctional Poly(Ethylene Glycol) Hydrogels: Structure and Mechanics. *Macromolecules* **2015**, *48*, 5402–5411.

[51] Lin-Gibson, S.; Jones, R. L.; Washburn, N. R.; Horkay, F. Structure-Property Relationships of Photopolymerizable Poly(Ethylene Glycol) Dimethacrylate Hydrogels. *Macromolecules* **2005**, *38*, 2897–2902.

[52] Cohen, N.; Eisenbach, C. D. Molecular Mechanics of Beta-Sheets. *ACS Biomater. Sci. Eng.* **2020**, *6*, 1940–1949.

[53] Lifson, S.; Sander, C. Antiparallel and Parallel β-Strands Differ in Amino Acid Residue Preferences. *Nature* **1979**, *282*, 109–111.

[54] Yan, C.; Altunbas, A.; Yucel, T.; Nagarkar, R. P.; Schneider, J. P.; Pochan, D. J. Injectable Solid Hydrogel: Mechanism of Shear-Thinning and Immediate Recovery of Injectable β-Hairpin Peptide Hydrogels. *Soft Matter* **2010**, *6*, 5143–5156.

[55] Congqi Yan; J. Pochan, D. Rheological Properties of Peptide -Based Hydrogels for Biomedical and Other Applications. *Chem. Soc. Rev.* **2010**, *39*, 3528–3540.

[56] Schwab, A.; Levato, R.; D'Este, M.; Piluso, S.; Eglin, D.; Malda, J.; D'Este, M.; Piluso, S.; Eglin, D.; Malda, J. Printability and Shape Fidelity of Bioinks in 3D Bioprinting. *Chem. Rev.* **2020**, *120*, 11028–11055.

# Chapter 3. Tailored polypeptide star copolymers for 3D printing of bacterial composites via direct ink writing

Portions of this work were published in:

Ronnie V. Garcia, Robert D. Murphy, Seung J. Oh, Tanner J. Wood , Javier Read de Alaniz, Ed Perkins, Craig J. Hawker, Tailored polypeptide star copolymers for 3D printing of bacterial composites via direct ink writing, *Adv.Mater.* **2023**, 220752. Reproduced with permission from John Wiley & Sons Inc.

## 3.1 Abstract

Hydrogels hold much promise for 3-D printing of functional living materials, however challenges remain in tailoring mechanical robustness as well as biological performance. In addressing this challenge, we describe the modular synthesis of functional hydrogels from 3-arm diblock copolypeptide stars composed of an inner poly(L-glutamate) domain and outer poly(L-tyrosine) or poly(L-valine) blocks. Physical crosslinking due to ß-sheet assembly of these star block copolymers gives mechanical stability during extrusion and the selective incorporation of methacrylate units allows for subsequent photocrosslinking to occur under biocompatible conditions. This permits direct ink write (DIW) printing of bacteria-based mixtures leading to 3D objects with high fidelity and excellent bacterial viability. The tunable stiffness of different copolypeptide networks enables control over proliferation and colony formation for embedded *E.coli* bacteria as demonstrated via isopropyl ß-D-1-thiogalactopyranoside (IPTG) induction of green fluorescent protein (GFP) expression. This translation of molecular structure to network properties highlights the versatility of these polypeptide hydrogel systems with the combination of writable structures and biological activity illustrating the future potential of these 3D printed biocomposites.

## 3.2 Introduction

Additive manufacturing, or 3D printing, has emerged as a valuable technology for the on-demand, customized production of complex parts that have utility in a wide variety of areas such as electronics,[1] pharmaceuticals,[2] and biomedicine.[3] Various feedstock materials have been successfully patterned into 3D objects including elastomers,[4,5] thermoset resins,[6,7] and hydrogels.[8,9] Continuous advances in the field have enabled less stringent printing conditions,[10]

and wider scope of materials for adaptation.[11] Hydrogels in particular are of interest as the 3D polymer network combines structural integrity with high water content leading to tunable 3D environments for incorporation of functional biological systems.[12] Their intrinsic mechanical properties can be readily modulated through embedded additive such as nanoparticles,[13] or multicomponent blends – which have been adapted for 3D printability.[14,15] For biocomposite 3D printing, stereolithography (SLA)[16] or digital light processing (DLP)[17] rely on low viscosity crosslinkable resin systems, whereas direct ink writing (DIW) 3D printing can be achieved with shear-thinning hydrogels.[18] For these DIW systems, a secondary photocrosslinking step can be employed to covalently stabilize the primary 3D printed objects.[19]

A popular adaption of DIW 3D printing is known as 'bioprinting', a strategy that permits the spatial and temporal distribution of living cells with the goal of enabling cell proliferation and maturation.[20,21] It should be noted that the behaviour of cellular components within the 3D environment may be regulated by the physical and chemical properties of the hydrogel network allowing for further tuning of performance.[22] This is of particular interest for DIW systems where 3D printed bacterial composites[23-25] hold significant potential in wound-healing,[26] bioremediation,[27] and biosensor applications.[28] In addition, the capability to control the biochemical and genetic machinery of bacteria through network interactions may create 'living' 3D materials with tunable metabolic activity, an underexplored space in synthetic biology.[29]

In considering material selection for DIW bioprinting, the majority of studies have centered on the use of biopolymers such alginate and gelatin.[30] However there are a number of

challenges with these systems including batch to batch variation and poor mechanical properties. As a result, there is a clear need for developing synthetic systems with tunable structure/performance relationships. For example, polypeptides offer tailored molecular weights, controlled secondary structures,[31] degradable backbones and functional side chains[32] for modulating physicochemical, bio-functional and mechanical properties.[33-35] As a result, the exploration of polypeptides hydrogels as 3D printable bioinks may offer significant potential for the 3D printing of bacteria-based biocomposites (Figure 3.1).

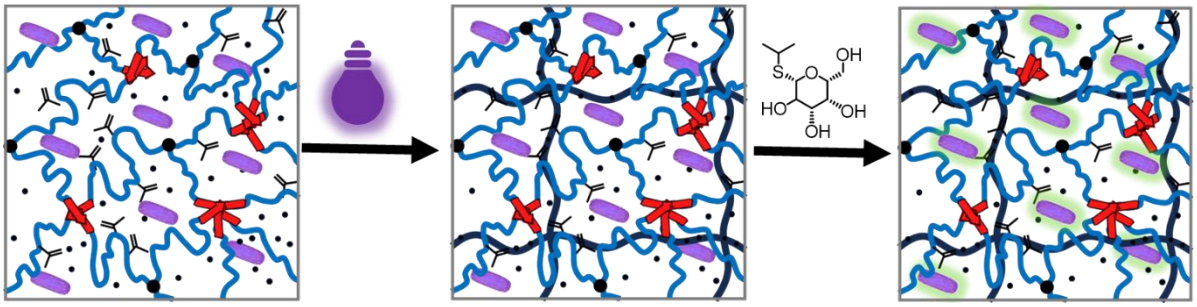


**Figure 3.1.** Schematic representation of 2-step assembly and crosslinking strategy for the 3D-printing of bacterial biocomposites.[52] Reproduced with permission from John Wiley & Sons Inc.

In this report we describe the design, synthesis and evaluation of 3-arm block copolypeptide stars for the 3D printing of bacterial biocomposites. From a trifunctional initiator, ring opening polymerization of the N-carboxyanhydride (NCA) of benzyl-L-glutamate is followed by chain extension with NCA tyrosine or valine monomers to give 3-arm block copolypeptides which spontaneously form hydrogels when dissolved in aqueous solution. This tunable assembly is driven by secondary interactions defined by the nature of the outer block (tyrosine or valine) and the degree of polymerization leading to hydrogels with controlled mechanical properties. Functionalization of the copolypeptides with methacrylate units allows for photocrosslinking and was directly probed via real-time rheological studies.

The biocompatibility of these hydrogels and the fidelity of the 3D printing process was then evaluated through the fabrication of 3D objects embedded with genetically modified *E.coli* bacteria. Significant differences in *E.coli* colony formation, aggregation and induced expression of green fluorescent protein (GFP) using isopropyl ß-D-1-thiogalactopyranoside (IPTG) was observed. These features could be directly correlated with both the modular design of the starting 3-arm block copolypeptide star and the corresponding secondary structure.

### 3.3 Results and discussion

#### 3.3.1 Synthesis and Self Assembly.

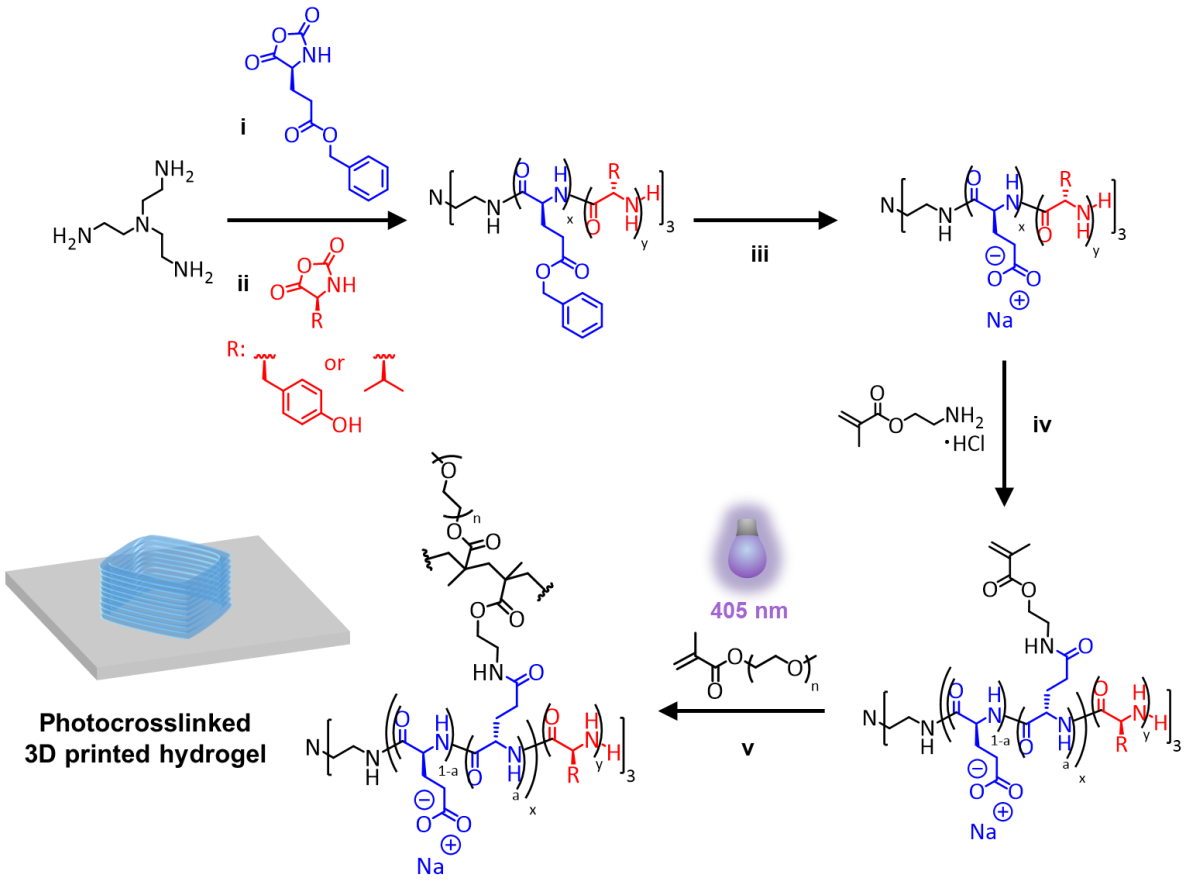


**Figure 3.2.** (i) $CHCl_3$/DMF, 18h, rt. (ii) DMF (for L-tyrosine NCA) or $CHCl_3$/DMF (for L-valine NCA), 18h, rt. (iii) TFA/$CHCl_3$, HBr 33 wt% in AcOH, 18 h, rt; NaOH, dialysis, 3 days. (iv) with 4-(4,6-Dimethoxy-1,3,5-

triazin-2-yl)-4-methylmorpholinium chloride (DMT-MM), deionized water, $NaHCO_3$, 36 h, rt; dialysis, 3 days. (v) deionized water, Lithium phenyl-2,4,6-trimethylbenzoylphosphinate (LAP – photoinitiator). [52] Reproduced with permission from John Wiley & Sons Inc.

**Synthesis and self-assembly.**

*N*-carboxyanhydride (NCA) monomers based on γ-benzyl-L-glutamate (BLG), L-tyrosine (LT) and L-valine (LV) were synthesized from an adapted literature procedure using epichlorohydrin as a HCl scavenger.[36] In each case, monomer yield and stability was improved compared to traditional procedures with $^1$H NMR, $^{13}$C NMR, and FTIR spectroscopy illustrating the high level of NCA purity (Figure A34-40). A trifunctional initiator, tris(2-aminoethyl)amine (TREN), was then selected for controlled ring opening polymerization of the inner domain based on γ-benzyl-L-glutamate (BLG) with full conversion being confirmed with FTIR and $^1$H NMR spectroscopy. In-situ chain extension of the PBLG star with either the NCA monomer derived from L-tyrosine (LT) or the NCA monomer derived from L-valine (LV) gives the desired 3-arm star block copolymers (Figure 3.2). The design of the block sequences, degree of polymerization and architecture is based on the facile assembly of multi-arm copolypeptides to give robust hydrogels. Significantly, these 3-arm block copolymers were shown to have superior mechanical properties when compared to their linear counterparts due to β-sheet assembly of the terminal tyrosine or valine blocks.[37,38] From a design perspective, the inner domain of glutamate residues provides a biocompatible aqueous environment for maintaining the viability of encapsulated bacteria.[39] In addition, functionalization of a limited number of carboxylate side chains can serve as a site to incorporate crosslinkable moieties for subsequent photopolymerization of the physically assembled biocomposites. The choice of tyrosine or valine as hydrophobic outer domains[40]

was based on the ability to tailor hydrogel properties and rheological performance through the formation of β-sheets.[41-45] The degree of polymerization and structure of the 3-arm poly(benzyl-L-glutamate-b-L-tyrosine) (3-PBLG$_{90}$-b-PLT$_{45}$) and poly(benzyl-L-glutamate-b-L-valine) (3-PBLG$_{90}$-b-PLV$_{45}$) block copolypeptides was determined using $^{1}$H NMR spectroscopy (Figure B8 and B10) and the molar mass and dispersities characterized by diffusion ordered spectroscopy (DOSY) NMR spectroscopy and size exclusion chromatography (SEC) (Figure B11 and Table B1). Excellent agreement between experimental and theoretical molecular weights are observed with low dispersities (Đ ~ 1.1) illustrating the controlled nature of the ring opening polymerization process. It should be noted that ultra-high molecular weight assemblies were observed in the SEC trace for the valine block copolymer (Figure B11) while DOSY NMR analysis shows a single population for the 3-PBLG$_{90}$-b-PLV$_{45}$ block copolymer (Figure B10). In contrast, analysis of the tyrosine-based materials reveal both a single SEC peak and DOSY NMR population. These results are in agreement with increased ß-sheet formation for poly(valine) domains when compared to the corresponding tyrosine systems and the ability of the DOSY NMR solvent (15% TFA in CDCl3) to more efficiently disrupt ß -sheet formation when compared to the SEC eluent (hexafluoro-iso-propanol). Another set of diblock copolymers having a larger ratio (4:1) of glutamate to outer tyrosine and valine blocks (3-PBLG$_{90}$-b-PLT$_{22}$, 3-PBLG$_{90}$-b-PLV$_{22}$) were also synthesized and characterized (Figure A46-47), in order to validate the choice of the lead diblock materials (ratio 3:1).

For all systems, removal of the benzyl protecting groups of the glutamate blocks was an efficient process using 33 wt% HBr in acetic acid to give the desired 3-arm star block copolypeptides. Significantly, the 3-PBLG$_{90}$-*b*-PLT$_{45}$ and 3-PBLG$_{90}$-*b*-PLV$_{45}$ derivatives gave

clear transparent hydrogels at a variety of concentrations in aqueous solution due to the amphiphilic polymer design coupled with β-motif structural assembly. For subsequent coupling, the carboxylic acid groups were initially activated by treatment with 4-(4,6-dimethoxy-1,3,5-triazin-2-yl)-4-methylmorpholinium chloride (DMT-MM), followed by addition of 2-aminoethyl methacrylate hydrochloride. Approximately 10-20 methacrylate units (90 glutamate units total) were targeted with the 3-arm methacrylated copolypeptides, now termed 3-CP-T and 3-CP-V respectively for simplicity, being fully analyzed by $^{1}$H NMR to confirm successful conjugation and the degree of substitution. For 3-CP-T, a degree of substitution of 18 was determined using phenol proton resonances as a reference (Figure A48), while for 3-CP-V a degree of substitution of 14 was determined using the α-protons as reference (Figure B15). Similar to the parent non-functionalized copolypeptides, these methacrylate derivatives were also observed to be water soluble and undergo spontaneous assemble into physically crosslinked hydrogels within the desired concentration ranges (~3-10 wt%) (Figure 3.2 and 3.7). As shown in Figure 1, hydrogelation stems from assembly of the hydrophobic tyrosine or valine sequences into a β-sheet motif with the 3-arm star architecture being critical for formation of a network structure to give a physically crosslinked, extrudable material.

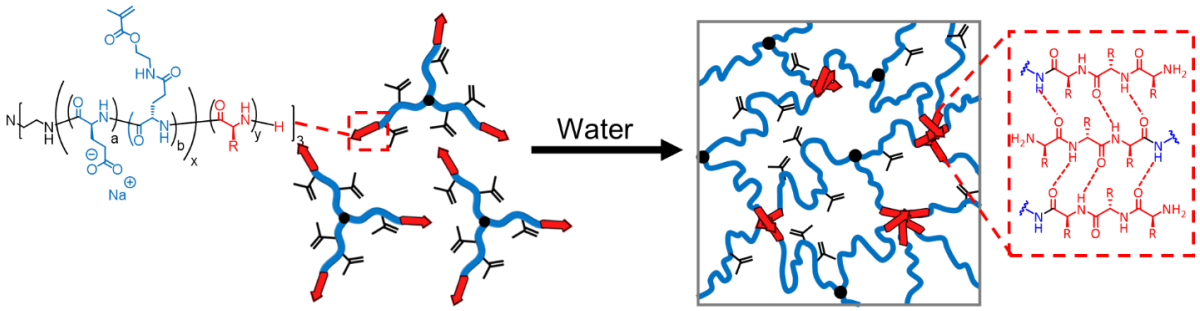


**Figure 3.3.** Graphic depicting yielding behaviour of copolypeptide hydrogels subject to shear and subsequent reformation upon removal of shear via β-motif directed H-bonding of amide bonds (A). Cyclic dynamic oscillatory amplitude time sweeps for 7.5 wt% hydrogels of 3-CP-T (B) and 3-CP-V (C) showing moduli response to low strains (0.1%) and high strains (100%) at intervals of 100 s at constant angular frequency of 6.2 rad/s. Viscosity sweep with increasing shear rate (D) illustrating shear-thinning behaviour of hydrogels. [52] Reproduced with permission from John Wiley & Sons Inc.

To confirm the formation of β-sheet assemblies, FTIR spectroscopy was used to examine the physically crosslinked 3-CP-T and 3-CP-V hydrogels (Figure 3.8). Multiple peptide backbone bands could be observed in the amide I region using $D_2O$ with prominent peaks denoting β-sheet formation being observed from 1630-1690 cm-1 for 3-CP-T and 3-CP-V respectively. In addition, characteristic β-turn peaks were also observed between 1660 and 1690 $cm^{-1}$ with absorbances for random coil structures attributed to unordered glutamate sequences (~1648 $cm^{-1}$) and α-helical peaks, possibly from methacrylated glutamine residues (~1656 $cm^{-1}$) being identified.[46] These β-sheet signatures in the FTIR spectra illustrate the power of hydrophobic amino acid residues [47] within the original 3-arm block copolypeptide design coupled with the utility of secondary structural self-assembly.

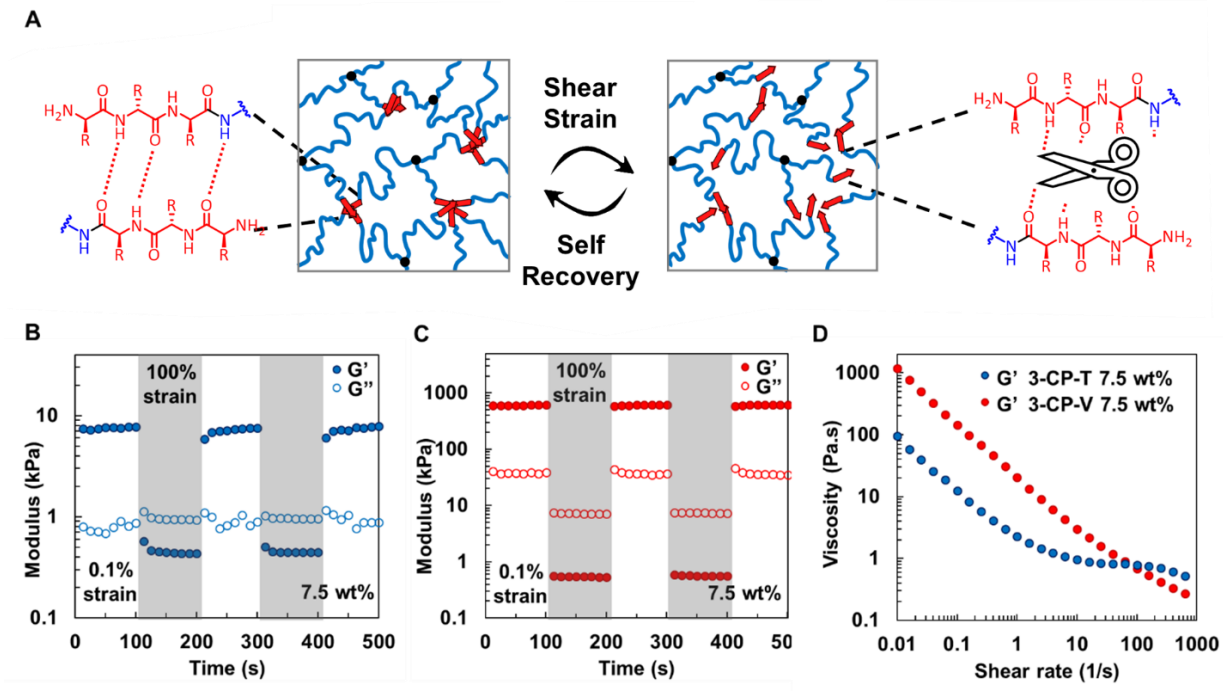


**Figure 3.4.** Graphic depicting yielding behaviour of copolypeptide hydrogels subject to shear and subsequent reformation upon removal of shear via β-motif directed H-bonding of amide bonds (A). Cyclic dynamic oscillatory amplitude time sweeps for 7.5 wt% hydrogels of 3-CP-T (B) and 3-CP-V (C) showing moduli response to low strains (0.1%) and high strains (100%) at intervals of 100 s at constant angular frequency of 6.2 rad/s. Viscosity sweep with increasing shear rate (D) illustrating shear-thinning behaviour of hydrogels. [52] Reproduced with permission from John Wiley & Sons Inc.

### 3.3.2 Tunable Hydrogel Viscoelasticity

While the ability to control gelation through secondary interactions is present for both the tyrosine and valine block copolypeptides, the mechanical properties were distinctly different. Both 3-CP-T and 3-CP-V derivatives were observed to gelate at concentrations as low as 3.75 and 3.5 wt% respectively using the inversion vial method (Figure 3.7). However, at these low concentrations, the hydrogels were soft and not ideally suited for extrusion-based 3D printing due to their high thixotropic nature. Rheological evaluation of the viscoelastic

nature of 3-CP-T and 3-CP-V hydrogels provided significant insight into the associated mechanical properties with oscillatory frequency sweeps being used to determine the stability of the parent hydrogels over a range of frequencies. For both hydrogels at 5.0 and 7.5 wt% respectively, storage modulus (G′) was higher than the loss modulus (G″) across different frequencies, indicating that the hydrogels display behaviour of stable viscoelastic solids with shear-yielding behaviour at higher strains (Figure 3.10 A-D). Beyond the linear viscoelastic region (LVR), the transition from solid-like to fluid-like was evident as G″ surpassed G′, suggesting yielding of the physical hydrogel network. Identical copolypeptides with lower DP blocks of tyrosine and valine (3-CP-T2, 3-CP-V2) had significantly inferior moduli and viscoelastic regimes in both oscillatory frequency and amplitude sweeps (Figure 3.9), validating the choice of outer block DP for lead materials investigated. As shown in Figure 3.4, cyclic oscillatory amplitude time sweeps clearly show the self-recovery properties of both hydrogel networks when subjected to low and high strain (Figure 3.4, 3.10). Hydrogel networks were physically stable at low strain (0.1%) and begin to exhibit shear-yielding behaviour at higher strain (100%). Recovery of the G' moduli from high strain values (100%) to low strain values (0.1%) over multiple cycles was observed, illustrating the rapid and reproducible reassembly of the peptide networks (Figure 3.4A), with only minor thixotropic behavior. For example, upon return to 0.1% strain, slower recovery of the tyrosine-derived hydrogel, 3-CP-T, was evident with G' stabilizing at 7.3 kPa after 25s (Figure 3.4B). In contrast, rapid recovery was observed for the valine-derived hydrogels, 3-CP-V, with G' recovering to 600 kPa within seconds (Figure 3.4C). Similarly, there was a stark difference in storage modulus between the two systems with a ~2 orders of magnitude change on going from the tyrosine to valine outer blocks. These observations are in line with the β-sheet structures

associated with valine containing peptide sequences, which are known to increase hydrogel strength through enhanced stabilization of H-bonds.[48,49] In both systems, hydrogel viscosity decreased with increasing shear rate (Figure 3.4D), correlating with the shear yielding behaviour observed in the amplitude sweeps. Together, these features are indicative of non-Newtonian fluids with their shear-thinning and self-recovery behavior being crucial components for extrudability and DIW 3D printing.

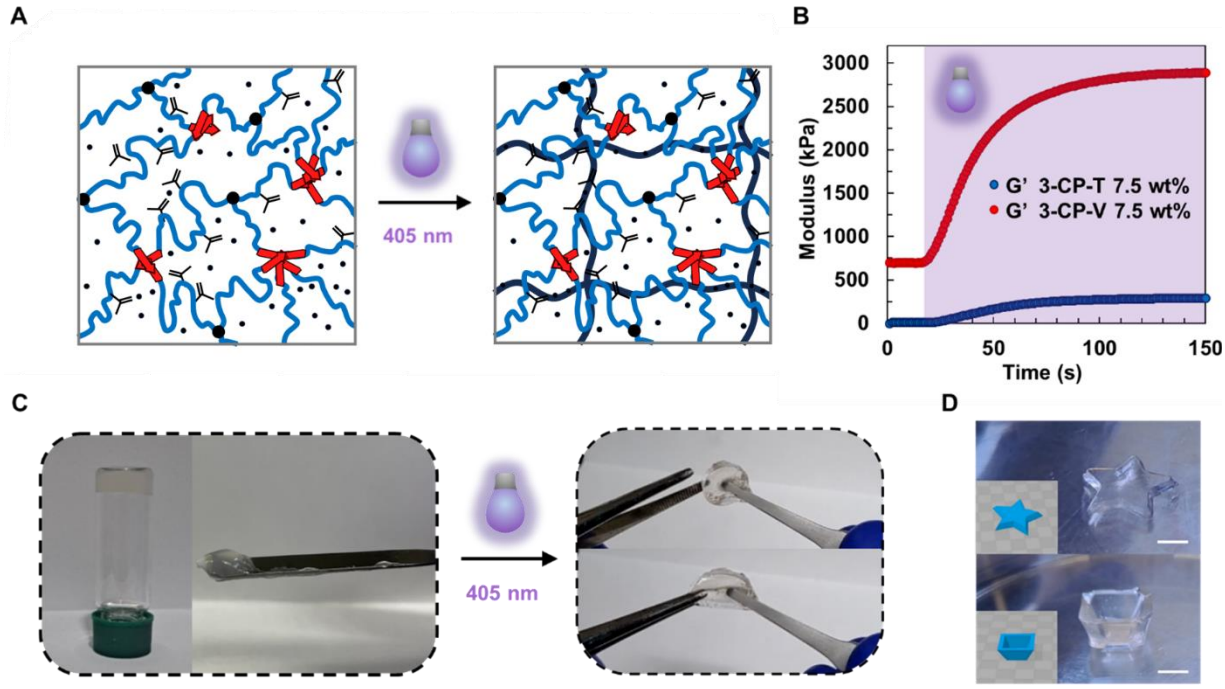


**Figure 3.4.** Graphic depicting photocrosslinking of copolypeptide hydrogel formulation containing PEGMEMA comonomer and LAP photoinitiator (A). Real-time visible light curing (405 nm) at intensity of 13 mW/cm$^2$ showing comparative moduli differences for 3-CP-T and 3-CP-V at 7.5 wt% (B) under constant angular frequency of 6.2 rad/s and constant oscillatory strain of 0.1 %. 3-CP-T hydrogel (7.5 wt%) before and after photocrosslinking forming a pliable, robust material (C). Direct ink write (DIW) 3D printing of 7.5 wt% 3-CP-V hydrogel (D) into a star structure (scale bar: 2 mm) and inverted pyramid (scale bar: 4 mm) with gradient layer changes. [52] Reproduced with permission from John Wiley & Sons Inc.

### 3.3.3 Secondary Crosslinking and 3D printing.

In further demonstrating the 3D printing potential of the 3-arm block copolypeptides, subsequent chemical crosslinking of these hydrogels through radical polymerization was examined. Based on the above rheological studies, aqueous formulations comprised of either 3-CP-T or 3-CP-V (7.5 wt%) functionalized with ~20 mole% pendant methacrylate groups was mixed with poly(ethylene glycol) methyl ether methacrylate (PEGMEMA - $M_n$ 300) comonomer (5 wt%) and lithium phenyl-2,4,6-trimethylbenzoylphosphinate (LAP) (0.1 wt%) as photoinitiator (Figure 3.4A). The addition of PEGMEMA was necessary to ensure cross-reactivity between peptide chains leading to a covalent network. Significantly, this secondary crosslinking step led to a change in properties from an initially soft, deformable hydrogel to a stiffer, elastic material (Figure 3.4C). These photocrosslinked hydrogels were shown to be more robust and stable, withstanding applied forces that would otherwise remold the parent physical hydrogel. To confirm these observations, gelation kinetics were studied using real-time rheology by monitoring changes in G' after irradiation with visible light (Figure 3.4B). In these experiments, the concentration of the methacrylate functionalized copolypeptide stars was varied from 5.0 to 7.5 wt% with constant irradiation (405 nm and 13 mW/cm$^2$). After 10 s incubation time, a significant evolution of moduli, G', was observed for all samples with complete photocuring after 90-140 s. In order to verify the absence of radical induced dityrosine crosslinking within the 3-CP-T hydrogel, a control without methacrylate functionalization was trialed for photocuring. No observable difference in moduli (Figure 3.11) was noted using identical conditions as described for the methacrylate derived materials, confirming that methacrylate derived 3-CP-T crosslinks exclusively through free radical polymerization of the methacrylate side chain. It should be noted that no yielding behavior of

the physical network is apparent during photocuring. Again, a noticeable difference is observed between the tyrosine and valine derivatives with a plateau G' modulus of ~300 kPa for 7.5 wt% 3-CP-T which is in direct contrast to 3-CP-V where a modulus of ~2900 kPa was observed (Figure 3.4B). For the 5.0 wt% formulations, a similar disparity in G' (85 kPa and 214 kPa for 3-CP-T and 3-CP-V respectively) is found (Figure 3.12) which illustrates the importance of both the initial ß-sheet assemblies and the chemically crosslinked, secondary poly(methacrylate) network. Mesh size and equilibrium swelling studies on hydrogels before and after photocrosslinking revealed distinct differences of 3-CP-T and 3-CP-V hydrogels (Table B2). Using equation S2, mesh size could be calculated for materials at each stage of processing. 3-CP-T does appear to have larger mesh sizes for native (7.6 nm) and photocrosslinked (2.5 nm) materials, likely due to the presence of the polar side chain phenol groups. 3-CP-V on the other hand has smaller meshes of 1.9 and 1.1 nm, for pre- and post-crosslinked samples respectively, potentially due to closely packed valine blocks. Additionally, photocrosslinked 3-CP-T also had a significantly higher equilibrium swelling ratio of 121.9, when compared to 17.8 for 3-CP-V. These fully swelled hydrogels also exhibited almost identical moduli values in oscillatory frequency sweeps, suggesting dissolution of ß-motif networks (Figure 3.13).

While both the tyrosine and valine hydrogels proved to be suitable for DIW 3D printing, the 3-CP-V based hydrogel affords higher fidelity 3D objects and was therefore selected for further study. As shown in Figure 3.4D, the 3-CP-V hydrogel could be readily printed to give sharp multi-cornered geometries via extrusion with accurate alignment of layers using a commercial printing system and standard conditions. The formation of successive

overhanging layers within the inverted pyramid structure demonstrates the rapid-recovery and stability of the initial 3-CP-V physical hydrogel upon removal of shear forces (Figure 3.13). Similarly, the printing of the star structure with receding widths was designed to demonstrate the ability to combine high resolution with layer cohesion and further illustrates the correlation between rheological studies and DIW 3D printing performance.

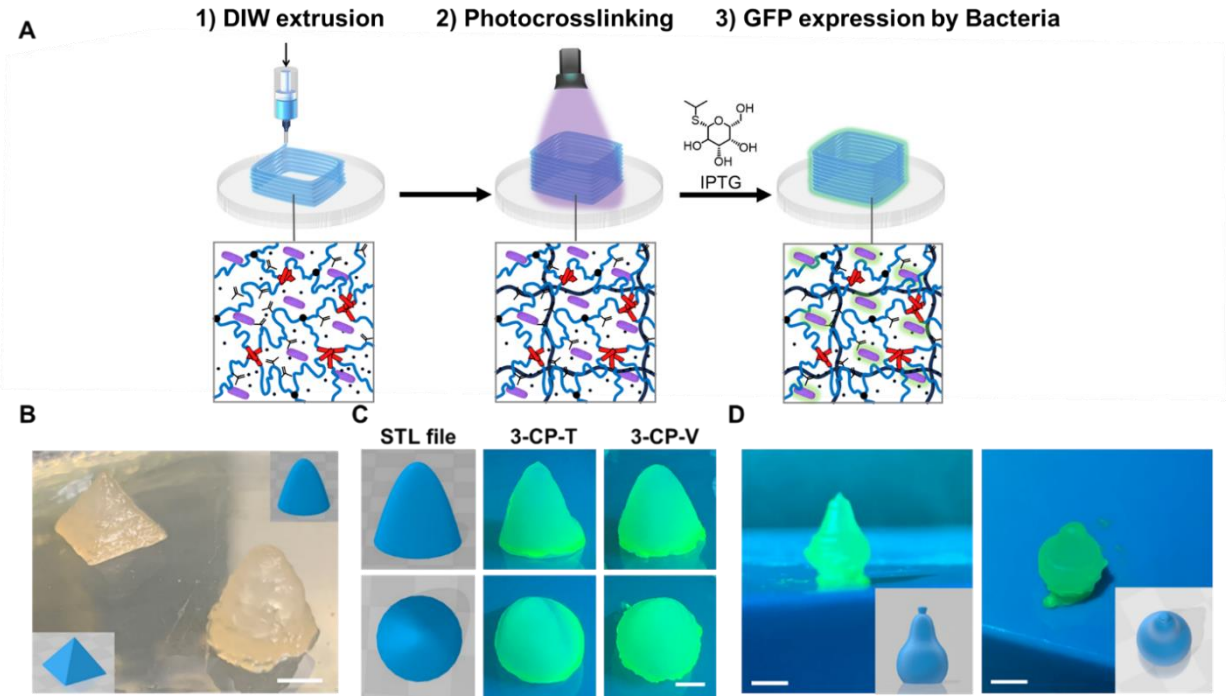


**Figure 3.5.** Graphic depiction of bioprinting process (A), (1) DIW extrusion process of hydrogel bioink formulation and (2) visible light curing (405 nm) solidifying 3D construct and (3) expression of green fluorescent protein (GFP) from 3D printed biocomposite. Bioprinted 3D pyramidal and parabolic constructs (B) (CAD files inset) seeded with genetically engineered *E.coli* in 7.5 wt% 3-CP-T hydrogel formulation (scale bar: 2.5 mm). 3D parabolic structures of 3-CP-T and 3-CP-V hydrogel bioinks (C) with encapsulated bacteria rendered in comparison to the CAD input file and demonstrating viability through GFP expression, imaged in the presence of UV light. Bioprinted 3D pear construct (D) embedded with genetically engineered *E.coli* that expresses GFP

upon IPTG induction, imaged in the presence of UV light (scale bar: 2 mm). [52] Reproduced with permission from John Wiley & Sons Inc.

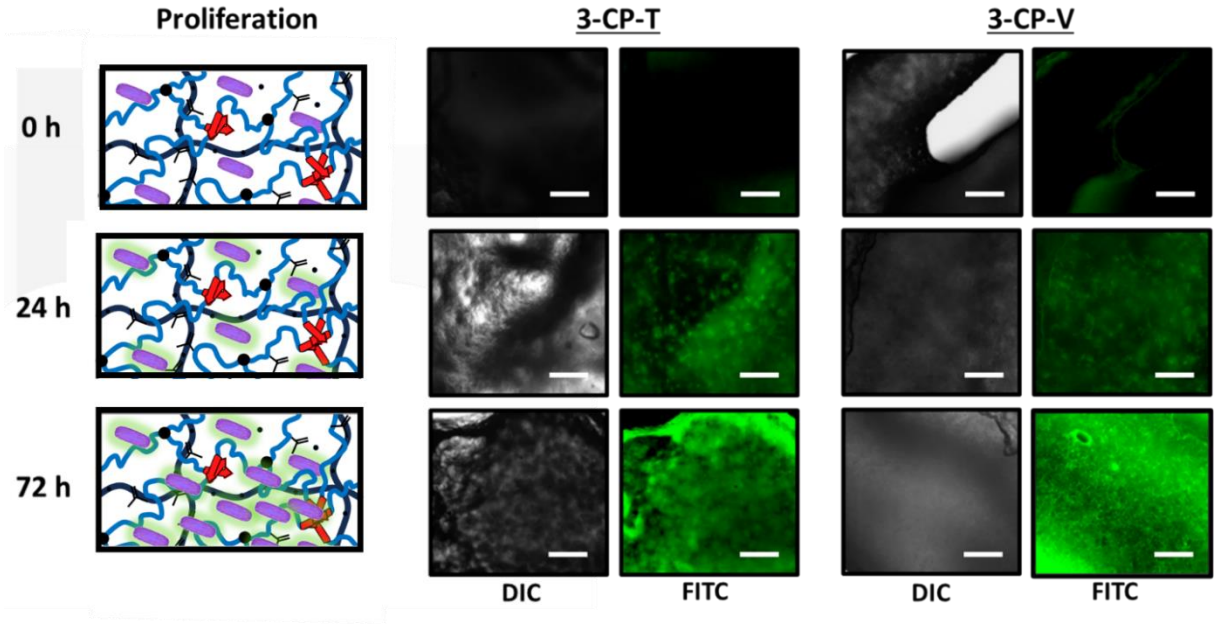


**Figure 3.6.** Confocal microscope images of 3-CP-T and 3-CP-V hydrogels (7.5 wt%) embedded with engineered E.coli that express GFP upon IPTG incubation up to 72 h after photocrosslinking and IPTG induction (scale bar: 100 µm). [52] Reproduced with permission from John Wiley & Sons Inc.

In order to examine the long-term viability and growth characteristics of embedded bacteria within the 3-CP-T and 3-CP-V hydrogels, GFP expression was monitored at different time points (Figure 3.5). Interestingly, neither the control photocrosslinked hydrogel with no added bacteria or the embedded systems at t = 0 h showed any fluorescence due to GFP expression. This was in stark contrast to 24 h when strong GFP fluorescence was observed and exponential bacterial growth demonstrated for both 3-CP-T and 3-CP-V composite systems. This suggests that both hydrogels had similar biocompatibility and can facilitate proliferation of bacterial cells in the initial stages of incubation. Interestingly at 72 h, a distinct difference between the two biocomposites was discerned with colony size and aggregation being far more pronounced with the 3-arm tyrosine-based block copolypeptide. As shown in Figure 5,

differential interference contrast (DIC) images reveal increased bacterial growth, which is correlated with the lower modulus for the 3-CP-T materials compared to the corresponding stiffer 3-CP-V systems. Based on this observation, it is postulated that the lower modulus matrix and increased mesh size for 3-CP-T allows for enhanced proliferation and agglomeration of bacterial colonies. Unfortunately, exact quantification of colonies was difficult to perform due to this distinct aggregation that does not allow single cell counting. Both 3-CP-T2 and 3-CP-V2 hydrogels with shorter outer block DPs and lower mechanical properties were also analyzed as bacteria laden depots (Figure 3.14). It is apparent that reduction in hydrogel stiffness can enable enhanced proliferation over a similar time scale 0-72 h. More importantly, the lower stiffness associated with 3-CP-T2 when compared to 3-CP-V2 hydrogels does also permit increased numbers of bacteria, correlating with observations noted for lead 3-CP-T and 3-CP-V materials. Although at 72 h, it is observable that colony formation is almost identical for tyrosine and valine derived materials, which highlights the importance of block length in designed copolypeptides. The aforementioned differences illustrate that bacterial cell growth and fate over different time scales can be programmed through pragmatic material design.

### 3.4 Conclusion

In conclusion, a DIW-based additive manufacturing approach for the 3D printing of biocompatible hydrogel networks based on peptide self-assembly is demonstrated. Key to the success of this strategy is the design of 3-arm block copolypeptides which undergo initial gelation through ß -sheet formation of outer tyrosine or valine blocks. This assembly allows for tuning of the rheological and mechanical properties leading to successful 3D printing of a variety of objects under mild, shear-based conditions. Additionally, methacrylate groups can

be incorporated to the central glutamate blocks to provide for secondary covalent photocrosslinking after DIW printing. The biocompatibility of these materials and the mild nature of the processing steps permits the incorporation and growth of genetically engineered *E. coli DH5α* that express the fluorescent GFP in response to IPTG. Significantly, the 3D printed objects incorporating these bacteria preserved viability and functionality over extended periods with differentiated growth and colony formation for the lower modulus peptide-based hydrogels based on tyrosine domains. This molecular design based on dynamic and covalent crosslinks illustrates a powerful strategy for the fabrication of 3D printed "living" biocomposites under mild conditions. The direct correlation between mechanical properties and the function of embedded living organisms further demonstrates the potential of these materials. Future work will broaden the scope of this approach and the ability to program proliferation, activity and colony formation for a variety of cell-based, synthetic biology systems.

## 3.5 Additional Experimental Results

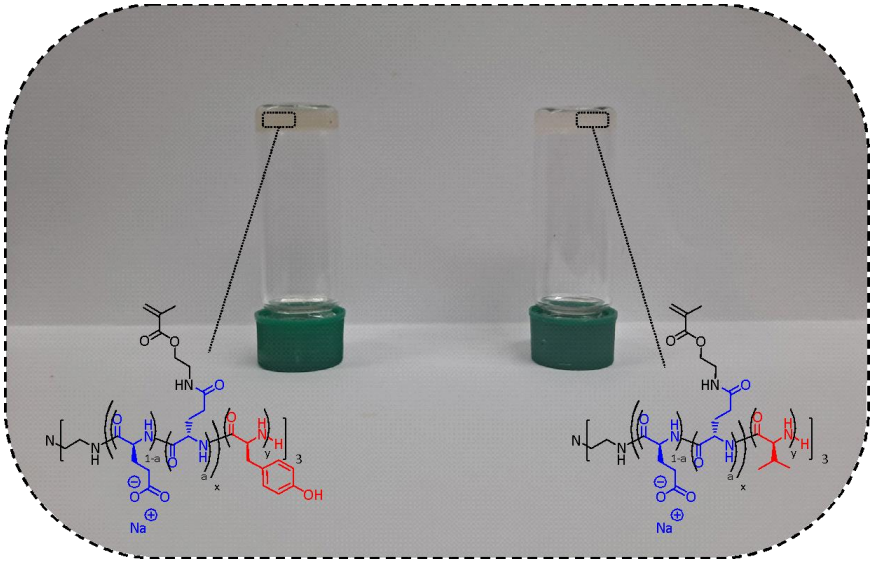

**Figure 3.7.** Inversion vial test of 3-CP-T and 3-CP-V hydrogels at concentrations of 3.75 and 3.5 wt% respectively.[52] Reproduced with permission from John Wiley & Sons Inc.

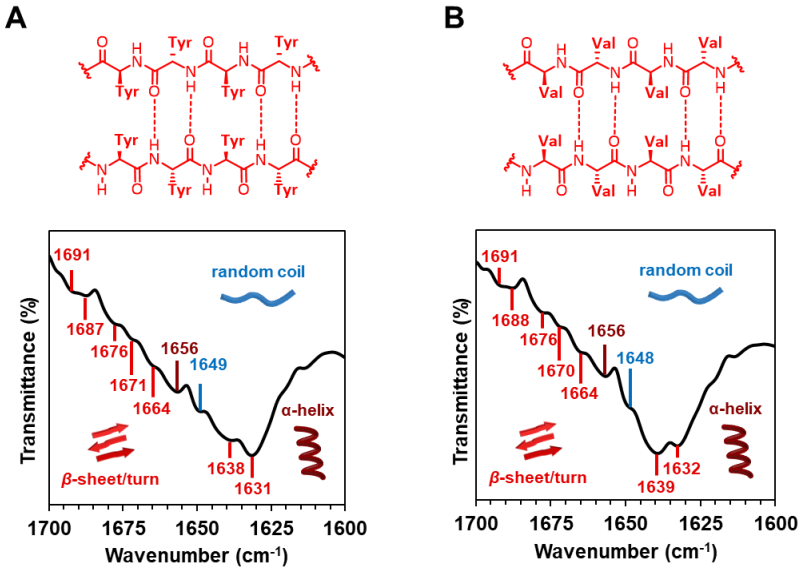


**Figure 3.8.** FTIR spectra showing secondary structures of physical 3-CP-T (A) and 3-CP-V (B) hydrogels in D2O.[52] Reproduced with permission from John Wiley & Sons Inc.

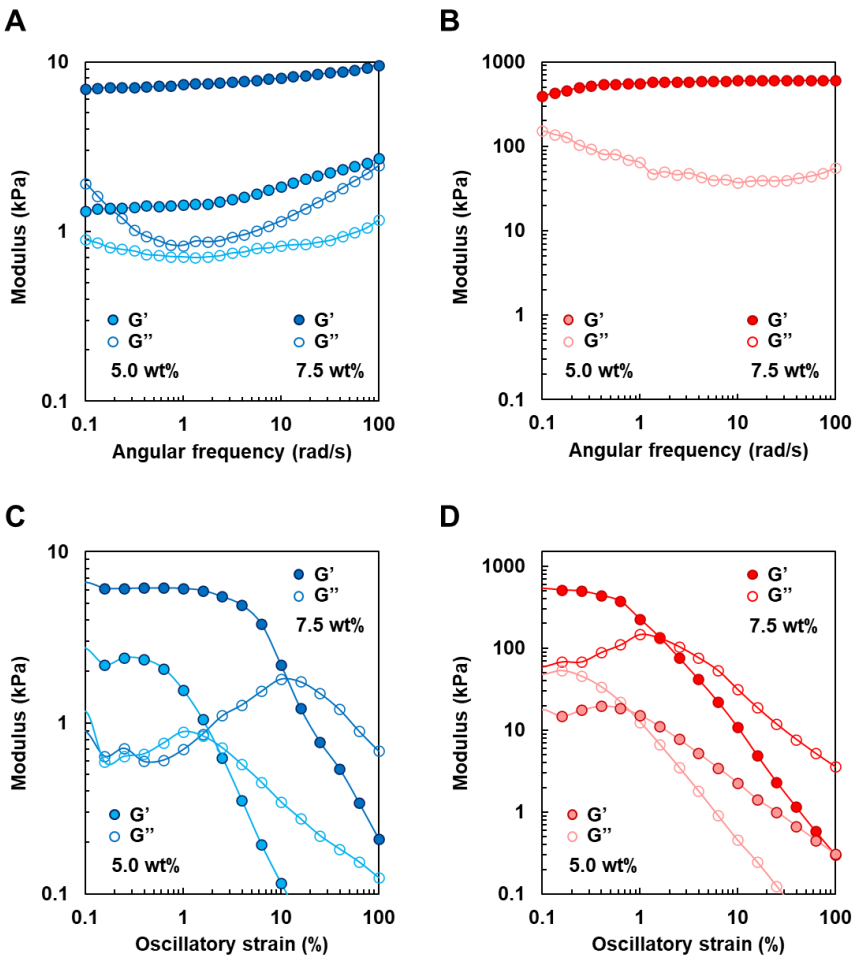


**Figure 3.9.** Frequency sweeps of 3-CP-T (A) and of 3-CP-V (B) hydrogels measuring moduli changes at 5.0 and 7.5 wt% using frequencies ranging from 0.1 to 100 rad/s at constant oscillatory strain of 0.1 %. Amplitude sweeps of 3-CP-T (C) and 3-CP-V (D) hydrogels measuring moduli changes at 5.0 and 7.5 wt% with increasing oscillatory strain ranging from 0.1 to 100% at constant angular frequency of 6.2 rad/s.[52] Reproduced with permission from John Wiley & Sons Inc.

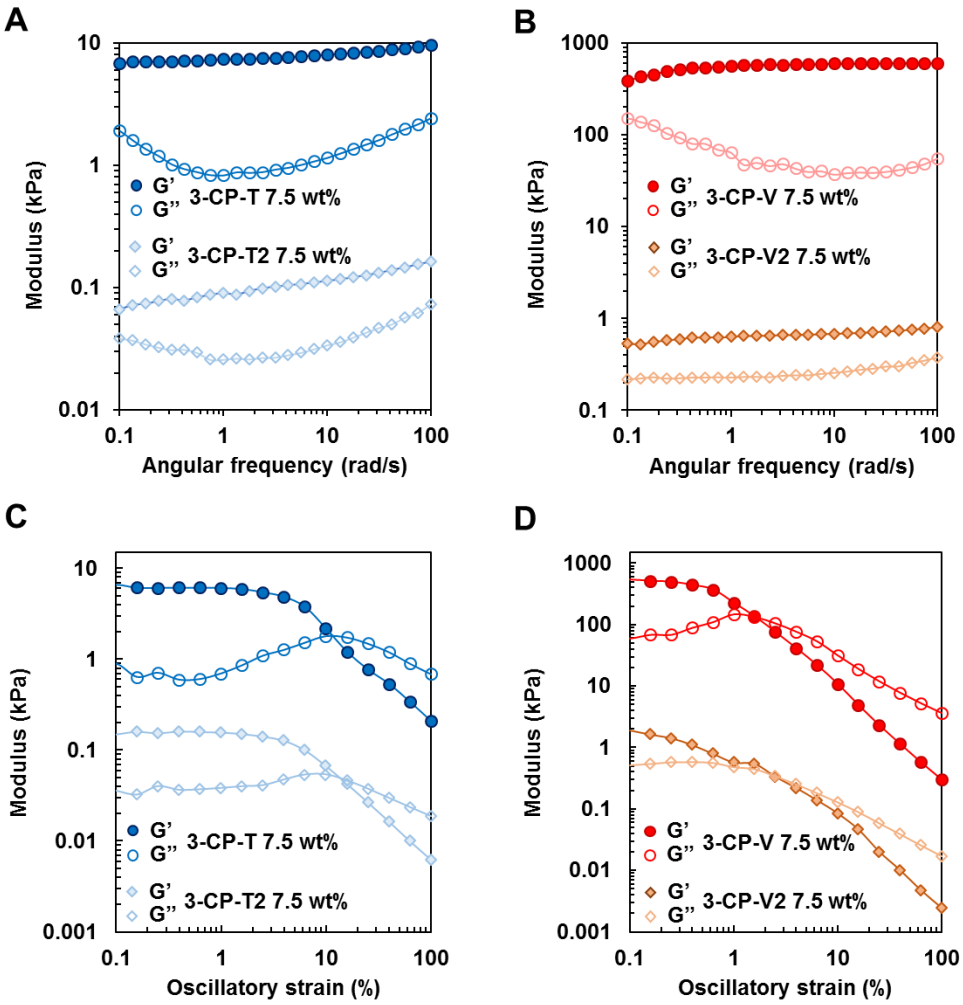


**Figure 3.10.** Frequency sweeps of 3-CP-T, 3-CP-T2 (A) and of 3-CP-V, 3-CP-T2 (B) hydrogels measuring moduli changes based on molecular weight using frequencies ranging from 0.1 to 100 rad/s at constant oscillatory strain of 0.1 %. Amplitude sweeps of 3-CP-T, 3-CP-T2 (C) and 3-CP-V, 3-CP-V2 (D) hydrogels measuring moduli changes based on molecular weight with increasing oscillatory strain ranging from 0.1 to 100% at constant angular frequency of 6.2 rad/s.[52] Reproduced with permission from John Wiley & Sons Inc.

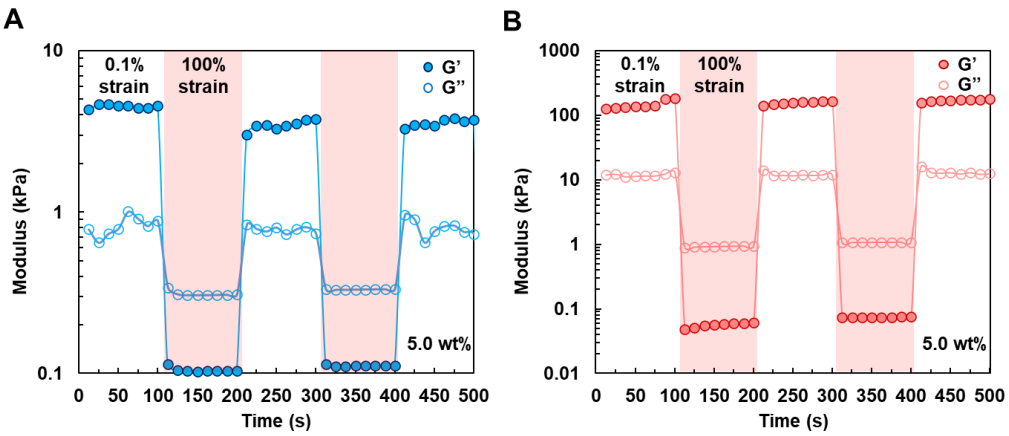


**Figure 3.11.** Cyclic oscillatory amplitude sweeps for 5.0 wt% hydrogels of 3-CP-T (A) and 3-CP-V (B) showing moduli response to low strains (0.1%) and high strains (100%) at intervals of 100 s at constant angular frequency of 6.2 rad/s.[52] Reproduced with permission from John Wiley & Sons Inc.

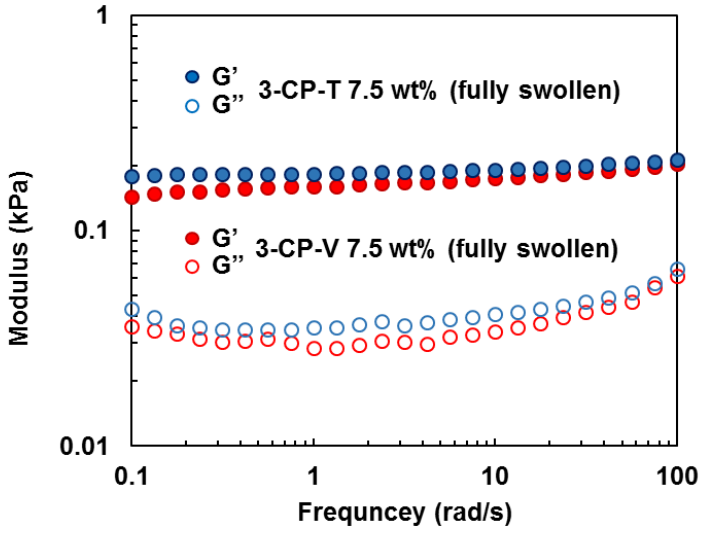


**Figure 3.12.**Frequency sweeps of post-crosslinked 3-CP-T (A) and of 3-CP-V (B) hydrogels (at 7.5 wt%) at equilibrium swelling using frequencies ranging from 0.1 to 100 rad/s at constant oscillatory strain of 0.1 %. [52] Reproduced with permission from John Wiley & Sons Inc.

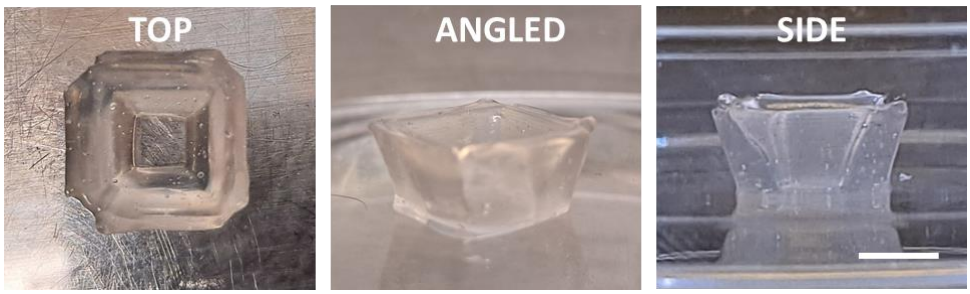


**Figure 3.13.** Different angles of 3D printed inverted pyramid showcasing overhanging layers and sharp corners (scale bar: 4 mm).[52] Reproduced with permission from John Wiley & Sons Inc.

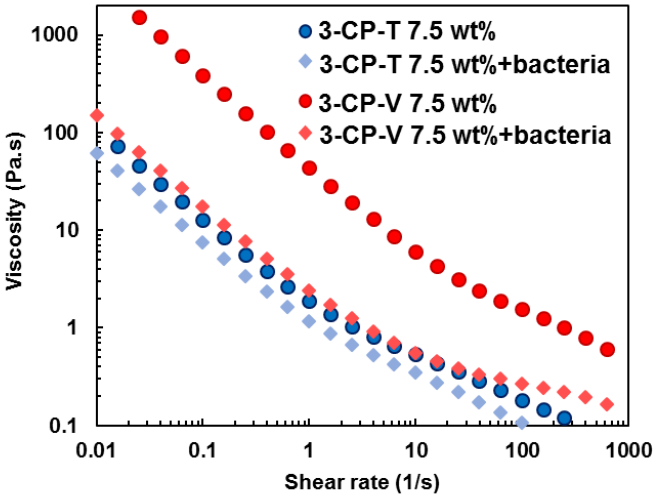


**Figure 3.14.** Viscosity sweep with increasing shear rate of 3-CP-T and of 3-CP-V hydrogels (at 7.5 wt%) with (incubated for 24h) and without bacteria embedded in LB Broth.[52] Reproduced with permission from John Wiley & Sons Inc.

### 3.6 References


[1] A. Ambrosi and M. Pumera, *Chem. Soc. Rev.*, **2016**, 45, 2740.

[2] G. Chen, Y. Xu, P. C. L. Kwok and L. Kang, *Addit. Manuf.*, **2020**, 34, 101209.

[3] J. Li, C. Wu, P. K. Chu and M. Gelinsky, *Mater. Sci. Eng. R Reports*, **2020**, 140, 100543.

[4] R. Xie, S. Mukherjee, A. E. Levi, V. G. Reynolds, H. Wang, M. L. Chabinyc and C. M. Bates, *Sci. Adv.*, **2020**, 6, 11.

[5] C. J. Thrasher, J. J. Schwartz and A. J. Boydston, *ACS Appl. Mater. Interfaces*, **2017**, 9, 39708.

[6] N. D. Dolinski, Z. A. Page, E. B. Callaway, F. Eisenreich, R. V. Garcia, R. Chavez, D. P. Bothman, S. Hecht, F. W. Zok and C. J. Hawker, *Adv. Mater.*, **2018**, 30, 1–6.

[7] J. J. Schwartz and A. J. Boydston, *Nat. Commun.*, **2019**, 10, 791.

[8] P. Heidarian, A. Z. Kouzani, A. Kaynak, M. Paulino and B. Nasri-Nasrabadi, *ACS Biomater. Sci. Eng.*, **2019**, 5, 2688.

[9] P. Jiang, P. Lin, C. Yang, H. Qin, X. Wang and F. Zhou, *Chem. Mater.*, **2020**, 32, 9983.

[10] A. Bagheri, C. W. A. Bainbridge, K. E. Engel, G. G. Qiao, J. Xu, C. Boyer and J. Jin, *ACS Appl. Polym. Mater.*, **2020**, 2, 782.

[11] X. Shi, V. A. Bobrin, Y. Yao, J. Zhang, N. Corrigan, and C. Boyer, *Angew. Chem. Int. Ed.*, **2022**, e202206272.

[12] D. Seliktar, *Science* 2012, 336, 1124.

[13]A. K. Grosskopf, O. A. Saouaf, H. Lopez Hernandez, E. A. Appel, *J. Polym. Sci.*, **2021**, 59, 2854.

[14]A. Sydney Gladman, E. Matsumoto, R. Nuzzo, L. Mahadevan and J. A. Lewis, *Nature Mater.*, **2016**, 15, 413.

[15] S. E. Bakarich, R. Gorkin, R. Gately, S. Naficy, M. in het Panhuis, G. M. Spinks, *Addit. Manuf.*, **2017**, 14, 24.

[16] P. T. Smith, B. Narupai, J. H. Tsui, S. C. Millik, R. T. Shafranek, D. H. Kim and A. Nelson, *Biomacromolecules*, **2020**, 21, 484.

[17] D. Xue, J. Zhang, Y. Wang and D. Mei, *ACS Biomater. Sci. Eng.*, **2019**, 5, 4825.

[18] A. Saha, T. G. Johnston, R. T. Shafranek, C. J. Goodman, J. G. Zalatan, D. W. Storti, M. A. Ganter and A. Nelson, *ACS Appl. Mater. Interfaces*, **2018**, 10, 13373.

[19] A. Bagheri and J. Jin, *ACS Appl. Polym. Mater.*, **2019**, 1, 593.

[20] S. Kumar, A. Tharayil and S. Thomas, *ACS Appl. Polym. Mater.*, **2021**, 3, 3685.

[21] J. H. Ahrens, S. G. M. Uzel, M. Skylar-Scott, M. M. Mata, A. Lu, K. T. Kroll, and J. A. Lewis, *Adv. Mat.*, **2022,** 34, 2200217.

[22] J. Saroia, W. Yanen, Q. Wei, K. Zhang, T. Lu and B. Zhang, *Bio-Design Manuf.*, **2018**, 1, 279.

[23] M. Schaffner, P. A. Rühs, F. Coulter, S. Kilcher and A. R. Studart, *Sci. Adv.*, **2017**, 3, eaao6804.

[24] X. Liu, H. Yuk, S. Lin, G. A. Parada, T. C. Tang, E. Tham, C. de la Fuente-Nunez, T. K. Lu and X. Zhao, *Adv. Mater.*, **2018**, 30, 9.

[25] T. G. Johnston, J. P. Fillman, H. Priks, T. Butelmann, T. Tamm, R. Kumar, P. J. Lahtvee and A. Nelson, *Macromol. Biosci.*, **2020**, 20, 7.

[26] I. Sulaeva, U. Henniges, T. Rosenau and A. Potthast, *Biotechnol. Adv.*, **2015**, 33, 1547.

[27] S. Verma and A. Kuila, *Environ. Technol. Innov.*, **2019**, 14, 100369.

[28] L. Su, W. Jia, C. Hou and Y. Lei, *Biosens. Bioelectron.*, **2011**, 26, 1788.

[29]S. Balasubramanian and A. S. Meyer, *ACS Synth. Biol.*, **2019**, 8, 1564.

[30] J. M. Unagolla and A. C. Jayasuriya, *Appl. Mater. Today*, **2020**, 18, 100479.

[31] Z. Song, H. Fu, R. Wang, L. A. Pacheco, X. Wang, Y. Lin and J. Cheng, *Chem. Soc. Rev.*, **2018,** 47, 7401.

[32] A. Rasines Mazo, S. Allison-Logan, F. Karimi, N. J.-A. Chan, W. Qiu, W. Duan, N. M. O'Brien-Simpson and G. G. Qiao, *Chem. Soc. Rev.*, **2020**, 49, 4737.

[33] H. He, M. Sofman, A. J. S. Wang, C. C. Ahrens, W. Wang, L. G. Griffith and P. T. Hammond, *Biomacromolecules*, **2020**, 21, 566.

[34] C. Chen, J. Lan, Y. Li, D. Liang, X. Ni and Q. Liu, *Chem. Mater.*, **2020**, 32, 1153.

[35] J. DvorÌáková, J. Trousil, B. Podhorská, Z. Miksovská, O. Janousková and V. Proks, *Biomacromolecules*, **2021**, 22, 1417.

[36] Z. Y. Tian, Z. Zhang, Z., S. Wang and H. Lu, *Nat. Commun.*, **2021**, 12, 5810.

[37]Y. Shen, S. Zhang, Y. Wan, W. Fu and Z. Li, *Soft Matter*, **2015**, 11, 2945.

[38] R. D. Murphy, M. In het Panhuis, S. A. Cryan and A. Heise, *Polym. Chem.*, **2018**, 9, 3908.

[39]G. Batoni, G. Maisetta and S. Esin, *Biochim. Biophys. Acta.*, **2016**, 1858, 1044.

[40] R. Murphy, T. Borase, C. Payne, J. O'Dwyer, S. A. Cryan and A. Heise, *RSC Adv.*, **2016**, 6, 23370.

[41] J. Huang, C. L. Hastings, G. P. Duffy, H. M. Kelly, J. Raeburn, D. J. Adams and A. Heise, *Biomacromolecules*, **2013**, 14, 200.

[42]Y. Sun, Y. Hou, X. Zhou, J. Yuan, J. Wang and H. Lu, *ACS Macro Lett.*, **2015**, 4, 1000–1003.

[43] A. P. Nowak, V. Breedveld, L. Pakstis, B. Ozbas, D. J. Pine and T. J. Deming, *Nature*, **2002**, 417, 424 .

[44] H. Song, G. Yang, P. Huang, D. Kong and W. Wang, *J. Mater. Chem. B*, **2017,** 5, 1724.

[45] N. J. A Chan, D. Gu, S. Tan, Q. Fu, T. G. Pattison, A. J. O'Connor and G. G Qiao, *Nat. Commun*., **2020,** 11, 1630.

[46] H. Yang, S. Yang, J. Kong, A. Dong and S. Yu, *Nat. Protoc.*, **2015,** 10, 382.

[47] C. M. Micklitsch, S. H. Medina, T. Yucel, K. J. Nagy-Smith, D. J. Pochan and J. P. Schneider, *Macromolecules*, **2015,** 48, 1281.

[48] S. Lifson and C. Sander, *Nature*, **1979,** 282, 109.

[49] I. M. Geisler and J. P. Schneider, *Adv. Funct. Mater.*, **2012,** 22, 529.

[50] M. Bobrovskyy and C. K. Vanderpool, *Mol. Microbiol.*, **2016,** 99, 254.

[51] E. Levine, Z. Zhang, T. Kuhlman and T. Hwa, *PLoS Biol.*, **2007**, 5, 1998.

[52] Murphy, R. D.; Garcia, R. V.; Oh, S. J.; Wood, T. J.; Jo, K. D.; Read de Alaniz, J.;

Perkins, E.; Hawker, C. J. Adv. Mater. 2023, 35, 2207542.

# Chapter 4. Star Copolypeptide as Degradable Rheological Modifiers for Direct Ink Writing of Gelatin

## 4.1 Abstract

Hydrogels hold much promise as scaffolds for 3-D printing of functional living materials with integrated mammalian cells, however challenges remain in materials with easy to print properties. Shear-recoverable hydrogels based on star copolypeptides with rapid self-recovery and degradable backbone has been shown as an efficient 3D printable biomaterial with tailorable material properties but lacks the adequate chemical environment for mammalian cell growth. In addressing this challenge, we describe a method to physically blend printable star copolypeptide with commercially available bioactive gelatin methacrylamide (GelMA) to form bio-inks that can be efficiently printed in physiological temperatures. Star copolypeptides were synthesized with a ß-sheet outer domain that forms physical crosslinks giving mechanical and thermal stability during heating and extrusion. This permits the star copolypeptide to act as a scaffold at physiological temperature, breaking the gelatin triple helix and subsequently giving the rheological properties desired for extrusion-based printing. Incorporated methacrylamide along the star copolypeptide backbone allows photocrosslinking with GelMA post-extrusion, giving scaffolds better material integrity and ability to diffuse nutrients. Due to the purely peptidic backbone of the two blended materials, biodegradation of crosslinked networks was explored to further showcase potential application in cell cultures. This general method of utilizing star copolypeptide as 3D printable rheological modifiers to bioactive material illustrates the future potential of integrating bioactive materials and fluids for facile tunable bioinks.

## 4.2 Introduction

The utilization of additive manufacturing or 3D-printing for hydrogels integrates intricate geometrical manipulation with the strategic selection of functional materials.[1–3] Consequently, the realm of 3D-printed hydrogels is gaining prominence, boasting advantages such as tunability, a high water content, and biocompatibility.[3–5] This caters to a broad spectrum of biomedical applications, spanning from living materials[6,7] to tissue engineering.[8] For light-based 3D-printing techniques like stereolithography (SLA) and digital-light processing (DLP), it is imperative to formulate hydrogels with low viscosities and the ability to undergo rapid crosslinking upon light irradiation.[9] In contrast, extrusion techniques like direct-ink writing (DIW) is constrained by larger rhoelogical requirements to achieve high shape fidelity.[2,10] By integrating bacterial or mammalian cells with shear processable hydrogel allows the creation of a new method of DIW called bioprinting.[3,8] This approach facilitates the spatial and temporal dispersion of living cells, aiming to foster cell proliferation and maturation. It is noteworthy that the behavior and survivability of cellular components within the 3D environment is dictated by the physical and chemical characteristics of the hydrogel matrix, providing an avenue for fine-tuning performance.[11] Specifically, mammalian cells need chemical anchors, such as cell penetrating peptides, to allow healthy attachment and proliferation.[12]

Traditionally, hydrogels based on collagen and other biopolymers are used as key building blocks due to their ability to chemically and mechanically mimic the extracellular matrix. Gelatin methacrylamide (GelMA) is a popular material for cell culture due to being chemically similar to collagen but can form reversible triple helix physical crosslinks at lower temperatures and irreversible chemical crosslinks with external stimuli.[13–15] Typically, GelMA

is heated in a syringe to break the physical network, allowing the material to be easily extruded and subsequently crosslinked on the platform with colder temperatures or light.[16] To achieve high shape fidelity, these materials either need highly controlled printers or well-controlled chemistry that allows immediate crosslinking upon extrusion onto the platform without clogging the nozzle. To circumvent the need for sophisticated printers or chemistry, additives are utilized to modify the rheological properties in order to get efficient printing at elevated temperatures without sacrificing shape fidelity.[15,17–20] For example, the Srivastava group took advantage of PEG-based coacervate-driven physical hydrogel as printable scaffolds for physiological printing of GelMA and subsequent photocrosslinking without cooling their system.[21,22] Current strategies rely on utilizing non-biodegradable fillers that only physically interact with the GelMA pre and post-chemical crosslinking. To further expand this area of research and diversify the palette of 3D-printable hydrogels, there is a need to explore rheological modifiers that chemically integrate with GelMA post extrusion and chemical crosslinking without sacrificing the inherent biodegradability.

Star copolypeptide, synthesized through the ring-opening polymerization (ROP) of *N*-carboxyanhydrides (NCAs), has been shown to be an attractive material for DIW due to its tailorable synthetic design, intrinsic biodegradability, material properties, and scalability.[23–26] These materials can be designed for extrusion by making the inner block highly water absorbing and the outer block(s) containing strongly associating β-sheet domains that self-assemble into networks stabilized by reversible physical crosslinks. Our groups utilized this single-component hydrogel to integrate *Escherichia coli* to 3D print biocomposites with the ability to modulate integrated microbe behavior by modulating the mechanical and chemical

properties of the star copolypeptide.[11] Star copolypeptide can be specifically tailored to have crosslinking groups along the peptidic backbone that allows photochemical curing post extrusion, but still retain a biodegradable backbone.

The natural succession to these studies is to integrate a variety of mammalian cells and showcase the ability to pattern complex geometries and control cell fate through the host matrix properties with the goal of utilizing it for tissue engineering.[27] Without chemical anchors on the star copolypeptide backbone, proper adhesion of mammalian cells cannot be realized without integrating additives that aid with cell recognition.[28] We thus propose a bioink that combines the bioactivity of GelMA with the ease of extrudability of star copolypeptide that can be stitched together photochemically without sacrificing the benefit of using a purely degradable system (Figure 4.1) . Thus expanding the tool kit of rheological modifiers for DIW.

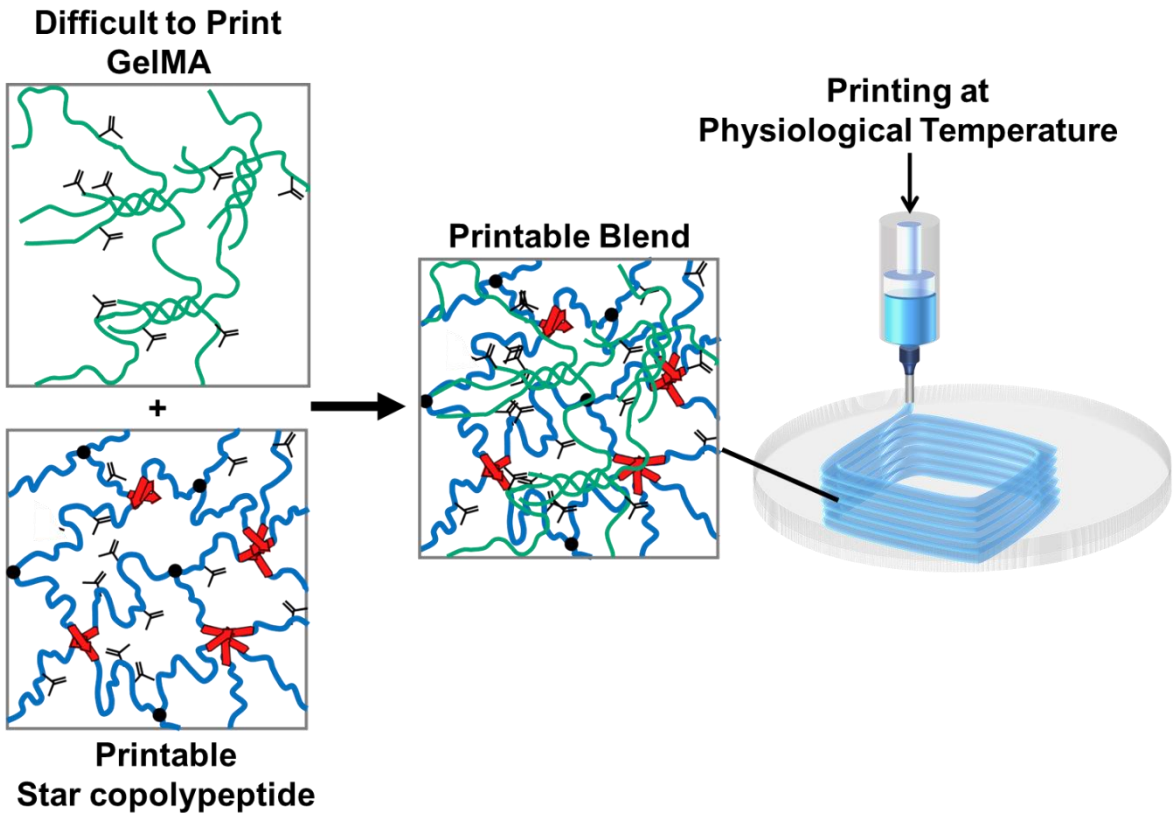


**Figure 4.1.** Schematic representation of blending GelMA and star copolypeptide for modular 3D printable bionk.

In this chapter we describe the synthesis and evaluation of 3-arm copolypeptide as biodegradable rheological modifiers to allow easy printability of commercial GelMA at physiologically relevant temperatures. Using a trifunctional amine initiator, ring opening polymerization of *N*-carboxyanhydride (NCA) of benzyl-L-glutamate is followed by chain extension with NCA phenyl glycine monomers to give 3-arm block copolypeptides that can then be functionalized with methacrylamide for a photo cross-linkable material. Upon immersion in water, the outer $\beta$-sheet domain drives assembly, allowing the formation of shear processable reversible physical networks. The stability of the star copolypeptide networks mixed with GelMA triple helix networks was evaluated using variable temperature rheology to show the selective preservation of the $\beta$-sheet assembled networks at physiological

temperature. Benchmark rheological experiments and initial 3D printing experiments were then utilized to show the ability of these materials to be extruded above the GelMA triple helix melting temperature. Due to both components containing acrylamide functional handles, the new materials were then photochemically crosslinked and directly probed via real-time rheological studies. The biodegradability was initially evaluated by tracking the release of covalently attached fluorophores in proteolytic solutions. These results show promising future studies in exploring the controlled degradation of complex geometric peptidic hydrogels for application in cell culturing .

## 4.3 Results and discussion

### 4.3.1 Synthesis and Self-Assembly of Rheological Modifier.

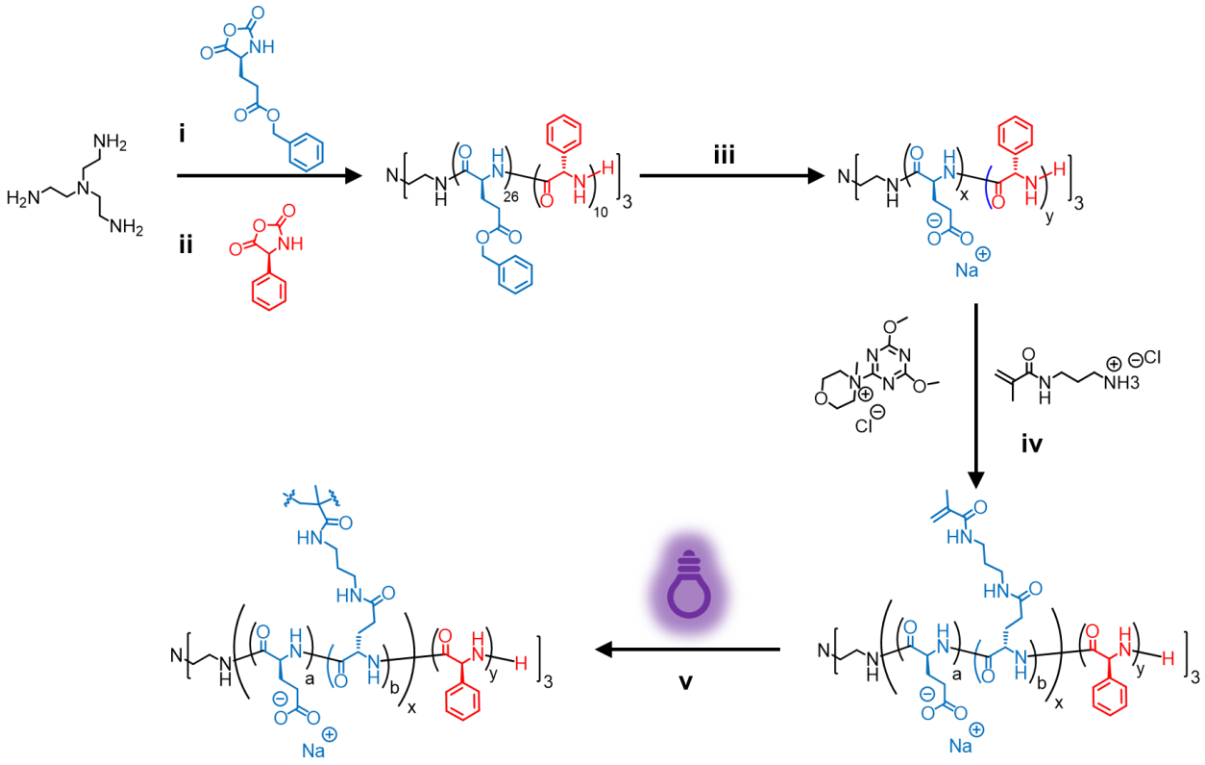


**Figure 4.2.** (i) $CHCl_3$/DMF, 18h, rt. (ii) $CHCl_3$/DMF, 18h, rt. (iii) TFA/$CHCl_3$, HBr 33 wt% in AcOH, 18 h, rt; NaOH, dialysis, 3 days. (iv) with 4-(4,6-Dimethoxy-1,3,5-triazin-2-yl)-4-methylmorpholinium chloride (DMT-

MM), deionized water, $NaHCO_3$, 36 h, rt; dialysis, 3 days. (v) deionized water, Lithium phenyl-2,4,6-trimethylbenzoylphosphinate (LAP – photoinitiator).

*N*-Carboxyanhydride (NCA) monomers based on γ-benzyl-L-glutamate (BLG), L-Phenyl Glycine (LPG) were synthesized from an adapted literature procedure using epichlorohydrin as a HCl scavenger.[29] In each case, monomer yield and stability was improved compared to traditional procedures with $^1$H NMR, $^{13}$C NMR, and FTIR spectroscopy illustrating the high level of NCA purity (Figure C1-6). A trifunctional initiator, tris(2-aminoethyl)amine (TREN), was then selected for controlled ring opening polymerization of the inner domain based on γ-benzyl-L-glutamate (BLG) with full conversion being confirmed with FTIR and $^1$H NMR spectroscopy. In-situ chain extension of the PBLG star with either the NCA monomer derived from L-Phenyl Glycine (LPG) gives the desired 3-arm star block copolymers (Figure 4.2). The design of the block sequences, degree of polymerization and architecture is based on the facile assembly of multi-arm copolypeptides to give robust hydrogels. Significantly, these 3-arm block copolymers were shown to have superior mechanical properties when compared to their linear counterparts due to $\beta$-sheet assembly of the terminal phenyl glycine.[30,31] From a design perspective, the inner domain of glutamate residues provides a biocompatible aqueous environment.[32] In addition, functionalization of a limited number of carboxylate side chains can serve as a site to incorporate crosslinkable moieties for subsequent photopolymerization.[33–36] The degree of polymerization and structure of the 3-arm poly(benzyl-L-glutamate-b-L-phenyl glycine) (3-PBLG$_{68}$-b-PLPG$_{26}$) block copolypeptides was determined using $^1$H NMR spectroscopy (Figure 4.6 and 4.9) and the molar mass and dispersities characterized by diffusion ordered spectroscopy (DOSY) NMR spectroscopy and size exclusion chromatography (SEC) (Figure C4 and C5). Excellent

agreement between experimental and theoretical molecular weights are observed with low dispersities (Đ ~ 1.1) illustrating the controlled nature of the ring opening polymerization process. It should be noted that ultra-high molecular weight assemblies were observed in the SEC trace for the valine block copolymer (Figure C5) while DOSY NMR analysis shows a single population for the 3-PBLG$_{68}$-b-PLPGY$_{26}$ block copolymer (Figure C4). In contrast, analysis of the tyrosine-based materials reveal both a single SEC peak and DOSY NMR population. These results are in agreement with increased -sheet formation for poly(valine) domains when compared to the corresponding tyrosine systems and the ability of the DOSY NMR solvent (15% TFA in $CDCl_3$) to more efficiently disrupt $\beta$ -sheet formation when compared to the SEC eluent (hexafluoro-iso-propanol).

For all systems, removal of the benzyl protecting groups of the glutamate blocks was an efficient process using 33 wt% HBr in acetic acid to give the desired 3-arm star block copolypeptides. Significantly, the 3-PBLG$_{68}$-*b*-PPG$_{26}$ derivatives gave clear transparent hydrogels at a variety of concentrations in aqueous solution due to the amphiphilic polymer design coupled with β-motif structural assembly. For subsequent coupling, the carboxylic acid groups were initially activated by treatment with 4-(4,6-dimethoxy-1,3,5-triazin-2-yl)-4-methylmorpholinium chloride (DMT-MM), followed by the addition of aminopropyl methacrylamide hydrochloride. Approximately 10-20 methacrylate units (90 glutamate units total) were targeted with the 3-arm methacrylamide copolypeptides, now termed 3-CP-PG respectively for simplicity, being fully analyzed by $^1$H NMR to confirm successful conjugation and the degree of substitution. For 3-CP-PG, a degree of substitution of 10 was determined using the α-protons as reference (Figure C7). Similar to the parent non-functionalized copolypeptides, these methacrylamide derivatives were also observed to be water soluble and

undergo spontaneous assemble into physically crosslinked hydrogels within the desired concentration ranges (~2-10 wt%).To confirm β-sheet assemblies, previously reported FTIR techniques were utilized to assign diagnostic peaks. It should be noted that, unlike the previous methacrylate counterparts, these materials can be photo crosslinked as a single component without the need for a co-monomer (Figure 4.11).

### 4.3.2 Blended Hydrogel Viscoelasticity

The thermal stability of the β-sheet driven hydrogels were evaluated using a temperature sweep at constant amplitude and frequencies (Figure 4.8). No changes in storage modulus (G′) and loss modulus (G″) were detected in ranges from 20 °C–45 °C. Since these materials network integrity survives physiological temperature, it was postulated that these materials would serve as a great additive to the temperature-sensitive GelMA. Blends were formulated by first dissolving GelMA in a 0.1 wt% solution of lithium phenyl-2,4,6-trimethylbenzoylphosphinate (LAP) in DI water at 45 °C and subsequently mechanically mixing in 3-CP-PG at 45 °C to avoid the gelatin triple helix formation. Since GelMA is typically printed at 5 wt%, the GelMA concentration was kept consistent but varying 3-CP-PG concentration. To evaluate the network stability, the blends were placed between parallel plates at 45 °C to allow proper adhesion and dispersion on the plates, then subsequently cooled to 20 °C and allowed to equilibrate over 15 minutes. The network stability was evaluated by heating 1 °C/min at constant frequency and amplitude to determine changes in G′ and G″.

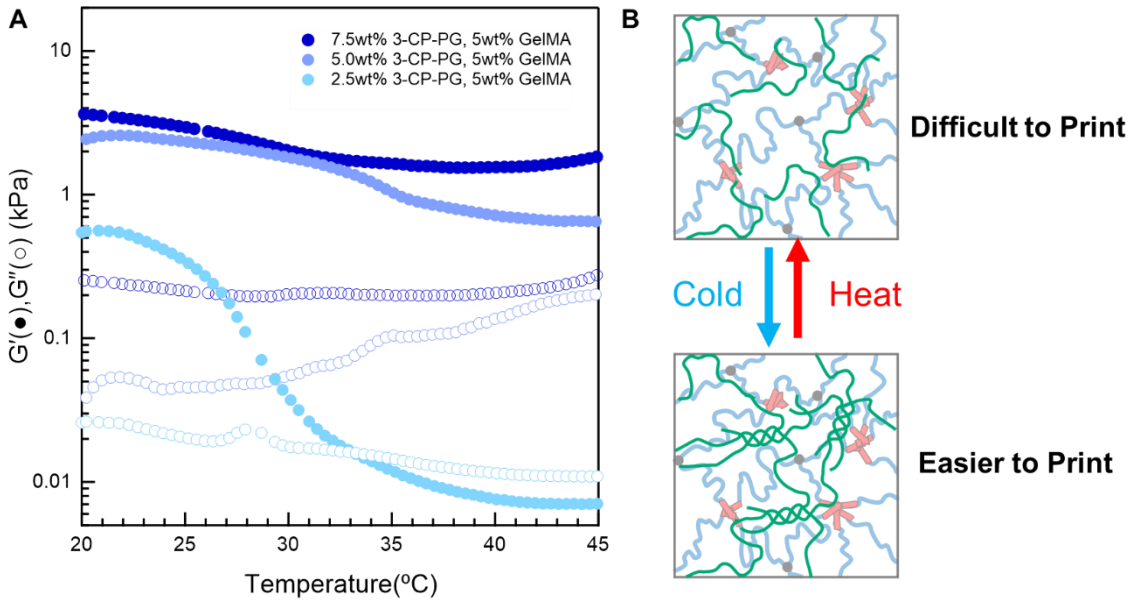


**Figure 4.3.** (A). Temperature sweeps of blended materials with various wt% of 3-CP-PG (B) Graphic depicting of gelatin's triple helix breaking and reforming with heat, while 3-CP-PG network remain unchanged.

At a low concentration (2.5wt%) of 3-CP-PG, the blends have a drop in G′ until there is a crossover with G″, indicating a transition from a viscoelastic solid to fluid. These GelMA-like thermal transitions can be hypothesized due to a lack of an interpercolated network purely of the β-sheet 3-CP-PG network. At 5 wt% and above there is a drop in the overall modulus, but no crossover is observed at the temperature of interest. The percent change in modulus is directly related to the concentration of the 3-CP-PG network, with higher concentration giving smaller changes. This can be due to the GelMA triple helix network contributing less to the overall material properties when diluted by more β-sheet networks. Future studies on the effect of GelMA weight percent with consistent 3-CP-PG are also of interest to modulate the thermomechanical properties of these blends further. To minimize both thermo-mechanical properties changes and the 3-CP-PG additive needed, the 7.5 wt% 3-CP-PG, 5 wt% GelMA was evaluated for use in 3D printing.

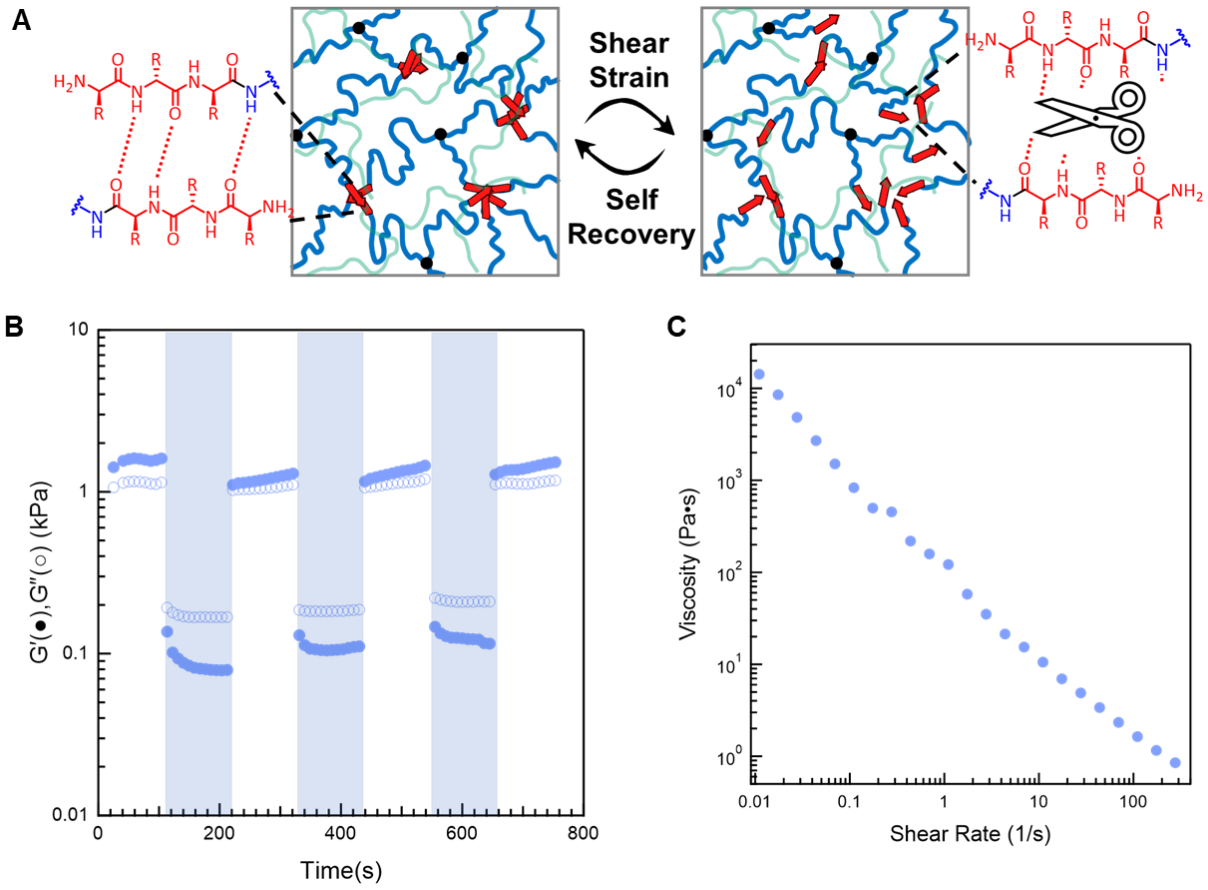


**Figure 4.4.** Graphic depicting yielding behaviour of copolypeptide hydrogels subject to shear and subsequent reformation upon removal of shear via β-motif directed H-bonding of amide bonds (A). Cyclic dynamic oscillatory amplitude time sweeps for 7.5 wt% 3-CP-PG, 5wt% GelMA hydrogels at 35°C. The white box indicates 1% strain, and the blue box indicates 200% strain (C), which shows moduli response to low strains (0.1%) and high strains (100%) at intervals of 100 s at a constant angular frequency of 6.2 rad/s. Viscosity sweep with increasing shear rate (D) illustrating shear-thinning behavior of hydrogels at 35°C.

### 4.3.3 Direct Ink Writing (DIW) Printing Evaluation.

The yielding and rapid self-recovery behavior of hydrogel networks are crucial rheological features necessary for extrusion applications, especially with 3D-printing techniques such as direct-ink writing (DIW). Previous reports have shown 3-arm star-shaped

analogs are observed to assemble faster into 3D hydrogel networks with rapid reassociation of β-sheet domains leading to self-recovery after shear-based extrusion compared to their linear counterpart.[31] Rheology and printing experiments were conducted at 35 °C to mimic physiological temperature and to fully break the GelMA triple helix network, according to previous 3D printing reports.

To simulate such an extrusion process, shear processing properties and recovery of our lead formulation (7.5 wt% 3-CP-PG and 5 wt% GelMA) were evaluated using cyclic oscillatory experiments, in which the strain amplitude was cycled in a stepwise fashion. Blends were subjected to low strains and shear-yielding behavior at higher strains. The blend was shown to have a rapid drop in storage modulus when going from 1 % strain to 200 % strain and then a rapid recovery back to its original modulus when the higher strain is removed, signifying network recovery (Figure 4.4B). Because effective extrusion needs fast network yielding in the printer nozzle and shear-thinning during extrusion onto the platform, rotational rheometry was deployed to see the viscosity drop as a shear rate function, indicating a shear-thinning material (Figure 4.4C).

To further demonstrate the simplicity of extruding these GelMA modified resin, the printability was evaluated on a commercial DIW 3D printing. Our optimal formulation (7.5 wt% 3-CP-PG and 5 wt% GelMA) were loaded into a 3mL syringe, heated to 37 °C, and extruded from a 21-gauge needle. Simple structures were successfully printed at physiological temperature without cooling the platform or utilizing precisely engineered printing processes (Figure 4.8). When pure GELMA (12.5 wt%) was loaded onto a syringe and heated to 37 °C, the ink undergo a transition from a gel to a watery liquid that dripped from the syringe without

pressure (Figure 4.10). Furthermore, it is observed that pressures to yield the network increase with temperature, and higher temperature leads to more clogging and poorer shape fidelity. It is speculated that this is due to higher temperatures increasing aggregation of β-sheet junctions, leading to harder-to-yield physical networks. Together, these rheological and printing experiments indicate a bioink that can easily be utilized for bioprinting within a physiological regime.

### 4.3.4 Secondary Crosslinking

Upon extrusion, the hydrogel is soft and re-moldable, which limits the utilization of printing complex objects that need better network stability. Cooling the network post extrusion increases network integrity due to the triple helix re-establishing, but it is limited due to slow gelatin network formation, lack of spatiotemporal control, and potentially subjecting cells to sub-physiological temperatures. Since both GelMA and 3-CP-PG contain methacrylamide that can be chemically crosslinked with radicals, utilizing the LAP photoinitiator that releases radicals upon light irradiation allows the ability to spatial-temporally crosslink at physiological temperature. Previous reported literature showcases that short irradiation time with minimum LAP can mitigate any possible cell death.[37]

To confirm these hypotheses, gelation kinetics were studied using real-time rheology by monitoring changes in G' before and during irradiation at 20 ℃ and 35 ℃ (Figure 4.4B). Without irradiation, there is no change in G' in both temperatures, but upon irradiation, there is an increase in G', indicating a chemical crosslinking occurring. Significantly, this secondary crosslinking step led to a change in properties from an initially soft, deformable hydrogel to a stiffer, elastic material with a more dramatic change compared to the hydrogel at physiological

temperature. These photo-crosslinked hydrogels were shown to be more robust and stable, withstanding applied forces that would otherwise remold the parent physical hydrogel. At both physiological temperature and triple helix forming temperature, there is a significant increase in modulus, with the hydrogel at colder temperature leading to a slightly higher modulus material. This indicates that either by cooling or keeping the hydrogel heated form comparable final material post extrusion and photo-crosslinking. Thus, furthering our hypothesis that cell-laden bio-inks can be processed at physiological temperature and photo-crosslinked without the need to cool the overall material to get network integrity.

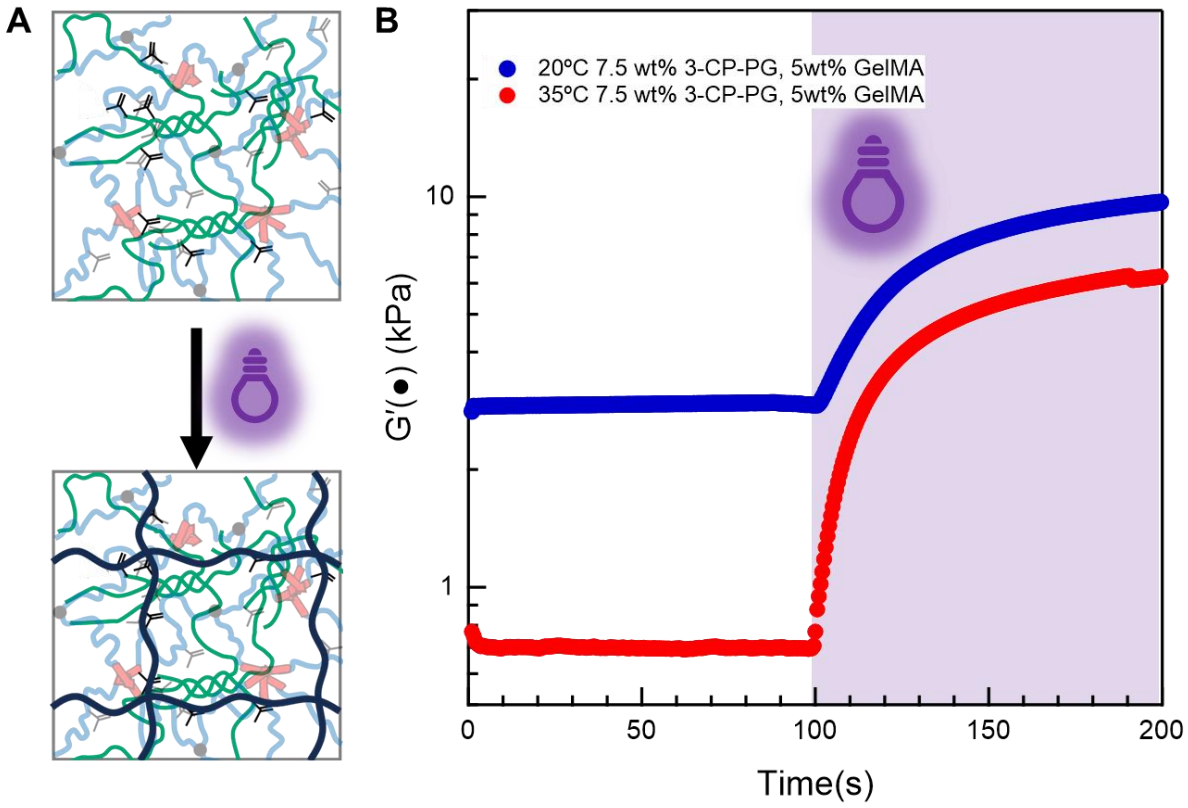


**Figure 4.4.** Graphic depicting photocrosslinking of 3-CP-PG, GelMA blends containing LAP photoinitiator (A). Real-time UV light curing at intensity of 25 mW/cm$^2$ at 20°C and 37°C

Previous reported rheological additives do not participate in chemical network formation and act like fillers in the GelMA network. This approach allows the integration of two degradable peptidic systems into one network system with the potential to control the network topology and heterogeneity by blending the material. The 3-CP-PG β-sheet network also has the added benefit of being degradable to chemical and enzymatic triggers

### 4.3.5 DIW and Enzymatic Biodegradation

To track the degradation of individual networks, either GelMA or 3-CP-PG, two dyes with different absorption and emission spectra were chemically coupled into individual components. First, the blue shifted umbelliferon amine was coupled onto the 3-CP-PG network facility using DMTMM coupling chemistry to yield a fluorescently active peptide labeled 3-CP-PG-Um (Figure 4.13). Following previously reported protocol, the red-shifted fluorescein isocyanate was coupled off the lysine residual in GelMA to form GelMA-Flu (Figure 4.13). The overlaid UV-Vis and fluorescence spectrum shows an overlapping absorption spectrum of 300−380 nm and a maximum emission at 405 nm and 550 nm for 3-CP-PG-Um and GelMA-Flu respectively (Figure 4.13). Pure GelMA-Flu, 3-CP-PG-Um, and blended material were crosslinked and incubated with 1 wt% proteinase K and fluorescence were taken of the solution after 36 hours (Figure 4.14). To showcase the ability of using star copolypeptide to 3D printing GelMA at physiological temperature without sacrificing inherent biodegradability, a formulation of 7.5 wt% 3-CP-PG and 5wt% GelMA-Fluo was prepared and loaded onto a syringe. Using a commercial pneumatic printer (Cellink's BioX), a three-dimensional inverted pyramid was printed with the blended material at 37 °C (Figure 4.5A). The inverted pyramid

was then fully degraded in less than 4 hours in the previously mentioned enzymatic solution (Figure 4.5B and Figure 4.12).

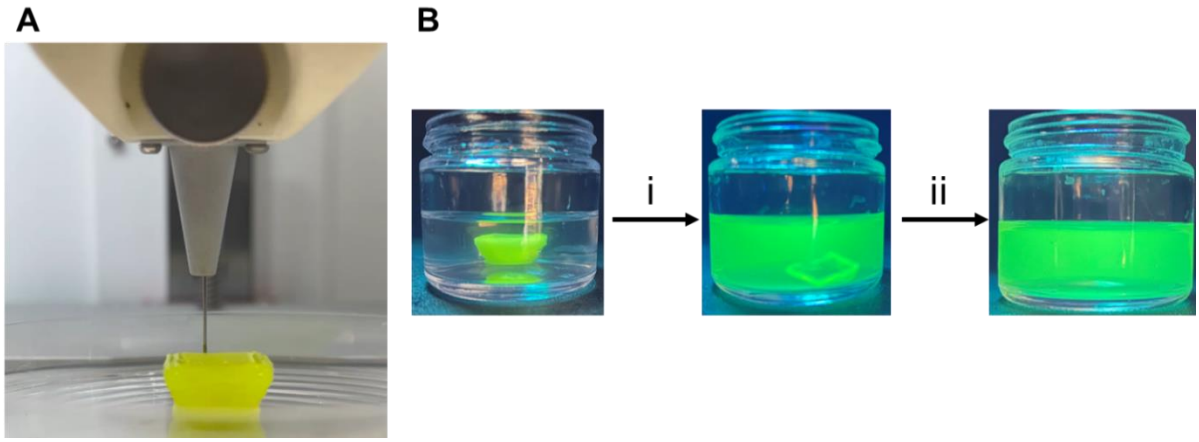


**Figure 4.5.** (A) DIW of 5wt% GelMA-Fluo and 7.5wt% 3-CP-PG into an inverted pyramid (B) Inverted pyramid incubated at 37°C in 1 wt% proteinase K/PBS solution at various time points i) 2 hrs; ii) 1.5 hrs

### 4.4 Conclusion and Future Direction

Previously, extrudable star copolypeptides hydrogels have been shown as a tailorable biomaterial with efficient 3D printability. To showcase the ease of using these materials for bioprinting, they were doped into commercially available bioinks based on bioactive GelMA. This strategy allows the extrusion of these materials at physiological temperatures without sacrificing shape fidelity or needing stringent printing conditions, a method unobtainable with pure GelMA. The success of this method is enabled by molecularly designing ß-sheet domains in the star copolypeptide that forms thermally stable physical crosslinks that serve as a scaffold during heated printing. Compared to previously utilized rheological modifiers that serves as fillers post photo-crosslinking, star copolypeptide can be designed to participate in the chemical crosslinking by incorporating acrylamides that copolymerizes with GelMA. By

taking advantage of the degradable backbone of the star copolypeptide additive, the overall proteolytic cleavage kinetics of the blends can be modulated, ultimately leading to a fully biodegradable scaffold. More in depth studies, including a degradation kinetic assessment, is needed to fully understand the contribution of the additive to the overall material degradation. Future work hopes to apply this to biological system by regulating encapsulated cellular behavior by degrading of three-dimensional hydrogels by cell-secreted protease. Utilizing this approach enables the bioprinting of intricate geometric scaffolds at body temperature, seamlessly integrating cells to modify the matrix structure. Moreover, by printing multi-material constructs with differing proportions of GelMA or star copolypeptide, there is potential to control degradation, leading to programmed proliferation and activity.

### 4.5 Additional Experimental Results

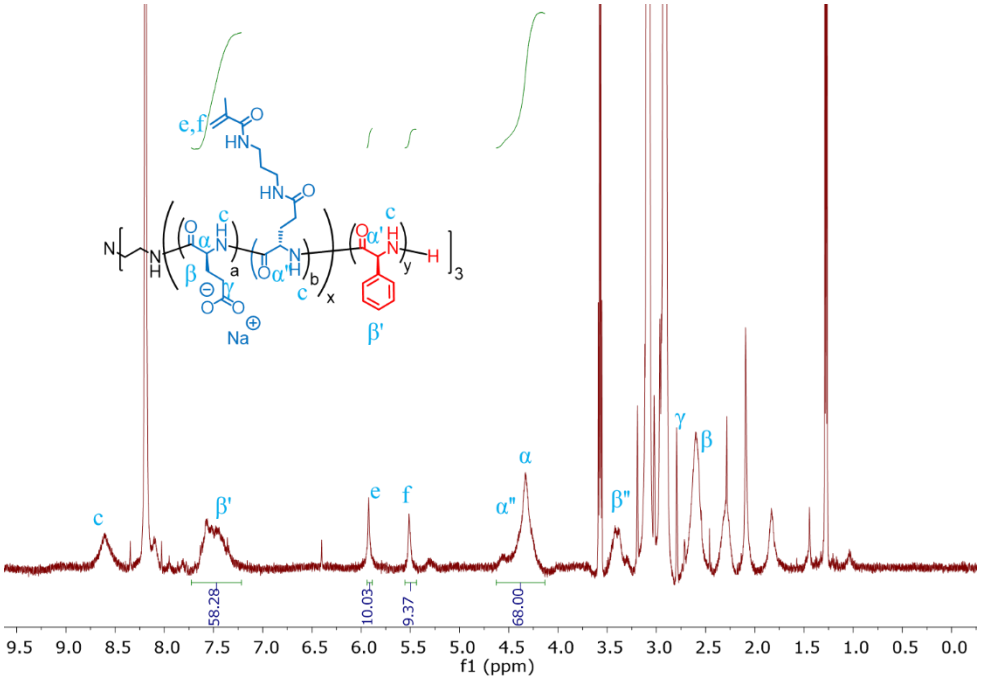


**Figure 4.6.** 1H NMR spectra of 3-PLG68-b-PPG26 functionalized with methacrylamide (3-CP-PG) and DOSY in DMF.

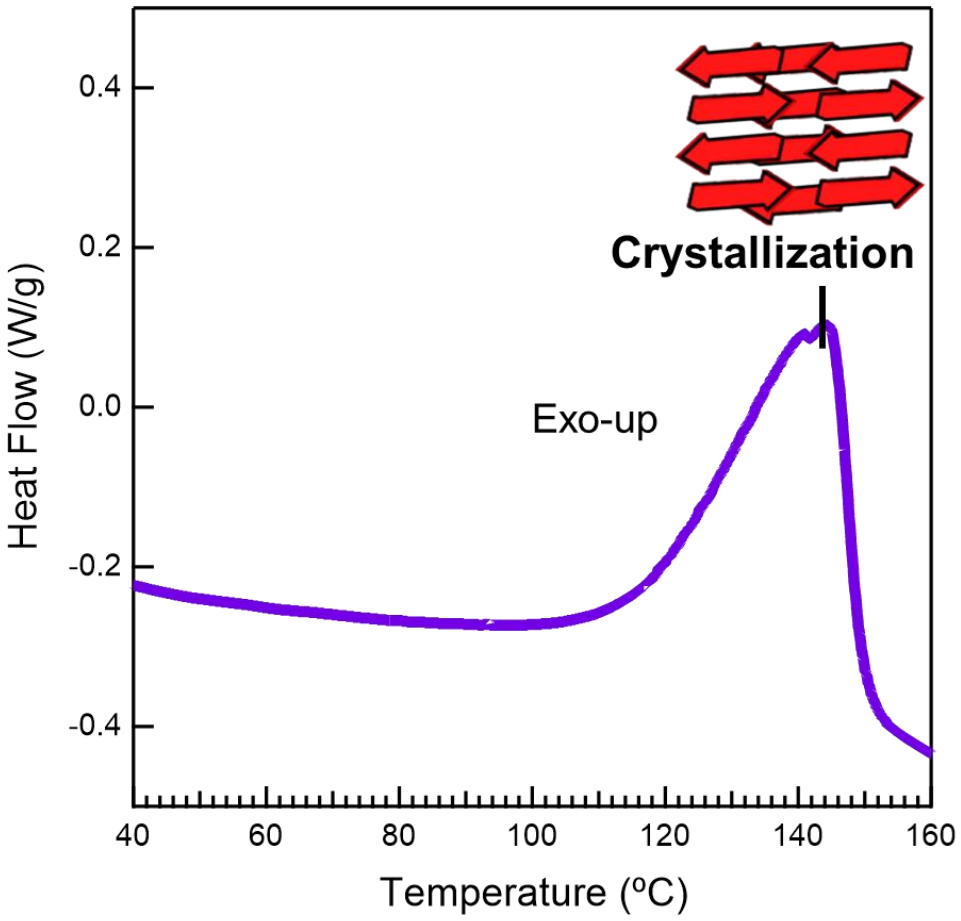


**Figure 4.7.** Differential Scanning Calorimetry (DSC) of 3-CP-PG in the solid state

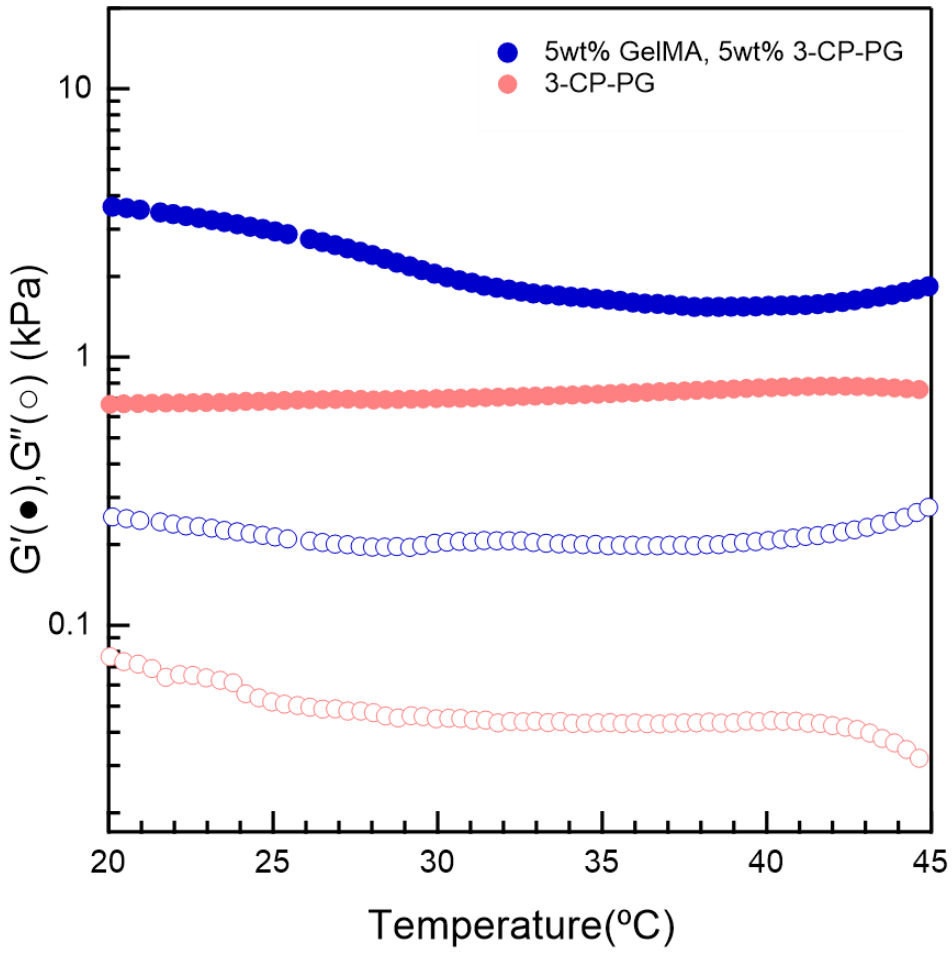


**Figure 4.8.** Temperature sweeps of representative blended material and of pure 3-CP-PG

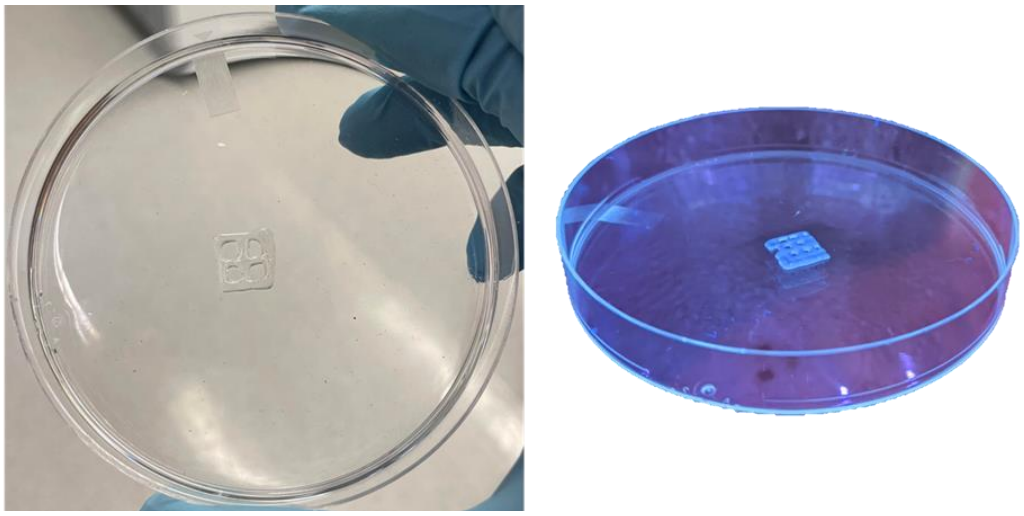

**Figure 4.9.** 7.5 wt% 3-CP-PG-Umb,5wt% GelMA blended material extruded with 21G needle at 37°C at 180Kpa.

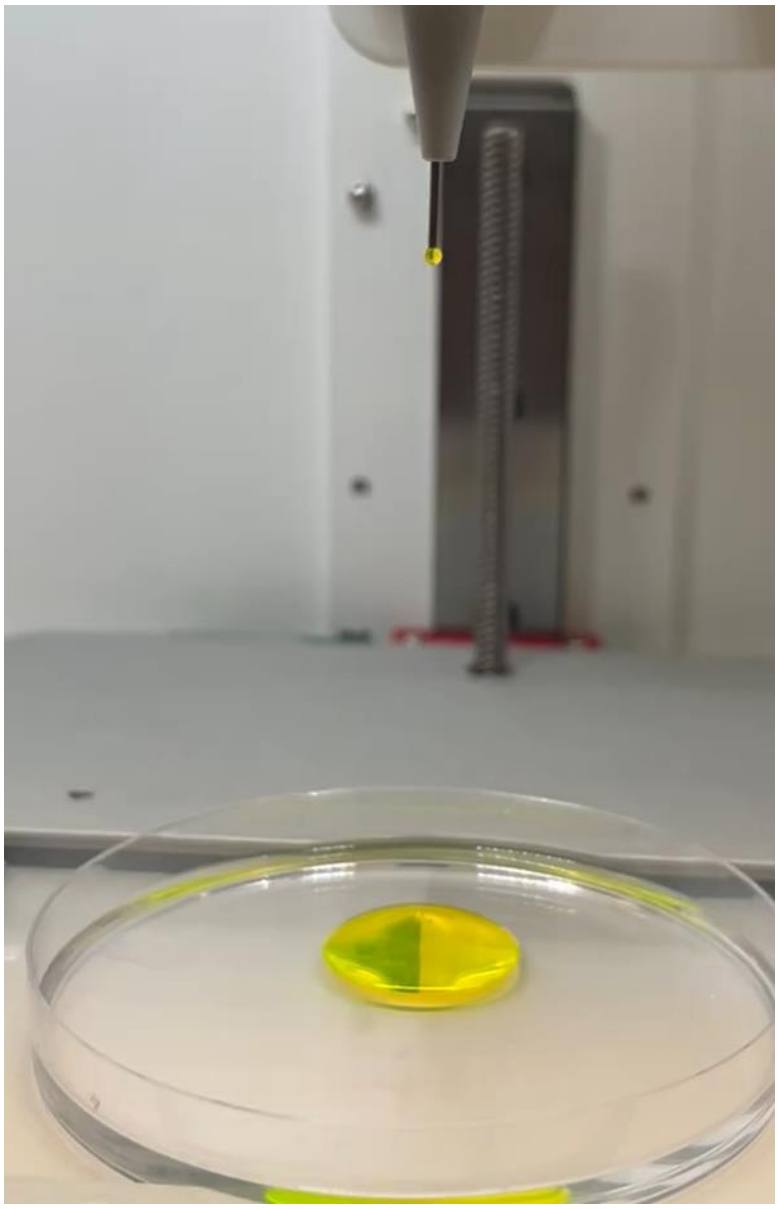

**Figure 4.10.** 12.5 wt% GelMA-Fluo dripping at 37°C on the commercial BioX without applied pressure

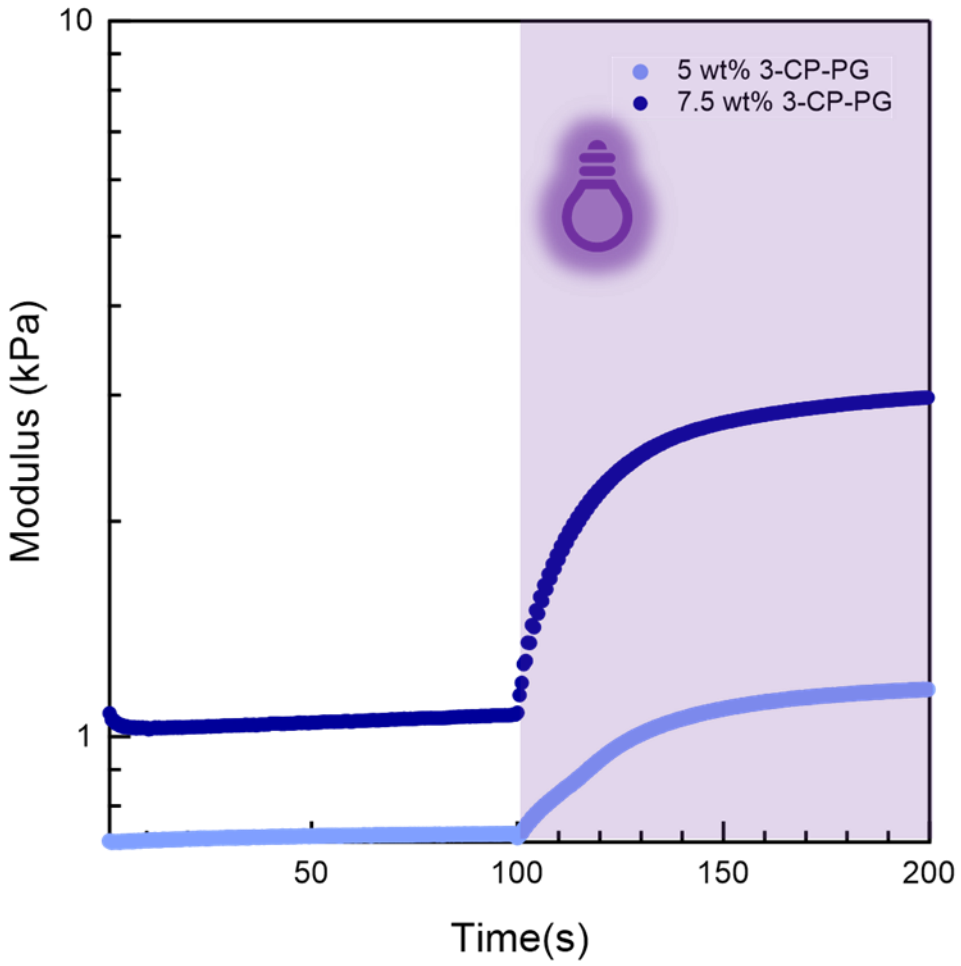


**Figure 4.11**. Real-time UV light curing at intensity of 25 mW/cm$^2$ at 37°C

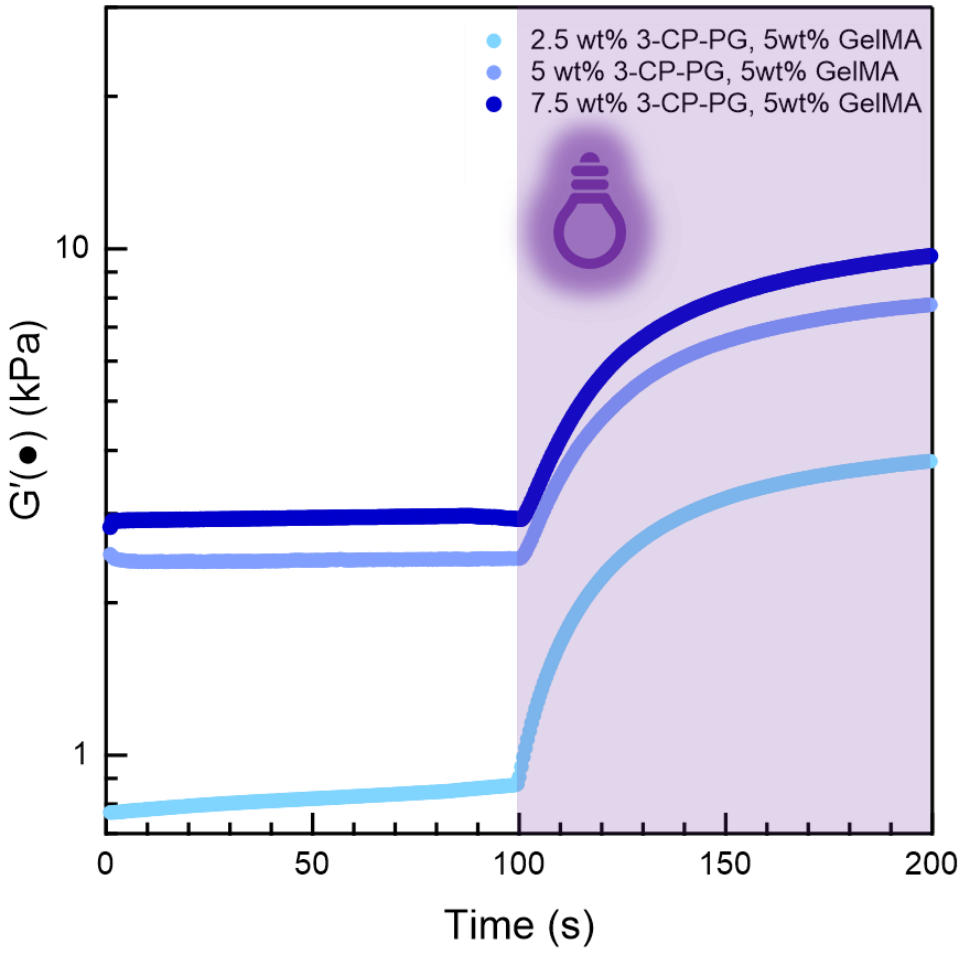


**Figure 4.12**. Real-time UV light curing at intensity of 25 mW/cm$^2$ at 0°C

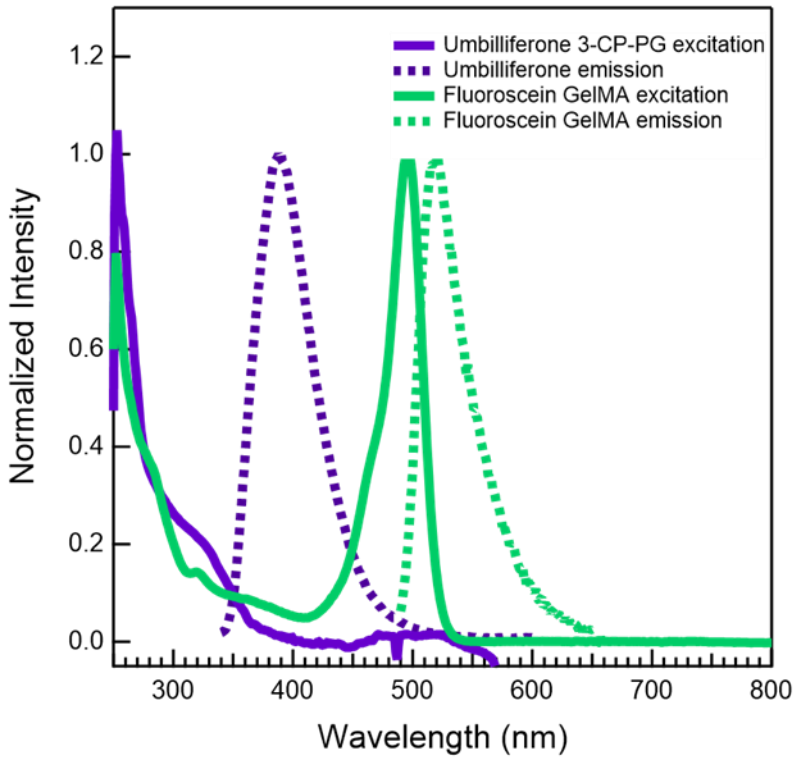


**Figure 4.13**. Normalized UV-Vis and fluorescence spectra for star copolypeptide tagged umbelliferon and GelMA tagged fluorescein.

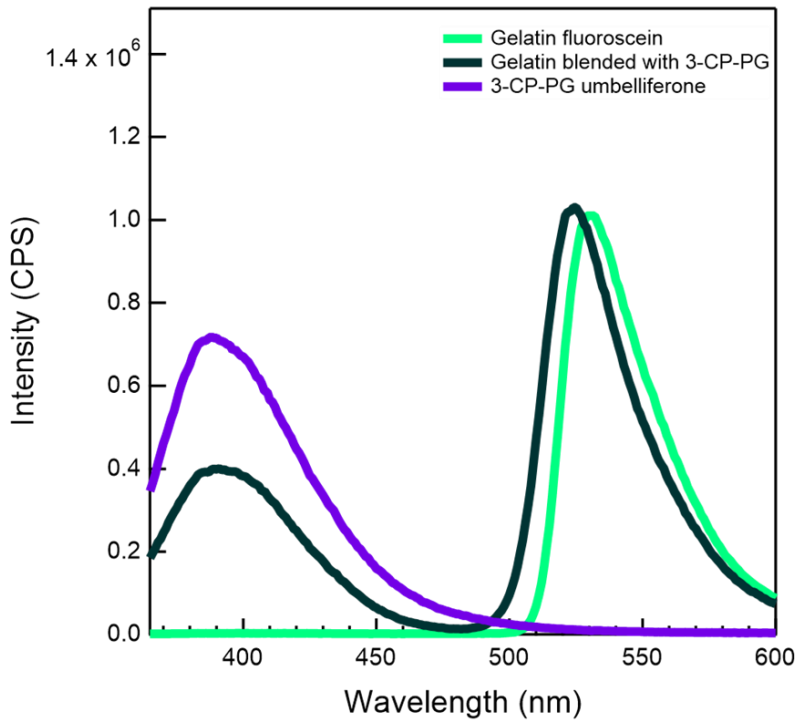


**Figure 4.14**. Fluorescence spectra scan of fluorescent network post proteinase K digestion excited at 325 nm

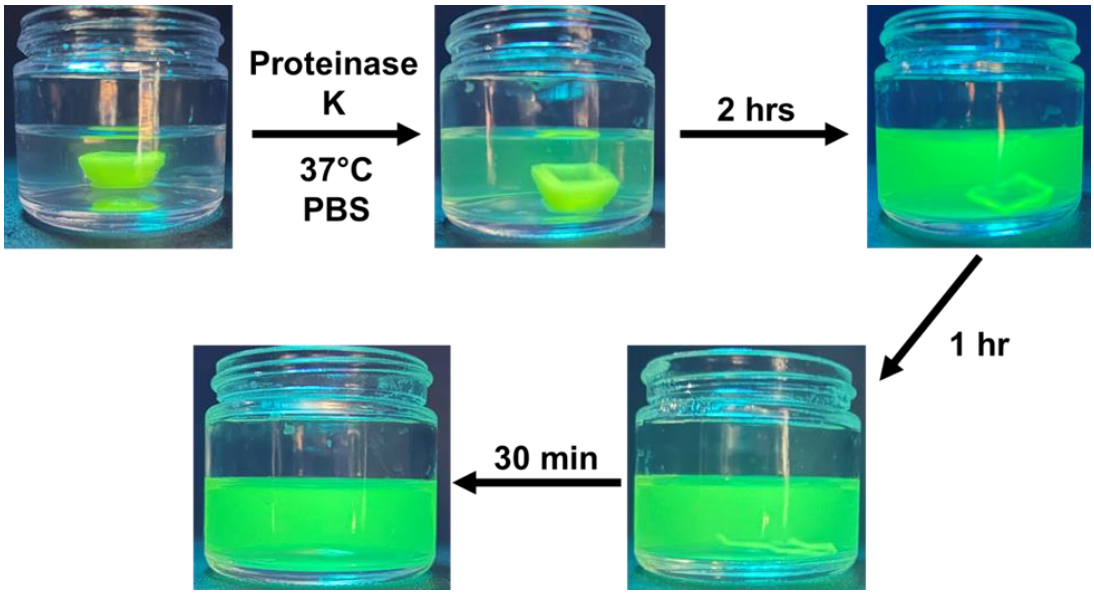


**Figure 4.15**. Inverted pyramid of blended material degrading in 1 wt% proteinase K in PBS buffer

## 4.6 References


[1] Chimene, D.; Lennox, K. K.; Kaunas, R. R.; Gaharwar, A. K. Advanced Bioinks for 3D Printing: A Materials Science Perspective. *Ann. Biomed. Eng.* **2016**, *44*, 2090–2102.

[2] Tang, M.; Zhong, Z.; Ke, C. Advanced Supramolecular Design for Direct Ink Writing of Soft Materials. *Chem. Soc. Rev.* **2023**, *52*, 1614–1649.

[3] Yu, C.; Schimelman, J.; Wang, P.; Miller, K. L.; Ma, X.; You, S.; Guan, J.; Sun, B.; Zhu, W.; Chen, S. Photopolymerizable Biomaterials and Light-Based 3D Printing Strategies for Biomedical Applications. *Chem. Rev.* **2020**, *120*, 10695–10743.

[4] Liu, A. P.; Appel, E. A.; Ashby, P. D.; Baker, B. M.; Franco, E.; Gu, L.; Haynes, K.; Joshi, N. S.; Kloxin, A. M.; Kouwer, P. H. J.; Mittal, J.; Morsut, L.; Noireaux, V.; Parekh, S.; Schulman, R.; Tang, S. K. Y.; Valentine, M. T.; Vega, S. L.; Weber, W.; Stephanopoulos, N.; Chaudhuri, O. The Living Interface between Synthetic Biology and Biomaterial Design. *Nat. Mater.* **2022**, *21*, 390–397.

[5] Correa, S.; Grosskopf, A. K.; Lopez Hernandez, H.; Chan, D.; Yu, A. C.; Stapleton, L. M.; Appel, E. A. Translational Applications of Hydrogels. *Chem. Rev.* **2021**, *121*, 11385–11457.

[6] Saha, A.; Johnston, T. G.; Shafranek, R. T.; Goodman, C. J.; Zalatan, J. G.; Storti, D. W.; Ganter, M. A.; Nelson, A. Additive Manufacturing of Catalytically Active Living Materials. *ACS Appl. Mater. Interfaces* **2018**, *10*, 13373–13380.

[7] Johnston, T. G.; Fillman, J. P.; Priks, H.; Butelmann, T.; Tamm, T.; Kumar, R.; Lahtvee, P.; Nelson, A. Cell-Laden Hydrogels for Multikingdom 3D Printing. *Macromol. Biosci.* **2020**, *20*, 2000121.

[8] Ouyang, L.; Yao, R.; Zhao, Y.; Sun, W. Effect of Bioink Properties on Printability and Cell Viability for 3D Bioplotting of Embryonic Stem Cells. *Biofabrication* **2016**, *8*, 035020.

[9] Smith, P. T.; Narupai, B.; Tsui, J. H.; Millik, S. C.; Shafranek, R. T.; Kim, D. H.; Nelson, A. Additive Manufacturing of Bovine Serum Albumin-Based Hydrogels and Bioplastics. *Biomacromolecules* **2020**, *21*, 484–492.

[10] Schwab, A.; Levato, R.; D'Este, M.; Piluso, S.; Eglin, D.; Malda, J.; D'Este, M.; Piluso, S.; Eglin, D.; Malda, J. Printability and Shape Fidelity of Bioinks in 3D Bioprinting. *Chem. Rev.* **2020**, *120*, 11028–11055.

[11] Murphy, R. D.; Garcia, R. V.; Oh, S. J.; Wood, T. J.; Jo, K. D.; Read de Alaniz, J.; Perkins, E.; Hawker, C. J. Tailored Polypeptide Star Copolymers for 3D Printing of Bacterial Composites Via Direct Ink Writing. *Adv. Mater.* **2023**, *35*, 2207542.

[12] Hahn, M. S.; Taite, L. J.; Moon, J. J.; Rowland, M. C.; Ruffino, K. A.; West, J. L. Photolithographic Patterning of Polyethylene Glycol Hydrogels. *Biomaterials* **2006**, *27*,

2519–2524.

[13] Zhou, M.; Lee, B. H.; Tan, Y. J.; Tan, L. P. Microbial Transglutaminase Induced Controlled Crosslinking of Gelatin Methacryloyl to Tailor Rheological Properties for 3D Printing. *Biofabrication* **2019**, *11*, 025011.

[14] O'Connell, C. D.; Zhang, B.; Onofrillo, C.; Duchi, S.; Blanchard, R.; Quigley, A.; Bourke, J.; Gambhir, S.; Kapsa, R.; Di Bella, C.; Choong, P.; Wallace, G. G. Tailoring the Mechanical Properties of Gelatin Methacryloyl Hydrogels through Manipulation of the Photocrosslinking Conditions. *Soft Matter* **2018**, *14*, 2142–2151.

[15] Qiao, Y.; Liu, X.; Zhou, X.; Zhang, H.; Zhang, W.; Xiao, W.; Pan, G.; Cui, W.; Santos, H. A.; Shi, Q. Gelatin Templated Polypeptide Co-Cross-Linked Hydrogel for Bone Regeneration. *Adv. Healthc. Mater.* **2020**, *9*, 1901239.

[16] Lee, B. H.; Lum, N.; Seow, L. Y.; Lim, P. Q.; Tan, L. P. Synthesis and Characterization of Types A and B Gelatin Methacryloyl for Bioink Applications. *Materials (Basel).* **2016**, *9*.

[17] Fan, Y.; Yue, Z.; Lucarelli, E.; Wallace, G. G. Hybrid Printing Using Cellulose Nanocrystals Reinforced GelMA/HAMA Hydrogels for Improved Structural Integration. *Adv. Healthc. Mater.* **2020**, *9*, 2001410.

[18] Zhang, Y.; Wang, Z.; Hu, Q.; Luo, H.; Lu, B.; Gao, Y.; Qiao, Z.; Zhou, Y.; Fang, Y.; Gu, J.; Zhang, T.; Xiong, Z. 3D Bioprinted GelMA-Nanoclay Hydrogels Induce Colorectal Cancer Stem Cells Through Activating Wnt/β-Catenin Signaling. *Small* **2022**, *18* (18), 2200364. https://doi.org/10.1002/SMLL.202200364.

[19] Gao, Q.; Niu, X.; Shao, L.; Zhou, L.; Lin, Z.; Sun, A.; Fu, J.; Chen, Z.; Hu, J.; Liu, Y.; He, Y. 3D Printing of Complex GelMA-Based Scaffolds with Nanoclay. *Biofabrication* **2019**, *11*, 035006.

[20] Chan, N. J. A.; Gu, D.; Tan, S.; Fu, Q.; Pattison, T. G.; O'Connor, A. J.; Qiao, G. G.; Jun-An Chan, N.; Gu, D.; Tan, S.; Fu, Q.; Geoffrey Pattison, T.; O, A. J.; Qiao, G. G. Spider-Silk Inspired Polymeric Networks by Harnessing the Mechanical Potential of β-Sheets through Network Guided Assembly. *Nat. Commun.* **2020**, *11*, 1–14.

[21] Li, D.; Ghovvati, M.; Annabi, N.; Srivastava, S. Polyelectrolyte Complex Scaffoldings for Photocrosslinked Hydrogels. *Mol. Syst. Des. Eng.* **2023**, *8*, 611–623.

[22] Göckler, T.; Li, D.; Grimm, A.; Mecklenburg, F.; Grün, M.; Schepers, U.; Srivastava, S.; Schepers, U.; Srivastava, *S. Polyelectrolyte Complex Hydrogel Scaffoldings Enable Extrusion-Based 3D Bioprinting of Low-Viscosity Bioinks. **2023**. https://doi.org/10.26434/CHEMRXIV-2023-V2TX2.

[23] Garcia, R. V.; Murphy, E. A.; Sinha, N. J.; Okayama, Y.; Urueña, J. M.; Helgeson, M. E.; Bates, C. M.; Hawker, C. J.; Murphy, R. D.; Read de Alaniz, J. Tailoring Writability and Performance of Star Block Copolypeptides Hydrogels through Side-Chain Design.

*Small* **2023**, *19*, 2302794.

[24] Murphy, R.; Walsh, D. P.; Hamilton, C. A.; Cryan, S. A.; In Het Panhuis, M.; Heise, A. Degradable 3D-Printed Hydrogels Based on Star-Shaped Copolypeptides. *Biomacromolecules* **2018**, *19*, 2691–2699.

[25] Murphy, R. D.; Delaney, C.; Kolagatla, S.; Florea, L.; Hawker, C. J.; Heise, A. Design of Statistical Copolypeptides as Multipurpose Hydrogel Resins in 3D Printing. *Adv. Funct. Mater.* **2023**, *33*, 2306710.

[26] Murphy, R. D.; Garcia, R. V.; Heise, A.; Hawker, C. J. Peptides as 3D Printable Feedstocks: Design Strategies and Emerging Applications. *Prog. Polym. Sci.* **2022**, *124*.

[27] Eswaramoorthy, S. D.; Ramakrishna, S.; Rath, S. N. Recent Advances in Three-Dimensional Bioprinting of Stem Cells. *JTERM*. 2019, 908–924.

[28] Hwang, J.; Lee, D. G.; Yeo, H.; Rao, J.; Zhu, Z.; Shin, J.; Jeong, K.; Kim, S.; Jung, H. W.; Khan, A. Proton Transfer Hydrogels: Versatility and Applications. *J. Am. Chem. Soc.* **2018**, *140*, 6700–6709.

[29] Tian, Z. Y.; Zhang, Z.; Wang, S.; Lu, H. A Moisture-Tolerant Route to Unprotected α/β-Amino Acid N-Carboxyanhydrides and Facile Synthesis of Hyperbranched Polypeptides. *Nat. Commun.* **2021**, *12*, 1–11.

[30] Murphy, R. D.; In het Panhuis, M.; Cryan, S. A.; Heise, A. Disulphide Crosslinked Star Block Copolypeptide Hydrogels: Influence of Block Sequence Order on Hydrogel Properties. *Polym. Chem.* **2018**, *9*, 3908–3916.

[31] Shen, Y.; Zhang, S.; Wan, Y.; Fu, W.; Li, Z. Hydrogels Assembled from Star-Shaped Polypeptides with a Dendrimer as the Core. *Soft Matter* **2015**, *11*, 2945–2951.

[32] Batoni, G.; Maisetta, G.; Esin, S. Antimicrobial Peptides and Their Interaction with Biofilms of Medically Relevant Bacteria. *Biochim. Biophys. Acta* **2016**, *1858*, 1044–1060.

[33] Huang, J.; Hastings, C. L.; Duffy, G. P.; Kelly, H. M.; Raeburn, J.; Adams, D. J.; Heise, A. Supramolecular Hydrogels with Reverse Thermal Gelation Properties from (Oligo)Tyrosine Containing Block Copolymers. *Biomacromolecules* **2013**, *14*, 200–206.

[34] Sun, Y.; Hou, Y.; Zhou, X.; Yuan, J.; Wang, J.; Lu, H. Controlled Synthesis and Enzyme-Induced Hydrogelation of Poly(L-Phosphotyrosine)s via Ring-Opening Polymerization of α-Amino Acid N-Carboxyanhydride. *ACS Macro Lett.* **2015**, *4*, 1000–1003.

[35] Nowak, A. P.; Breedveld, V.; Pakstis, L.; Ozbas, B.; Pine, D. J.; Deming, T. J. Rapidly Recovering Hydrogel Scaffolds from Self-Assembling Diblock Copolypeptide Amphiphiles. *Nature* **2002**, *417*, 424–428.

[36] Song, H.; Yang, G.; Huang, P.; Kong, D.; Wang, W. Self-Assembled PEG–Poly(L-Valine) Hydrogels as Promising 3D Cell Culture Scaffolds. *J. Mater. Chem. B* **2017**, *5*, 1724–1733.

[37] Nieto, D.; Marchal Corrales, J. A.; Jorge De Mora, A.; Moroni, L. Fundamentals of Light-Cell-Polymer Interactions in Photo-Cross-Linking Based Bioprinting. *APL Bioengineering*. 2020, 041502.

# Appendix A: Supporting Information for Chapter 2

## Materials

All chemicals were obtained from Sigma Aldrich unless otherwise noted. γ-benzyl-l-glutamate (BLG) was purchased Carbosynth. l-tyrosine (LT) and trifluoroacetic acid (TFA) was purchased from Fisher Scientific. Triphosgene was purchased from Oakwood Chemical. 10 kDa MWCO SnakeSkin® membrane were purchased from Thermo Fisher Scientific.

## Methods

$^{1}$H NMR and DOSY NMR spectra were acquired on a Varian Unity Inova AS600 600 MHz using $CDCl_3$/TFA and DMSO-$d_6$ as solvents. $^{13}$C NMR spectra were acquired on a Varian Unity Inova 500 MHz using $CDCl_3$/TFA and DMSO-$d_6$ as solvents. FTIR spectra were acquired on a Thermo Nicolet iS10 FTIR Spectrometer equipped with a Smart Diamond attenuated total reflectance (ATR) accessory in the region of 4000-400 $cm^{-1}$. Background measurements were initially performed before analyzing the sample, with 8 scans completed using a resolution of 2 $cm^{-1}$. Size exclusion chromatography (SEC) was measured using a PSS SECurity™ GPC system equipped with a PFG 7 µm 8 × 50 mm pre-column, a PSS 100 Å, 7 µm 8 × 300 mm and a PSS 1000 Å, 7 µm 8 × 300 mm column in series and a differential refractive index (RI) detector at a flow rate of 1.0 mL $min^{-1}$ to determine the dispersities ($Đ$) and molecular weights of polymers. 1,1,1,3,3,3-hexafluoro-2-propanol (HFiP) was used as the eluent. The systems were calibrated against Agilent Easi-Vial linear poly(methyl methacrylate) (PMMA) standards and analyzed by the software package PSS winGPC UniChrom. SAXS measurements of bulk samples were conducted using a custom-built SAXS diffractometer at

the Materials Research Laboratory (MRL) X-ray facility (University of California, Santa Barbara). For these experiments, 1.54 Å Cu Kα X-rays were generated using a Genix 50 W X-ray microsource (50 μm micro-focus) equipped with FOX2D collimating multilayer optics (Xenocs, France) and high efficiency scatterless single crystal/metal hybrid slits.

**Rheology**

Rheological characterization was performed on a strain-controlled rheometer (TA Instruments, ARES-G2) at room temperature. A parallel plate (25 mm) was used for the oscillatory amplitude sweep, oscillatory frequency sweep, and cyclic dynamic oscillatory amplitude sweep experiments. Both cone (25 mm, 0.4 rad) and plate (25 mm) geometries were used for flow rheology to maintain consistent shear during viscosity measurement.

**Small Angle X-Ray Scattering**

SAXS experiments were conducted using a custom-built SAXS diffractometer at the Materials Research Laboratory (MRL) X-ray facility (University of California, Santa Barbara). For these experiments, 1.54 Å Cu Kα X-rays were generated using a Genix 50 W X-ray microsource (50 μm micro-focus) equipped with FOX2D collimating multilayer optics (Xenocs, France) and high efficiency scatterless single crystal/metal hybrid slits. A sample-to-detector distance of 1.7 m was employed. 2D-data were reduced to a one-dimensional form of intensity as a function of the magnitude of the wave vector $q = |\boldsymbol{q}| = 4\pi \sin(\theta/2)/\lambda$, where $\lambda$ is the X-ray wavelength and $\theta$ is the scattering angle. SAXS experiments were conducted at room temperature. All experimental detector systems were calibrated using silver behenate as a

distance standard. Mesh sizes of physical gels were calculated from the *q* value at the onset of the scattering intensity upturn in the low *q* region.

**Monomer and polymer synthesis:**

**γ-benzyl-l-glutamate *N*-carboxyanhydride synthesis:** Triphosgene (31.89 g, 107.48 mmol) and epichlorohydrin (79.53 g, 859.81 mmol) were initially dissolved in 850 mL of tetrahydrofuran (THF) in a 1 L round-bottomed flask with stirring. γ-benzyl-l-glutamate (51.0 g, 214.95 mmol) was then added in one portion and the reaction suspension was heated under reflux (68 °C). The reaction was continued until all solids disappeared and the solution became clear (1–2 h). The solution was then cooled using an argon balloon, any unreacted γ-benzyl-l-glutamate was filtered off and the solution was reduced to a third of its original volume in vacuo. The NCA was precipitated by addition of 1.2 L of hexane and stored overnight at –18 °C to fully precipitate. The solid NCA was dried in vacuo and then re-dissolved in 350 mL ethyl acetate. This solution was then precipitated into excess hexane (1.4 L), filtered and dried (this was completed two to three times). It was then dried in vacuo to afford a white fluffy solid (yield: 51.4 g, 91 %). $^{1}$H NMR (600 MHz, $CDCl_3$/TFA, δ, ppm): 7.34-7.4 (m, 5H, -CH2*C5H6*), 6.36 (s, 1H, *NH*), 5.14 (s, 2H, -*CH2*C5H6), 4.37 (t, 1H, -CO*CH*NH-), 2.60 (t, 2H, -CO*CH2*CH2-), 2.10-2.31 (m, 2H, -COCH2*CH2*-); $^{13}$C NMR (500 MHz, $CDCl_3$/TFA, δ, ppm): 173.79, 168.70, 154.31, 134.58, 128.66, 67.94, 29.38, 26.49.

**l-tyrosine *N*-carboxyanhydride synthesis:** Triphosgene (3.28 g, 11.0 mmol) and epichlorohydrin (8.43 g, 88.3 mmol) were initially dissolved in 130 mL of acetonitrile in a 250

mL round-bottomed flask with stirring. l-tyrosine (4.00 g, 22.1 mmol) was then added in one portion and the suspension was heated to 85 °C. The reaction was continued until all solids disappeared and the solution became clear (3 h). The solution was then cooled using an argon balloon and reaction was concentration. The NCA was suspended in 20 mL ethyl acetate and then 200 mL of hexane was added, followed by storage overnight at –18 °C to fully precipitate the NCA. The solid was dried and then re-dissolved in 110 mL THF. This solution was then precipitated into excess hexane (550 mL), filtered and dried in vacuo to afford a white powder with a yellow tinge (yield: 3.8 g, 84 %). $^{1}$H NMR (600 MHz, DMSO-d6, δ, ppm): 9.31 (s, 1H, -C4H4*OH*), 9.02 (s, 1H, *NH*), 6.96-6.68 (dd, 4H, -*C4H4*OH), 4.70 (s, 1H, -CO*CH*NH-), 2.90 (s, 2H, -*CH2*C4H4-); $^{13}$C NMR (500 MHz, DMSO-d6, δ, ppm): 171.15, 56.90, 52.11, 131.12, 125.01, 116.93, 58.93, 35.91.

**General l-Leucine/ l-Valine/ l-Phenyl Alanine/ l-Phenyl Glycine *N*-carboxyanhydride synthesis:** Triphosgene (0.4 eq) and epichlorohydrin (4 eq) were initially dissolved in 130mL of tetrahydrofuran (THF) in a 250 mL round-bottomed flask with stirring. Desired amino acid (1 eq) was then added in one portion and the reaction suspension was heated under reflux (68 °C). The reaction was continued until all solids disappeared and the solution became clear (1 h). The solution was then cooled using an argon balloon, filtered and then reduced to 1/3 of its original volume using a cold trap in the fumehood. The NCA was precipitated by addition of 200 mL of hexane and stored overnight at -18 °C to fully precipitate. The solid NCA was dried under vacuum and then re-dissolved in a minimum amount of ethyl followed by precipitation into excess hexane (200 mL), filtered and dried under vacuum (two to three times). It was then vacuum dried to afford a crystalline solid

**l-Valine:** (yield: 7.20 g, 62 %). $^{1}$H NMR (600 MHz, $CDCl_3$/TFA, δ, ppm): 7.16 (s, 1H, *NH*), 4.28 (d, 1H, -CO*CH*NH-), 2.27 (m, 1H, -*CH*C2H6), 1.10-1.04 (dd, 6H, -CH*C2H6*); $^{13}$C NMR (500 MHz, $CDCl_3$/TFA, δ, ppm): 167.87, 155.40, 63.13, 30.70, 17.94, 16.67.

**l-Leucine:** (yield: 5.32 g, 50 %). $^{1}$H NMR (600 MHz, $CDCl_3$/TFA, δ, ppm): 6.42 (s, 1H, *NH*), 4.28 (ddd, 1H, -CO*CH*NH-), 1.82(m, 2H, -C*H*CHC2H6), 1.68 (m, 1H, -*CH*C2H6), 1.02-0.97 (dd, 6H, -CH*C2H6*); $^{13}$C NMR (500 MHz, $CDCl_3$/TFA, δ, ppm):169.93,152.60, 56.26,4 0.99,25.24,22.83, 21.68.

**l-Phenyl Alanine:** (yield: 9.42 g, 85 %). $^{1}$H NMR (600 MHz, $CDCl_3$/TFA, δ, ppm):7.39-7.3, 7.22-7.19 (m, 5H, -*C4H4*), 5.87 (s, 1H, *NH*), 4.52 (dd, 1H, -CO*CH*NH-), 3.31 (dd, 1H, -*CH2*C4H4), 2.99 (dd,1H, -*CH2*C4H4-); $^{13}$C NMR (500 MHz, $CDCl_3$/TFA, δ, ppm): 168.70,151.64,134.09,129.47,129.25,128.12,58.95,38.10.

**l-Phenyl Glycine:** (yield: 10.21 g, 91 %). $^{1}$H NMR (600 MHz, $CDCl_3$/TFA, δ, ppm): 7.49-7.39 (m, 5H, -*C4H4*), 6.35 (s, 1H, *NH*), 5.34 (s, 1H, -CO*CH*NH-);$^{13}$C NMR (500 MHz, $CDCl_3$/TFA, δ, ppm): 167.87, 155.40, 63.13, 30.70, 17.94, 16.67.

**3-Arm poly(benzyl-l-glutamate) (3-PBLG) polypeptide synthesis:** γ-benzyl-L-glutamate NCA was dissolved in a CHCl3: DMF (10:1) mixture in a 250 mL flask with stirring. Tris(2-aminoethyl)amine (TREN) in CHCl3 was then quickly added to the flask in one portion. The flask was initially evacuated under vacuum to remove $CO_2$ and then a balloon filled with argon (Ar) was slowly purged through the solution with stirring continued at room temperature until NCA was fully consumed via FTIR spectroscopy. An aliquot of the solution was taken and kept for size exclusion chromatography (SEC) measurements and NMR analysis.

**Macroinitiation of 3-arm poly(benzyl- l-glutamate) to form diblock copolypepeptide:** After full consumption of γ -benzyl- l-glutamate NCA, the previous reaction was split into equal parts to ensure equal concentration of macroinitiator. Desired β-sheet NCA was dissolved in 30 mL DMF and then quickly added to their respected reaction in one part. The flasks were evacuated under vacuum to remove $CO_2$ and then a balloon filled with Ar was slowly purged through the solution with stirring continued at room temperature until NCA was fully consumed via FTIR spectroscopy. The diblock copolymers were then precipitated into excess diethyl ether (1 L), centrifuged, and fully dried under vacuum.

**General block copolypeptide deprotection:** The copolymer was fully suspended in 100 mL $CHCl_3$, after which 80 mL TFA was added. 20 mL of 33 wt% HBr in acetic acid was then added dropwise over 10 min, and the solution was stirred overnight at room temperature. The solution was then precipitated into excess diethyl ether (1.5 L) and dried in vacuo. The solid was suspended in 50 mL deionised water, and then the pH was adjusted to 7-8 until a viscous translucent solution formed. The solution was dialysed against deionised water for 2 days in a 10 kDa MWCO SnakeSkin® membrane with frequent water replacement followed by lyophilization to yield a white fluffy solid.

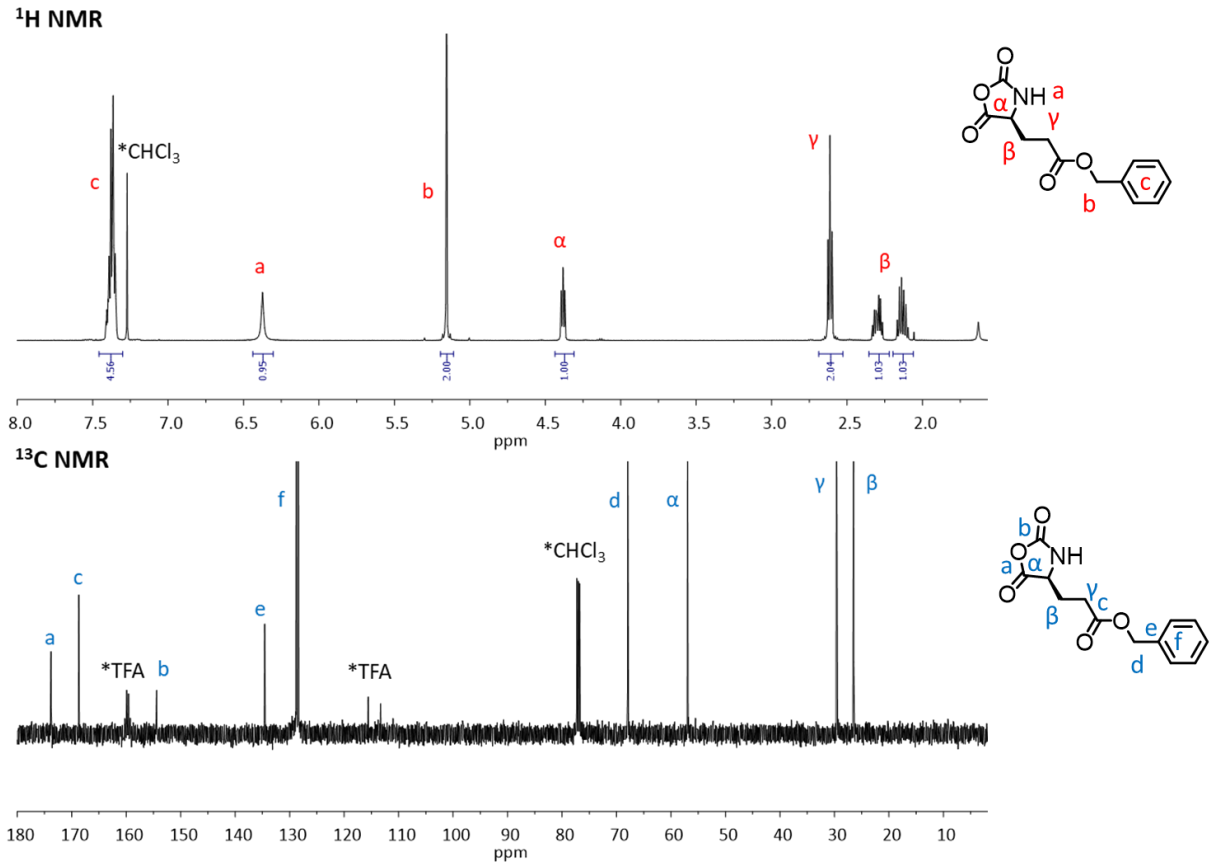


Figure A1: $^{1}H$ NMR and $^{13}C$ NMR spectra of γ-benzyl-*l*-glutamate *N*-carboxyanhydride (BLG NCA) in 15% TFA in $CDCl_3$.

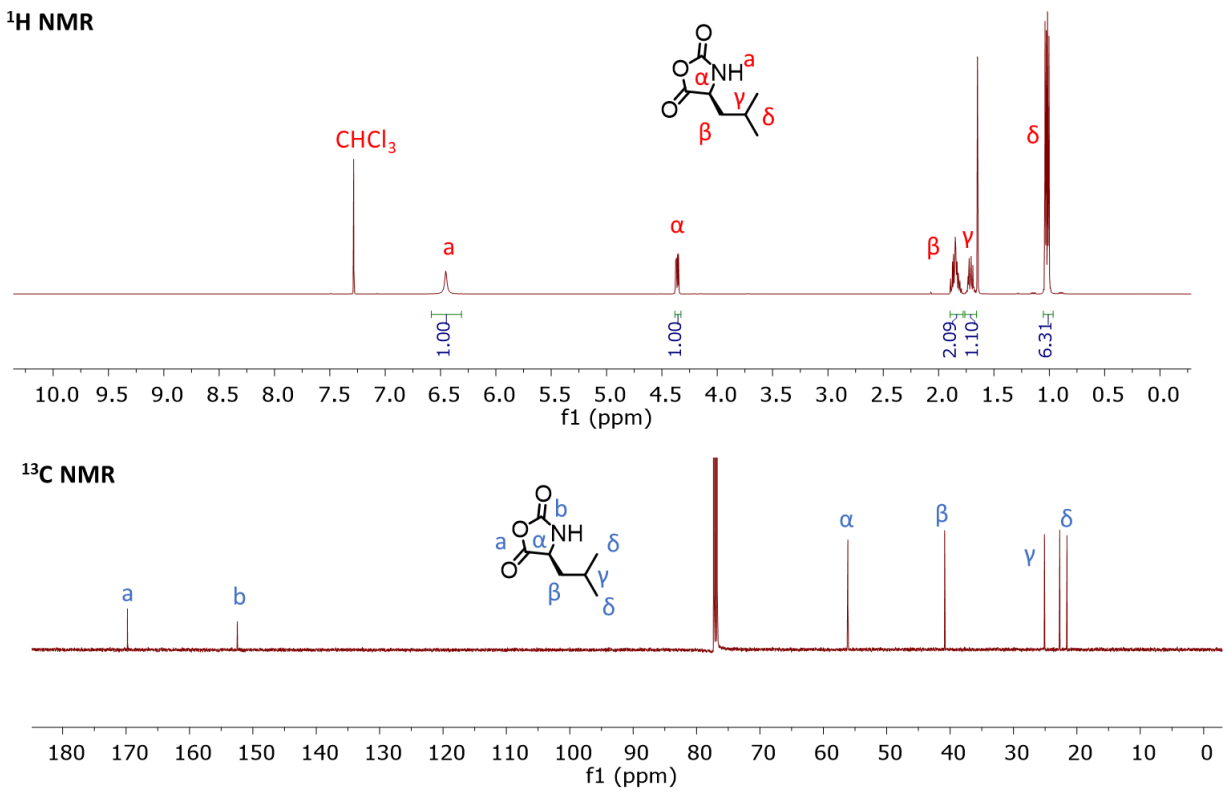


Figure A2: $^{1}H$ NMR and $^{13}C$ NMR spectra of *l*-valine N-carboxyanhydride (BLG NCA) in $CDCl_3$.

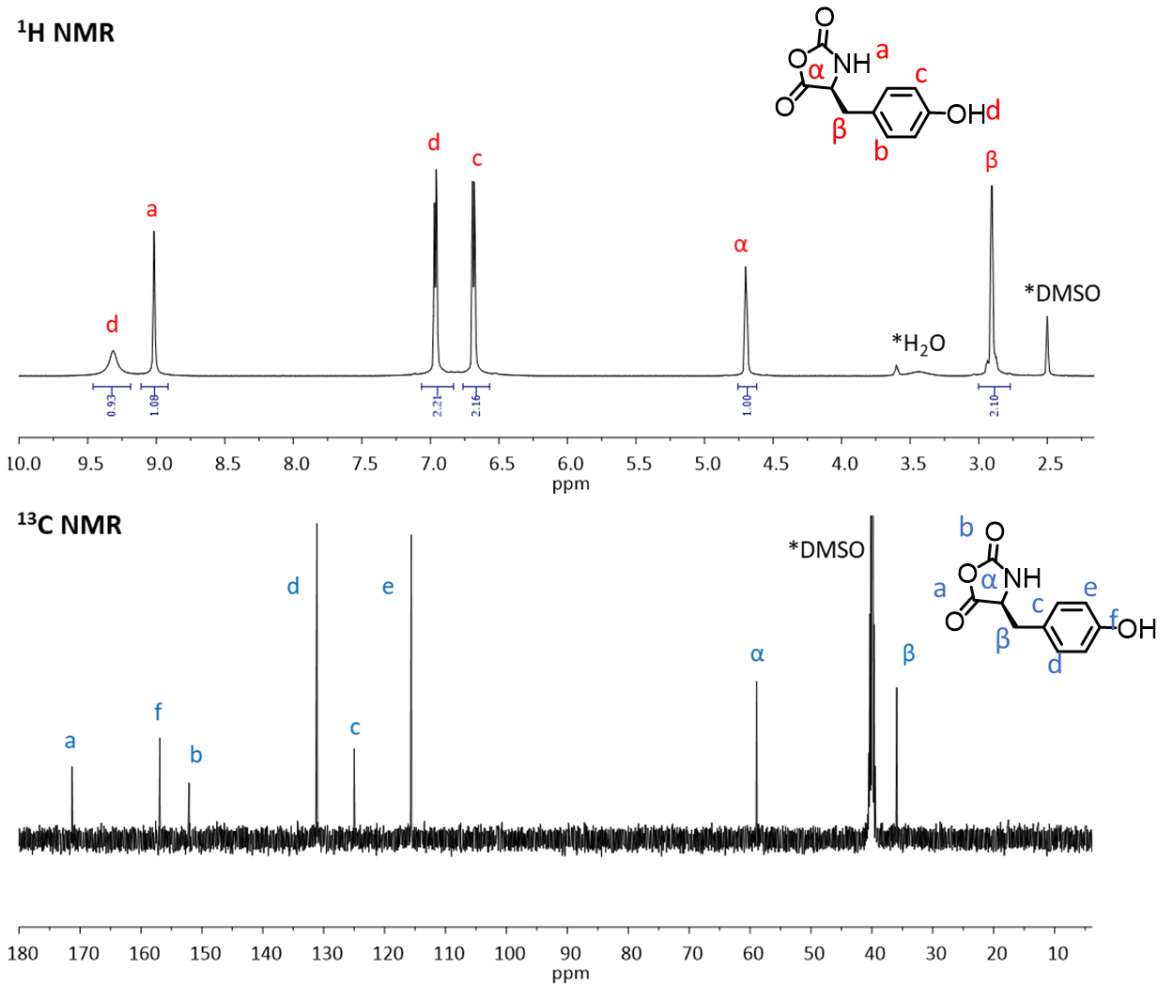


Figure A3: $^{1}$H NMR and $^{13}$C NMR spectra of *l*-tyrosine *N*-carboxyanhydride (LT NCA) in DMSO.

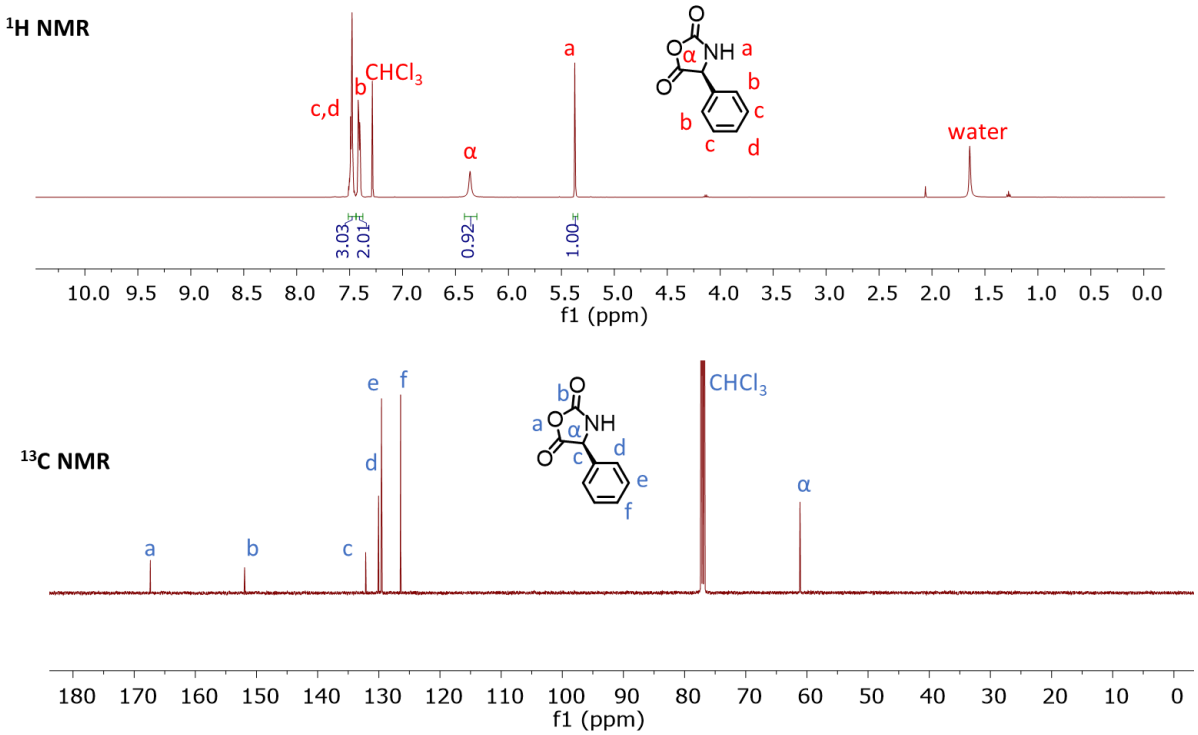


Figure A4: $^{1}H$ NMR and $^{13}C$ NMR spectra of *l*-phenylglycine *N*-carboxyanhydride (LPG NCA) in $CDCl_3$.

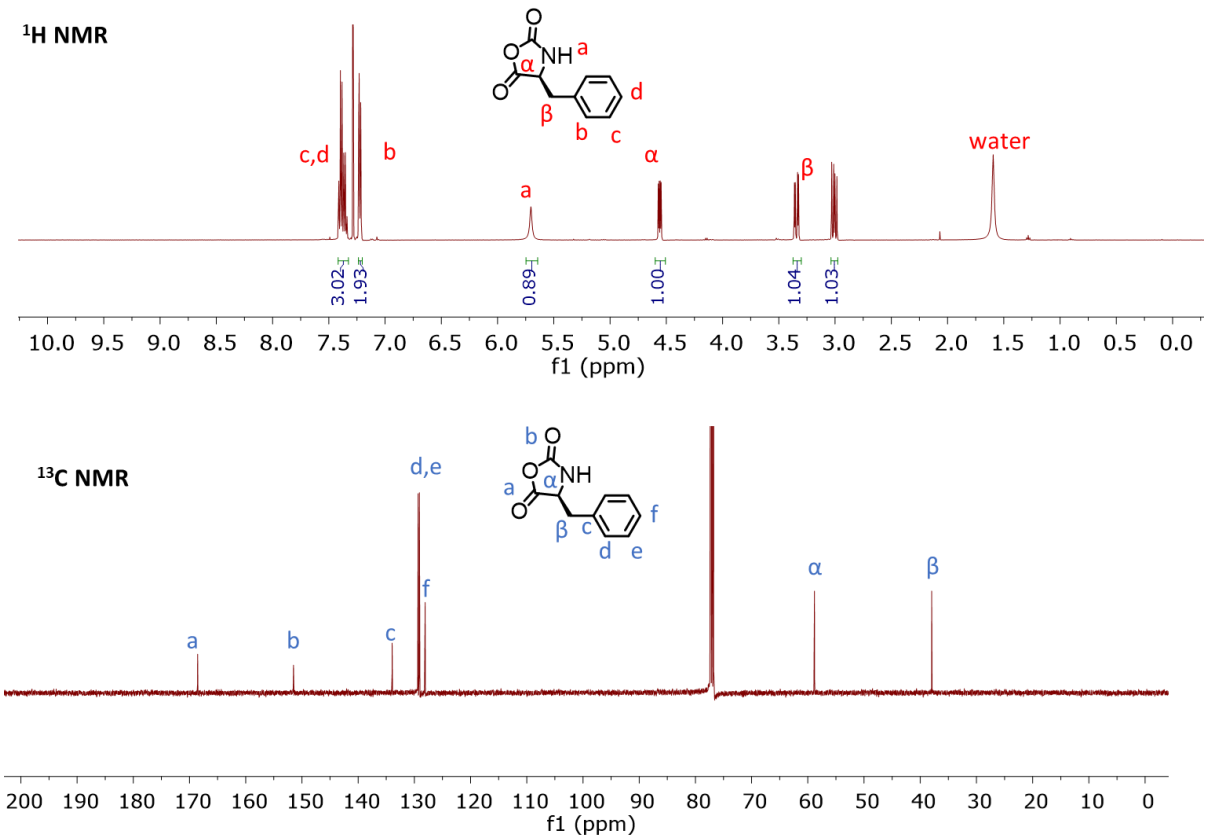


Figure A5: $^{1}H$ NMR and $^{13}C$ NMR spectra of *l*-phenylalanine *N*-carboxyanhydride (LPA NCA) in $CDCl_3$.

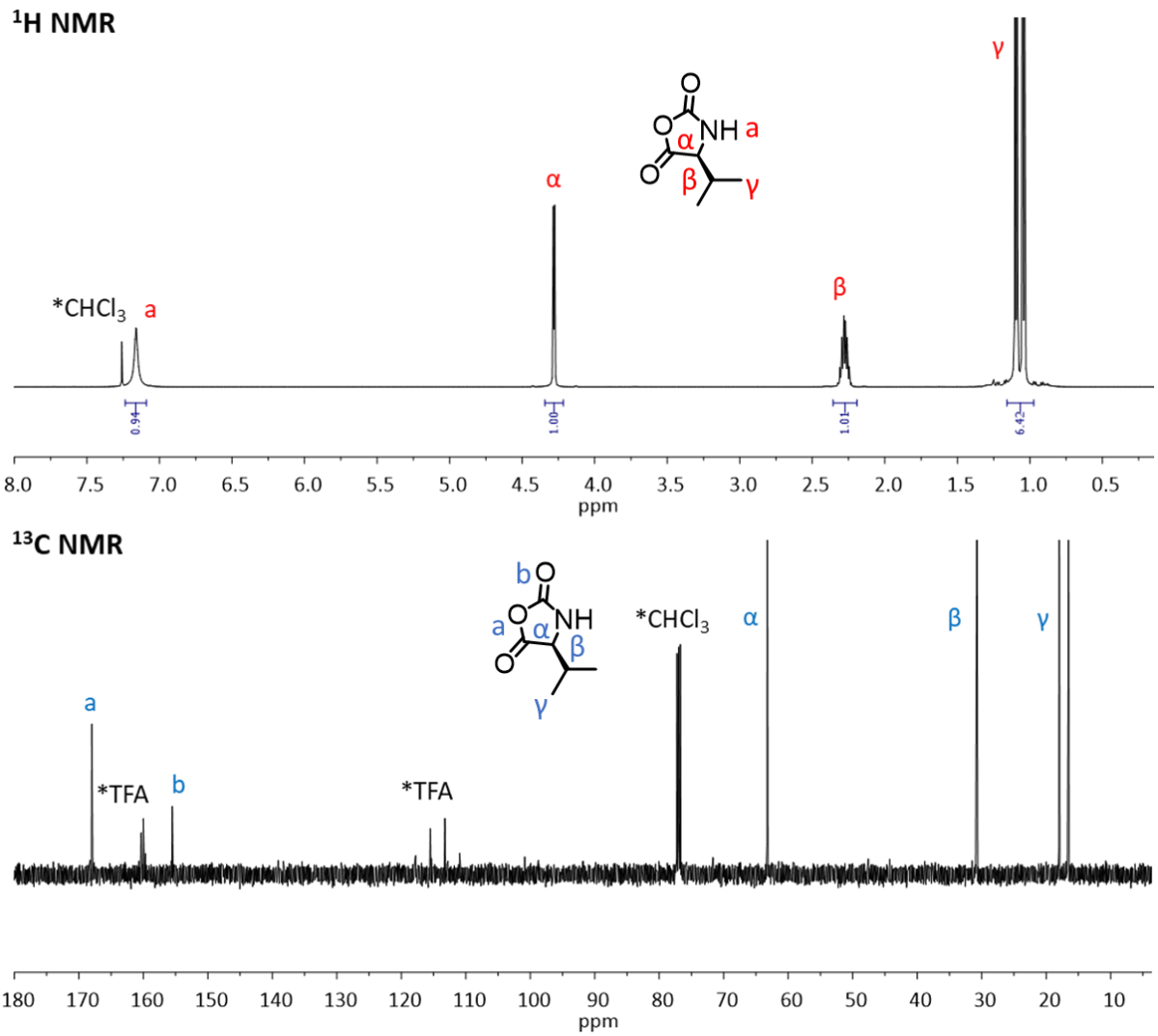


Figure A6: $^{1}H$ NMR and $^{13}C$ NMR spectra of *l*-valine *N*-carboxyanhydride (LV NCA) in $CDCl_3$.

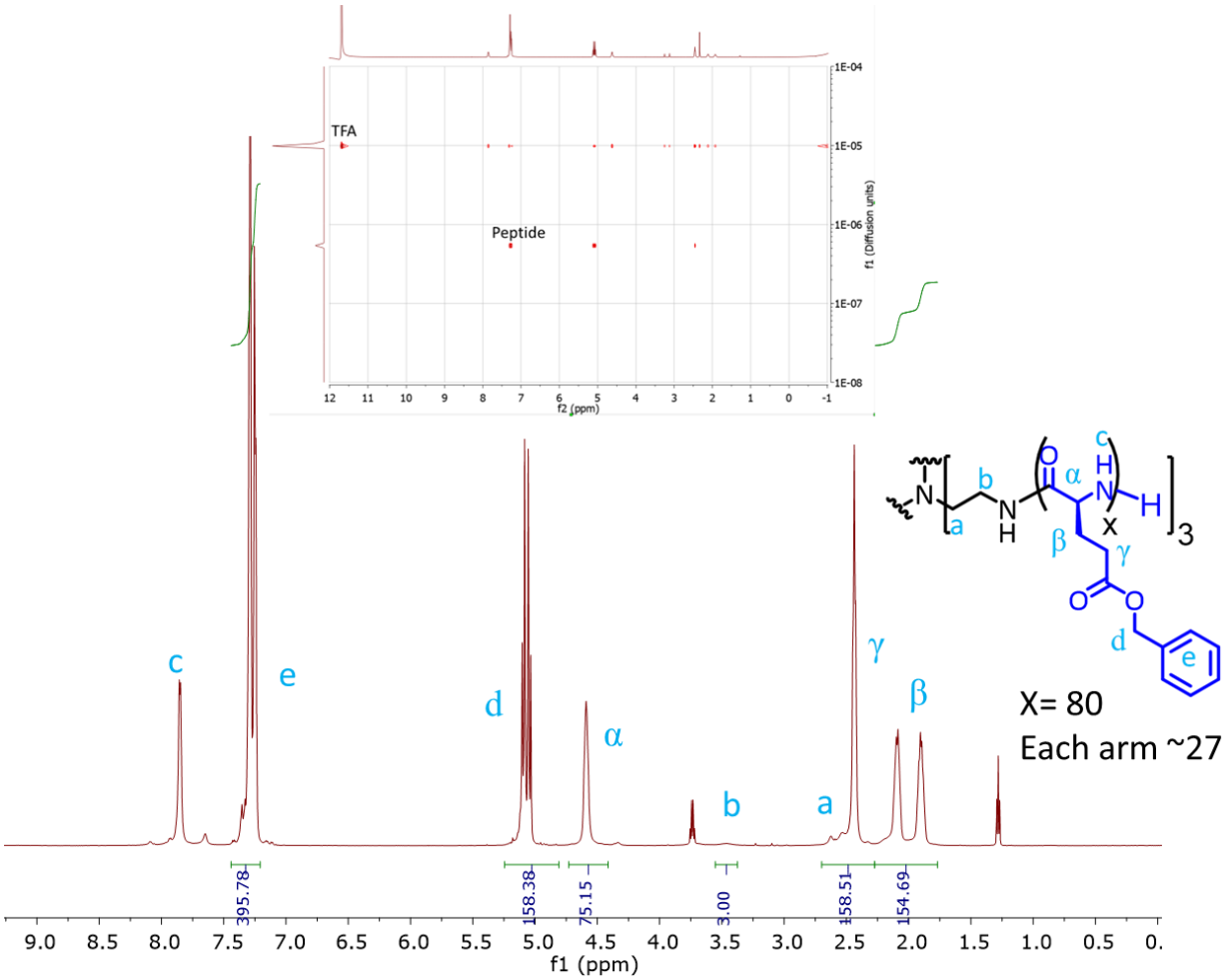


Figure A7: $^{1}H$ NMR spectra of homopolypeptide (3-PBLG$_{80}$) and DOSY in 15% TFA in $CDCl_3$.

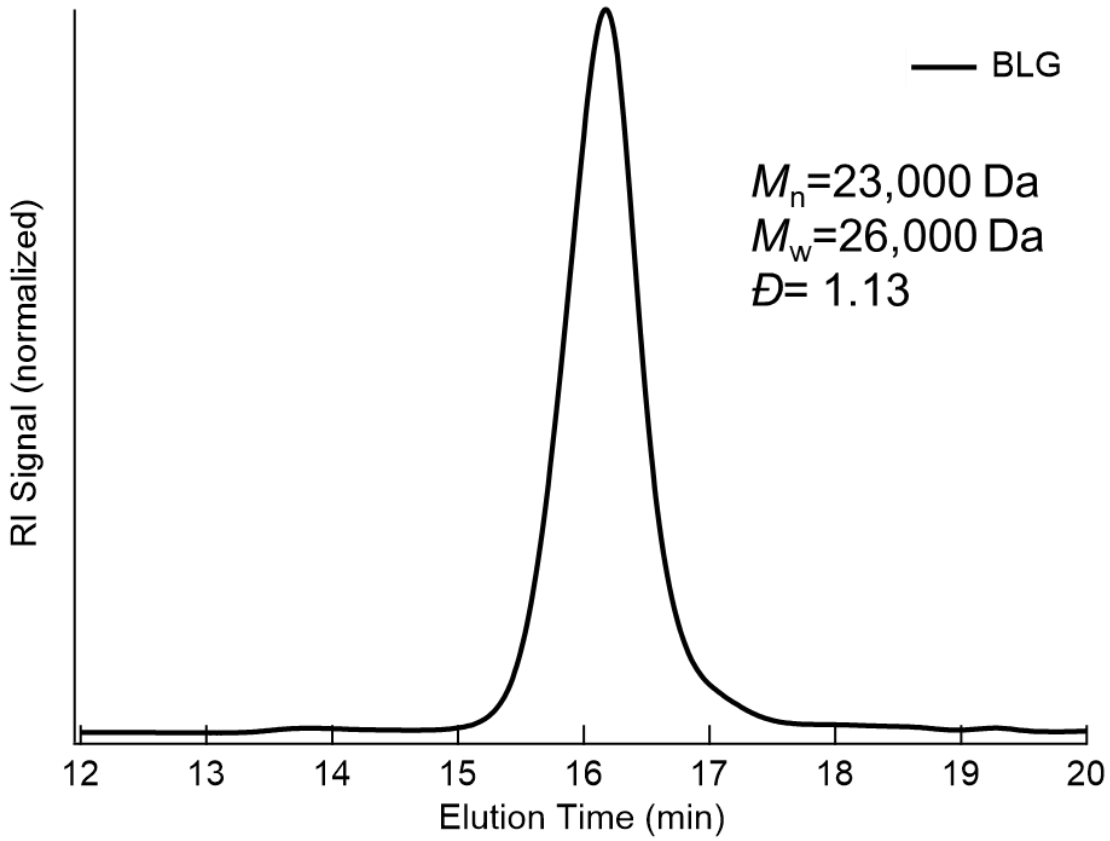


Figure A8: Size exclusion chromatography (SEC) trace of 3-PBLG$_{80}$ in HFIP.

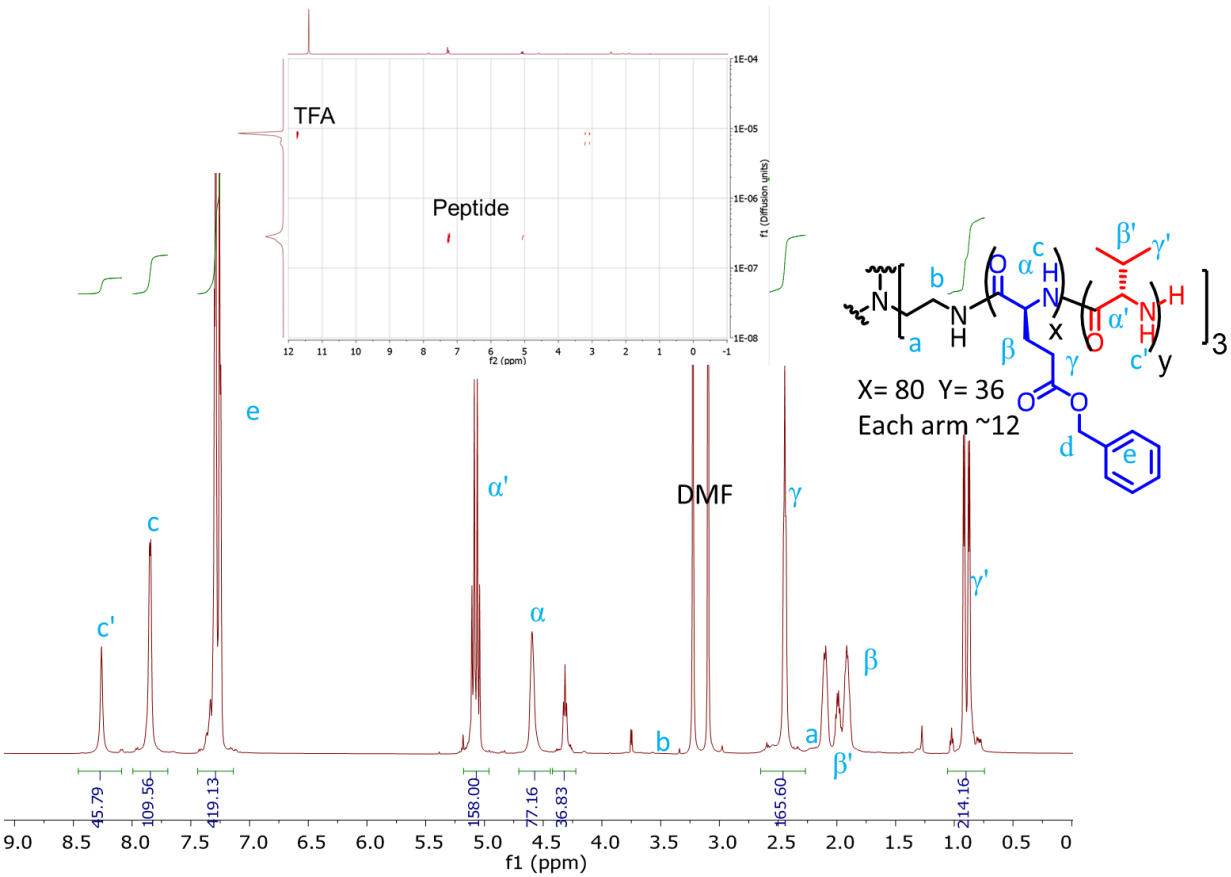


Figure A9: $^{1}H$ NMR spectra of 3- $PBLG_{80}$-b-$PLV_{36}$ (3-CP-V) and DOSY in 15% TFA in $CDCl_3$.

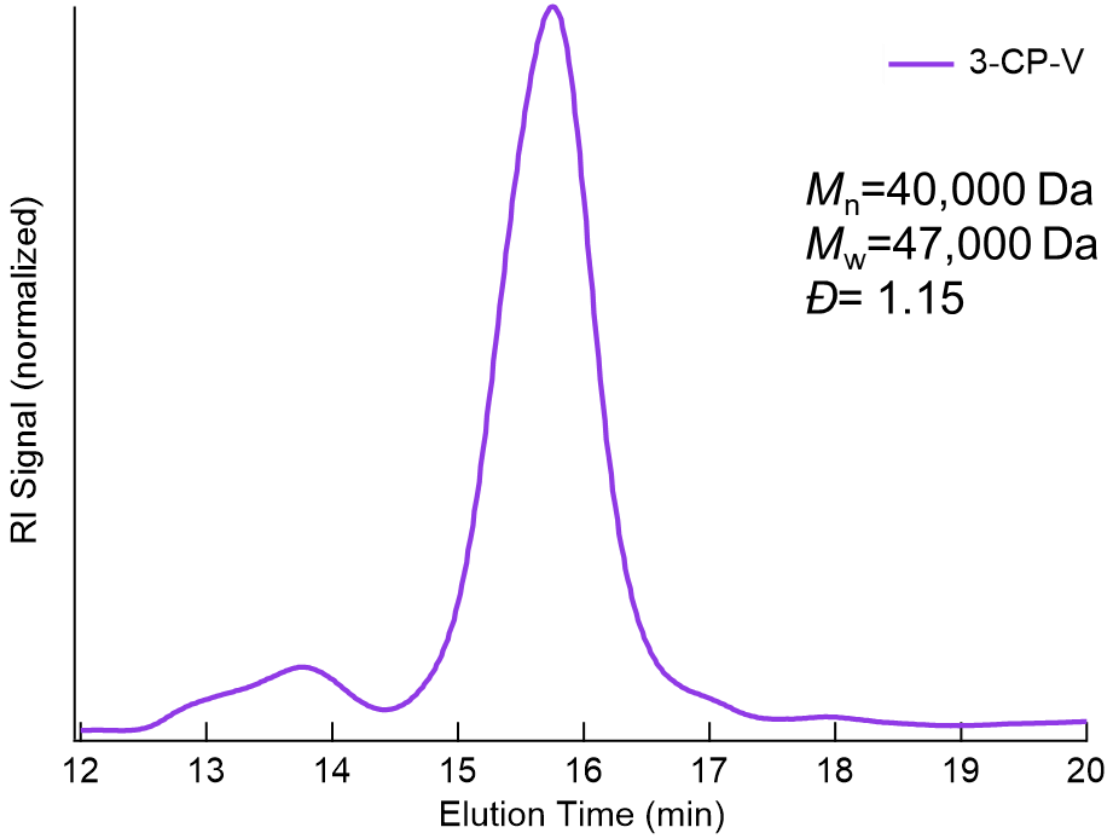


Figure A10: SEC of 3- $PBLG_{80}$-b-$PLV_{36}$ (3-CP-V) in HFIP.

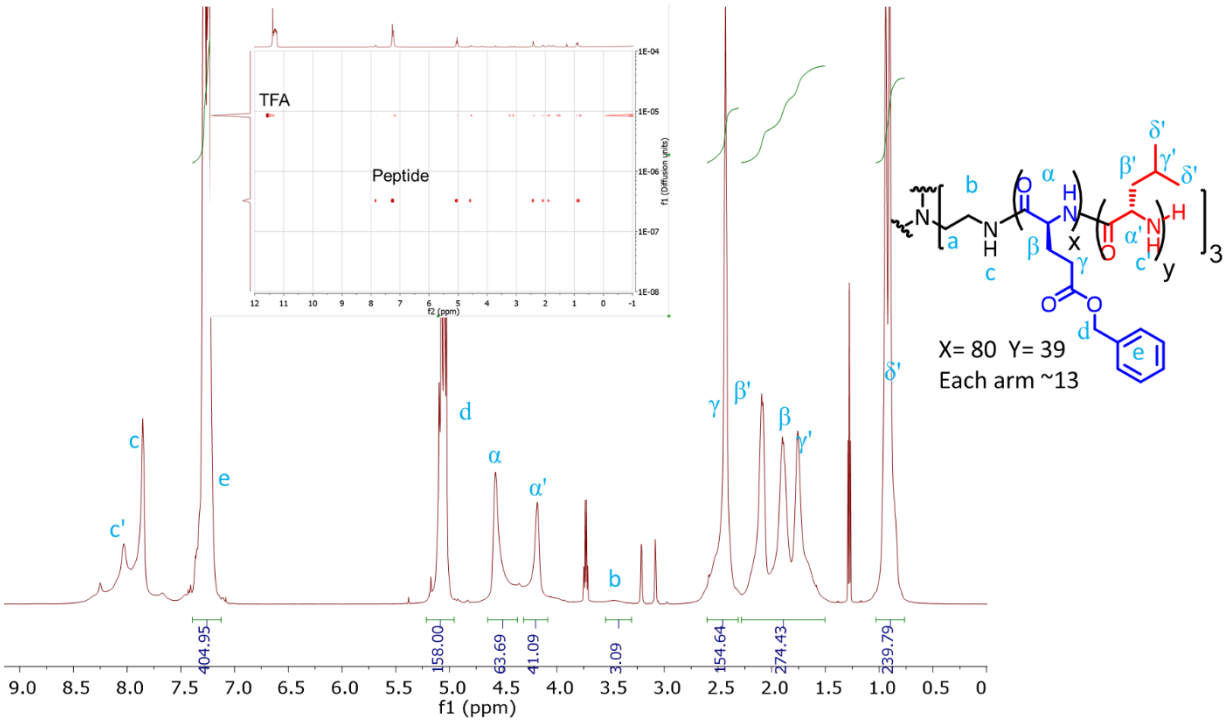


Figure A11: $^{1}$H NMR spectra of 3- PBLG$_{80}$-b-PLL$_{39}$ (3-CP-L) and DOSY in 15% TFA in $CDCl_3$.

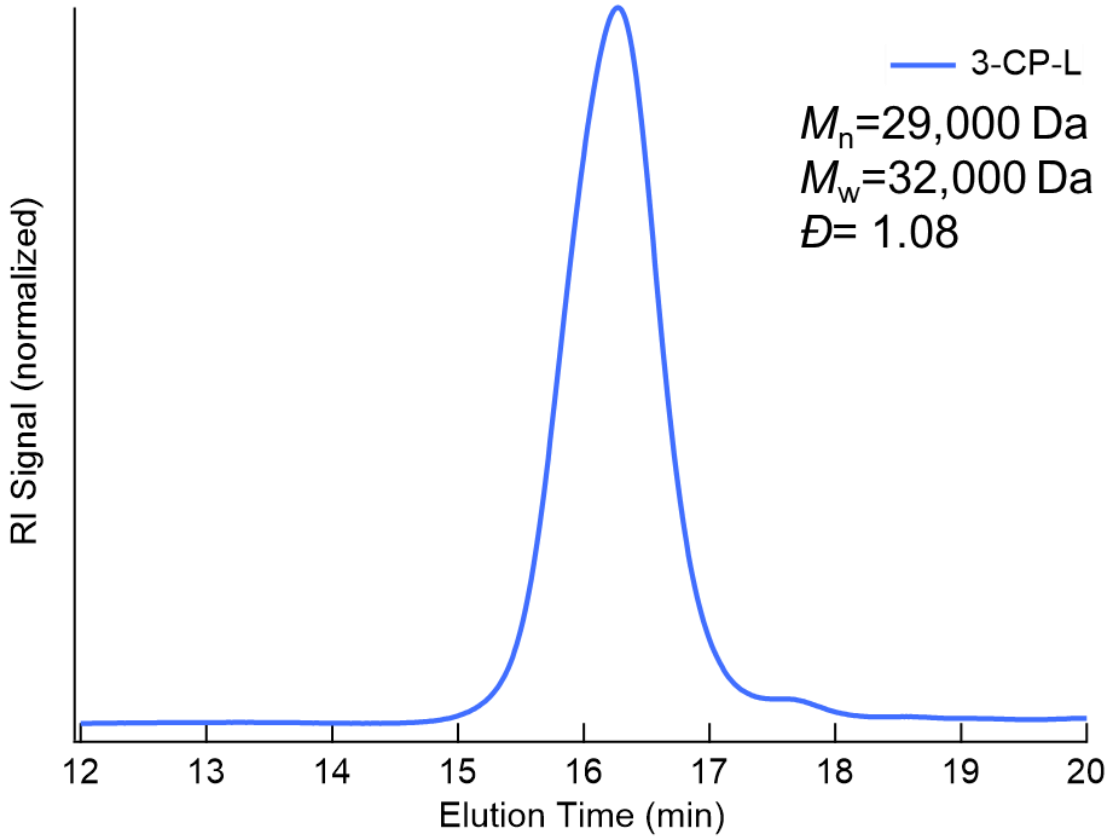


Figure A12: SEC of 3- $PBLG_{80}$-b-$PLL_{39}$ (3-CP-L) in HFIP.

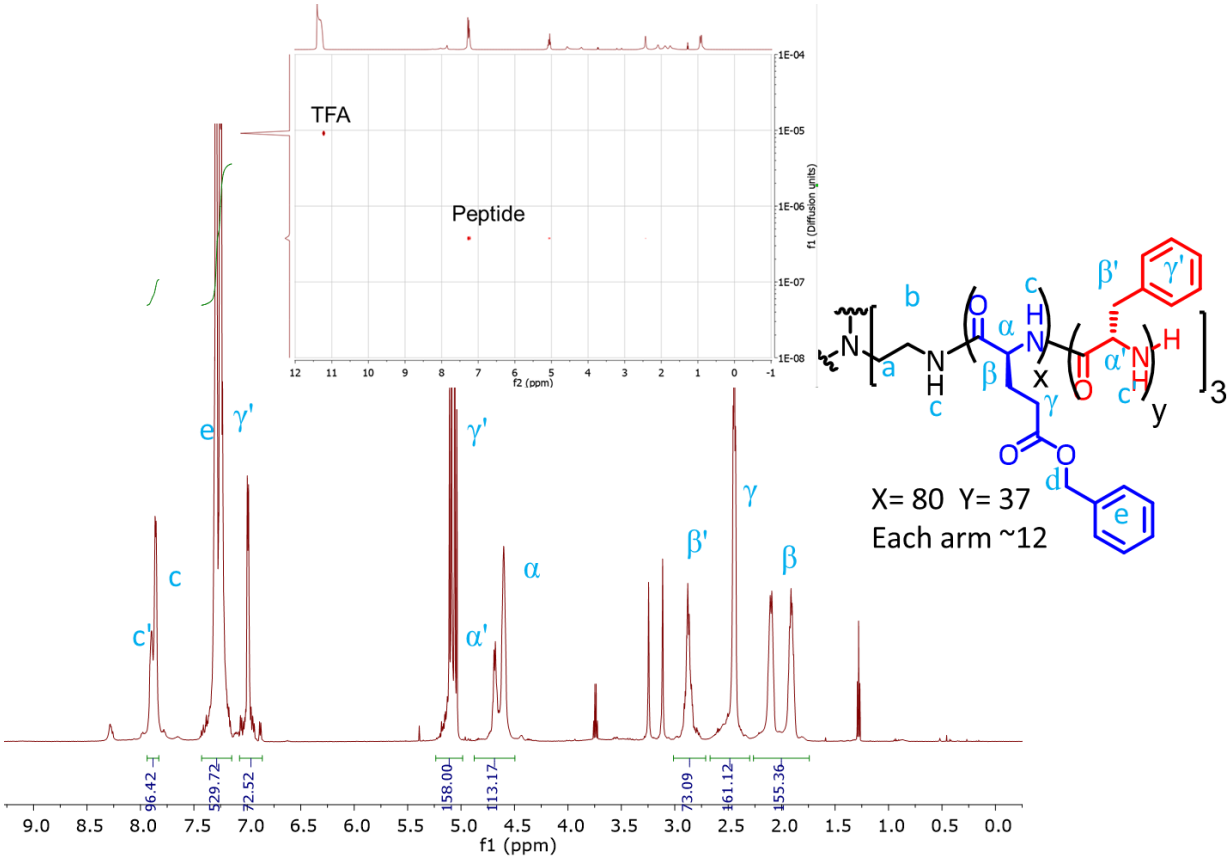


Figure A13: $^{1}H$ NMR spectra of 3- $PBLG_{80}$-b-$PLPA_{37}$ (3-CP-PA) and DOSY in 15% TFA in $CDCl_3$.

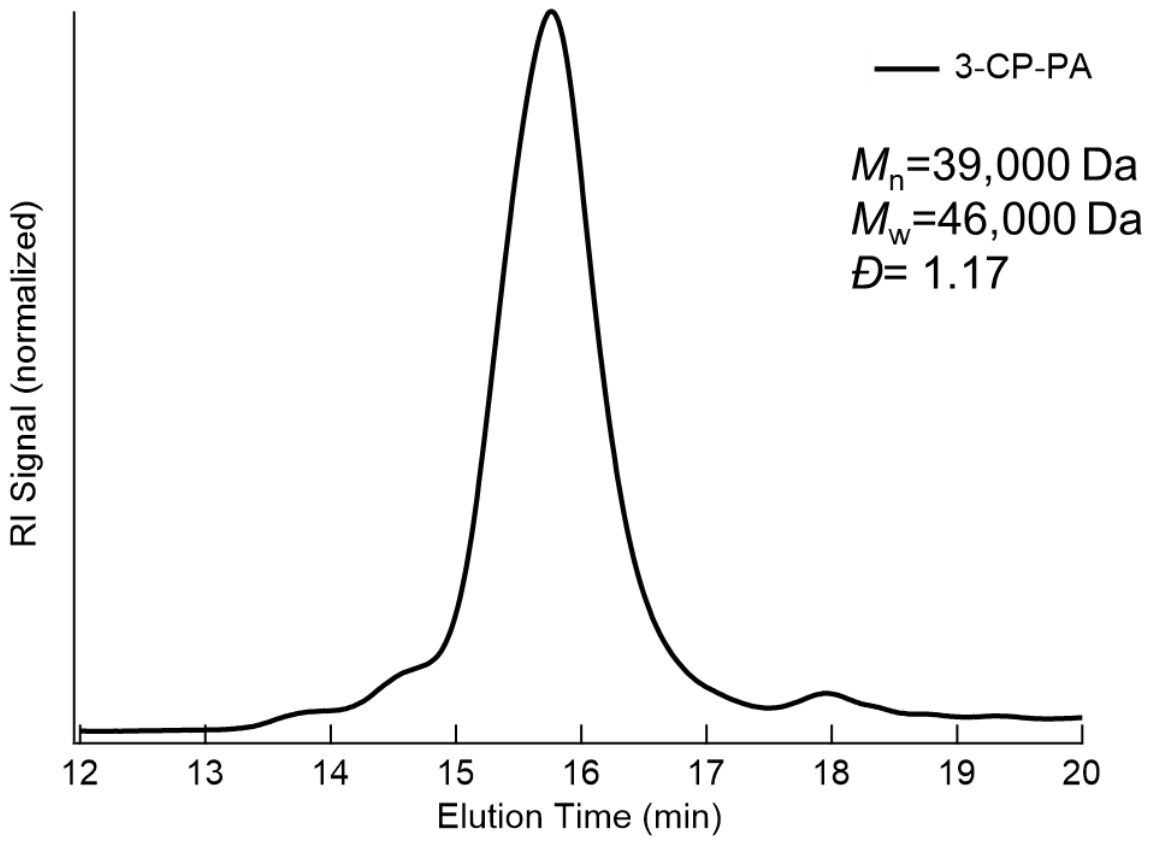


Figure A14: SEC of 3- $PBLG_{80}$-b-$PLPA_{37}$ (3-CP-PA) in HFIP.

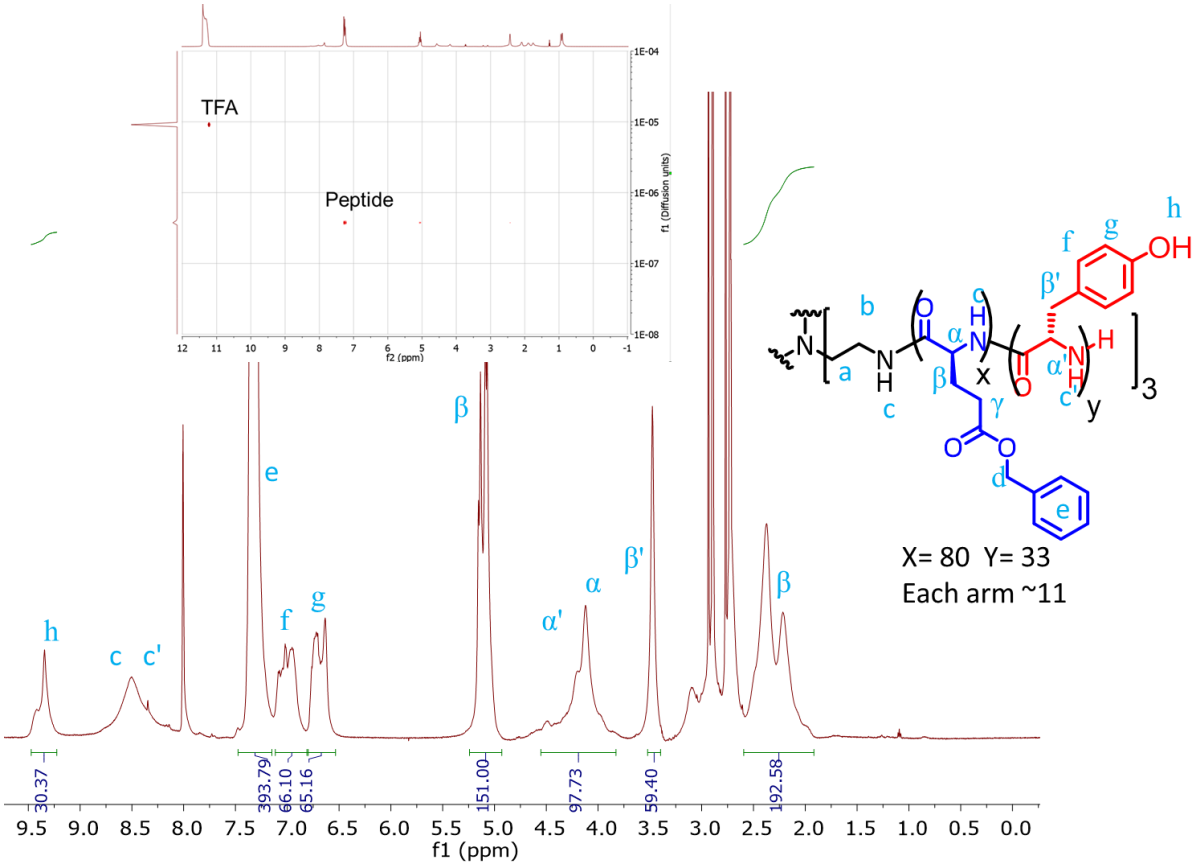


Figure A15: $^{1}H$ NMR spectra of 3- $PBLG_{80}$-b-$PLPA_{37}$ (3-CP-T) and DOSY in 15% TFA in $CDCl_3$.

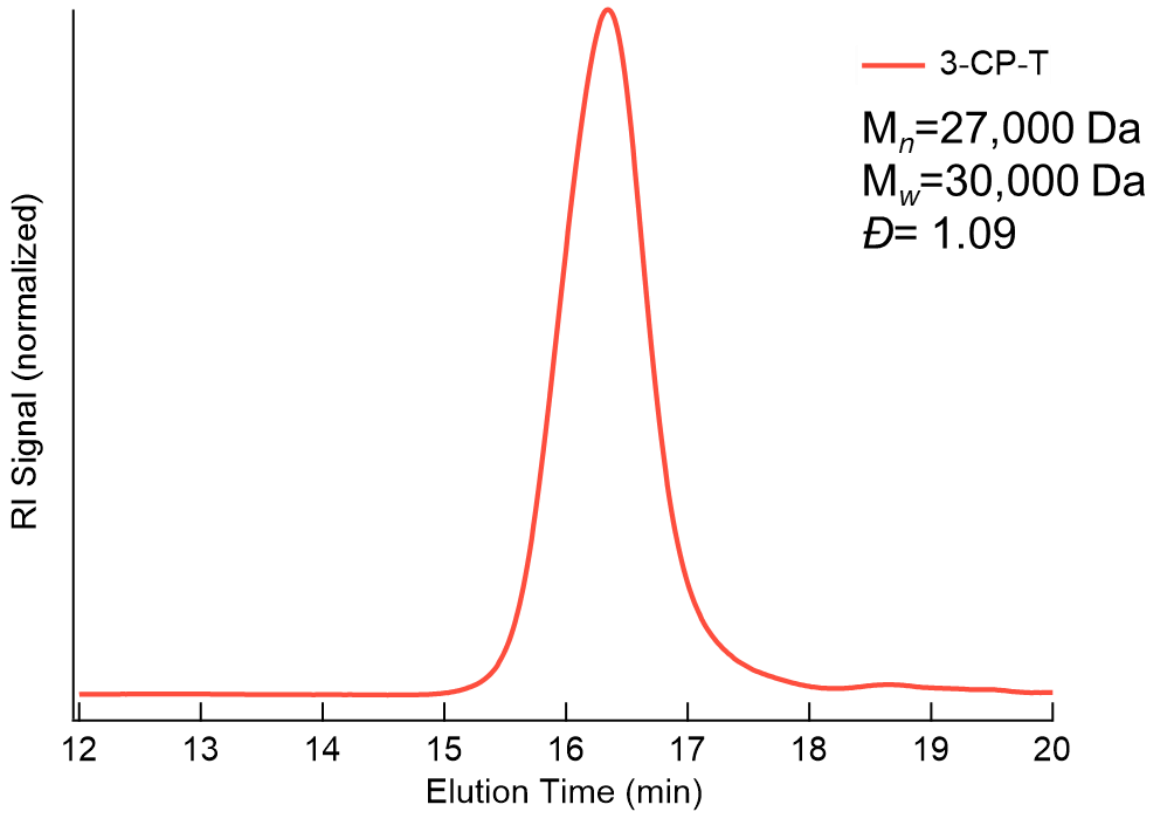


Figure A16: SEC of 3- $PBLG_{80}$-b-$PLPA_{37}$ (3-CP-T) in HFIP.

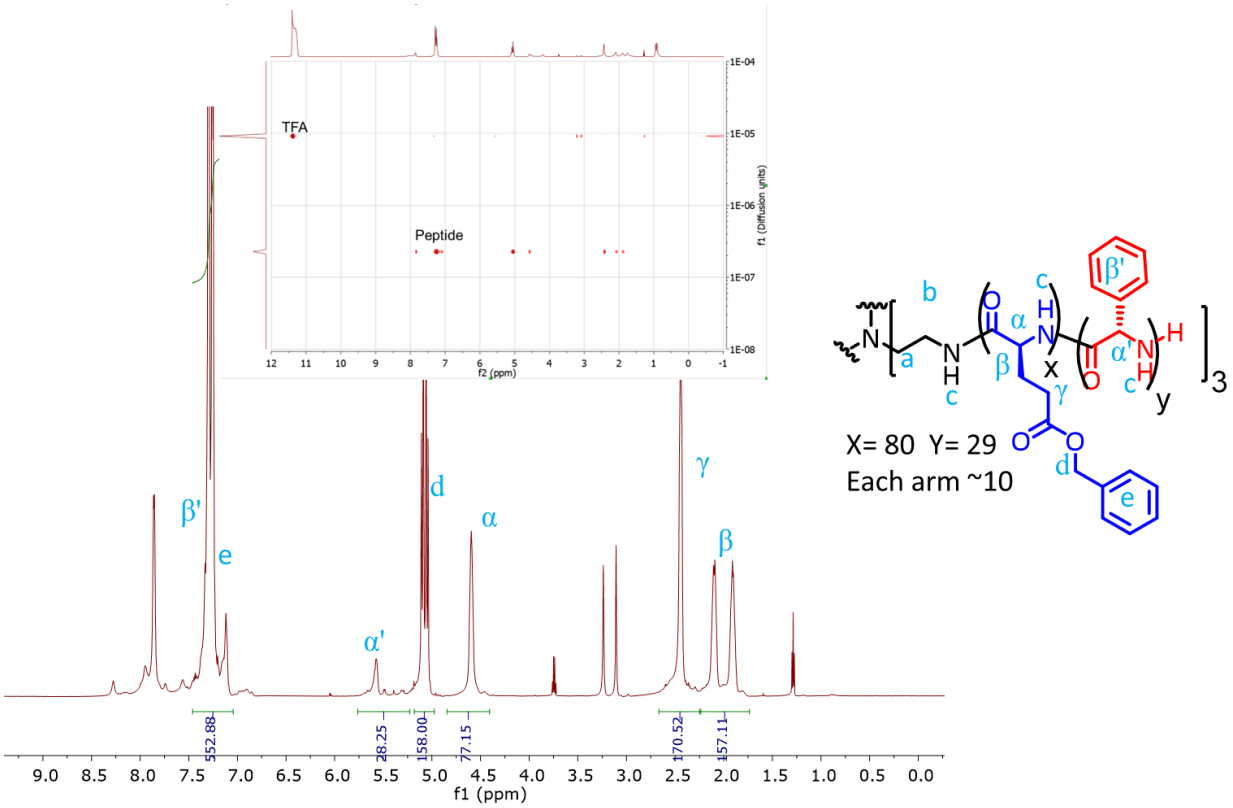


Figure A17: $^{1}H$ NMR spectra of 3- $PBLG_{80}$-b-$PPG_{29}$ (3-CP-PG) and DOSY in 15% TFA in $CDCl_3$.

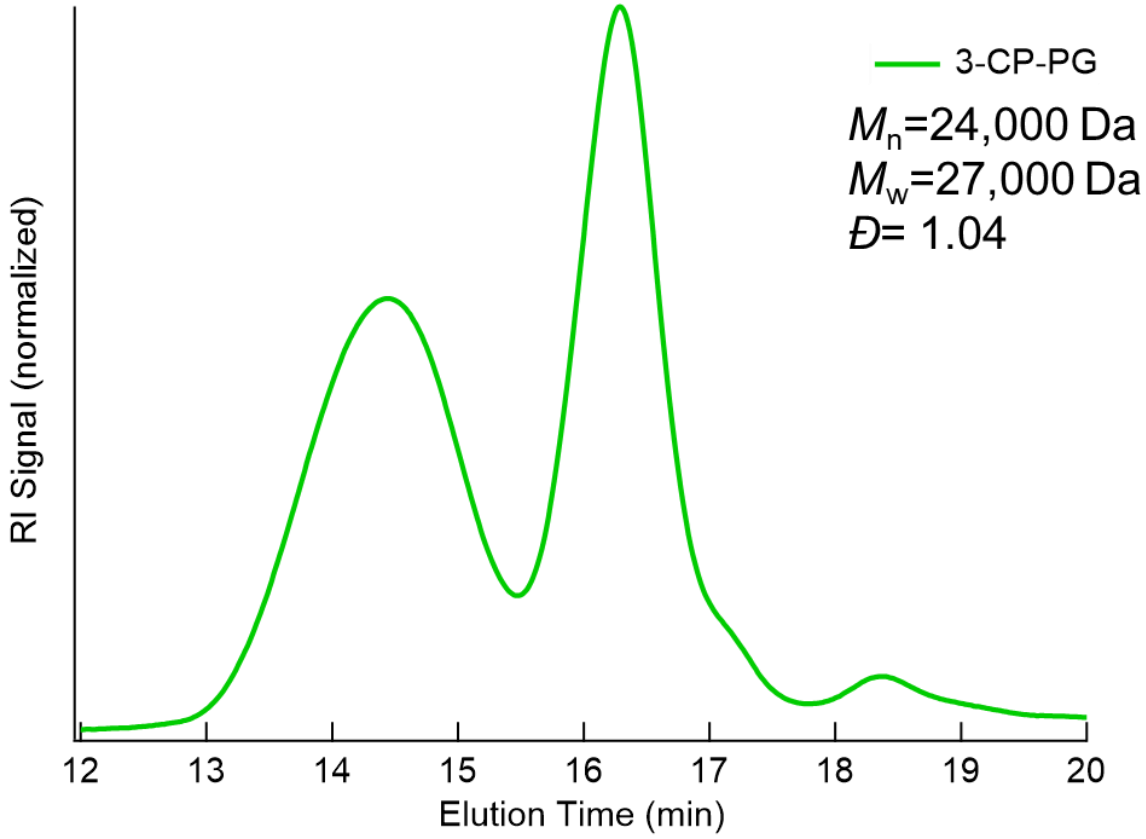


Figure A18: SEC of 3- $PBLG_{80}$-b-$PPG_{29}$ (3-CP-PG) with high molecular weight assemblies in HFIP.

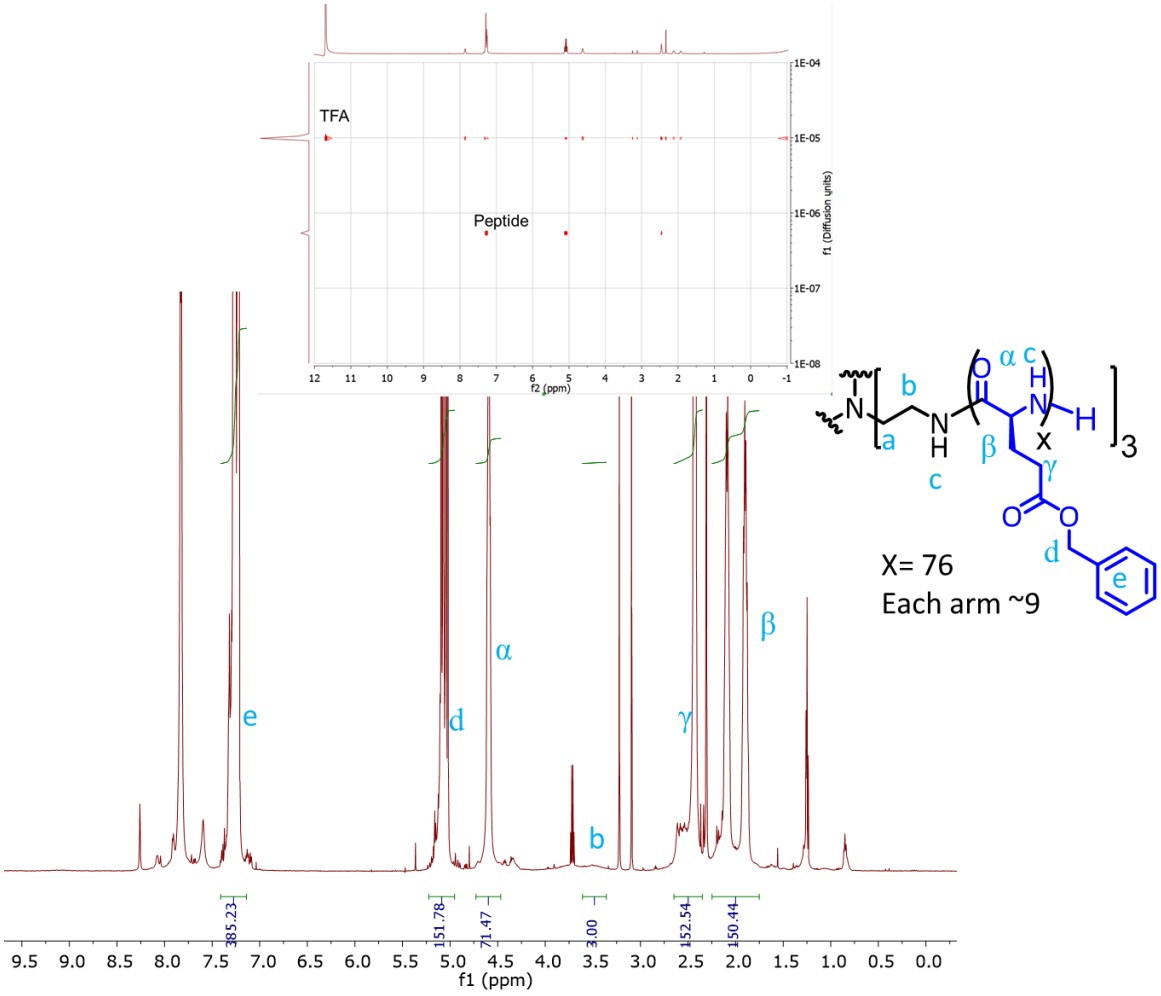


Figure A19: $^{1}H$ NMR spectra of 3- $PBLG_{76}$ and DOSY in 15% TFA in $CDCl_3$.

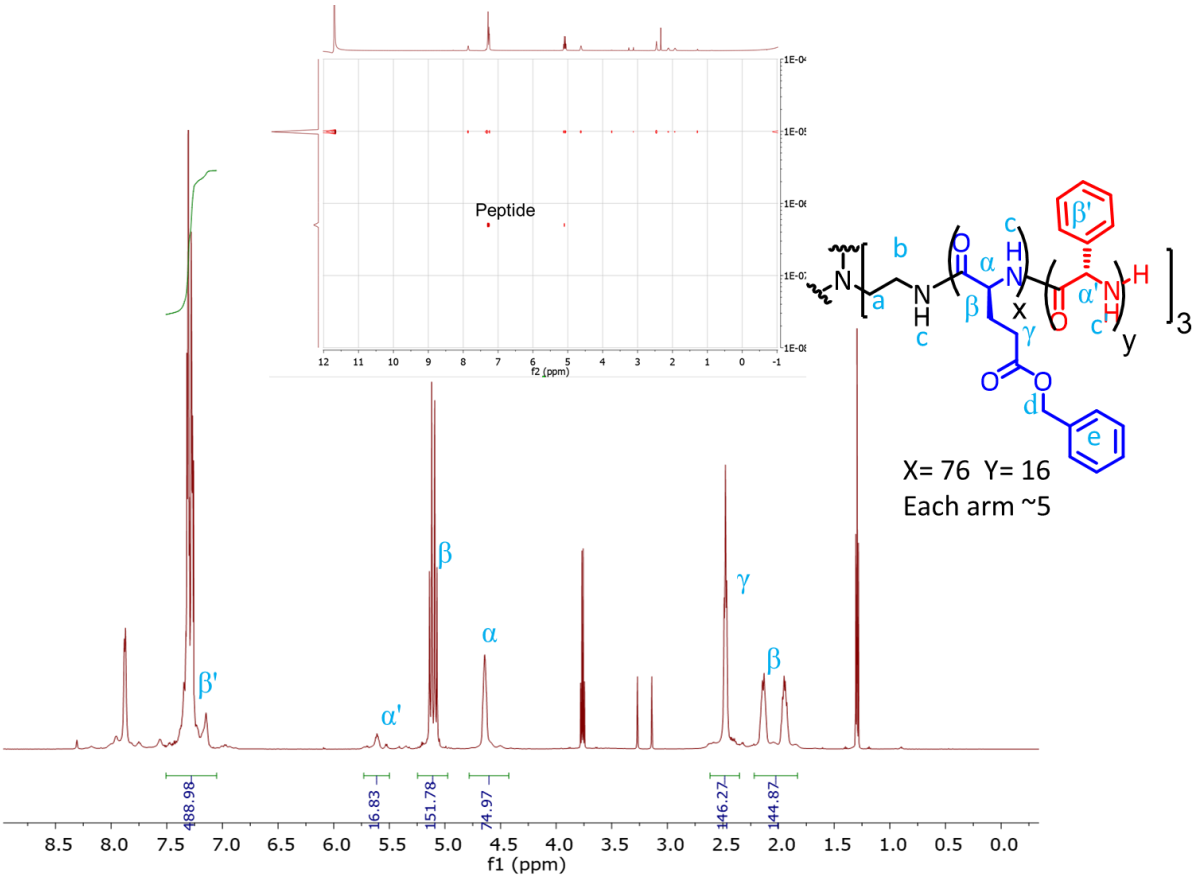


Figure A20: $^{1}H$ NMR spectra of 3- $PBLG_{76}$-b-$PPG_{16}$ (3-CP-PG-1) and DOSY in 15% TFA in $CDCl_3$.

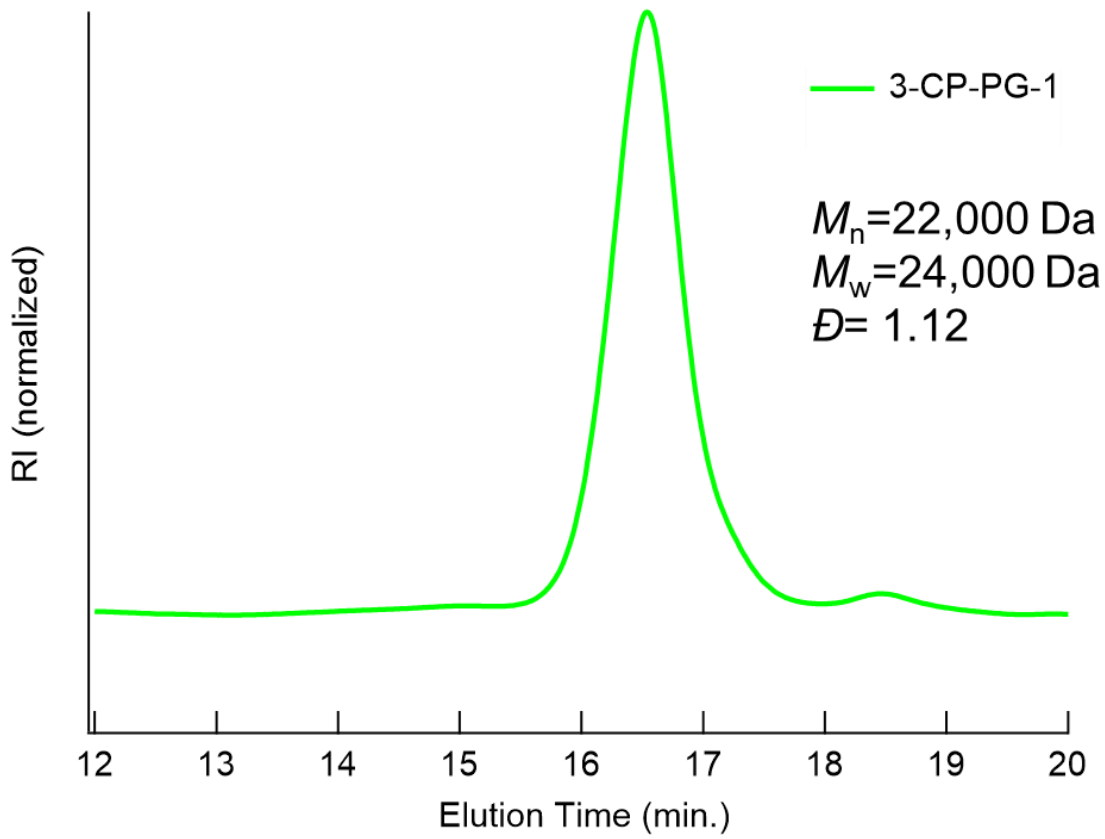


Figure A21: SEC of 3- $PBLG_{76}$-b-$PPG_{16}$ (3-CP-PG-1) in HFIP.

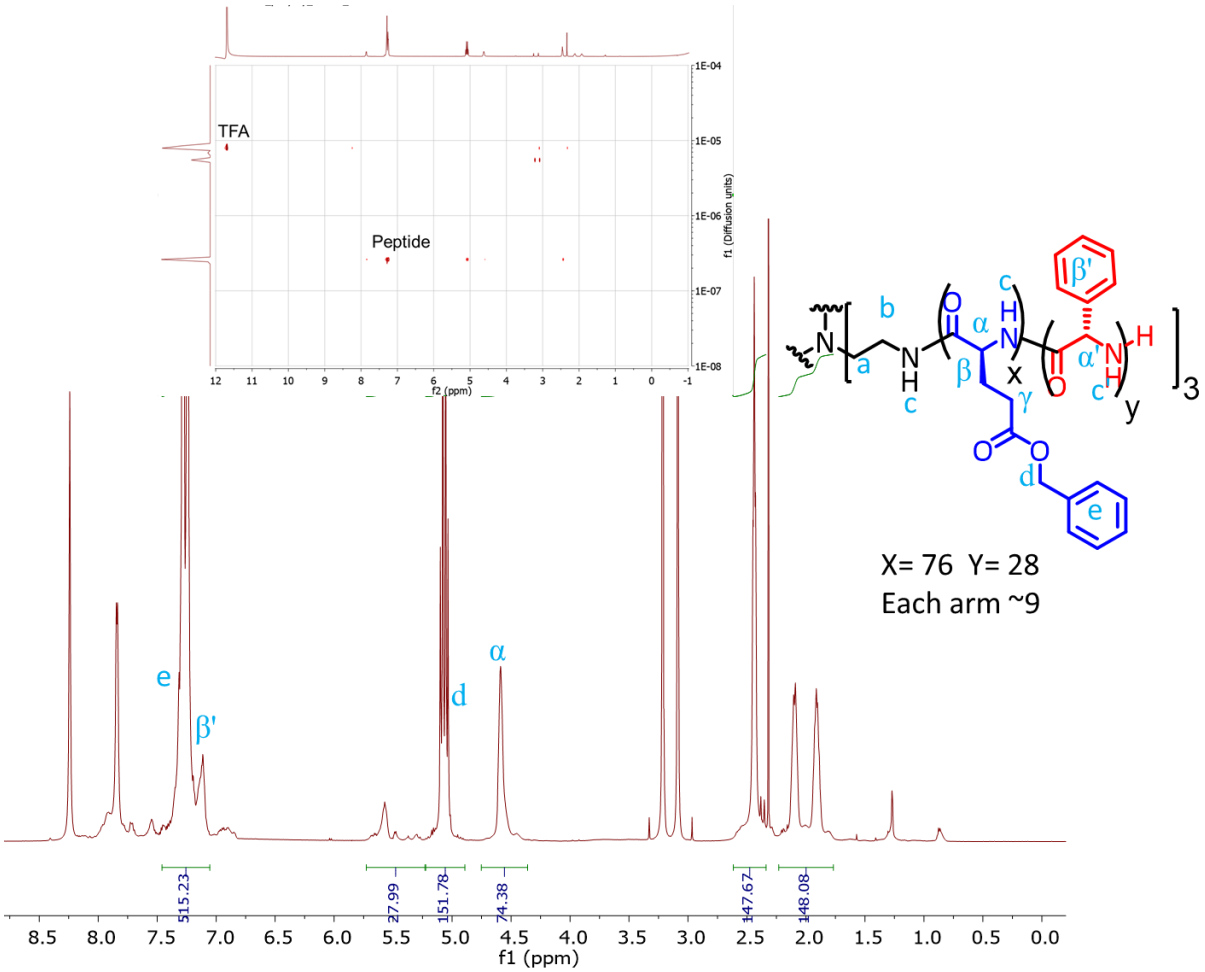


Figure A22: $^{1}$H NMR spectra of 3- PBLG$_{76}$-b-PPG$_{28}$ (3-CP-PG-2) and DOSY in 15% TFA in $CDCl_3$.

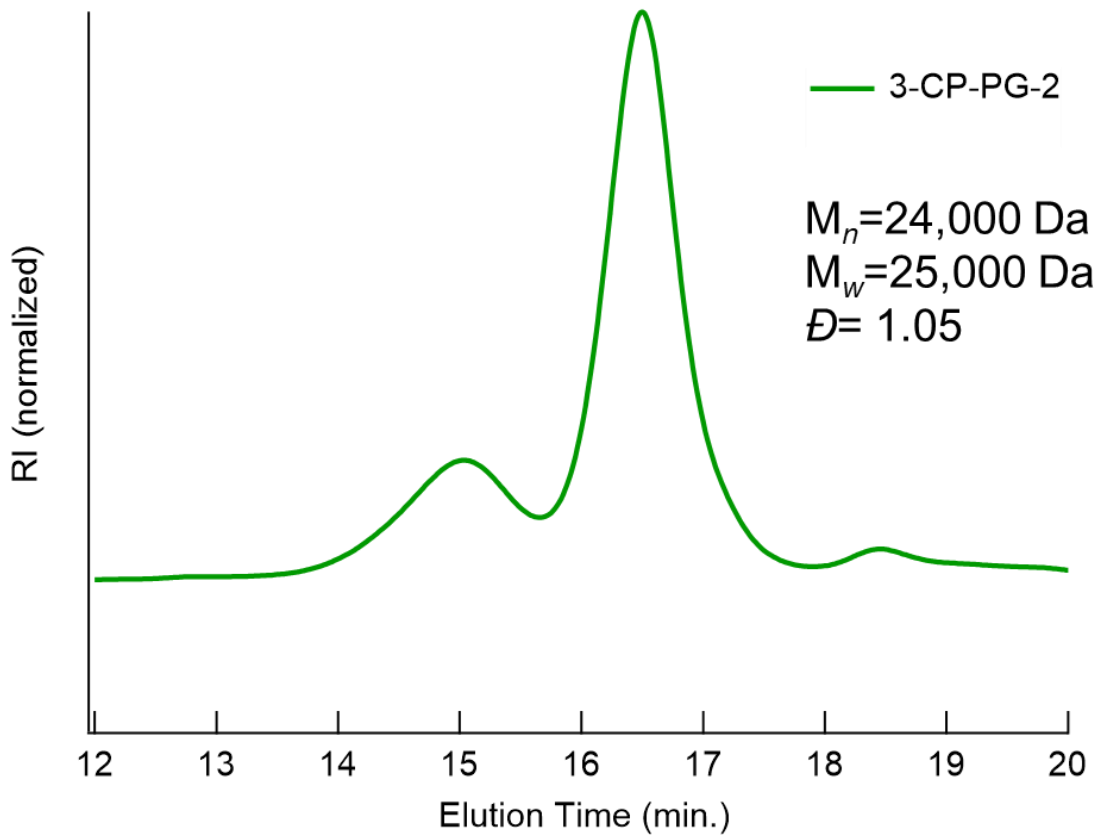


Figure A23: SEC of 3- $PBLG_{76}$-b-$PPG_{28}$ (3-CP-PG-2) with high molecular weight due to assemblies in HFIP.

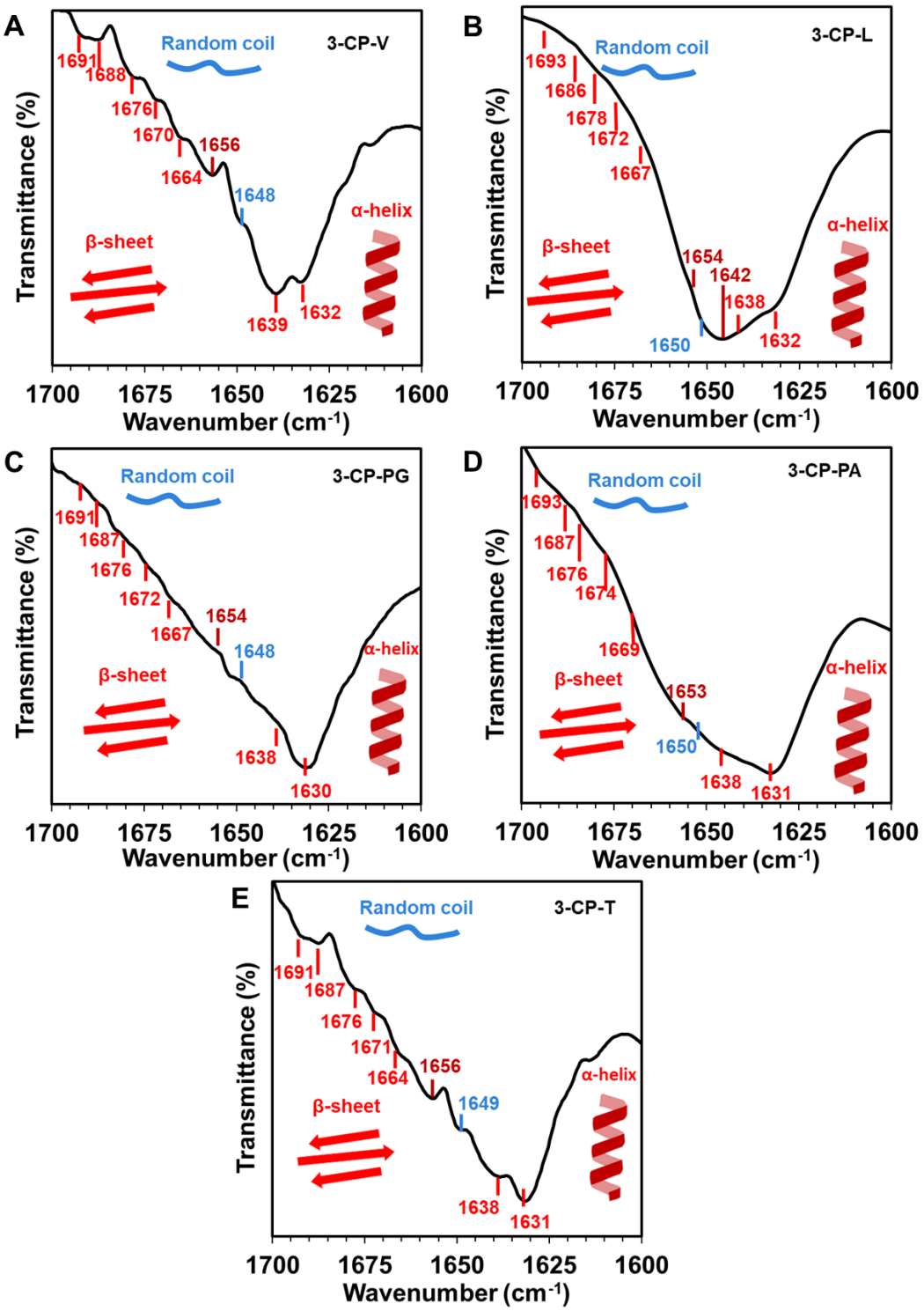


Figure A24: FTIR spectra showing secondary structures of (A) 3-CP-V, (B) 3-CP-L, (C) 3-CP-PG, (D) 3-CP-PA, and (E) 3-CP-T physical hydrogels in $D_2O$.

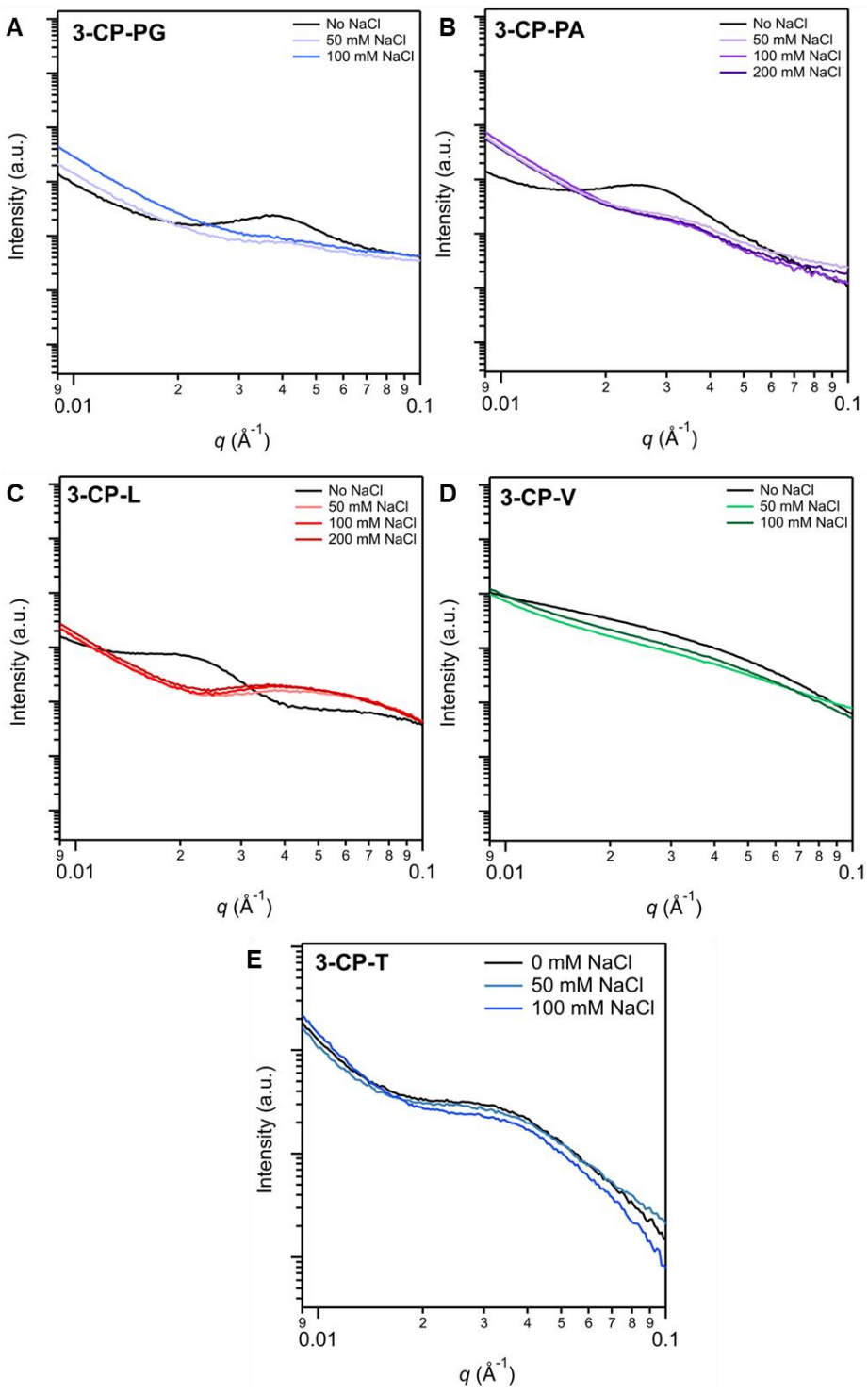


Figure A25: SAXS of 40 wt% of (A) 3-CP-PG, (B) 3-CP-PA, (C) 3-CP-L, (D) 3-CP-V, and (E) 3-CP-T in various aqueous solution.

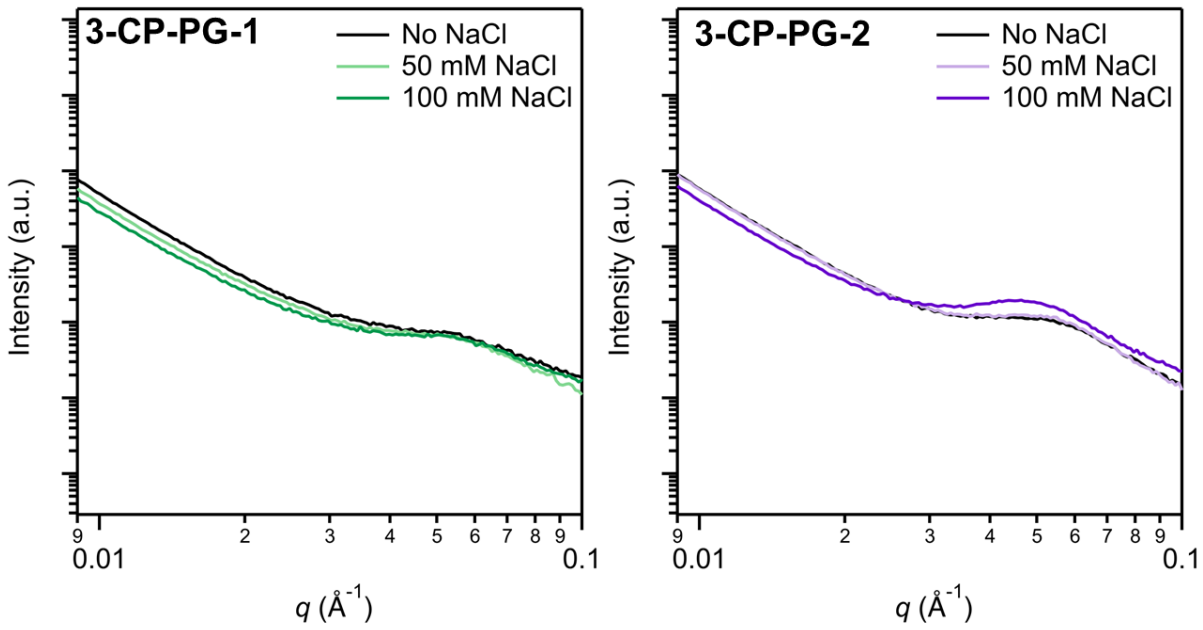


Figure A26: SAXS of 40 wt% of 3-CP-PG-1 and 3-CP-PG-2 in various aqueous solution.

$\varepsilon = 2\pi/q^*$

$\varepsilon$=interdomain spacing, $q^*$= scattering wave vector

Equation A1: interdomain spacing equation based on SAXS data.

| Sample | q(Å) | ε (nm) |
|---|---|---|
| 3-CP-T | 0.016 | 40.4 |
| 3-CP-L | 0.019 | 33.0 |
| 3-CP-V | N/A | N/A |
| 3-CP-PA | 0.019 | 33 |
| 3-CP-PG | 0.027 | 23.0 |
| 3-CP-PG-1 | 0.04 | 16.0 |
| 3-CP-PG-2 | 0.03 | 21.0 |

Table A1: Interdomain spacing calculation based on SAXS of 40wt% hydrogel.

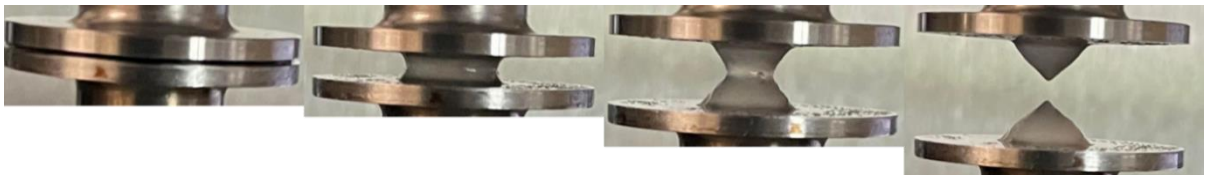

Figure A27: Time lapse images of 20wt% hydrogel capillary thinning and breakup between parallel plates.

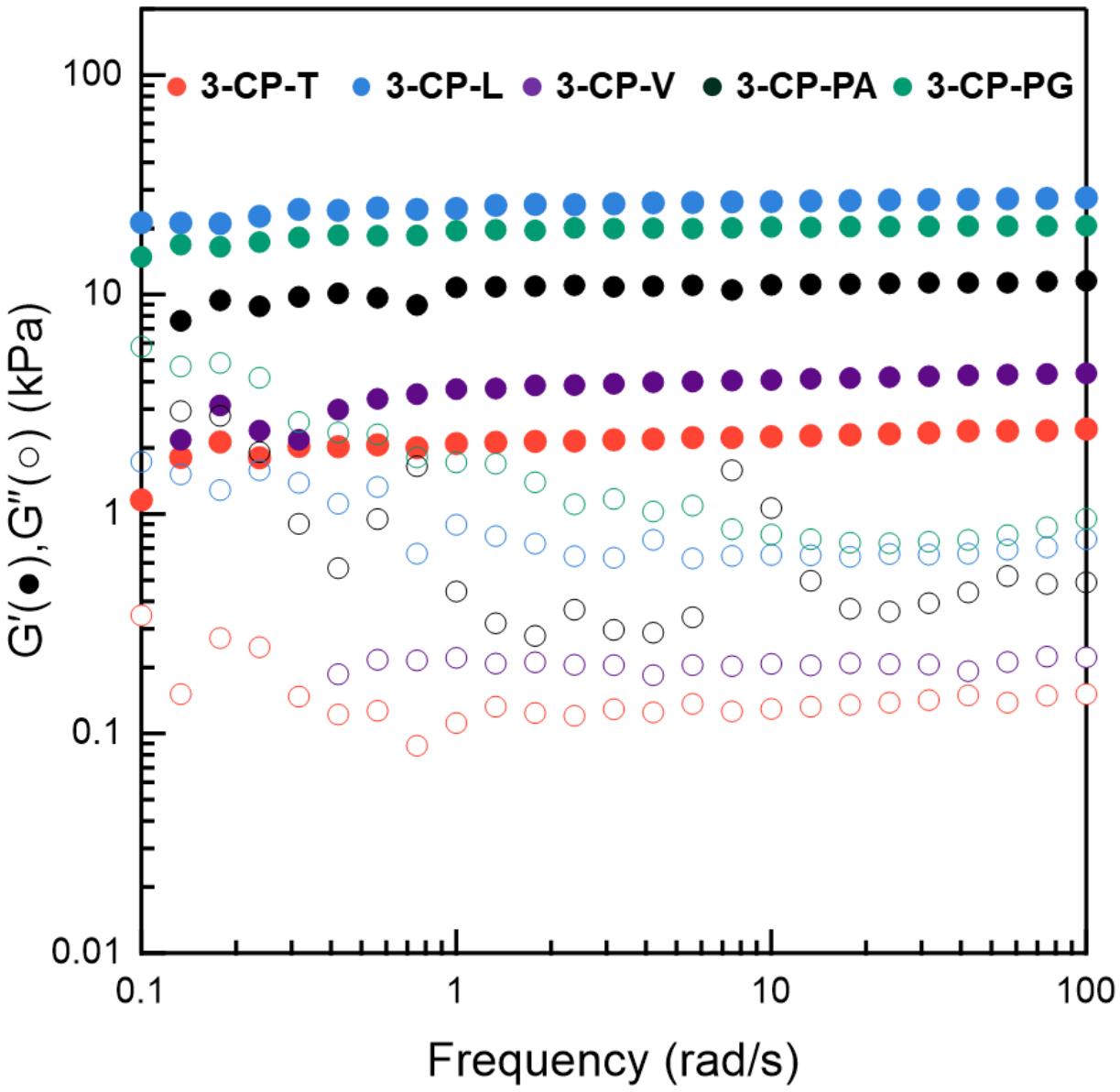


Figure A28: Frequency sweep of 20 wt% (green) 3-CP-PG, (blue) 3-CP-L, (purple) 3-CP-V, (black) 3-CP-PA, and (pink) 3-CP-T hydrogels at 0.1% strain.

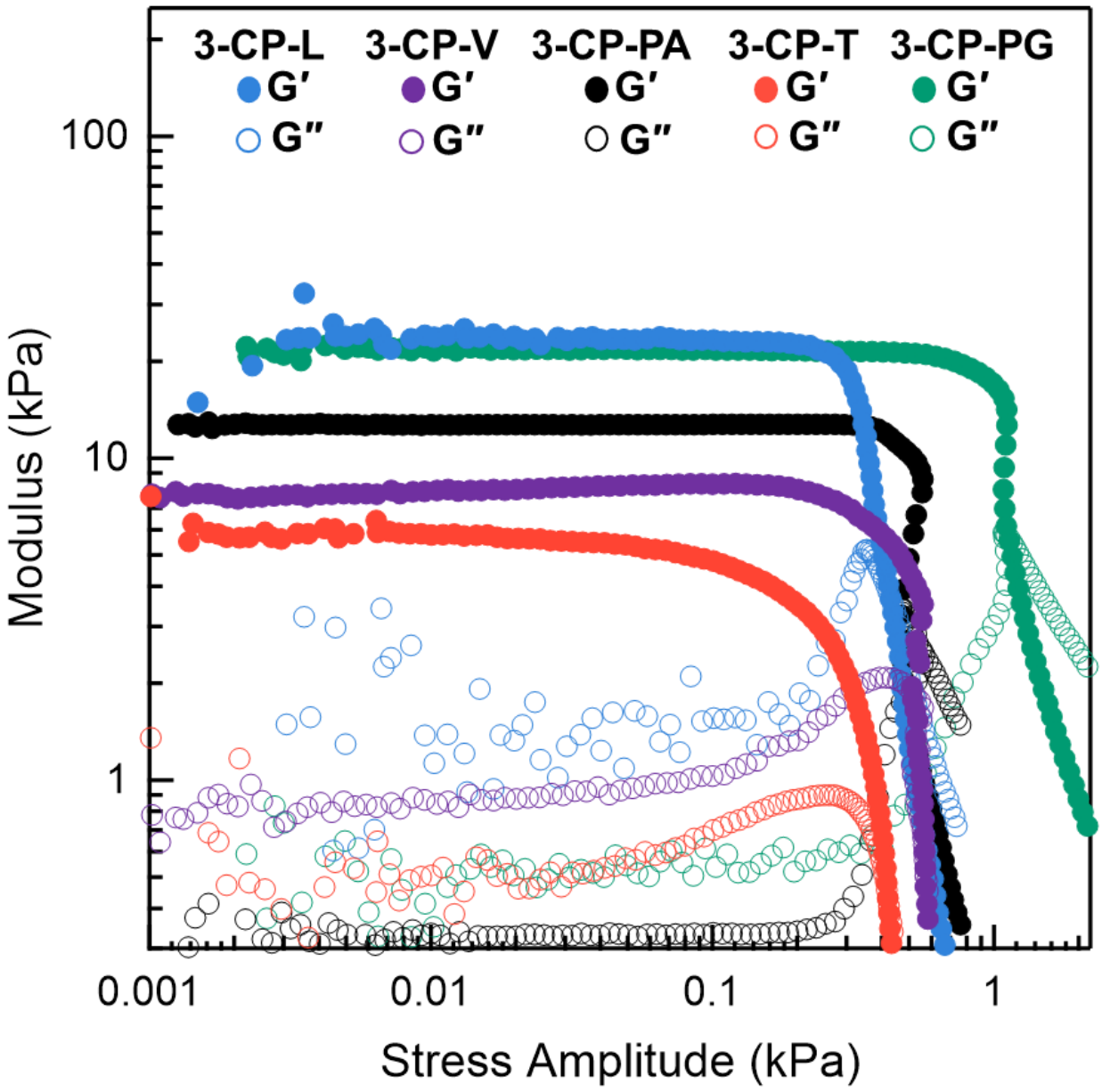


Figure A29: Stress amplitude sweep of 20 wt% (green) 3-CP-PG, (blue) 3-CP-L, (purple) 3-CP-V, (black) 3-CP-PA, and (pink) 3-CP-T hydrogels at 6.2 rad/s.

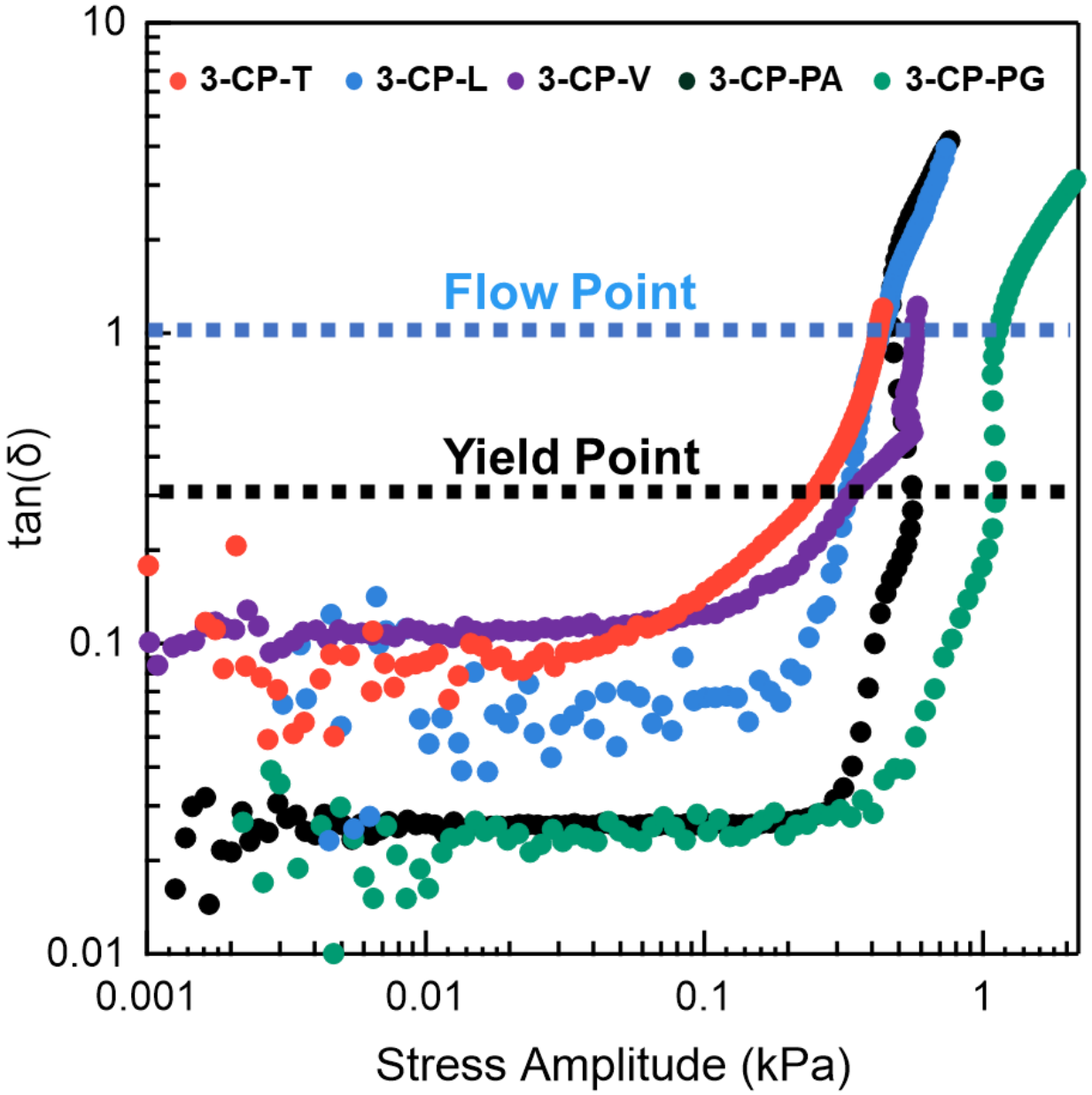


Figure A30: tan δ of amplitude sweep of 20wt% hydrogel with flow and yield point marked with a dash arrow.

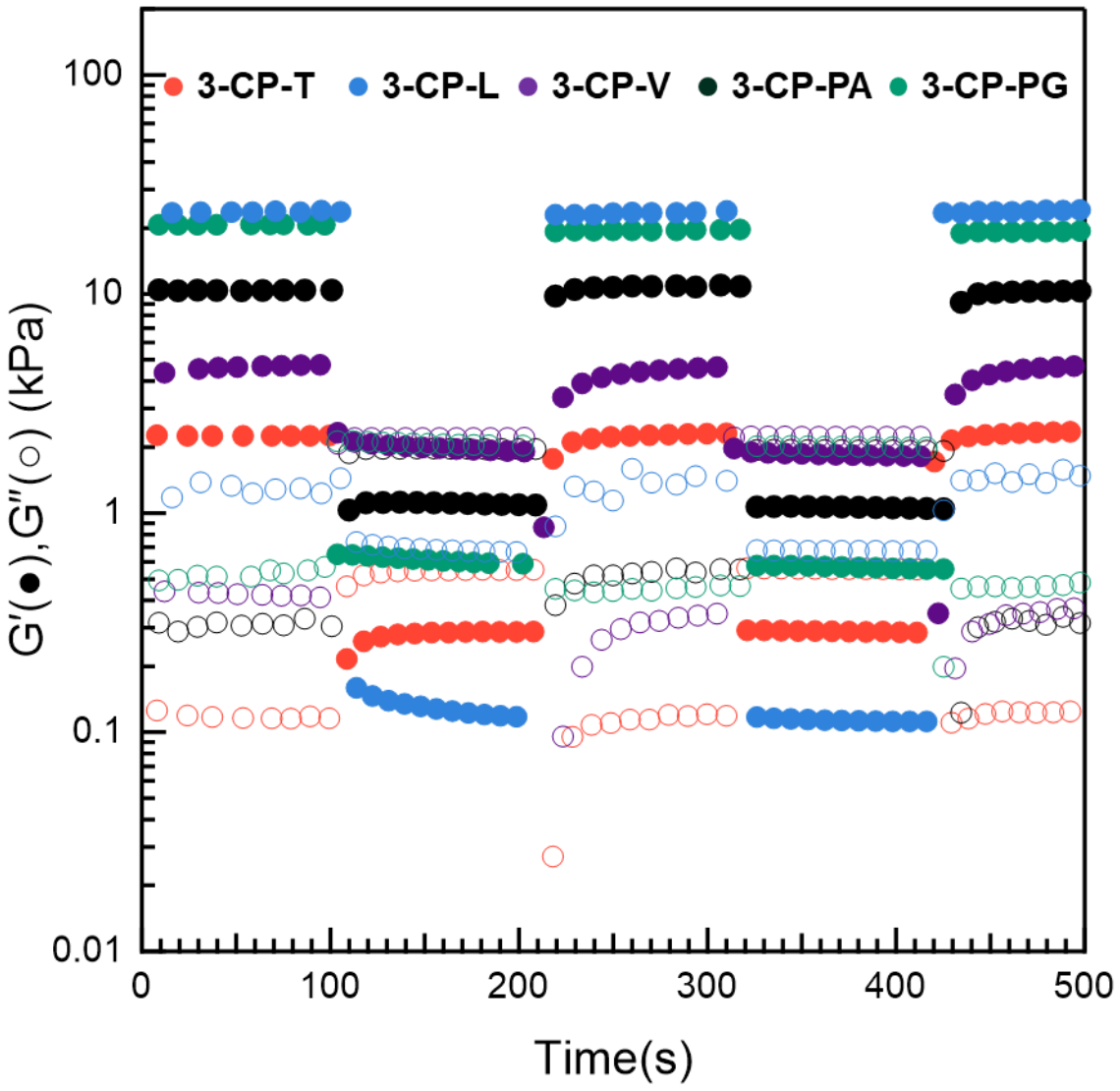


Figure A31: Cyclic dynamic time sweep of 20wt% (green) 3-CP-PG, (blue) 3-CP-L, (purple) 3-CP-V, (black) 3-CP-PA, and (pink) 3-CP-T hydrogels at 6.2 rad/s with 100 s interval of 0.1% strain and 100% strain.

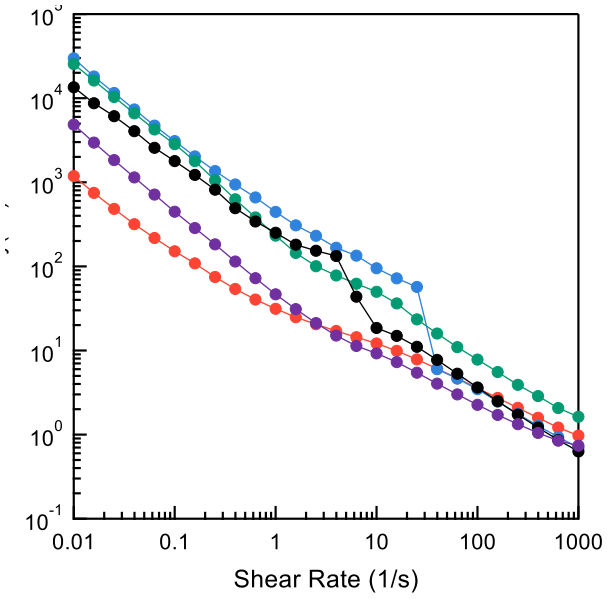


Figure A32: Continuous flow shear rheology of 20wt% (green) 3-CP-PG, (blue) 3-CP-L, (purple) 3-CP-V, (black) 3-CP-PA, and (pink) 3-CP-T hydrogels.

$$C = \frac{4\pi A}{L^2}$$

C= circularity, A= area, L=parameter

Equation A2: Formula for Circularity of a circle[1]

$$P_r = \frac{\sqrt{3}\pi}{9} \cdot \frac{1}{C} = \frac{\sqrt{3}}{36} \cdot \frac{L^2}{A}$$

$P_r$=Printability, C= circularity, A= area, L=parameter

Equation A3: Formula for printability of an equilateral triangle [1]

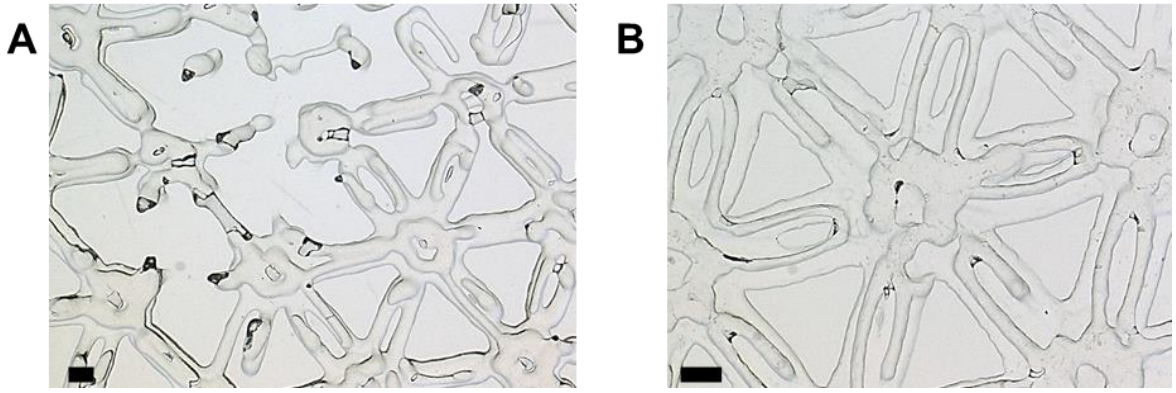


Figure A33: Microscopy images of (left) 3-CP-T extruded at 40 kPa and (right) 3-CP-PG extruded at 170 kPa through 27 G needle (scale bar: 500 µm).

**References**

[1] Ouyang, L.; Yao, R.; Zhao, Y.; Sun, W. Effect of Bioink Properties on Printability and Cell Viability for 3D Bioplotting of Embryonic Stem Cells. *Biofabrication* **2016**, *8*, 035020.

# Appendix B: Supporting Information for Chapter 3

## Materials

All chemicals were obtained from Sigma Aldrich unless otherwise noted. L-Glutamic acid 5-benzyl ester (or γ-benzyl-L-glutamate) was purchased Carbosynth. L-tyrosine, 4-(4,6-Dimethoxy-1,3,5-triazin-2-yl)-4-methylmorpholinium chloride (DMT-MM), trifluoroacetic acid (TFA) was purchased from Fisher Scientific. Triphosgene was purchased from Oakwood Chemical. Isopropyl ß-D-1-thiogalactopyranoside and a 3.5 kDa MWCO SnakeSkin® membrane were purchased from Thermo Fisher Scientific.

## Methods

$^{1}$H NMR and DOSY NMR spectra were acquired on a Varian Unity Inova A S600 600MHz using CDCl3/TFA and DMSO-d6 as solvents. $^{13}$C NMR spectra were acquired on a Varian Unity Inova 500 MHz using $CDCl_3$/TFA and DMSO-$d_6$ as solvents. FTIR spectra were acquired on a Thermo Nicolet iS10 FTIR Spectrometer equipped with a Smart Diamond attenuated total reflectance (ATR) accessory in the region of 4000-400 $cm^{-1}$. Background measurements were initially performed before analyzing the sample, with 8 scans completed using a resolution of 2 $cm^{-1}$. Size exclusion chromatography (SEC) was measured using a PSS SECurity™ GPC system equipped with a PFG 7 µm 8 × 50 mm pre-column, a PSS 100 Å, 7 µm 8 × 300 mm and a PSS 1000 Å, 7 µm 8 × 300 mm column in series and a differential refractive index (RI) detector at a flow rate of 1.0 mL $min^{-1}$ to determine the dispersities ($Đ_M$) and molecular weights of polymers. 1,1,1,3,3,3-Hexafluoro-2-propanol (HFiP) was used as the

eluent. The systems were calibrated against Agilent Easi-Vial linear poly(methyl methacrylate) (PMMA) standards and analyzed by the software package PSS winGPC UniChrom.

**Rheology**

Rheological characterization was performed on a strain-controlled rheometer (TA Instruments, ARES-G2) at room temperature. A parallel plate (25mm) was used for the oscillatory amplitude sweep, oscillatory frequency sweep, and cyclic dynamic oscillatory amplitude sweep experiments. Both cone (25mm, 0.4 rad) and plate (25mm) geometries were used for flow rheology to maintain consistent shear during viscosity measurement. A quartz parallel plate (25mm) was attached to the instrument for real-time photocuring studies, to permit hydrogel formulation irradiation during the dynamic time sweep test to see storage and loss modulus changes over time.

**Swelling ratio and mesh calculation**

For swelling studies, the hydrogel was fabricated at a 7.5 wt% formulation in cylindrical molds. After photocrosslinking, the mass was recorded and hydrogels were then swollen in excess water for 72 h to ensure equilibration of the networks. The swollen hydrogel was then removed from water, patted dry to remove excess water on the surface and the mass was recorded again. The procedure was conducted in triplicate. The equilibrium swelling ratio (Q) can be calculated based on equation S1:

$$\boldsymbol{Swelling\ Ratio} = \frac{\boldsymbol{Ws - Wd}}{\boldsymbol{Wd}}$$

Where ***Ws***=mass of swollen hydrogel and ***Wd***=mass of pre-swollen hydrogel. Using the storage modulus values from oscillatory rheology, a mesh size was approximated following equation S2:

$$\xi = \left(\frac{G' N_A}{RT}\right)^{-\frac{1}{3}}$$

Where $\xi$=mesh size, $G'$=storage modulus, $N_A$=Avogadro's number, $R$=Molar gas constant and $T$= Temperature.

**Photocrosslinkable hydrogel formulation preparation**

Initially, a 0.1 wt% solution of the photoinitiator lithium phenyl-2,4,6-trimethylbenzoylphosphinate (LAP) was prepared, followed by addition of poly(ethylene glycol) methyl ether methacrylate (5 wt%), and finally the lyophilized hydrogel powder (either 3-CP-T or 3-CP-V at 7.5 wt%). It was blended homogenously and then subject to photoirradiation using a 405 nm visible light (M405L3-C1, THORLABS) at time intervals in line with observations from rheological photocrosslinking experiments. The light intensity was measured at 13 mW/cm$^2$ using a Newport Optical Power/Energy Meter (Model 842-PE).

**Prototype direct ink writing (DIW) without bacteria**

Hydrogel 3D printability was initially trialled using a BIO X (CELLINK) 3D printer with HeartOS operating system. Hydrogels were formulated firstly by dissolution of LAP (0.1 wt%) in deionised water. The PEGMEMA conomoner (5 wt%) was then added and the solution was homogenized. The lyophilized hydrogel (either 3-CP-T or 3-CP-V at 7.5 wt%) was then swollen in the photoinitiator/comonomer solution and mixed until homogenized. DIW extrusion was completed using a 26 G needle. Print speeds were altered between 3 and 6 mm/s and pressure was maintained between 15 and 20 kPa for optimum print resolution. Constructs were then photo irradiated using 405 nm visible light (M405L3-C1, THORLABS).

**Strain and culture conditions**

*Escherichia coli (E. coli*) *DH5α* with a plasmid pZEMB8 that contained an Isopropyl ß-D-1-thiogalactopyranoside (IPTG) inducible gene (responsible for green fluorescent protein (GFP) expression) was provided by Dr. Mohammad S. Azam at University of Illinois, Urbana-Champaign (UIUC) [1]. The *E. coli* was grown at 37°C in LB-Miller media (BD) or on LB agar plates (BD). For induction of GFP expression, 1.0 mM of IPTG was added and incubated for the times indicated.

**Bioink preparation**

For the bacteria cell laden bioink, *E.coli* were initially grown overnight at 37°C in LB in the presence of 100 ug/mL of ampicillin (GoldBio) or carbenicillin (Sigma-Aldrich). After 16-18 h, the overnight bacteria culture was freshly grown in fresh LB until $OD_{600}$ reached 0.6. $OD_{600}$ was measured using a portable OD spectrometer (Biowave Cell Density Meter CO8000, Biochrom WPA). For the examination of the cell growth in extended time (0h, 24h, and 72h),

the freshly grown bacteria cultures that reached $OD_{600}$ of 0.5~0.6 were further diluted 200 times in LB to facilitate the visualization of GFP expression of individual bacteria cells embedded in hydrogels. The bacteria culture was then sequentially mixed with photoinitiator LAP (concentration 0.1 wt%), PEGMEMA (5 wt%), and the lyophilized hydrogel powder (either 3-CP-T or 3-CP-V at 7.5 wt%). The bioink with embedded bacteria was then loaded into a 3 mL Luer-Lok syringe and covered to prevent light transmission into the syringe. The syringe could be stored at 4°C (up to 30mins) prior to use.

**DIW bioprinting**

For All CAD models were designed on Tinkercad or found on Thingiverse. The bioink containing syringe was mounted onto the extruder syringe pump, and extruded onto a 10 cm petri dish. Printing was controlled by using Cura-lulzbot 3.6.1 software via a micro SD card or USB connected computer. Bioink constructs were then photo irradiated using 405 nm visible light (M405L3-C1, THORLABS) followed by incubation at 37°C for times indicated. Images of the 3D constructs were captured using iPhone Xs (Apple Inc).

**Fluorescent microscopy analysis**

Functionality of the bioink was analyzed via gene expression upon IPTG induction with indicated concentrations. Initially, the bioink was incubated at 37°C on LB agar plate. For the examination of the cell growth in extended time, the bacteria were grown under ambient temperature to facilitate the visualization of GFP expression of individual bacteria cells embedded in hydrogels. After indicated times of incubation, the bioink was either spread on a glass microplate with cover glass or transferred a 6 well microplates (Falcon) using disposable

spatula, and was then examined under a fluorescent microscope (Olympus IX-81). Images taken were analyzed using Metamorph (version 6.2.1, Molecular Device Inc).

**Modification of 3D printer for bioprinting**

A modified Lulzbot Taz 6 was used to print the bacteria laden copolypeptide hydrogels. The front, top, horizontal beam was removed to accommodate the BioStruder toolhead and an adjustable build plate was installed to fit a 10 cm petri dish. The BioStruder toolhead, named to copy Lulzbot's naming convention, used a Lulzbot Single Extruder as a base. Likewise, the firmware used was the Single Extruder firmware. The extruder consisted of a motor, X end stop, and a closed-loop Z end stop and leveling cable. These items mimicked the basic design of a Single Extruder. The BioStuder also used a resistor in place of a thermistor that read a constant 163°C, which allowed the motor to move without the use of a heating element. The actuator motor was replaced with the Single Extruder motor. Custom toolhead mounting components were designed to hold the actuator, hold the Single Extruder components, and house the wires and cables of the toolhead. In order to add light curability, a blue light LED (M405L3-C1, THORLABS) was attached. To evenly project the light, an assembly was made using an Aspheric Condenser Lens with Diffuser (ACL2520U-A, THORLABS), an OEM Flange to SM1 Thread Adapter (SM1F1, THORLABS) and a lens tube. This assembly was mounted to a custom made, adjustable angle, bracket attached to the toolhead actuator. In order to control the light, a T-Cube LED Driver (LEDD1B) was connected to the blue light LED and powered using a 15v power supply (KPS101, THORLABS). To use the BioStruder toolhead, various software changes were made on the printer and the computer controller software. On the printer, the E-steps, which determine the distance the syringe plunger moves when given

the input of 10mm of movement, were changed to 3,200, and the Z probe offset was changed to about +1.60mm. The computer controller software used was Cura Lulzbot Edition (version 3.6.1.). A custom printer profile was created and added to the base software. This printer profile used a different set of start and end g-code that allowed the printer to avoid unnecessary steps such as heating and cooling the nozzle and facilitate printing of hydrogel on an agar plate. Additionally, the material and nozzle sizes were changed to match that of the syringes used, 8.65mm and .6mm respectively. A custom material profile was also created that matched the properties of hydrogel and used a different set of default printing parameters. The default printing parameters used were a print speed of 20 mm/s, a retraction distance of 0.2mm, and 70% "line" infill.

**Monomer and polymer synthesis**

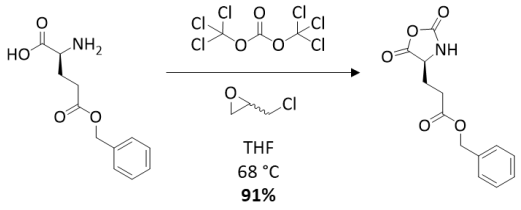


**γ-benzyl-L-glutamate *N*-carboxyanhydride synthesis:** Triphosgene (31.89 g, 107.48 mmol) and epichlorohydrin (79.53 g, 859.81 mmol) were initially dissolved in 850 mL of THF in a 1 L round-bottomed flask with stirring. γ-benzyl-L-glutamate (51.00 g, 215.00 mmol) was then added in one portion and the reaction suspension was heated under reflux (68 °C). The reaction was continued until all solids disappeared and the solution became clear (1-2 h). The solution was then cooled using an argon balloon, any unreacted γ-benzyl-L-glutamate was filtered off and the solution was reduced to 1/3 of its original volume in vacuo. The NCA was precipitated

by addition of 1.2 L of hexane and stored overnight at -18 °C to fully precipitate. The solid NCA was dried in vacuo and then re-dissolved in 350 mL ethyl acetate. This solution was then precipitated into excess hexane (1.4 L), filtered and dried (this was completed two to three times). It was then dried in vacuo to afford a white fluffy solid (yield: 51.4 g, 91 %). $^{1}$H NMR (600 MHz, $CDCl_3$/TFA, δ, ppm): 7.34-7.4 (m, 5H, -CH2*C5H6*), 6.36 (s, 1H, *NH*), 5.14 (s, 2H, -*CH2*C5H6), 4.37 (t, 1H, -CO*CH*NH-), 2.60 (t, 2H, -CO*CH2*CH2-), 2.10-2.31 (m, 2H, -COCH2*CH2*-); $^{13}$C NMR (500 MHz, $CDCl_3$/TFA, δ, ppm): 173.79, 168.70, 154.31, 134.58, 128.66, 67.94, 29.38, 26.49.

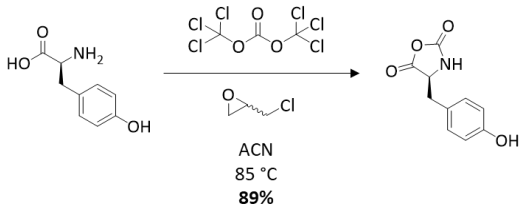


**L-tyrosine *N*-carboxyanhydride synthesis:** Triphosgene (3.28 g, 11.04 mmol) and epichlorohydrin (8.43 g, 88.30 mmol) were initially dissolved in 130mL of acetonitrile in a 250 mL round-bottomed flask with stirring. L-tyrosine (4.00 g, 22.07 mmol) was then added in one portion and the reaction suspension was heated to 85 °C. The reaction was continued until all solids disappeared and the solution became clear (2 h). The solution was then cooled using an argon balloon and acetonitrile was removed in vacuo. The NCA was suspended in 20 mL ethyl acetate and then 200 mL of hexane was added, followed by storage overnight at -18 °C to fully precipitate the NCA. The solid was dried under vacuum and then re-dissolved in 110 mL THF. This solution was then precipitated into excess hexane (550 mL), filtered and

dried in vacuo to afford a white powder with a yellow tinge (yield: 4.1 g, 89 %). $^{1}$H NMR (600 MHz, DMSO-d6, δ, ppm): 9.31 (s, 1H, -C4H4*OH*), 9.02 (s, 1H, *NH*), 6.96-6.68 (dd, 4H, -*C4H4*OH), 4.70 (s, 1H, -CO*CH*NH-), 2.90 (s, 2H, -*CH2*C4H4-); $^{13}$C NMR (500 MHz, DMSO-d6, δ, ppm): 171.15, 56.90, 52.11, 131.12, 125.01, 116.93, 58.93, 35.91.

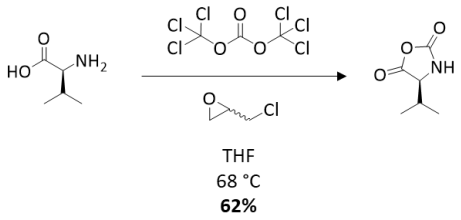


**L-valine N-carboxyanhydride synthesis:** Triphosgene (10 g, 33.70 mmol) and epichlorohydrin (31.40 g, 33.94×10$^{1}$ mmol) were initially dissolved in 130mL of THF in a 250 mL round-bottomed flask with stirring. L-valine (10.00 g, 85.34 mmol) was then added in one portion and the reaction suspension was heated under reflux (68 °C). The reaction was continued until all solids disappeared and the solution became clear (1 h). The solution was then cooled using an argon balloon, filtered and then reduced to 1/3 of its original volume using a cold trap in the fumehood. The NCA was precipitated by addition of 200 mL of hexane and stored overnight at -18 °C to fully precipitate. The solid NCA was dried under vacuum and then re-dissolved in a minimum amount of ethyl followed by precipitation into excess hexane (200 mL), filtered and dried under vacuum (two to three times). It was then vacuum dried to afford a crystalline solid (yield: 7.57 g, 62 %). $^{1}$H NMR (600 MHz, $CDCl_3$/TFA, δ, ppm): 7.16 (s, 1H, *NH*), 4.28 (d, 1H, -CO*CH*NH-), 2.27 (m, 1H, -*CH*C2H6), 1.10-1.04 (dd, 6H, -

CH*C2H6*); $^{13}$C NMR (500 MHz, $CDCl_3$/TFA, δ, ppm): 167.87, 155.40, 63.13, 30.70, 17.94, 16.67.

**3-arm poly(benzyl-L-glutamate-b-L-tyrosine) (3-PBLG-b-PLT) diblock copolypeptide synthesis:** γ-benzyl-L-glutamate NCA (6.96 g, 26.43 mmol) was dissolved in 110 mL of $CHCl_3$ and 10 mL DMF in a 250 mL flask with stirring. Tris(2-aminoethyl)amine or TREN (42.90 mg, $2.94\times10^{-1}$ mmol) in 10 mL of $CHCl_3$ was then quickly added to the flask in one portion. The flask was initially evacuated under vacuum to remove $CO_2$ and then a balloon filled with Ar was slowly purged through the solution with stirring continued at room temperature until NCA was fully consumed via FTIR spectroscopy. An aliquot of the solution was taken and kept for size exclusion chromatography (SEC) measurements and NMR analysis. L-tyrosine NCA (2.74 g, 13.21 mmol) was dissolved in 30 mL of DMF and then quickly added to the flask in one portion. The flask again was initially evacuated under vacuum to remove $CO_2$ and then a balloon filled with Ar was slowly purged through the solution with stirring continued at room temperature until NCA was fully consumed via FTIR spectroscopy. The diblock copolymer was then precipitated into excess diethyl ether (1 L) using centrifugation and decanting, and then fully dried under vacuum (yield: 6.70 g, 84 %).

**3-PBLG-b-PLT diblock copolypeptide deprotection:** The copolymer (6.60 g, 2.53 mmol) was fully suspended in 100 mL $CHCl_3$, after which 80 mL TFA was added. 20 mL of 33wt% HBr in acetic acid was then added dropwise over 10 mins, and the solution was stirred overnight at room temperature. The solution was then precipitated into excess diethyl ether (1.5 L) and dried in vacuo. The solid was suspended in 50 mL deionised water, and then the pH was adjusted to 7-8 until a viscous translucent solution formed. The solution was dialysed

against deionised water for 2 days in a 3.5 kDa MWCO SnakeSkin® membrane with frequent water replacement followed by lyophilisation (yield: 4.81 g, 93 %).

**Methacrylate functionalization of diblock copolypeptide (3-CP-T):** The deprotected copolymer (4.70 g, $2.51\times10^{-1}$ mmol) was dissolved in 400 mL of deionised water and pH adjusted to 8 with $NaHCO_3$. 25 equivalents of DMT-MM (1.73 g, 6.28 mmol) was then added and stirring was continued for 10 min to activate the carboxyl groups. 2-aminoethyl methacrylate hydrochloride (1.04 g, 6.28 mmol) in 10 mL deionised water was then added and stirring was continued for 2 days in darkness at room temperature. The solution was then dialysed against deionised water for 3 days in darkness in a 3.5 kDa MWCO SnakeSkin® membrane with frequent water replacement followed by lyophilisation (yield: 4.34 g, 84 %).

**3-arm poly(benzyl-L-glutamate-b-L-valine) (3-PBLG-b-PLV) diblock copolypeptide synthesis:** γ-benzyl-L-glutamate NCA (8.45 g, 32.10 mmol) was dissolved in 100 mL of $CHCl_3$ and 10 mL DMF in a 250 mL flask with stirring. Tris(2-aminoethyl)amine or TREN (52.00 mg, $3.56\times10^{-1}$ mmol) in 5 mL of $CHCl_3$ was then quickly added to the flask in one portion. The flask was initially evacuated under vacuum to remove $CO_2$ and then a balloon filled with Argon was slowly purged through the solution with stirring continued at room temperature until NCA was fully consumed via FTIR spectroscopy. An aliquot of the solution was taken and kept for size exclusion chromatography (SEC) measurements and NMR analysis. L-valine NCA (2.29 g, 16.01 mmol) was dissolved in 10 of $CHCl_3$ and 1 mL DMF and then quickly added to the flask in one portion. The flask again was initially evacuated under vacuum to remove $CO_2$ and then a balloon filled with Ar was slowly purged through the solution with stirring continued at room temperature until NCA was fully consumed via FTIR

spectroscopy. The diblock copolymer was then precipitated into excess diethyl ether (1 L) using centrifugation and decanting, and then fully dried under vacuum (yield: 8.03 g, 93 %).

**3-PBLG-b-PLV diblock copolypeptide deprotection:** The copolymer (7.93 g, $3.51\times10^{-1}$ mmol) was dissolved in 70 mL $CHCl_3$, after which 30 mL TFA was added. 27 mL of 33wt% HBr in acetic acid was then added dropwise over 10 mins, and the solution was stirred overnight at room temperature. The solution was then precipitated into excess diethyl ether (1.5 L) and dried in vacuo. The solid was suspended in 100 mL deionised water, and then the pH was adjusted to 7-8 until a viscous translucent solution formed. The solution was dialysed against deionised water for 2 days in a 3.5 kDa MWCO SnakeSkin® membrane with frequent water replacement followed by lyophilisation (yield: 5.80 g, 97 %).

**Methacrylate functionalization of diblock copolypeptide (3-CP-V):** The deprotected copolymer (5.70 g, $3.37\times10^{-1}$ mmol) was dissolved in 800 mL of deionised water and pH adjusted to 8 with $NaHCO_3$. 25 equivalents of DMT-MM (2.20 g, 7.91 mmol) was then added and stirring was continued for 10 min to activate the carboxyl groups. 2-aminoethyl methacrylate hydrochloride (1.31 g, 7.91 mmol) in 10 mL deionised water was then added and stirring was continued for 2 days in darkness at room temperature. The solution was then dialysed against deionised water for 3 days in darkness in a 3.5 kDa MWCO SnakeSkin® membrane with frequent water replacement followed by lyophilisation (yield: 4.04 g, 67 %).

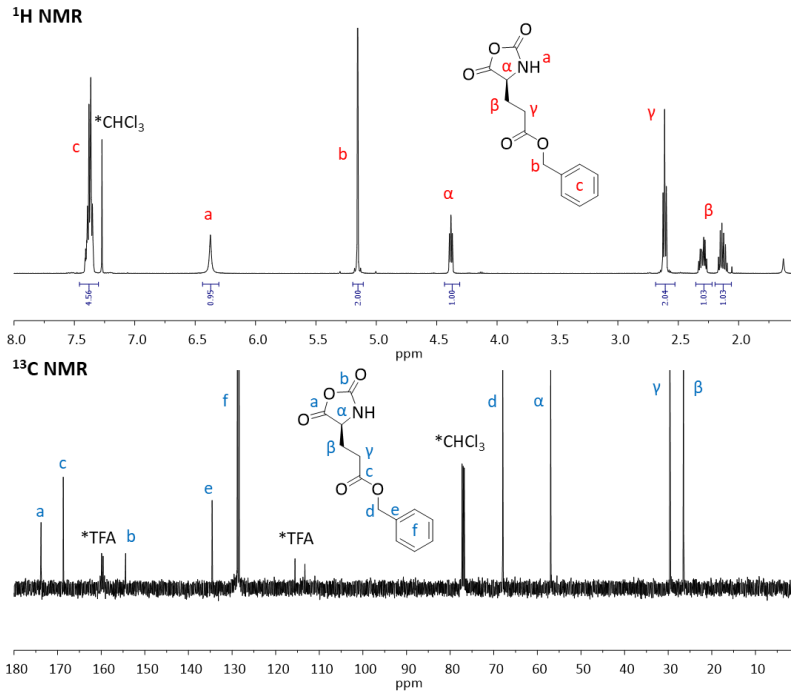


Figure B1: $^{1}$H NMR and $^{13}$C NMR spectra of γ-benzyl-L-glutamate *N*-carboxyanhydride (BLG NCA) in 15% TFA in $CDCl_3$.

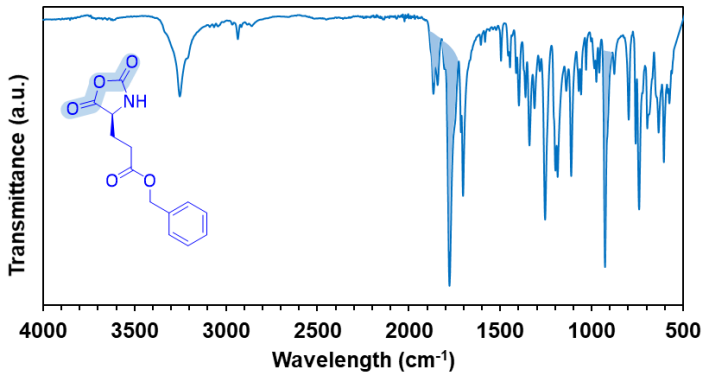


Figure B2: FTIR spectra of γ-benzyl-L-glutamate *N*-carboxyanhydride (BLG NCA).

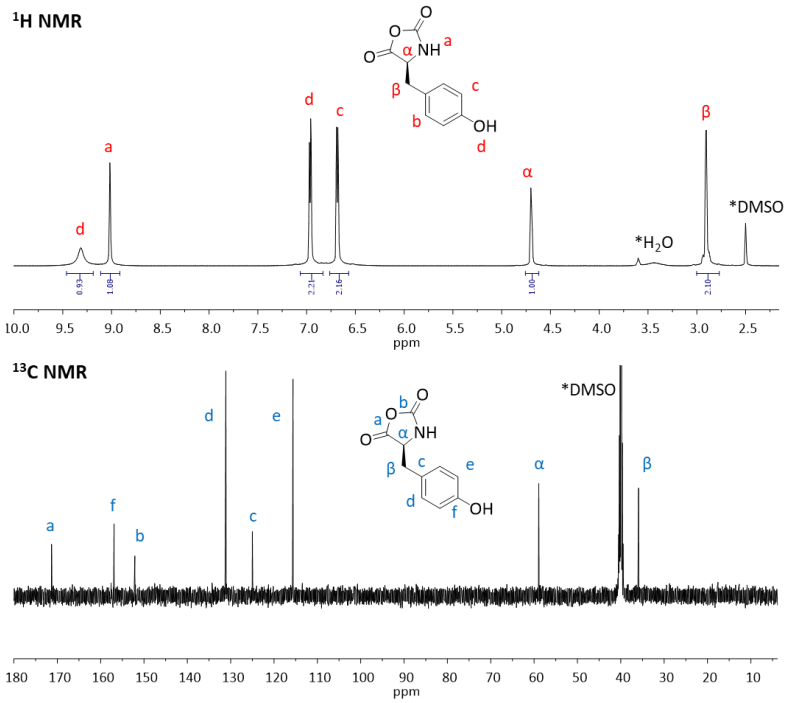


Figure B3: $^{1}H$ NMR and $^{13}C$ NMR spectra of L-tyrosine *N*-carboxyanhydride (LT NCA) in DMSO-$d_6$.

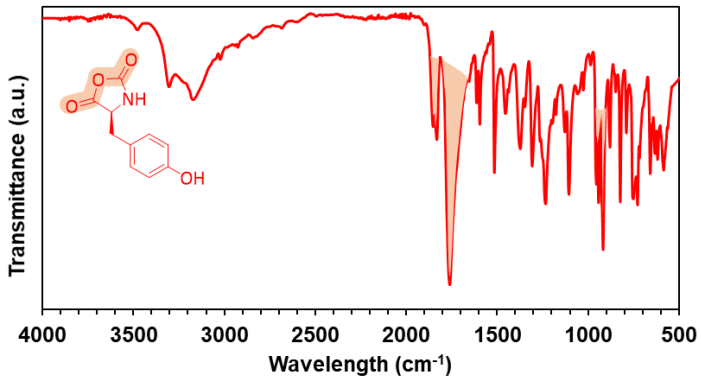


Figure B4: FTIR spectra of L-tyrosine *N*-carboxyanhydride (LT NCA).

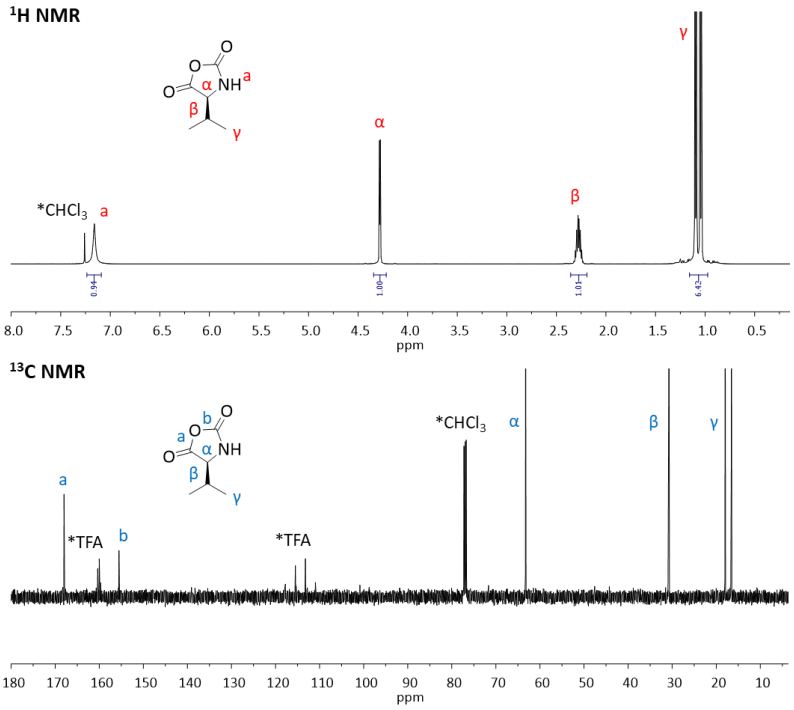


Figure B5: $^{1}H$ NMR and $^{13}C$ NMR spectra of L-valine *N*-carboxyanhydride (LV NCA) in 15% TFA in $CDCl_3$.

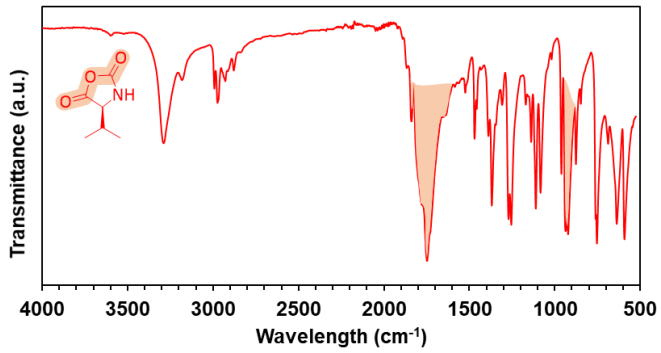


Figure B6: FTIR spectra of L-valine *N*-carboxyanhydride (LV NCA).

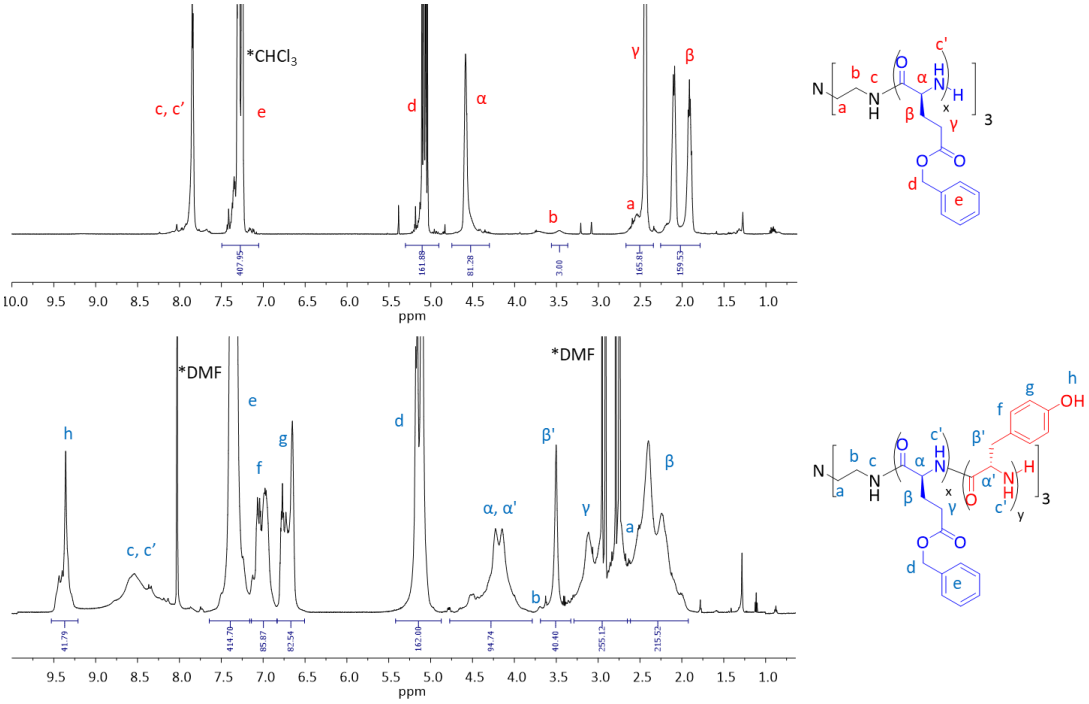


Figure B7: $^{1}$H NMR spectra of homopolypeptide ($PBLG_{90}$) in 15% TFA in $CDCl_3$, and diblock copolypeptide ($PBLG_{90}$-b-$PLT_{45}$) in DMF-$d_7$.

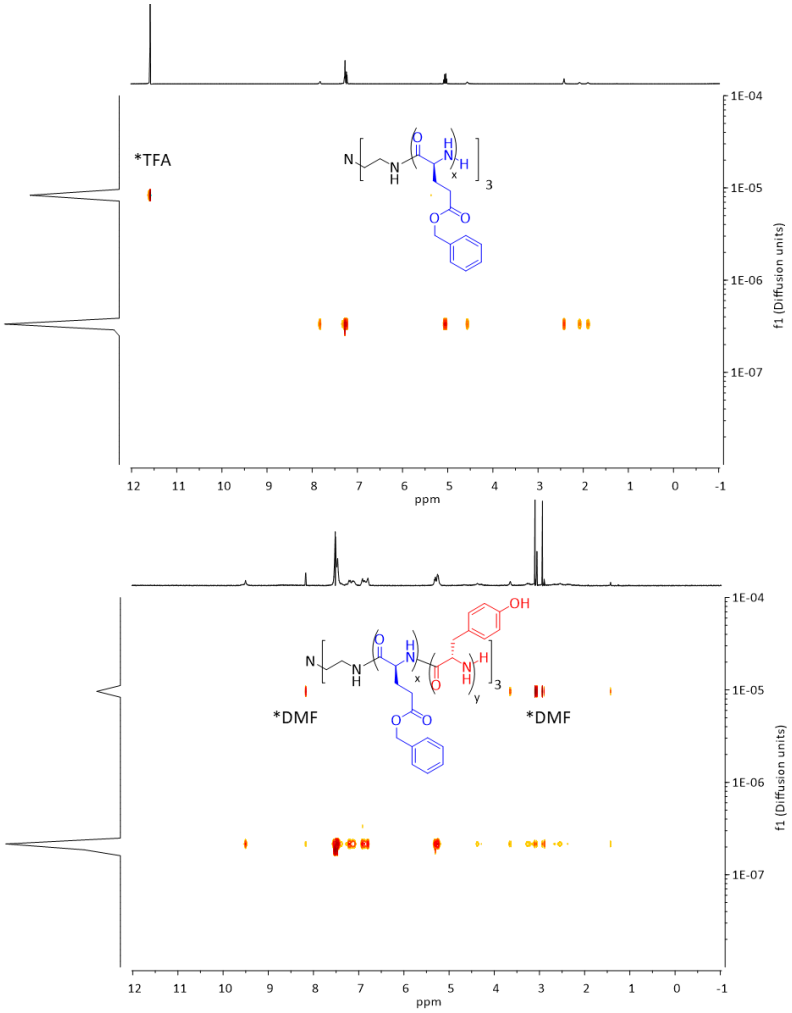


Figure B8: DOSY NMR spectra of homopolypeptide (3-PBLG$_{90}$) in 15% TFA in $CDCl_3$, and diblock copolypeptide (PBLG$_{90}$-b-PLT$_{45}$) in DMF-$d_7$.

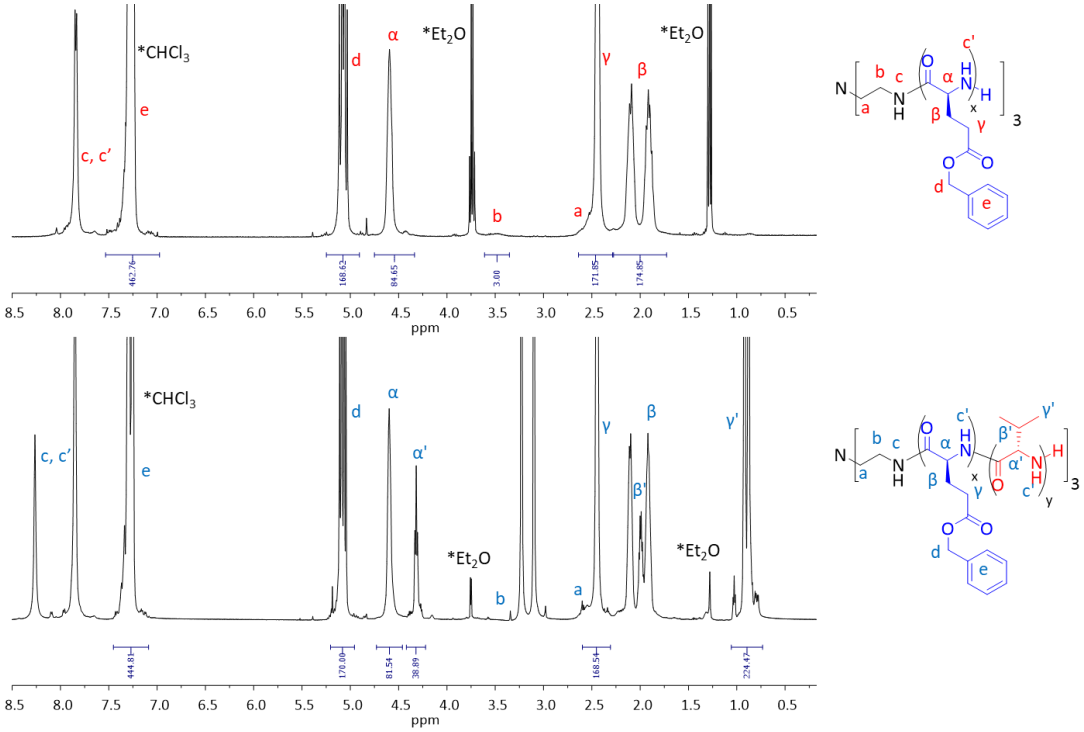


Figure B9: $^{1}$H NMR spectra of homopolypeptide (3-PBLG$_{90}$), and diblock copolypeptide (3-PBLG$_{90}$-b-PLV$_{45}$) in 15% TFA in $CDCl_3$.

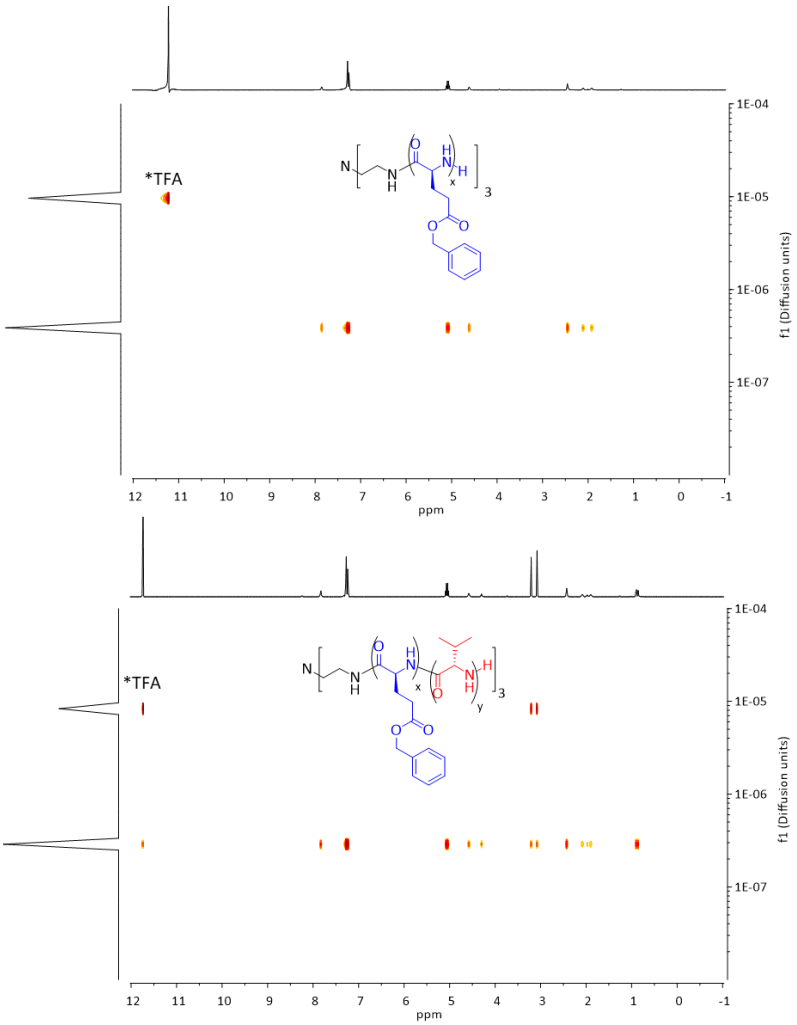


Figure B10: DOSY NMR spectra of homopolypeptide (3-PBLG$_{90}$), and diblock copolypeptide (3-PBLG$_{90}$-b-PLV$_{45}$) in 15% TFA in $CDCl_3$.

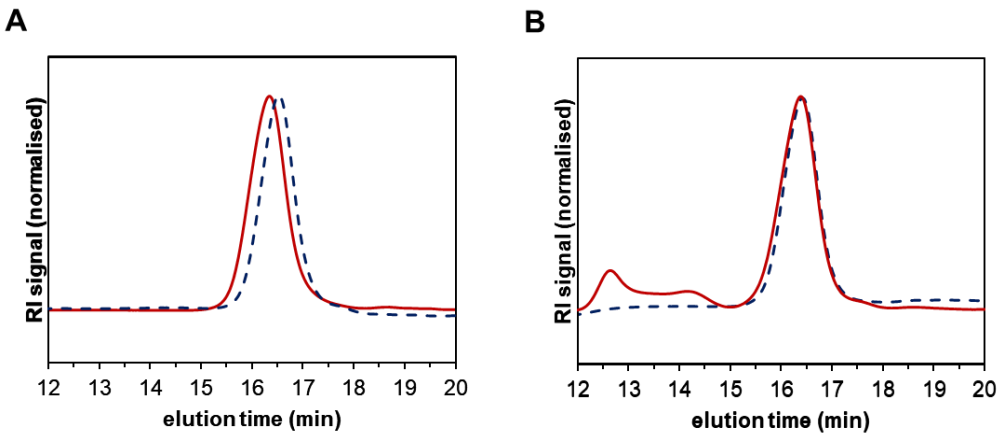


Figure B11: Size exclusion chromatography (SEC) traces of 3-PBLG$_{90}$ chain extended to 3-PBLG$_{90}$-*b*-PLT$_{45}$ (A), and 3-PBLG$_{90}$ chain extended to 3-PBLG$_{90}$-*b*-PLV$_{45}$ (B) with self-assembly noted.

**Table B1.** Molar mass and dispersity characteristics of diblock copolypeptides.

| Entry | Polymer block | $M_n{}^a$ | $M_n{}^b$ | $M_n{}^c$ | $Đ_M{}^c$ |
|---|---|---|---|---|---|
| | 3-PBLG$_{90}$ | 19,900 | 17,900 | 24,100 | 1.07 |
| 3-CP-T | 3-PBLG$_{90}$-*b*-PLT$_{45}$ | 27,200 | 24,600 | 27,200 | 1.09 |
| | 3-PBLG$_{90}$ | 19,900 | 18,800 | 26,800 | 1.06 |
| 3-CP-V | 3-PBLG$_{90}$-*b*-PLV$_{45}$ | 24,400 | 22,700 | 27,300 | 1.08 |

[a]Molar mass theoretical expectation based on stoichiometric feed ratio. [b]Molecular mass as determined by $^1$H-NMR monomer ratio. [c]Molecular mass and dispersities determined by SEC (PMMA standards).

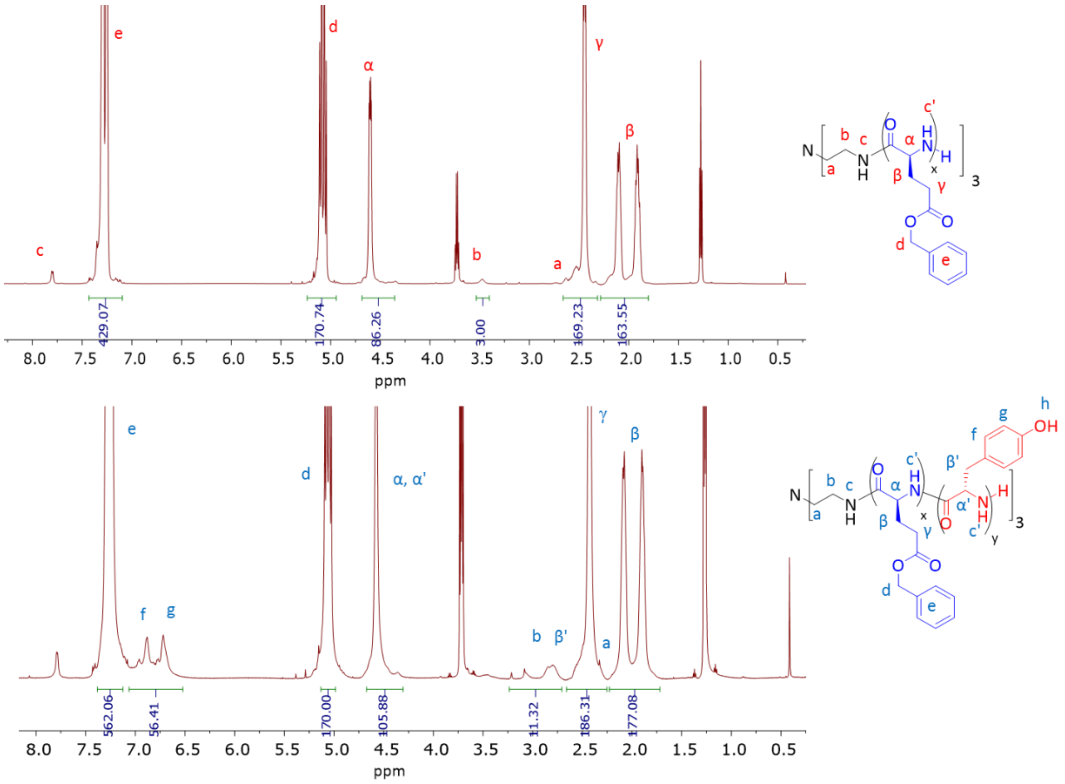


Figure B12: $^1$H NMR spectra of homopolypeptide (3-PBLG$_{90}$) in 15% TFA in $CDCl_3$, and diblock copolypeptide (3-PBLG$_{90}$-b-PLT$_{22}$) in DMF-$d_7$.

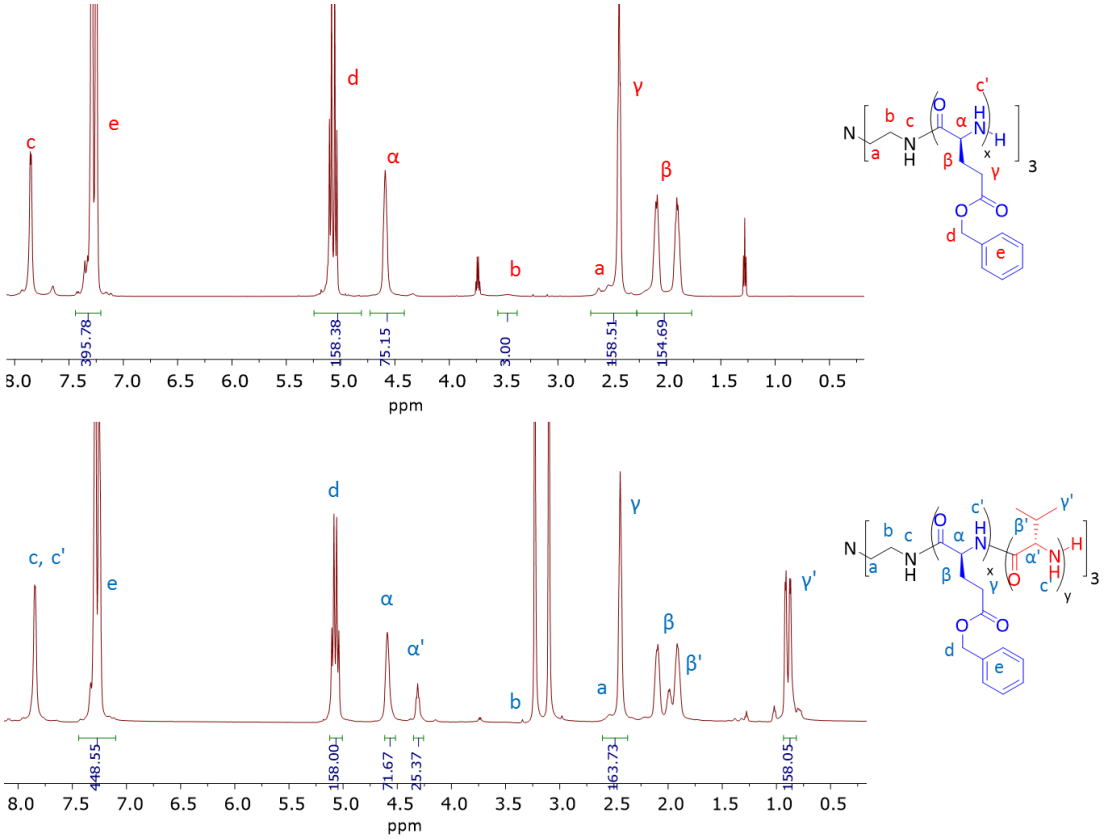


Figure B13: $^{1}H$ NMR spectra of homopolypeptide (3-$PBLG_{90}$), and diblock copolypeptide (3-$PBLG_{90}$-b-$PLV_{22}$) in 15% TFA in $CDCl_3$.

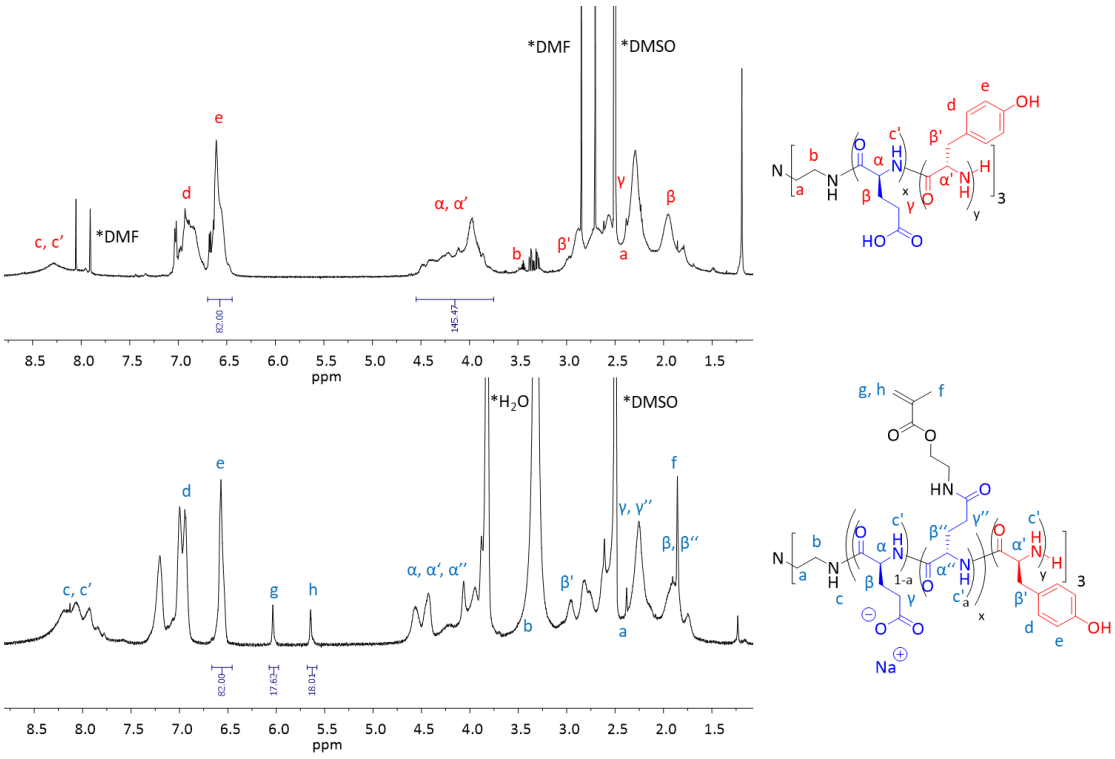


Figure B14: $^{1}$H NMR spectra of free acid form of deprotected diblock copolypeptide (3-PLG$_{90}$-b-PLT$_{45}$) and its methacrylate functionalized derivative (3-CP-T) in DMSO-d$_6$.

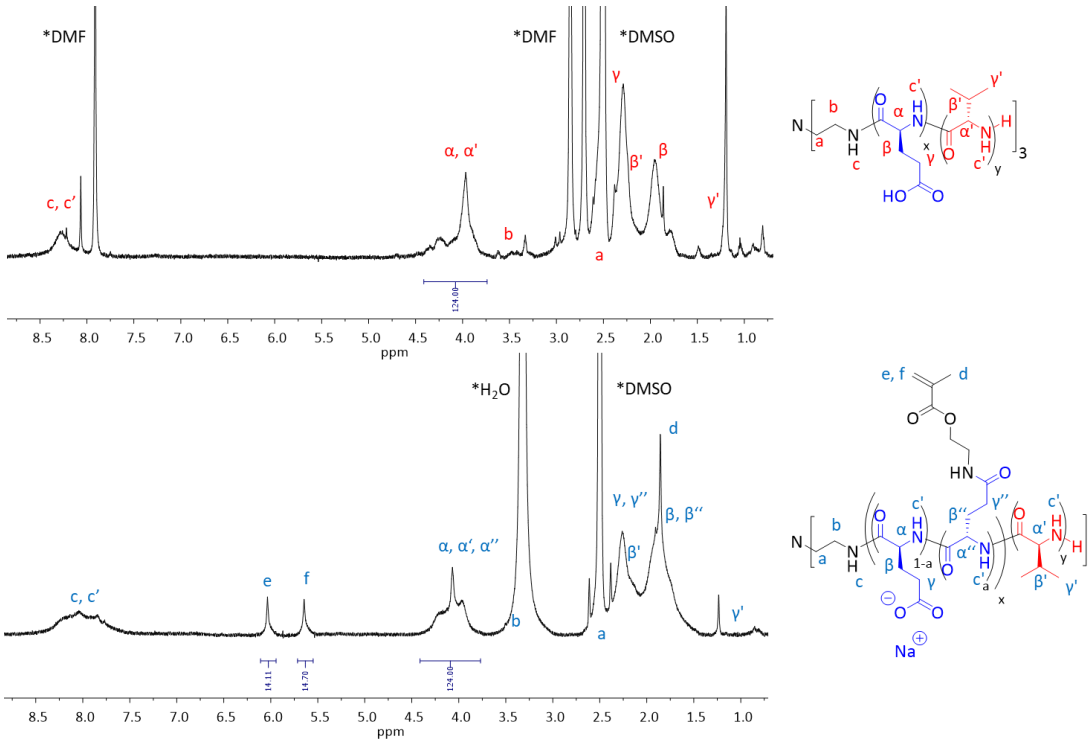


Figure B15: $^{1}$H NMR spectra of free acid form of deprotected diblock copolypeptide (3-PLG$_{90}$-b-PLV$_{45}$) and its methacrylate functionalized derivative (3-CP-V) in DMSO-d$_6$.

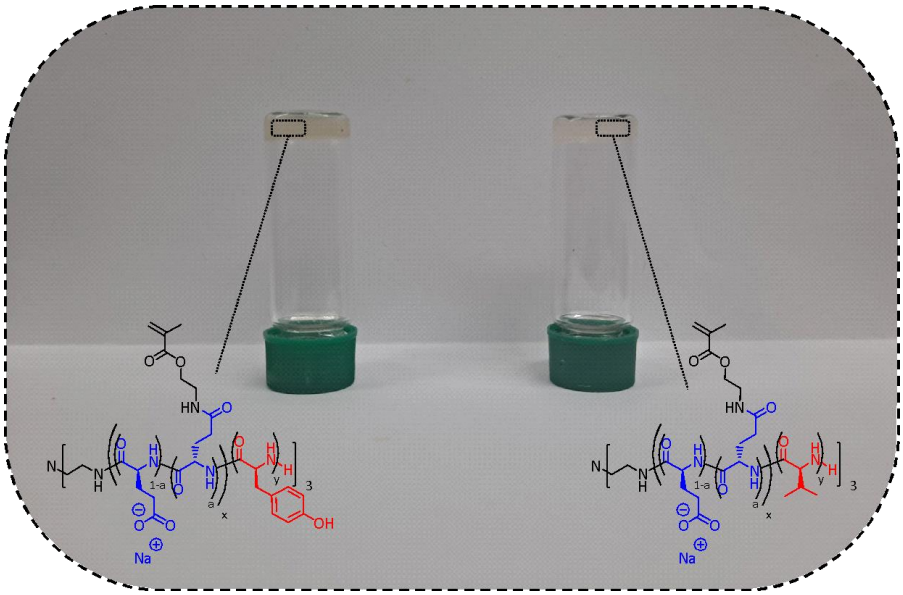

Figure B16: Inversion vial test of 3-CP-T and 3-CP-V hydrogels at concentrations of 3.75 and 3.5 wt% respectively.

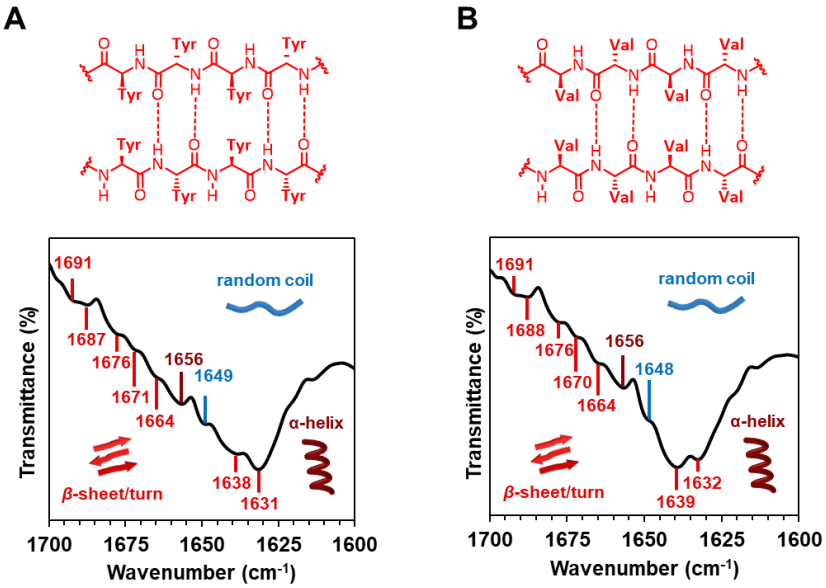


Figure B17: FTIR spectra showing secondary structures of physical 3-CP-T (A) and 3-CP-V (B) hydrogels in $D_2O$

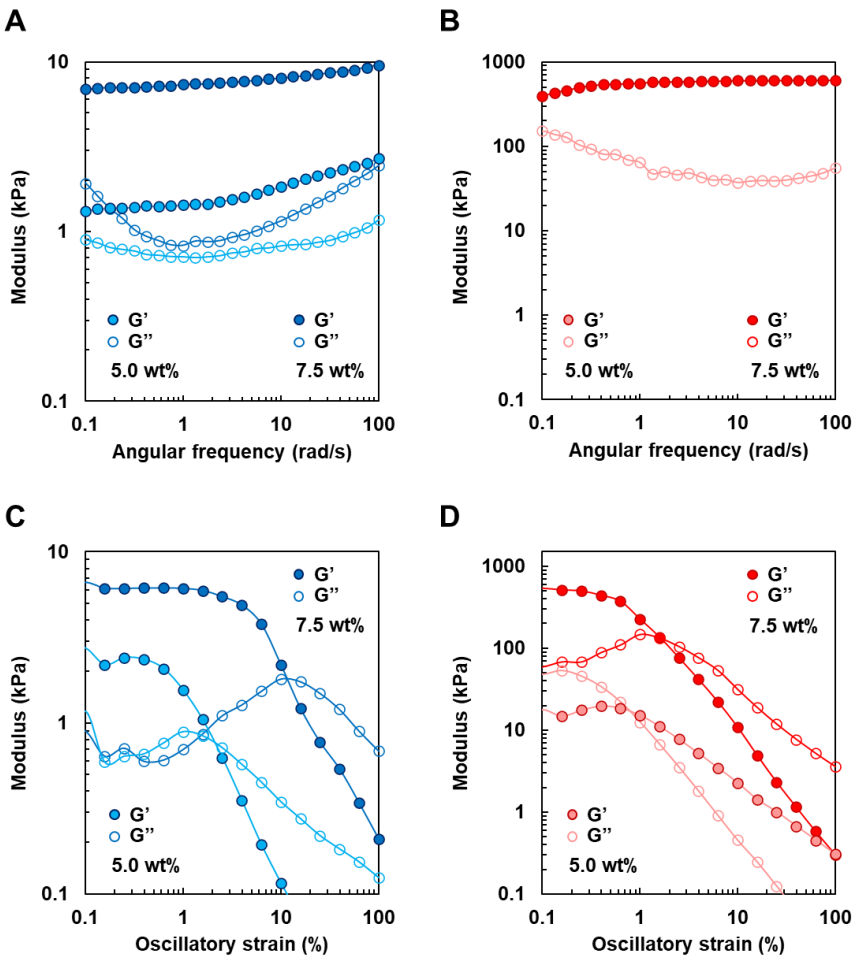


Figure B18: Frequency sweeps of 3-CP-T (A) and of 3-CP-V (B) hydrogels measuring moduli changes at 5.0 and 7.5 wt% using frequencies ranging from 0.1 to 100 rad/s at constant oscillatory strain of 0.1 %. Amplitude sweeps of 3-CP-T (C) and 3-CP-V (D) hydrogels measuring moduli changes at 5.0 and 7.5 wt% with increasing oscillatory strain ranging from 0.1 to 100% at constant angular frequency of 6.2 rad/s.

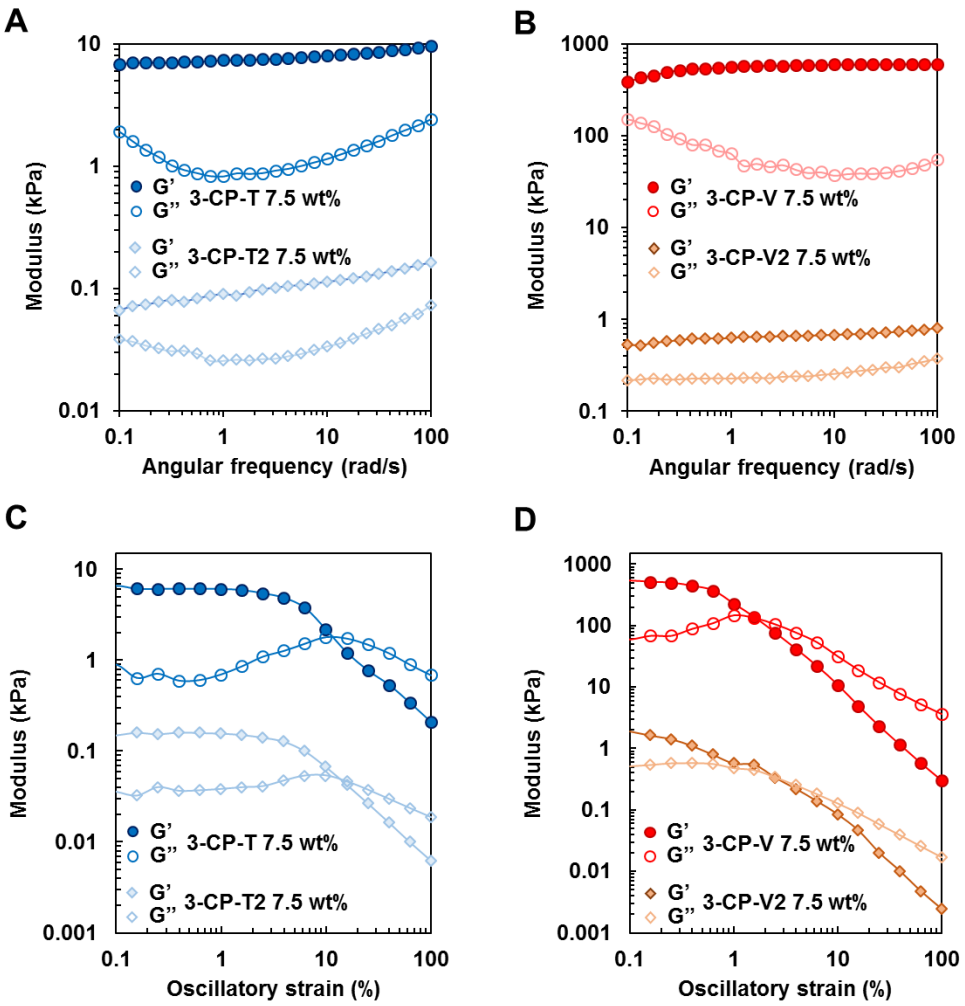


Figure B20: Frequency sweeps of 3-CP-T, 3-CP-T2 (A) and of 3-CP-V, 3-CP-T2 (B) hydrogels measuring moduli changes based on molecular weight using frequencies ranging from 0.1 to 100 rad/s at constant oscillatory strain of 0.1 %. Amplitude sweeps of 3-CP-T, 3-CP-T2 (C) and 3-CP-V, 3-CP-V2 (D) hydrogels measuring moduli changes based on molecular weight with increasing oscillatory strain ranging from 0.1 to 100% at constant angular frequency of 6.2 rad/s.

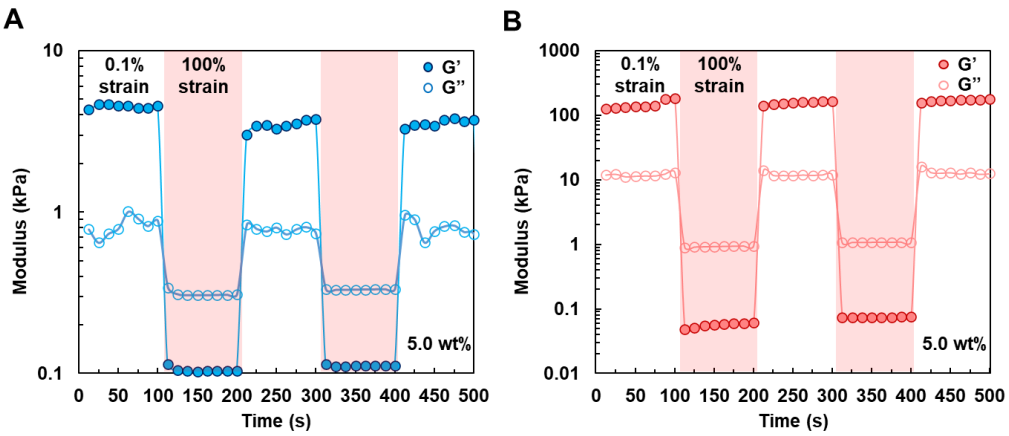


Figure B21: Cyclic oscillatory amplitude sweeps for 5.0 wt% hydrogels of 3-CP-T (A) and 3-CP-V (B) showing moduli response to low strains (0.1%) and high strains (100%) at intervals of 100 s at constant angular frequency of 6.2 rad/s.

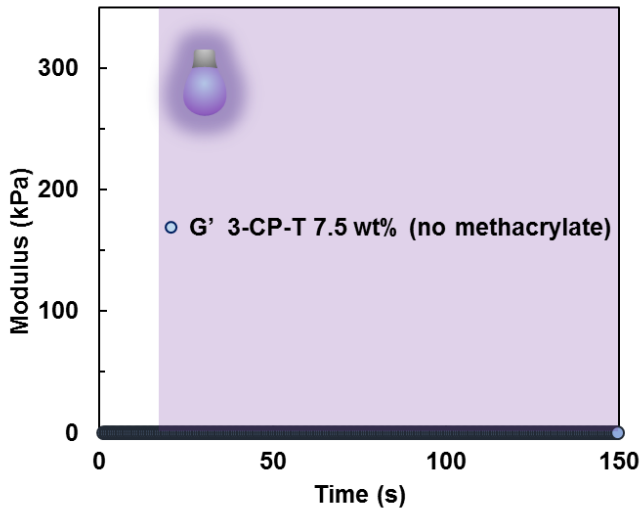


Figure B22: Real-time visible light curing (405 nm) at intensity of 13 mW/cm$^2$ showing no moduli changes for unfunctionalized 3-CP-T at 7.5 wt%, at constant angular frequency of 6.2 rad/s and constant oscillatory strain of 0.1 %.

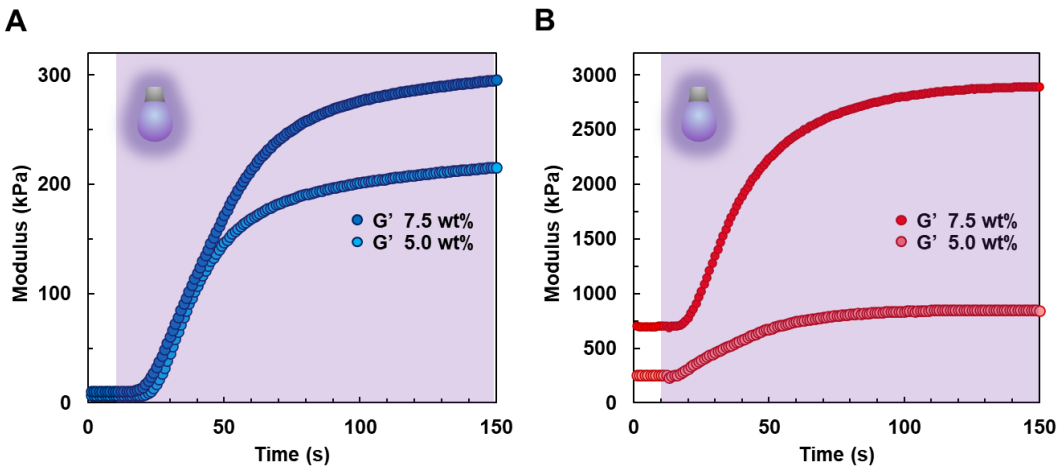


Figure B23: Real-time visible light curing (405 nm) at intensity of 13 mW/cm$^2$ showing comparative moduli differences for 3-CP-T at 5.0 wt% and 7.5 wt% (A), and 3-CP-V at 5.0 wt% and 7.5 wt% (B) at constant angular frequency of 6.2 rad/s and constant oscillatory strain of 0.1 %.

**Table B2.** Mesh size and swelling ratio characteristics of 3-CP-T and 3-CP-V hydrogels.

| | **Storage modulus (Pa)** | **Mesh size (nm)** | **Swelling ratio (Q)** |
|---|---|---|---|
| **3-CP-T** | 9690 | 7.6 | - |
| **3-CP-V** | 60500 | 1.9 | - |
| **3-CP-T (crosslinked)** | 295000 | 2.4 | 121.9 ± 21.9 |
| **3-CP-V (crosslinked)** | 2892000 | 1.1 | 17.8 ± 5.4 |
| **3-CP-T (crosslinked+swelled)** | 213 | 27.2 | - |
| **3-CP-V (crosslinked+swelled)** | 204 | 27.6 | - |

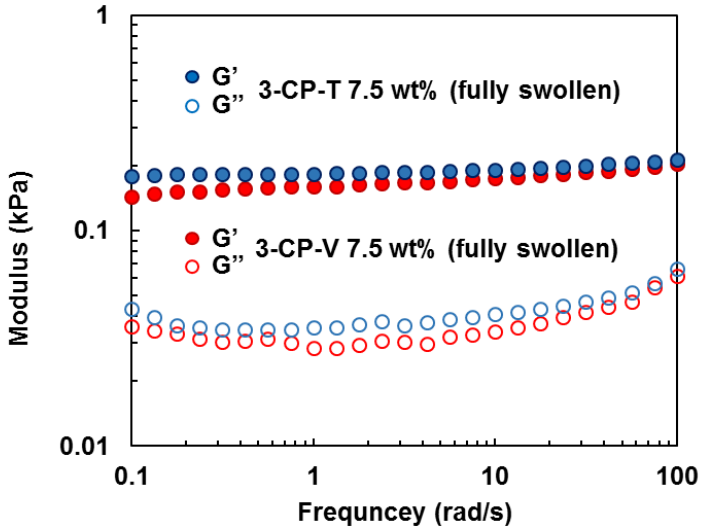


Figure B24: Frequency sweeps of post-crosslinked 3-CP-T (A) and of 3-CP-V (B) hydrogels (at 7.5 wt%) at equilibrium swelling using frequencies ranging from 0.1 to 100 rad/s at constant oscillatory strain of 0.1 %.

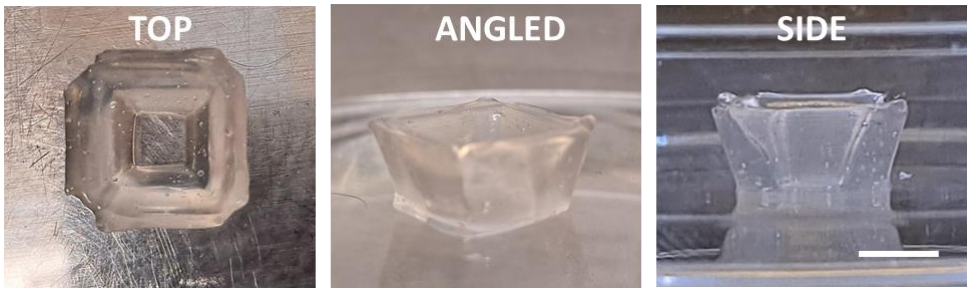


Figure B25: Different angles of 3D printed inverted pyramid showcasing overhanging layers and sharp corners (scale bar: 4 mm).

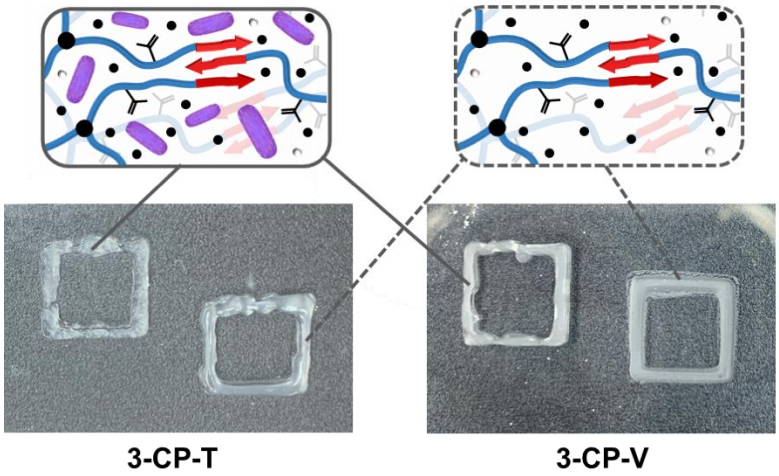


Figure B26: Turbidity comparison of hydrogels without and without embedded bacteria.

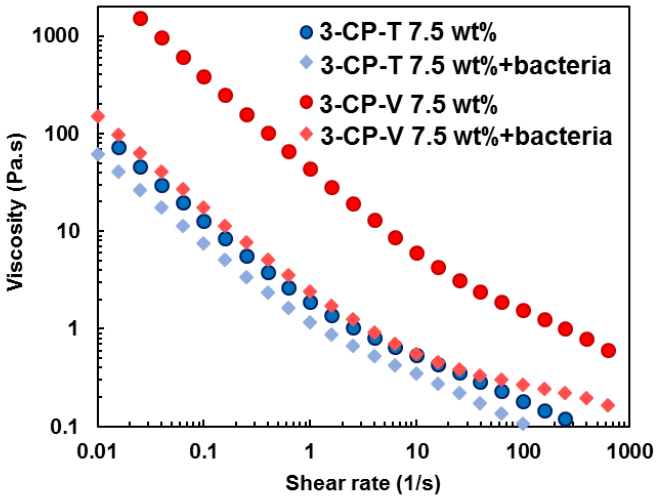


Figure B27: Viscosity sweep with increasing shear rate of 3-CP-T and of 3-CP-V hydrogels (at 7.5 wt%) with (incubated for 24h) and without bacteria embedded in LB Broth.

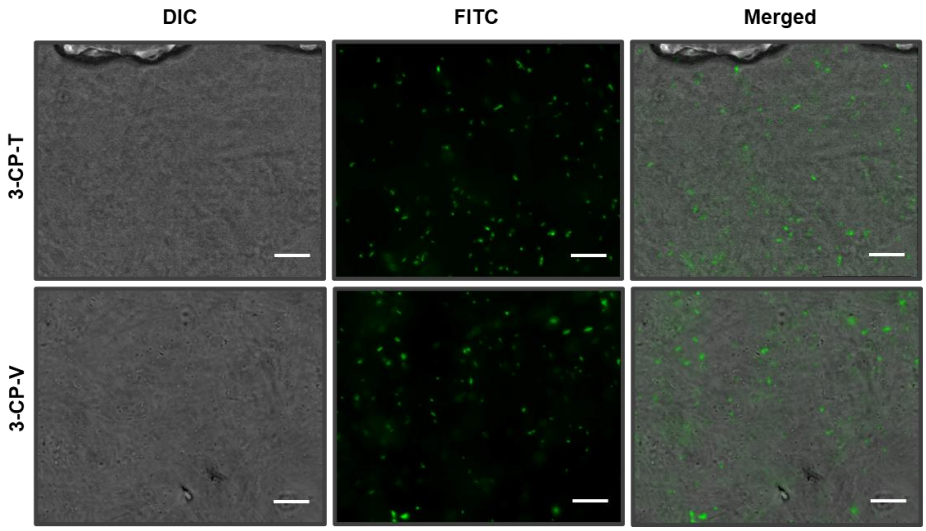


Figure B28: Confocal microscope images (E) of 3-CP-T and 3-CP-V hydrogels (7.5 wt%) embedded with engineered *E.coli* that express GFP upon IPTG incubation after 24 hours of photocrosslinking and IPTG induction. (scale bar: 25 μm).

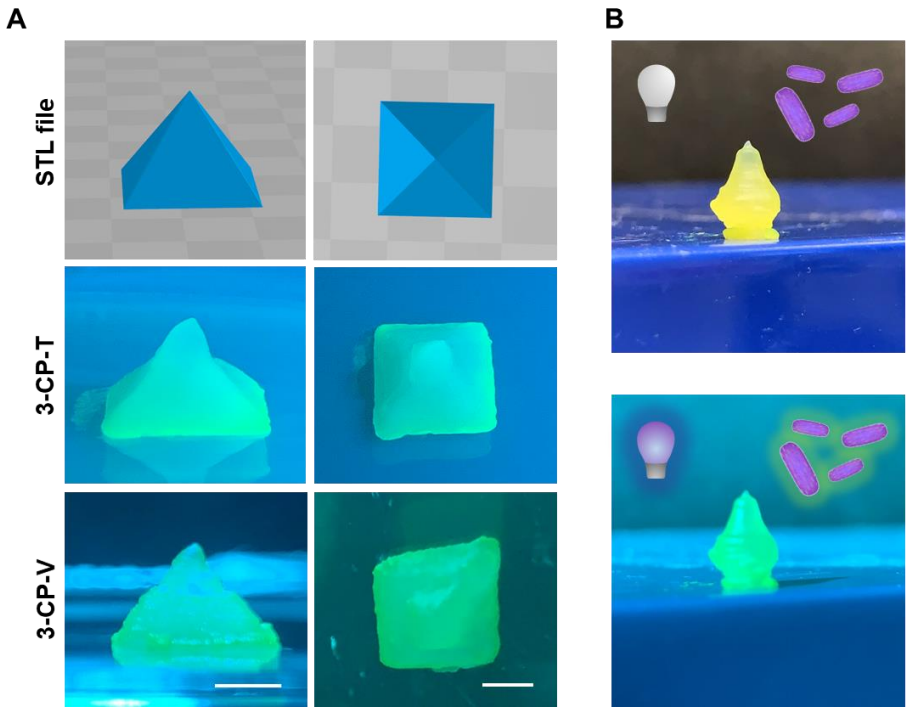


Figure B29: 3D pyramidal structures of 3-CP-T and 3-CP-V hydrogel bioinks (A) with encapsulated bacteria rendered in comparison to the CAD input file (scale bar: 3 mm), and demonstrating viability of 3D printed pear shape (B) through GFP expression imaged in the presence of UV light (scale bar: 3 mm).

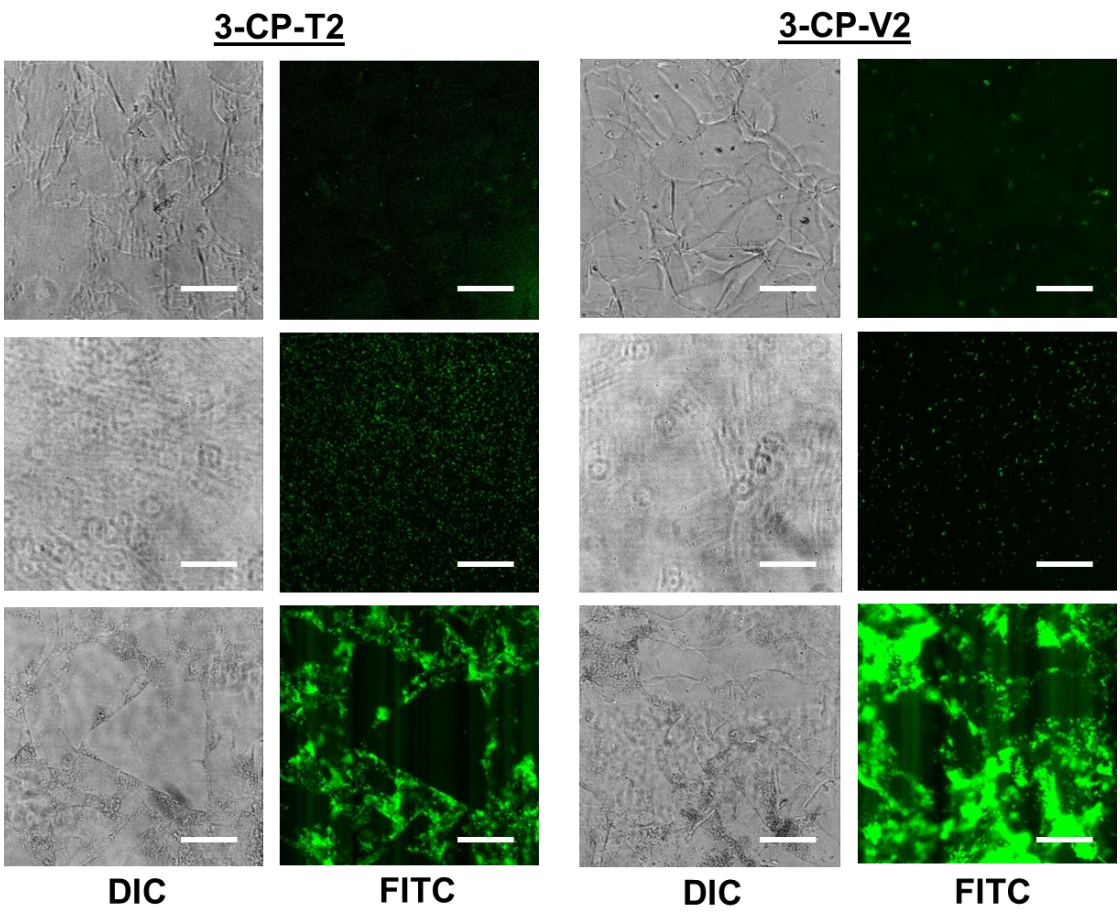


Figure B30: Confocal microscope images of 3-CP-T2 and 3-CP-V2 hydrogels (7.5 wt%) embedded with engineered *E.coli* that express GFP upon IPTG incubation up to 72 h after photocrosslinking and IPTG induction (scale bar: 100 μm).

# Appendix C: Supporting Information for Chapter 4

## Materials

All chemicals were obtained from Sigma Aldrich unless otherwise noted. γ-benzyl-l-glutamate (BLG) was purchased Trifluoroacetic acid (TFA) was purchased from Fisher Scientific. Triphosgene was purchased from Oakwood Chemical. 10 kDa MWCO SnakeSkin® membrane were purchased from Thermo Fisher Scientific. PhotoGel® 50% DS (GelMA) was purchased as lyophilized powder from Cellink.

## Methods

$^{1}$H NMR and DOSY NMR spectra were acquired on a Varian Unity Inova AS600 600 MHz using $CDCl_3$/TFA and DMSO-$d_6$ as solvents. $^{13}$C NMR spectra were acquired on a Varian Unity Inova 500 MHz using $CDCl_3$/TFA and DMSO-$d_6$ as solvents. FTIR spectra were acquired on a Thermo Nicolet iS10 FTIR Spectrometer equipped with a Smart Diamond attenuated total reflectance (ATR) accessory in the region of 4000-400 $cm^{-1}$. Background measurements were initially performed before analyzing the sample, with 8 scans completed using a resolution of 2 $cm^{-1}$. Size exclusion chromatography (SEC) was measured using a PSS SECurity™ GPC system equipped with a PFG 7 µm 8 × 50 mm pre-column, a PSS 100 Å, 7 µm 8 × 300 mm and a PSS 1000 Å, 7 µm 8 × 300 mm column in series and a differential refractive index (RI) detector at a flow rate of 1.0 mL $min^{-1}$ to determine the dispersities ($Đ$) and molecular weights of polymers. 1,1,1,3,3,3-hexafluoro-2-propanol (HFIP) was used as the

eluent. The systems were calibrated against Agilent Easi-Vial linear poly(methyl methacrylate) (PMMA) standards and analyzed by the software package PSS winGPC UniChrom.

**Rheology**

Rheological characterization was performed on a strain-controlled rheometer (TA Instruments, ARES-G2) at room temperature. A parallel plate (25 mm) was used for the oscillatory amplitude sweep, oscillatory frequency sweep, and cyclic dynamic oscillatory amplitude sweep experiments. Both cone (25 mm, 0.4 rad) and plate (25 mm) geometries were used for flow rheology to maintain consistent shear during viscosity measurement.

**Monomer and polymer synthesis:**

**γ-benzyl-l-glutamate *N*-carboxyanhydride synthesis:** Triphosgene (31.89 g, 107.48 mmol) and epichlorohydrin (79.53 g, 859.81 mmol) were initially dissolved in 850 mL of tetrahydrofuran (THF) in a 1 L round-bottomed flask with stirring. γ-benzyl-l-glutamate (51.0 g, 214.95 mmol) was then added in one portion and the reaction suspension was heated under reflux (68 °C). The reaction was continued until all solids disappeared and the solution became clear (1–2 h). The solution was then cooled using an argon balloon, any unreacted γ-benzyl-l-glutamate was filtered off and the solution was reduced to a third of its original volume in vacuo. The NCA was precipitated by addition of 1.2 L of hexane and stored overnight at –18 °C to fully precipitate. The solid NCA was dried in vacuo and then re-dissolved in 350 mL ethyl acetate. This solution was then precipitated into excess hexane (1.4 L), filtered and dried (this was completed two to three times). It was then dried in vacuo to afford a white fluffy solid

(yield: 51.4 g, 91 %). $^{1}$H NMR (600 MHz, $CDCl_3$/TFA, δ, ppm): 7.34-7.4 (m, 5H, -CH2*C5H6*), 6.36 (s, 1H, *NH*), 5.14 (s, 2H, -*CH2*C5H6), 4.37 (t, 1H, -CO*CH*NH-), 2.60 (t, 2H, -CO*CH2*CH2-), 2.10-2.31 (m, 2H, -COCH2*CH2*-); $^{13}$C NMR (500 MHz, $CDCl_3$/TFA, δ, ppm): 173.79, 168.70, 154.31, 134.58, 128.66, 67.94, 29.38, 26.49.

**l-Phenyl Glycine *N*-carboxyanhydride synthesis:** Triphosgene (0.4 eq) and epichlorohydrin (4 eq) were initially dissolved in 130mL of tetrahydrofuran (THF) in a 250 mL round-bottomed flask with stirring. Desired amino acid (1 eq) was then added in one portion and the reaction suspension was heated under reflux (68 °C). The reaction was continued until all solids disappeared and the solution became clear (1 h). The solution was then cooled using an argon balloon, filtered and then reduced to 1/3 of its original volume using a cold trap in the fumehood. The NCA was precipitated by addition of 200 mL of hexane and stored overnight at -18 °C to fully precipitate. The solid NCA was dried under vacuum and then re-dissolved in a minimum amount of ethyl followed by precipitation into excess hexane (200 mL), filtered and dried under vacuum (two to three times). It was then vacuum dried to afford a crystalline

(yield: 9 g, 85 %). $^{1}$H NMR (600 MHz, $CDCl_3$/TFA, δ, ppm): 7.49-7.39 (m, 5H, -*C4H4*), 6.35 (s, 1H, *NH*), 5.34 (s, 1H, -CO*CH*NH-);$^{13}$C NMR (500 MHz, $CDCl_3$/TFA, δ, ppm): 167.87, 155.40, 63.13, 30.70, 17.94, 16.67.

**3-Arm poly(benzyl-l-glutamate) (3-PBLG) polypeptide synthesis:** γ-benzyl-L-glutamate NCA was dissolved in a CHCl3: DMF (10:1) mixture in a 250 mL flask with stirring. Tris(2-aminoethyl)amine (TREN) in CHCl3 was then quickly added to the flask in one portion. The flask was initially evacuated under vacuum to remove $CO_2$ and then a balloon filled with argon (Ar) was slowly purged through the solution with stirring continued at room temperature until

NCA was fully consumed via FTIR spectroscopy. An aliquot of the solution was taken and kept for size exclusion chromatography (SEC) measurements and NMR analysis.

**Macroinitiation of 3-arm poly(benzyl- l-glutamate) to form diblock copolypepeptide:** After full consumption of γ -benzyl- l-glutamate NCA, l-phenylglycine NCA was dissolved in 30 mL DMF and then quickly added to their respected reaction in one part. The flasks were evacuated under vacuum to remove $CO_2$ and then a balloon filled with Ar was slowly purged through the solution with stirring continued at room temperature until NCA was fully consumed via FTIR spectroscopy. The diblock copolymers were then precipitated into excess diethyl ether (1 L), centrifuged, and fully dried under vacuum.

**General block copolypeptide deprotection:** The copolymer was fully suspended in 100 mL $CHCl_3$, after which 80 mL TFA was added. 20 mL of 33 wt% HBr in acetic acid was then added dropwise over 10 min, and the solution was stirred overnight at room temperature. The solution was then precipitated into excess diethyl ether (1.5 L) and dried in vacuo. The solid was suspended in 50 mL deionised water, and then the pH was adjusted to 7-8 until a viscous translucent solution formed. The solution was dialysed against deionised water for 2 days in a 10 kDa MWCO SnakeSkin® membrane with frequent water replacement followed by lyophilization to yield a white fluffy solid.

**Methacrylamide functionalization of diblock copolypeptide (3-CP-PG):** The deprotected copolymer (2 g, $1.47\times10^{-1}$ mmol) was dissolved in 800 mL of deionised water and pH adjusted to 8 with $NaHCO_3$. 25 equivalents of DMT-MM (1g, 3.7mmol) was then added and stirring was continued for 10 min to activate the carboxyl groups. 3-aminopropyl methacrylamide hydrochloride (0.66 g, 3.7 mmol) in 10 mL deionised water was then added and stirring was

continued for 2 days in darkness at room temperature. The solution was then dialysed against deionised water for 3 days in darkness in a 3.5 kDa MWCO SnakeSkin® membrane with frequent water replacement followed by lyophilisation (yield: 1.43g)

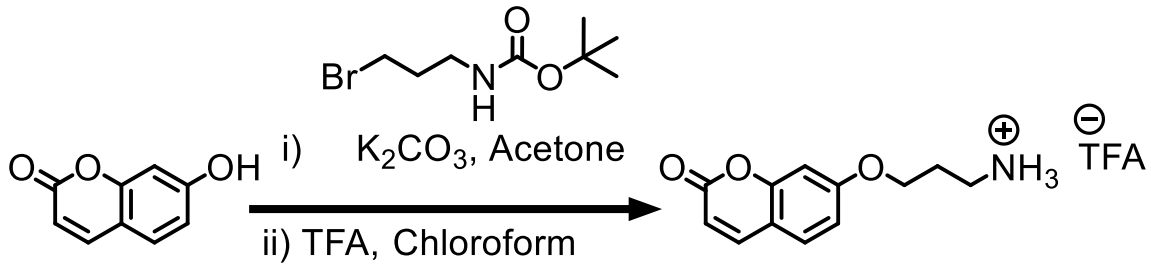


**Umbilleferone amine Synthesis:** Umbilleferone (90.8mg ,0.56mmol), *tert*-butyl-*N*-(3-brompropyl)-carbamate (200mg, 0.84 mmol) and anhydrous potassium carbonate was dissolved in anhydrous acetone and refluxed for 24 hours. The reaction was monitored by TLC to track the full consumption of the umbelliferon starting material. After completion, the solids were filtered off, and the solvent was evaporated under reduced pressure. The product was then dissolved in chloroform and washed 3 times with water, subsequently with brine, and dried under magnesium sulfate. Trifluoro acetic acid was then added and allowed to react for 3 hours. The solids were then filtered, collected, and washed with excess warm chloroform to yield the final product as a white solid (yield: 90mg, 48%)

**Methacrylamide and Umbilleferone functionalization (3-CP-PG-Um):** The deprotected copolymer (2 g, $1.47\times10^{-1}$ mmol) was dissolved in 800 mL of deionised water and pH adjusted to 8 with $NaHCO_3$. 26 equivalents of DMT-MM (1.01g, 3.7mmol ) was then added and stirring was continued for 10 min to activate the carboxyl groups. 3-aminopropyl methacrylamide hydrochloride (0.66 g, 3.7 mmol) and umbilleferone amine (0.0032g, $1.47\times10^{-2}$ mmol ) were

added simultaneously in 10 mL deionised water was then added and stirring was continued for 2 days in darkness at room temperature. The solution was then dialysed against deionised water for 3 days in darkness in a 3.5 kDa MWCO SnakeSkin® membrane with frequent water replacement followed by lyophilisation (yield: 1.20 g)

**Fluoresceine functionalization of GelMA (GelMA-Flu):** GelMA (0.35g ) and Fluorescein isothiocyanate (0.0021g) was dissolved in 250mL of PBS buffer (pH=7.4). The solution was stirred overnight at room temperature in the dark for 24 hours. The solution was then dialysed against deionised water for 3 days in darkness in a 3.5 kDa MWCO SnakeSkin® membrane with frequent water replacement followed by lyophilisation (yield: 0.2 g)

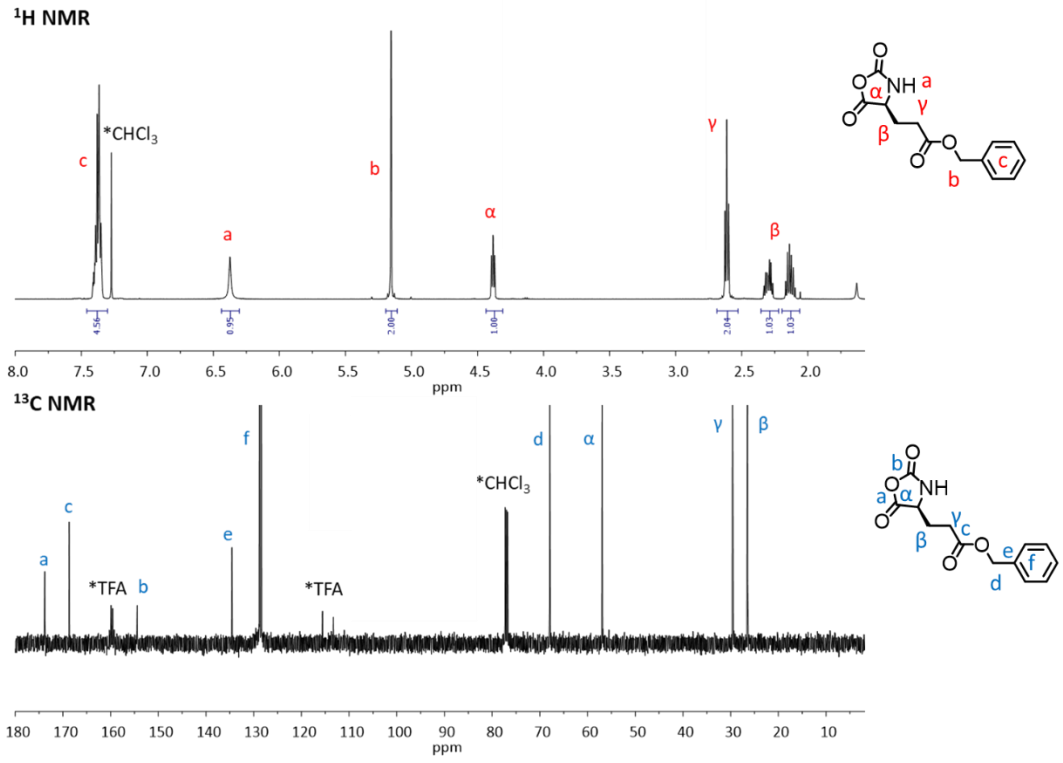


Figure C1: $^{1}$H NMR and $^{13}$C NMR spectra of γ-benzyl-*l*-glutamate *N*-carboxyanhydride (BLG NCA) in 15% TFA in $CDCl_3$.

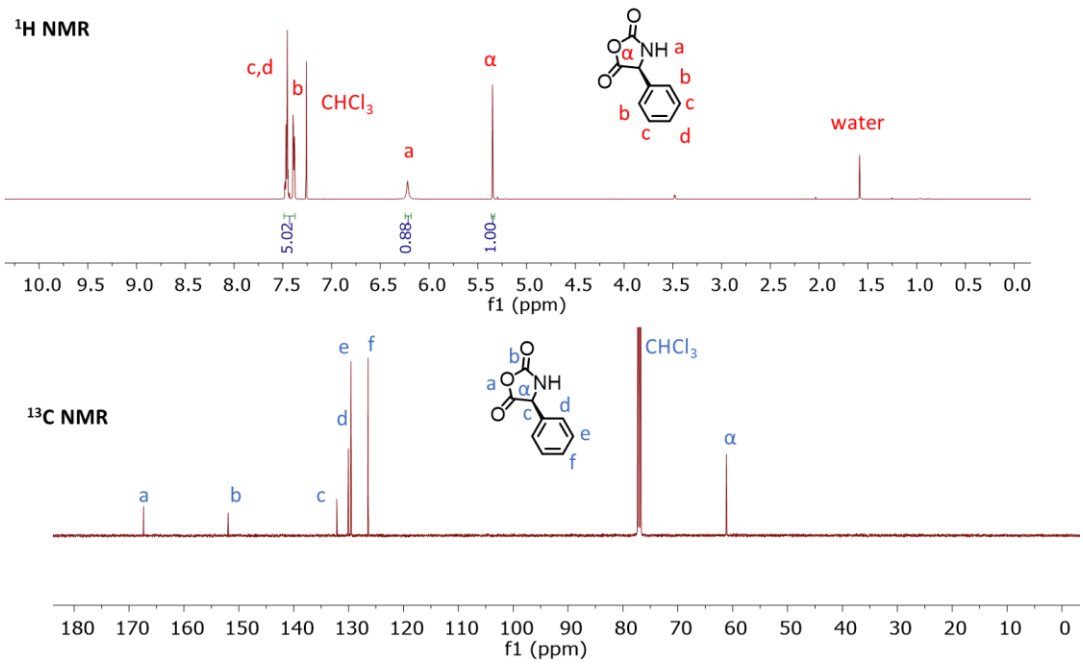


Figure C2: $^{1}$H NMR and $^{13}$C NMR spectra of *l*-phenylglycine *N*-carboxyanhydride (LPG NCA) in $CDCl_3$.

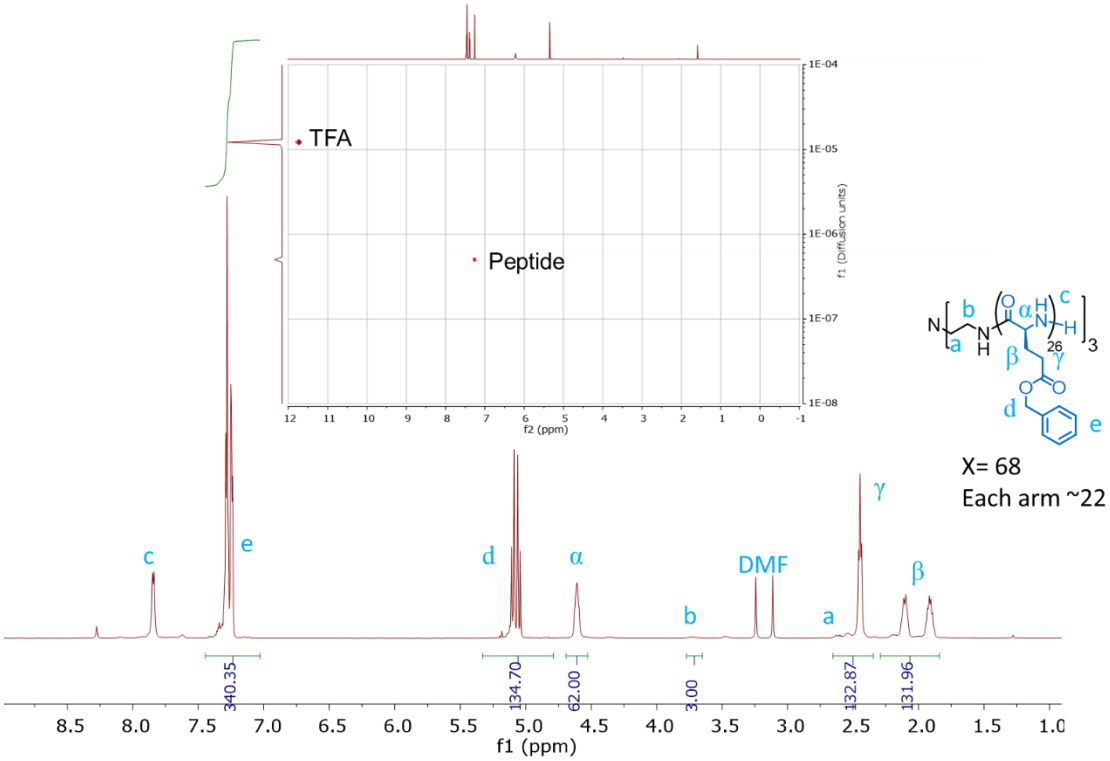


Figure C3: $^{1}H$ NMR spectra of 3- $PBLG_{68}$ and DOSY in 15% TFA in $CDCl_3$.

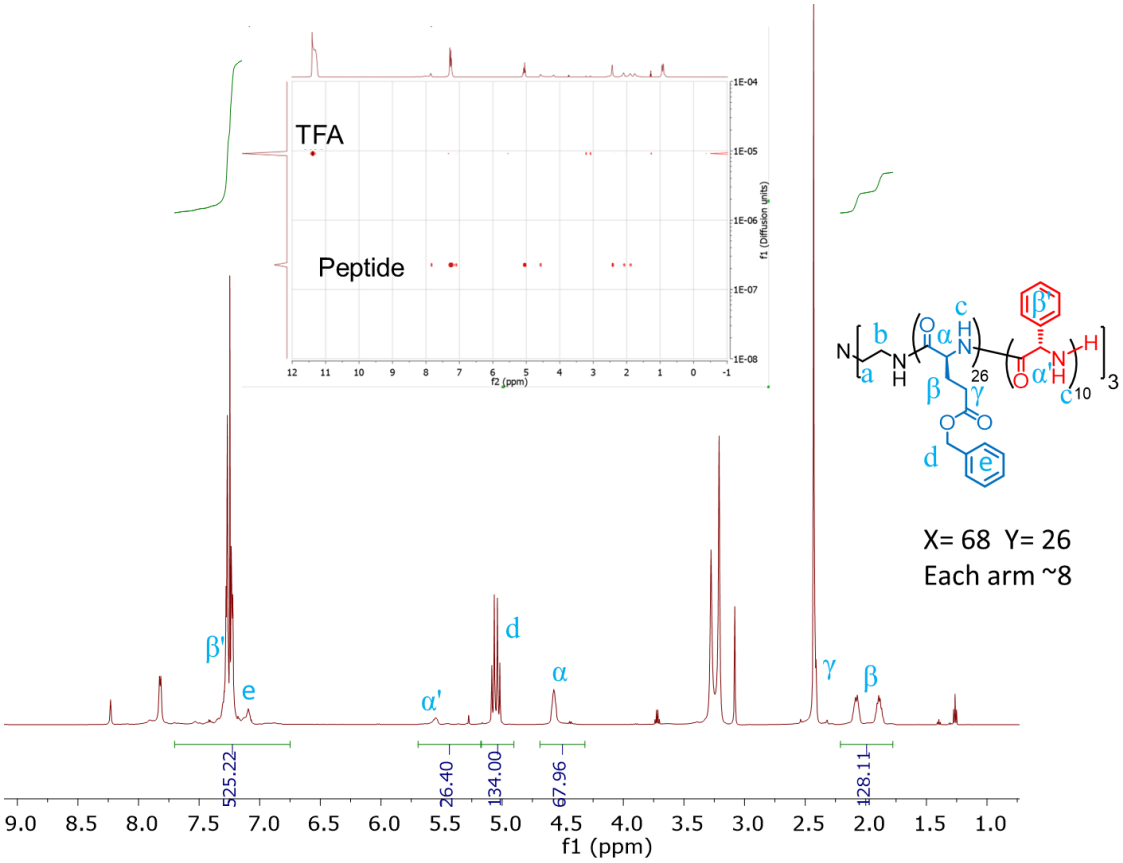


Figure C4: $^{1}$H NMR spectra of 3-PBLG$_{68}$-*b*-PPG$_{26}$ and DOSY in 15% TFA in $CDCl_3$.

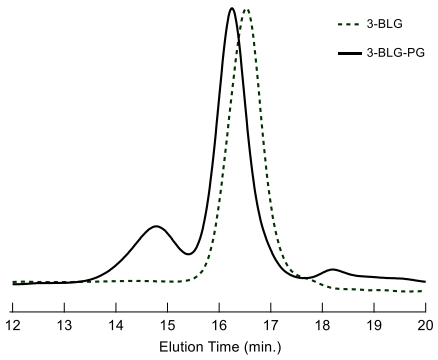


Figure C5: SEC of 3- PBLG$_{68}$(3-BLG) and 3- PBLG$_{68}$-b-PPG$_{26}$ (3-BLG-PG) in HFIP.

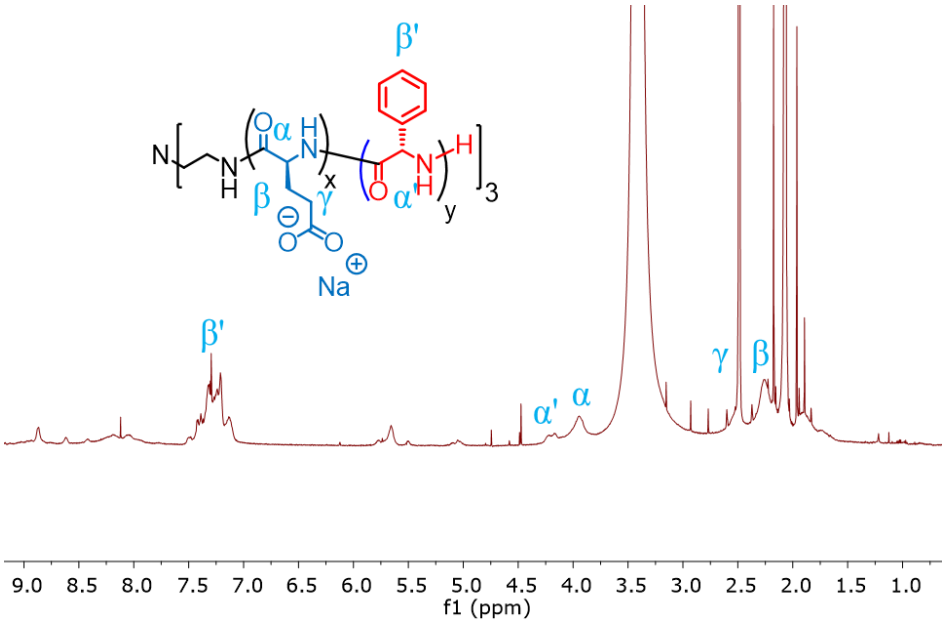


Figure C6: $^{1}$H NMR spectra of 3-PLG$_{68}$-*b*-PPG$_{26}$ and DOSY in DMF.

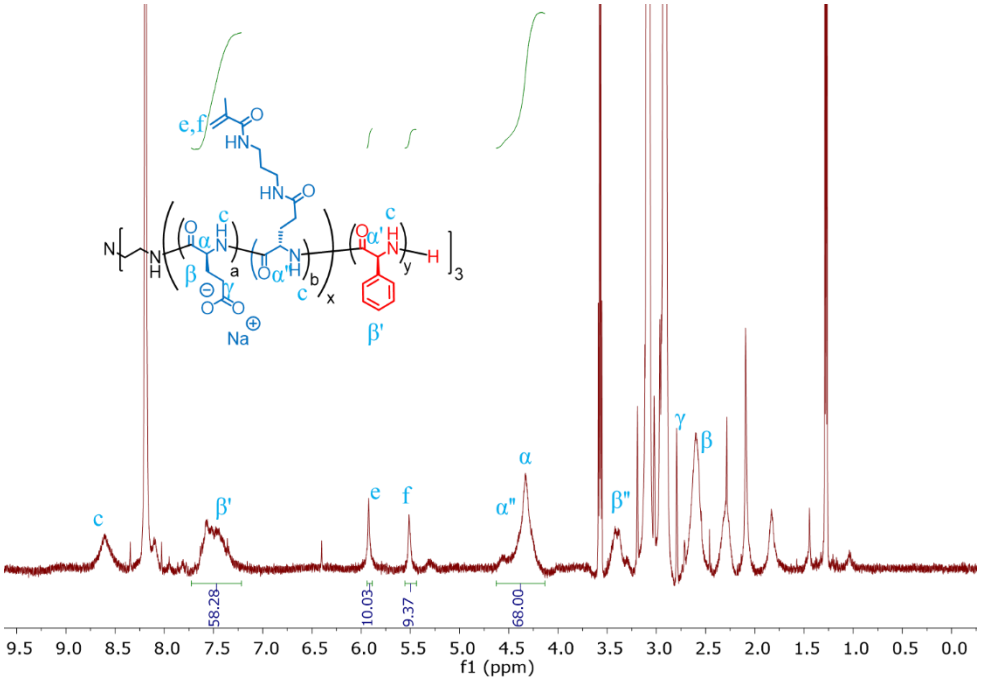


Figure C7: $^{1}$H NMR spectra of 3-PLG$_{68}$-*b*-PPG$_{26}$ functionalized with methacrylamide (3-CP-PG) and DOSY in DMF.

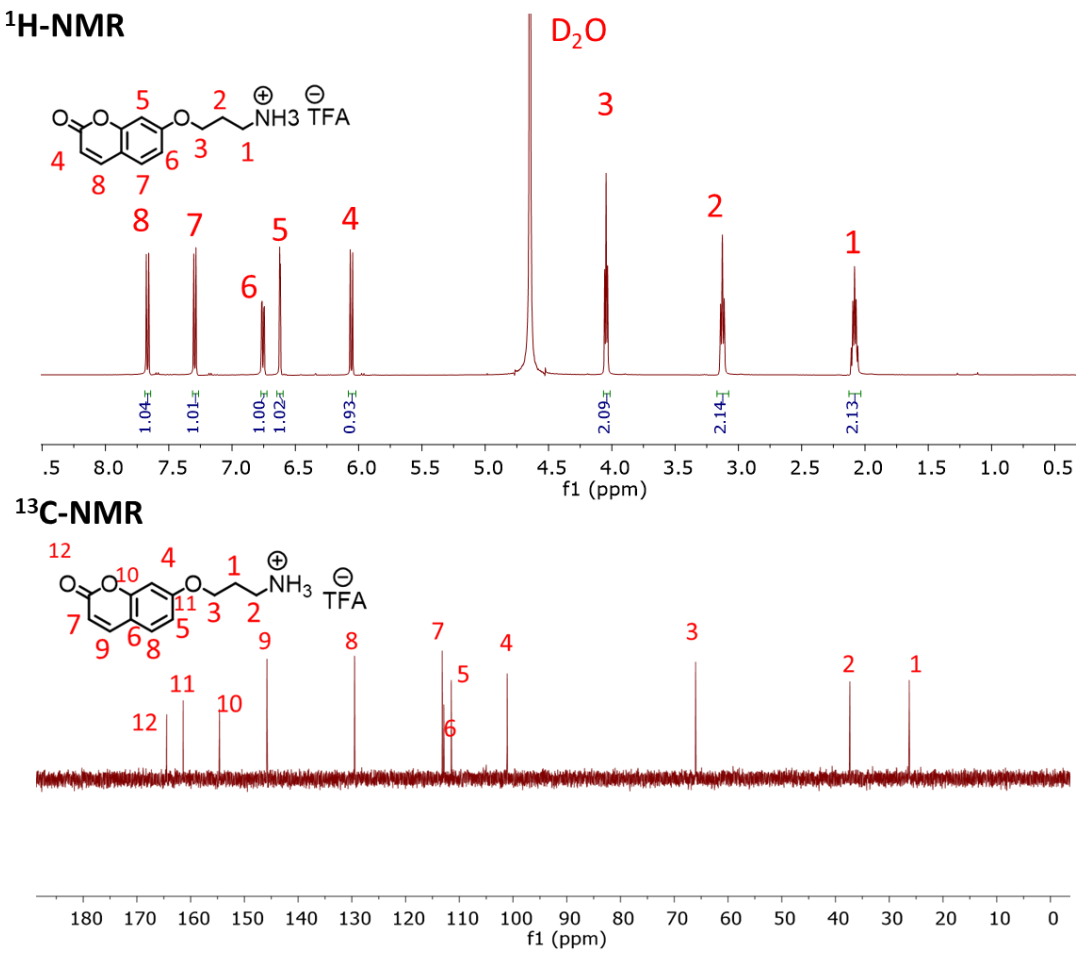


Figure C8: $^{1}H$ NMR and $^{13}C$ NMR spectra of umbelliferon amine in $D_2O$.

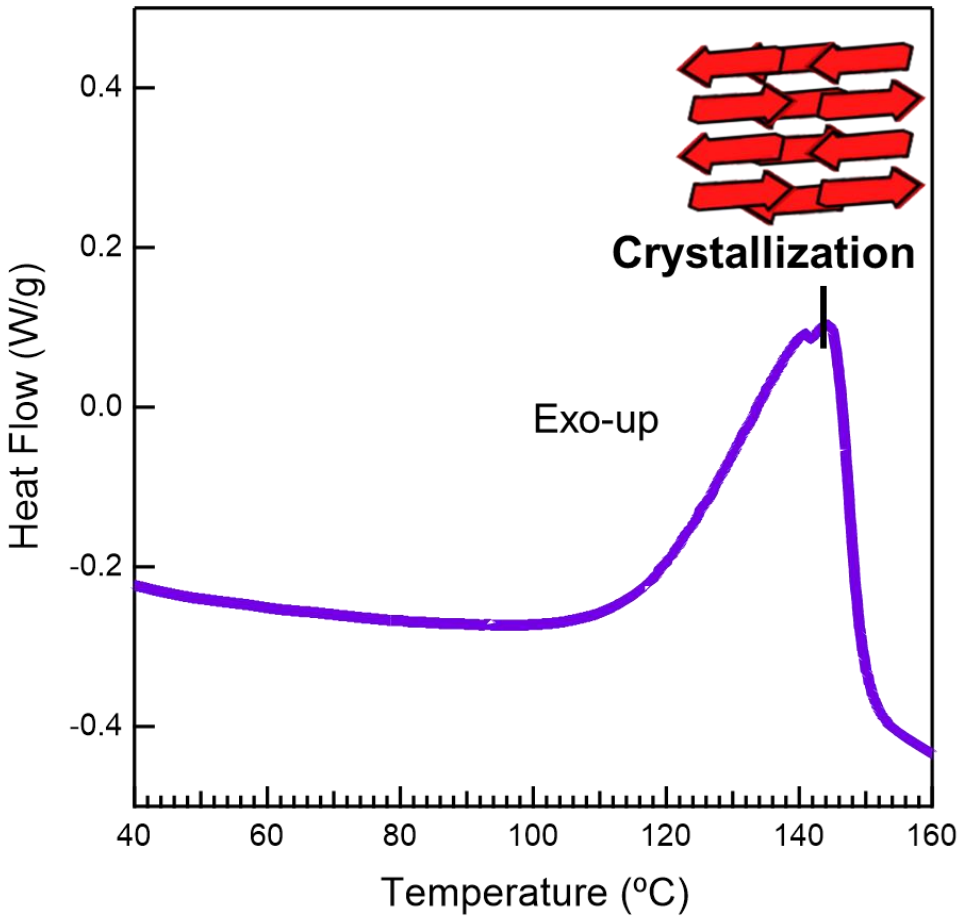


Figure C9: Differential Scanning Calorimetry (DSC) of 3-CP-PG in the solid state

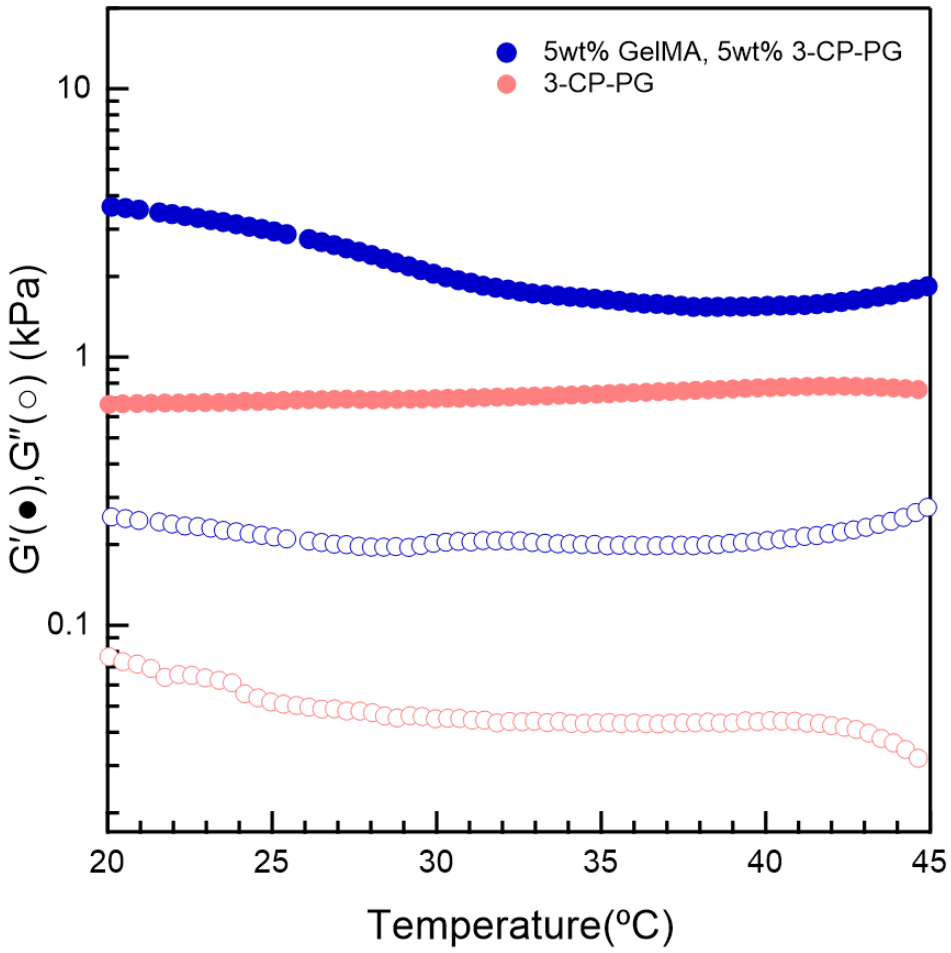


Figure C10: Temperature sweeps of representative blended material and of pure 3-CP-PG

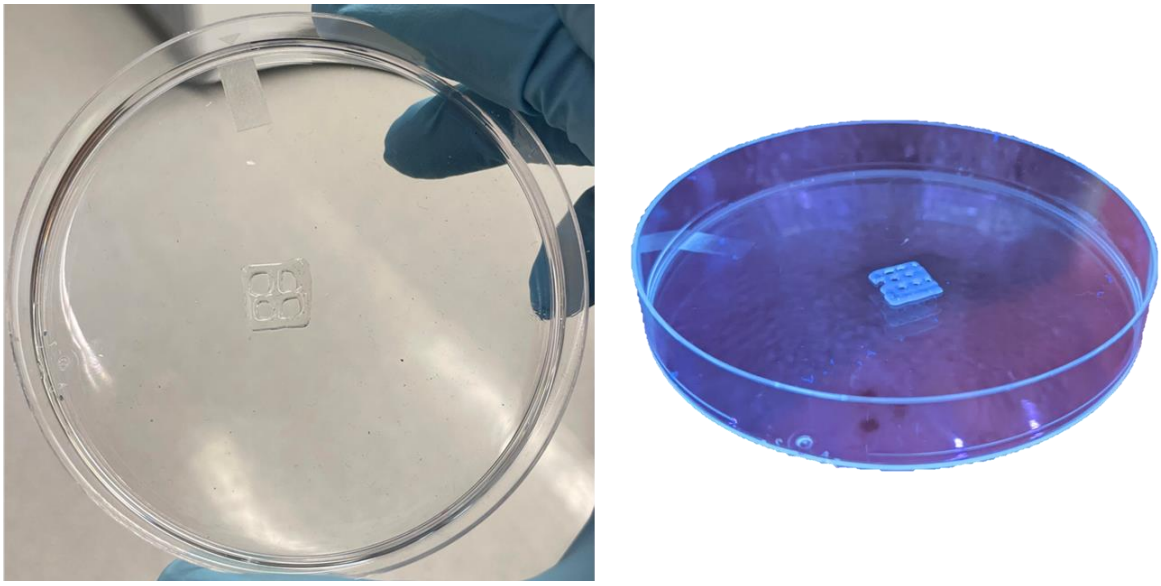

Figure C11: 7.5 wt% 3-CP-PG-Umb,5wt% GelMA blended material extruded with 21G needle at 37°C at 180KPa

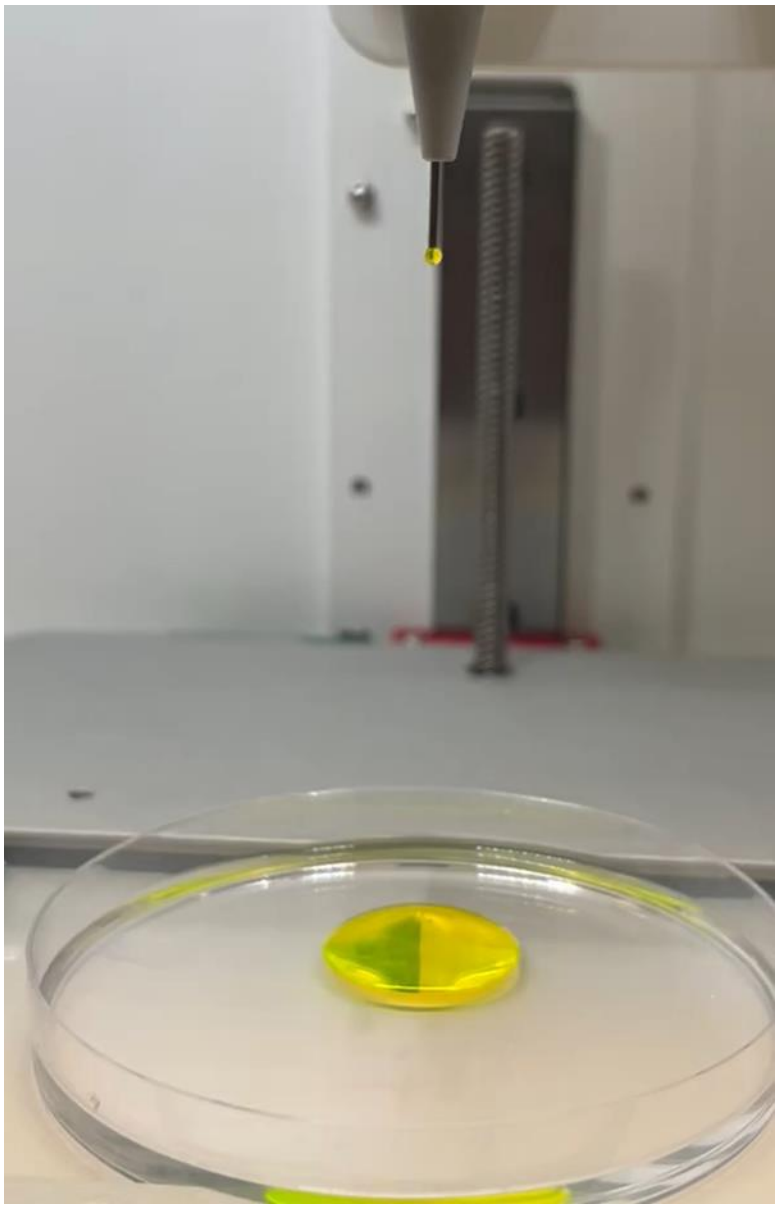

Figure C12: 12.5 wt% GelMA-Fluo dripping at 37°C on the commercial BioX without applied pressure

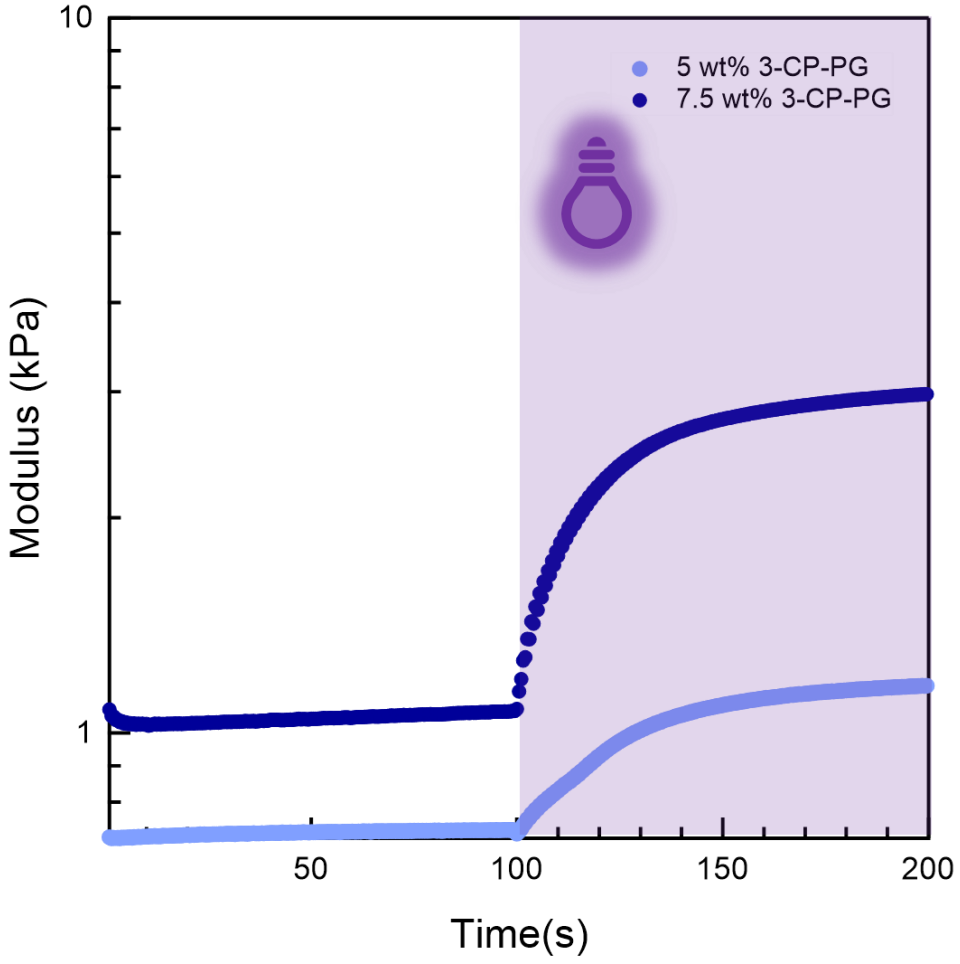


Figure C13: Real-time UV light curing at intensity of 25 mW/cm$^2$ at 37°C

Table C1: Swelling ratio and gel fraction of pure peptide networks

| Initial Wt% peptide | Swelling Ratio | Gel Fraction | Final wt% peptide swollen |
|---|---|---|---|
| 7.5wt% | 80±10% | 93±3% | 5.2±2% |
| 5wt% | 102±10% | 92±5% | 2.3±3% |
| 2.5wt% | 67% | 37%±8% | 1.1%±10% |

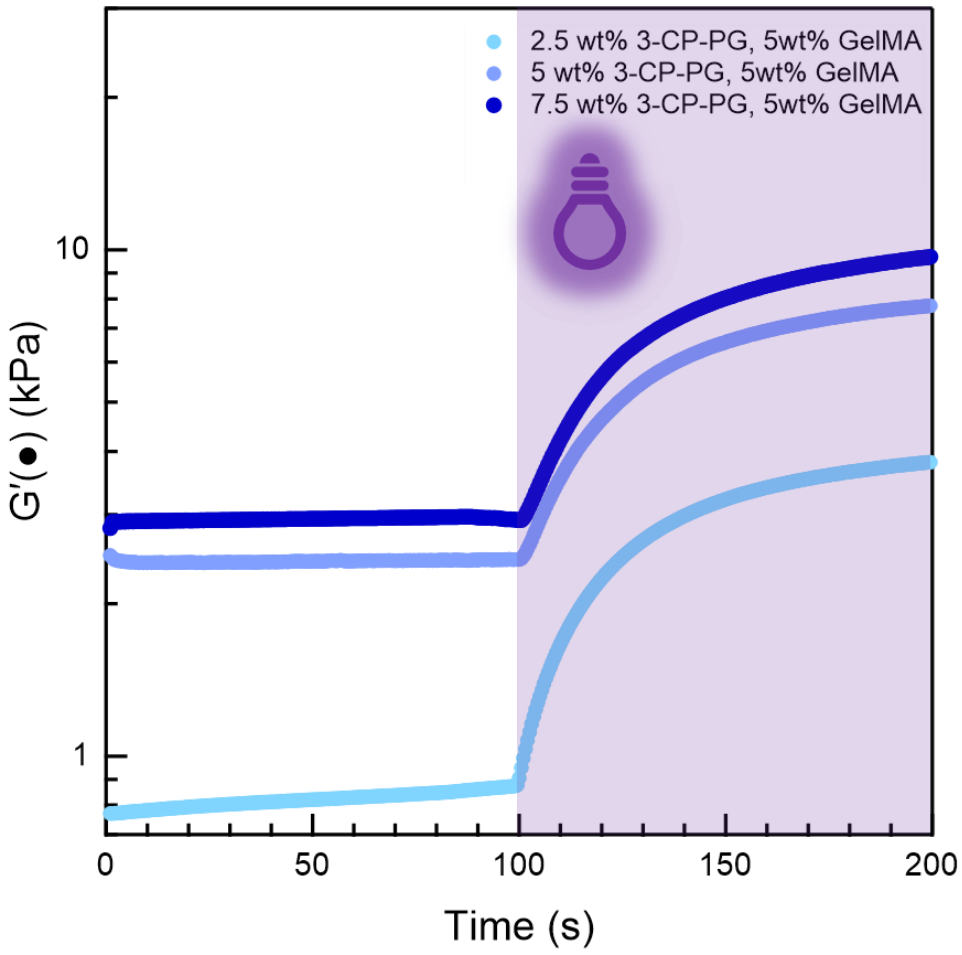


Figure C14: Real-time UV light curing at intensity of 25 mW/cm2 at 0°C

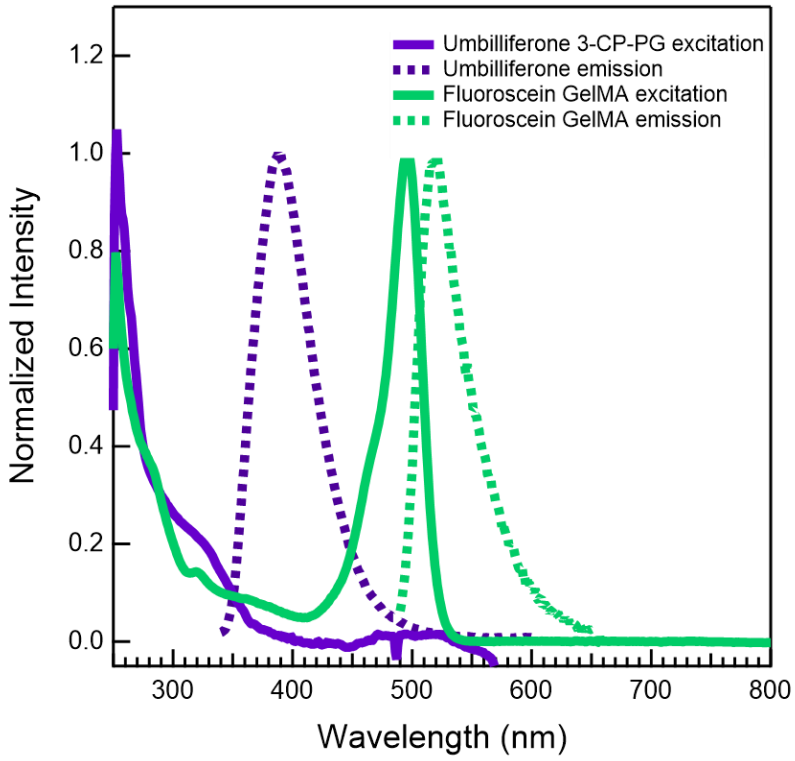


Figure C15: Normalized UV-Vis and fluorescence spectra for star copolypeptide tagged umbelliferon and GelMA tagged fluorescein.

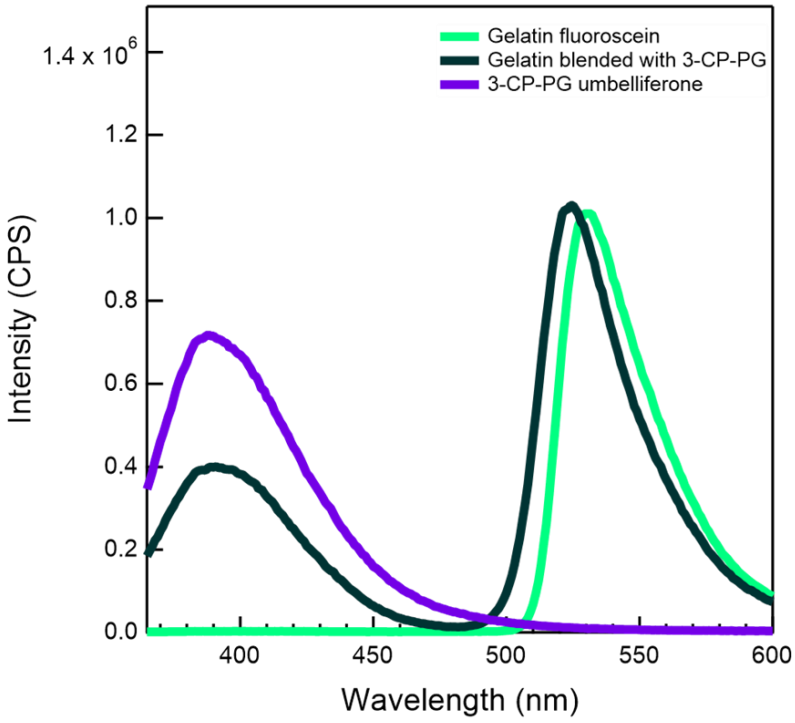


Figure C16: Fluorescence spectra scan of fluorescent network post proteinase K digestion excited at 325 nm

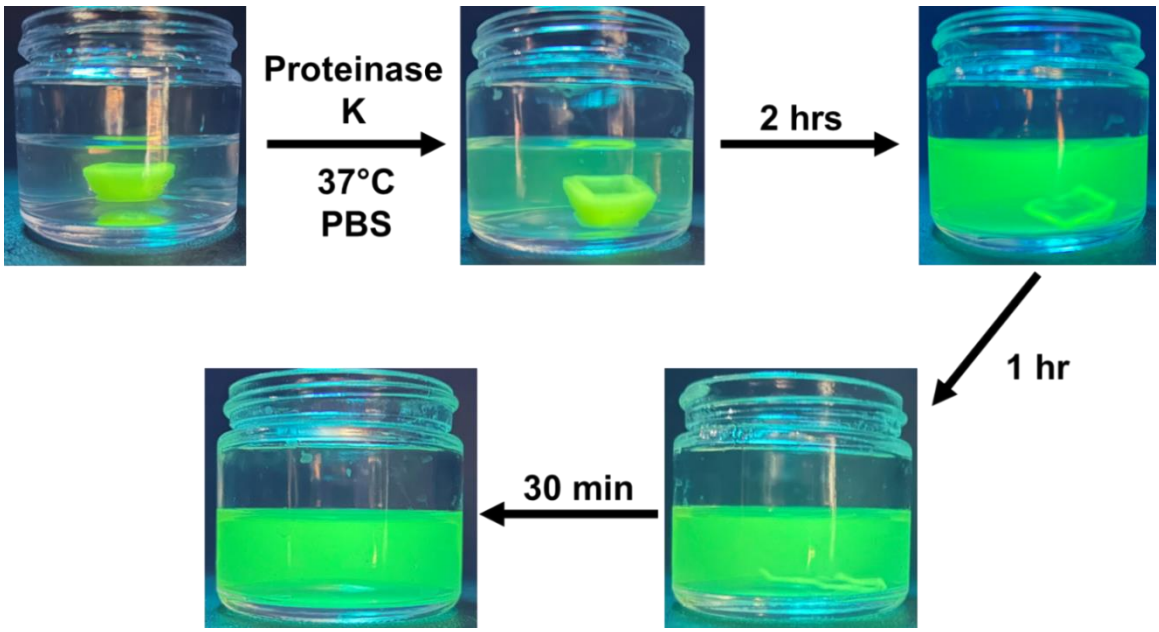


Figure C17: Inverted pyramid of blended material degrading in 1 wt% proteinase K in PBS buffer